

ISTANBUL TECHNICAL UNIVERSITY ★ GRADUATE SCHOOL OF SCIENCE
ENGINEERING AND TECHNOLOGY

**A PERFORMANCE IMPROVEMENT STUDY OF A PERMANENT-MAGNET
ASSISTED SYNCHRONOUS MOTOR USED IN WASHERS**



M.Sc. THESIS

Liridon XHELADINI

Department of Electrical Engineering

Electrical Engineering Programme

SEPTEMBER 2017

ISTANBUL TECHNICAL UNIVERSITY ★ GRADUATE SCHOOL OF SCIENCE
ENGINEERING AND TECHNOLOGY

**A PERFORMANCE IMPROVEMENT STUDY OF A PERMANENT-MAGNET
ASSISTED SYNCHRONOUS MOTOR USED IN WASHERS**



M.Sc. THESIS

Liridon XHELADINI
(504151075)

Department of Electrical Engineering

Electrical Engineering Programme

Thesis Advisor: Assoc.Prof. Dr. Lale Tükenmez ERGENE

SEPTEMBER 2017

ISTANBUL TEKNİK ÜNİVERSİTESİ ★ FEN BİLİMLERİ ENSTİTÜSÜ

**KALICI MIKNATIS DESTEKLİ SENKRON RELÜKTANS MOTORLARDA
PERFORMANS ARTIRMAYA YÖNELİK BİR ÇALIŞMA**

YÜKSEK LİSANS TEZİ

**Liridon XHELADİNİ
(504151075)**

Elektrik Mühendisliği Anabilim Dalı

Elektrik Mühendisliği Programı

Tez Danışmanı: Doç.Dr. Lale Tükenmez ERGENE

EYLÜL 2017

Liridon Xheladini, a M.Sc. student of İTÜ Graduate School of Science Engineering and Technology with student ID 504151075, successfully defended the thesis entitled “A PERFORMANCE IMPROVEMENT STUDY OF A PERMANENT-MAGNET ASSISTED SYNCHRONOUS MOTOR USED IN WASHERS”, which he prepared after fulfilling the requirements specified in the associated legislations, before the jury whose signatures are below.

Thesis Advisor : **Assoc. Prof. Dr. Lale Tükenmez ERGENE**
Istanbul Technical University

Jury Members : **Asst.Prof. Dr. Murat YILMAZ**
İstanbul Technical University

Assoc.Prof. Dr. Nur BEKİRÖĞLU
Yıldız Technical University

Date of Submission : 13 September 2017

Date of Defense : 18 September 2017





To my family,



FOREWORD

First of all, I would like to thank my advisor Assoc. Prof. Dr. Lale Tükenmez ERGENE for her trust, continuous motivation, giving me the opportunity to work together on this project and accomplish my master studies.

During the project work, for their help and useful advices, I would like to thank Asst. Prof. Dr. Murat Yılmaz, Dr. Murat Imeryüz and Dr. Taşdemir Aşan.

For all the tiring hours, days and weeks spent together in front of the computer trying to finish our project tasks and for his great help on writing this thesis, I would like to tell my friend Alper Tap that I am so grateful and I will never forget it.

For their support, motivation, continuous care and love during the past 6 years of studies, I would like to thank my father Xhezair XHELADINI, my mother Ziavere Nuhiu XHELADINI and my sisters Ferdese and Dardane XHELADINI.

For all their work and struggle, on both bachelor and master studies, I would like to thank all professors and teaching assistants of Electrical Engineering Department that never turned us back when we needed them for help.

I would like also to thank all my friends, especially Gentian ALILI and Arlind BUÇINCA, who have supported and helped me during this project and during other challenges of everyday life.

The work done on this thesis was taken from the TUBITAK 1001 project with number 115E416. For their support during this project, I would like to thank the Scientific and Technological Research Council of Turkey (TUBITAK).

September 2017

Liridon XHELADINI
Electrical Engineer

TABLE OF CONTENTS

	<u>Page</u>
FOREWORD	ix
TABLE OF CONTENTS	xi
ABBREVIATIONS	xv
SYMBOLS	xvii
LIST OF TABLES	xix
LIST OF FIGURES	xxi
SUMMARY	xxvii
ÖZET	xxix
1. INTRODUCTION	1
1.1 Purpose of the Thesis	2
1.2 Literature Review	3
1.3 Working Principle and Mathematical Model of SynRM	12
1.3.1 PMSynRM's mathematical model	16
2. ANALYTICAL ROTOR DESIGN AND INDUCTANCE CALCULATIONS	17
2.1 Pole Number.....	17
2.2 Number of Barriers.....	18
2.3 Insulation Ratios.....	18
2.4 Positioning of Barriers and Segments	19
2.5 Segment Width	20
2.6 Flux Barrier Width in Q-axis	22
2.7 Barrier Width in D-axis.....	23
2.8 Direct and Quadrature Inductance Calculation	24
3. FINITE ELEMENT METHOD	31
3.1 Maxwell Equations.....	31
3.2 Boundary Conditions and Periodicity	32
3.3 Discretization of Model and Mesh Structure	33
4. OPTIMIZATION ANALYSIS OF THE SAMPLE PROTOTYPE	35
4.1 Analysis of Air-gap Length's Effects.....	36
4.1.1 Motor model with $g=1\text{mm}$	36
4.1.2 Motor model with $g=0.9\text{mm}$	37
4.1.3 Motor model with $g=0.8\text{mm}$	38
4.1.4 Motor model with $g=0.7\text{mm}$	38
4.1.5 Motor model with $g=0.6\text{mm}$	39
4.1.6 Motor model with $g=0.5\text{mm}$	39
4.1.7 Comparison results and analysis	40
4.2 Selection of the Magnet Type and Dimensions	43
4.3 The Effects of Distance Between First Barriers "D"	45
4.3.1 Magnet volume, air-gap length and "D" length's effects	46
4.3.1.1 Motor model with $g=0.8\text{mm}/D=22.1\text{mm}$	48

4.3.1.2	Motor model with $g=0.7\text{mm}/D=22.1\text{mm}$	48
4.3.1.3	Motor model with $g=0.7\text{mm}/D=39.66\text{mm}$	49
4.3.1.4	Comparison of results and analysis	49
4.4	Stator Yoke and Teeth Optimization.....	53
4.4.1	Motor model with $g=0.5\text{mm}$	53
4.4.2	Motor model with $g=0.6\text{mm}$	54
4.4.3	Motor model with $g=0.7\text{mm}$	54
4.4.4	Motor model with $g=0.8\text{mm}$	55
4.4.5	Motor model with $g=0.9\text{mm}$	55
4.4.6	Motor model with $g=1\text{mm}$	56
4.4.7	Comparison of results and analysis	56
4.5	Analysis of Multilayer Winding's Effects.....	60
4.5.1	Motor model with 20° shifted winding layer	62
4.5.2	Motor model with 40° shifted winding layer	63
4.5.3	Comparison results and analysis	63
4.6	Effects of the Ferromagnetic Material.....	67
4.7	Analysis of the Slot Opening Dimensions' Effects.....	70
4.7.1	Slot opening width	71
4.7.2	Slot opening height.....	74
4.8	Analysis of the Slot Shape's Effects	75
4.8.1	Effect of parallel tooth edges and parallel slot edges.....	75
4.8.2	Effect of slot's inner wall	79
4.9	Effects of Tooth Bottom's Shape	80
4.10	Final Electromagnetic Comparison	85
4.11	Test Results of the Optimized Prototype Motor.....	88
4.12	Complete Performance of Sample and Optimized Prototype.....	91
5.	THERMAL ANALYSIS	95
5.1	Heat Transfer	96
5.1.1	Conduction	96
5.1.2	Convection	98
5.1.3	Radiation	98
5.1.4	Motor-CAD software	99
5.2	Thermal Analysis of the Sample Prototype.....	99
5.2.1	Geometry settings.....	100
5.2.2	Windings settings	100
5.2.3	Loss parameters.....	101
5.2.4	Material settings	102
5.2.5	Interface settings	103
5.2.6	Radiation settings	104
5.2.7	Natural convection settings	105
5.2.8	Front and rear end-space	105
5.2.9	Washing mode thermal results of the sample prototype	107
5.2.9.1	Spinning mode thermal results of the sample prototype	111
5.3	Thermal Analysis of the Optimized Prototype	112
5.3.1	Washing mode thermal circuit and thermal results.....	113
5.3.2	Spinning mode thermal analysis	117
5.4	Comparison of Thermal Analysis Results.....	118
6.	MECHANICAL STRESS ANALYSIS.....	119
6.1	Spinning Mode Test of the Sample Prototype.....	119
6.2	Washing Mode Test of the Sample Prototype	121

6.3 Spinning Mode Test of the Optimized Prototype.....	123
6.4 Washing Mode Test of the Optimized Prototype.....	124
6.5 Comparison of Mechanical Stress Analysis Results	126
7. RESULTS AND RECOMMENDATIONS	127
REFERENCES	129
CURRICULUM VITAE.....	133





ABBREVIATIONS

SynRM	: Synchronous Reluctance Motor
PMaSynRM	: Permanent Magnet Assisted Synchronous Reluctance Motor
FEM	: Finite Element Method
P.U.	: Per unit
MMF	: Magneto-motive Force
NdFeB	: Neodymium Iron Boron
FFT	: Fast Fourier Transform
BPM	: Brushless Permanent Magnet Motor
BLDC	: Brushless Direct Current Motor
RMS	: Root Mean Square



SYMBOLS

L_d	: d-axis inductance [H]
L_q	: q-axis inductance [H]
L_{abc}	: a,b and c phase inductances [H]
$L_{s\sigma}$: Stator winding leakage inductance [H]
ξ	: Saliency ratio
n_s	: Stator slot number per pole pair
n_r	: Rotor slot number per pole pair
m	: Phase number
p	: Pole pair number
ω_r	: Rotational speed [rad/s]
θ_r	: Rotor angle [°]
L	: Stator stack length [mm]
α	: Barrier pitch angle [°]
k	: Barrier number
h	: Iron segment index
$f_{d,q,h}$: Per-unit MMF value under iron segment
S	: Segment width [mm]
P	: Number of poles
$I_{d,q}$: Direct and quadrature axis current [A]
k_w	: Winding factor
B_{ic}	: i^{th} barrier central magnetic flux density [T]
B_{is}	: i^{th} barrier side magnetic flux density [T]
B_{gi}	: i^{th} blocks air-gap magnetic flux density [T]
$W_{id,q}$: i^{th} barrier width in d, q-axis [m]
D_s	: Stator inner diameter [m]
l_d	: Total length available in d-axis [m]
L_{ic}	: i^{th} barrier central length [m]
L_{is}	: i^{th} barrier side length [m]
$\Phi_{d,q}$: Magnetic flux in d, q-axis [Wb]
$\Psi_{d,q}$: Flux linkage in d,q-axis [Wb]
D	: Distance between first barriers [m]
Q	: Heat amount [W]
T	: Temperature value [°C]
A	: Cross sectional area [m ²]
Q'	: Generated heat in unit volume [W/m ³]
c	: Material specific heat capacity [J/kg°C]
ρ	: Material density [kg/m ³]
k_c	: Conduction constant [W/m°C]
h_c	: Convection constant [W/m ² °C]
σ	: Stefan-Boltzman constant [W/m ² K ⁴]
h_{nc}	: Heat transfer factor
B_r	: Remanent magnetic flux density [T]



LIST OF TABLES

	<u>Page</u>
Table 2.1 : Inductance values and saliency ratios.	29
Table 4.1 : Characteristics of the sample prototype [3].	35
Table 4.2 : Harmonic component amplitudes for different g.	42
Table 4.3 : Average and RMS data comparison for different g.	42
Table 4.4 : The effects of magnet volume and air-gap length on the induced torque.	43
Table 4.5 : Air-gap length and magnet volume’s effects using ferrite magnet.	44
Table 4.6 : Air-gap length and magnet volume’s effects using NdFeB magnet.	45
Table 4.7 : Effect of distance “D” on the induced torque and ripple.	46
Table 4.8 : Effects of D, magnet volume and air-gap length on the average torque and ripple.....	47
Table 4.9 : Harmonic component amplitude for different g and D values.....	52
Table 4.10 : Average and RMS data comparison of the three selectable models.	52
Table 4.11 : Stator yoke and tooth optimization results.....	57
Table 4.12 : Harmonic component amplitudes at different air-gap values for the optimized tooth and yoke.	59
Table 4.13 : Average and RMS data comparison for different improved models. ...	60
Table 4.14 : Winding factors for single and double layer models.	61
Table 4.15 : Harmonic component amplitudes for single and double layer models. ...	66
Table 4.16 : Average and RMS data comparison for single and double layer models.	66
Table 4.17 : Average and RMS data comparison for different materials.	69
Table 4.18 : Effect of ferromagnetic material on core loss and efficiency.	70
Table 4.19 : The effect of the slot opening width on torque, core loss and efficiency.	71
Table 4.20 : Effect of slot opening height on the average torque and ripple.	74
Table 4.21 : Harmonic component amplitudes for different slot types.....	79
Table 4.22 : Comparison results of parallel tooth and parallel slot edge models.	79
Table 4.23 : Effect of slot’s inner wall on average torque and ripple.	80
Table 4.24 : Harmonic component amplitudes for different tooth bottom.	84
Table 4.25 : Effect of tooth bottom shape on induced torque.	84
Table 4.26 : Average and RMS data comparison for different tooth bottom.....	85
Table 4.27 : Electromagnetic comparison of the sample and optimized prototype. .	85
Table 4.28 : Sample and optimized prototype’s air-gap flux density harmonics.....	88
Table 4.29 : Test and simulation torque values of the optimized prototype for different input current.	89
Table 4.30 : Test and simulation efficiencies of the optimized prototype for different input current.	90
Table 4.31 : Complete parameter values for sample prototype.....	93
Table 4.32 : Complete parameter values for optimized prototype.	94

Table 5.1 : Thermal analysis final results..... 118
Table 6.1 : Mechanical characteristics of rotor materials. 119
Table 6.2 : Mechanical stress analysis maximum results..... 126



LIST OF FIGURES

	<u>Page</u>
Figure 1.1 : Geometry of the sample PMSynRM [3].	2
Figure 1.2 : Axially laminated anisotropy rotor [14].	4
Figure 1.3 : Transversally laminated flux barrier rotor with cut-outs in the q-axis [14].	4
Figure 1.4 : Performance of difference PM insertions [25].	6
Figure 1.5 : Torque ripple of asymmetric barrier configuration. IPMSM A magnet is 300 kA/m and IPMSM B is 900 kA/m [26].	7
Figure 1.6 : Two barrier conventional PMSynRM & Evaluation of Machaon from R&J [28].	8
Figure 1.7 : 2 barrier PMSynRM rotor b) R&J rotor c) Machaon rotor all at $I = 5.3$ A [28].	9
Figure 1.8 : Structures against demagnetization [29].	10
Figure 1.9 : Demagnetization percentages against demagnetizing excitation of different barrier types [29].	11
Figure 1.10 : Torque ripple results of analytical model and FEA simulations [31].	11
Figure 1.11 : 3 phase 2 pole SynRM [21].	12
Figure 1.12 : d & q-axis equivalent circuits neglecting core losses [21].	16
Figure 1.13 : d & q-axis equivalent circuits including core losses [21].	16
Figure 2.1 : Barrier number effect on torque ripple [33].	18
Figure 2.2 : Change of inductance values with respect to q-axis insulation ratio [34].	19
Figure 2.3 : Barrier pitch, imaginary angle and insulation ratio [35].	20
Figure 2.4 : P. u. MMF distribution in the d-axis [35].	21
Figure 2.5 : P. u. MMF distribution in the q-axis [35].	22
Figure 2.6 : Determination of point C and distance l_d on the geometry [35].	24
Figure 2.7 : Magnetic flux lines in the q-axis [35].	25
Figure 2.8 : MMF lines along the flux barriers [35].	26
Figure 2.9 : MMF lines along the flux segments [35].	28
Figure 3.1 : (a) Single dimension (b) Two dimension (c) Three dimensional mesh element geometries [37].	33
Figure 4.1 : Magnetizing curve of M700 ferromagnetic material [38].	36
Figure 4.2 : Geometry of prototype model with $g=1$ mm.	36
Figure 4.3 : Magnetic flux density and equi-flux lines of model prototype model with $g=1$ mm.	37
Figure 4.4 : Magnetic flux density and equi-flux lines of model prototype model with $g=0.9$ mm.	37
Figure 4.5 : Magnetic flux density and equi-flux lines of model prototype model with $g=0.8$ mm.	38
Figure 4.6 : Magnetic flux density and equi-flux lines of model prototype model with $g=0.7$ mm.	38

Figure 4.7 : Magnetic flux density and equi-flux lines of model prototype model with $g=0.6$ mm.	39
Figure 4.8 : Magnetic flux density and equi-flux lines of model prototype model with $g=0.5$ mm.	39
Figure 4.9 : Torque graph comparison for different air-gap lengths.....	40
Figure 4.10 : Induced voltage graph comparison for different air-gap lengths.....	40
Figure 4.11 : Air-gap magnetic flux density comparison for different air-gap lengths.	41
Figure 4.12 : Harmonic amplitude comparison for different air-gap lengths.	41
Figure 4.13 : Prototype motor with increased magnet volume.	43
Figure 4.14 : Prototype motor with 19.2 cm^3 (left) and 25.34 cm^3 (right) volume of magnet.	44
Figure 4.15 : Distance between first flux barriers "D".	45
Figure 4.16 : Cross sectional view of models with different D and magnet volume.....	46
Figure 4.17 : Magnetic flux density and equi-flux line of model with $g=0.8\text{mm}/D=22.1\text{mm}$	48
Figure 4.18 : Magnetic flux density and equi-flux line of model with $g=0.7\text{mm}/D=22.1\text{mm}$	48
Figure 4.19 : Magnetic flux density and equi-flux line of model with $g=0.8\text{mm}/D=22.1\text{mm}$	49
Figure 4.20 : Torque graph comparison for different g and D values.....	50
Figure 4.21 : Induced voltage graph comparison for different g and D values.....	50
Figure 4.22 : Air-gap magnetic flux density comparison for different g and D values.	51
Figure 4.23 : Harmonic amplitude comparison for different g and D values.	51
Figure 4.24 : Magnetic flux density and equi-flux lines of model with $g= 0.5$ mm.	53
Figure 4.25 : Magnetic flux density and equi-flux lines of model with $g= 0.6$ mm.	54
Figure 4.26 : Magnetic flux density and equi-flux lines of model with $g= 0.7$ mm.	54
Figure 4.27 : Magnetic flux density and equi-flux lines of model with $g= 0.8$ mm.	55
Figure 4.28 : Magnetic flux density and equi-flux lines of model with $g= 0.9$ mm.	55
Figure 4.29 : Magnetic flux density and equi-flux lines of model with $g= 1$ mm.	56
Figure 4.30 : Torque graph comparison at different air-gap values for the optimized tooth and yoke.	57
Figure 4.31 : Induced voltage graph comparison at different air-gap values for the optimized tooth and yoke.	58
Figure 4.32 : Air-gap magnetic flux density comparison at different air-gap values for the optimized tooth and yoke.....	58
Figure 4.33 : Harmonic amplitude comparison at different air-gap values for the optimized tooth and yoke.	59
Figure 4.34 : Theoretical MMF of single and double layer models.....	61
Figure 4.35 : Geometry of the double layer- 20° shifted model with $g= 0.8\text{mm}$	62
Figure 4.36 : Magnetic flux density and air-gap flux density of the double layer- 20° shifted model with $g= 0.8$ mm.	62
Figure 4.37 : Geometry of the double layer- 40° shifted model with $g= 0.8\text{mm}$	63
Figure 4.38 : Magnetic flux density and air-gap flux density of the double layer- 40° shifted model with $g= 0.8$ mm.	63
Figure 4.39 : Torque graph comparison of single and double layer models.	64
Figure 4.40 : Induced voltage graph comparison of single and double layer models.	64

Figure 4.41 : Air-gap magnetic flux density comparison of single and double layer models.	65
Figure 4.42 : Harmonic amplitude comparison of single and double layer models.	65
Figure 4.43 : Magnetizing graphs of M700 and M350 ferromagnetic materials [38,39].	67
Figure 4.44 : Loss graphs of M700 and M350 ferromagnetic materials at 50 Hz [38,39].	68
Figure 4.45 : Magnetic flux density and equi-flux lines of $g=0.8\text{mm}$ model with M350 ferromagnetic material.	68
Figure 4.46 : Torque graph comparison of models with M700 and M350.	69
Figure 4.47 : Air-gap magnetic flux density of models with M700 and M350.	69
Figure 4.48 : Induced voltage graph comparison of models with M700 and M350.	70
Figure 4.49 : Stator yoke and tooth magnetic flux density of model with slot opening of 1 mm.	71
Figure 4.50 : Stator yoke and tooth magnetic flux density of model with slot opening of 1.5 mm.	72
Figure 4.51 : Stator yoke and tooth magnetic flux density of model with slot opening of 2 mm.	72
Figure 4.52 : Stator yoke and tooth magnetic flux density of model with slot opening of 2.5 mm.	73
Figure 4.53 : Stator yoke and tooth magnetic flux density of model with slot opening of 3 mm.	73
Figure 4.54 : Geometrical definition of slot opening height “H”.	74
Figure 4.55 : Geometry of $g=0.8\text{mm}$ model with parallel slot edges.	76
Figure 4.56 : Magnetic flux density and equi-flux lines of $g=0.8\text{mm}$ model with parallel slot edges.	76
Figure 4.57 : Torque graph comparison of $g=0.8\text{mm}$ models with parallel tooth and parallel slot edges.	77
Figure 4.58 : Induced voltage graph comparison of $g=0.8\text{mm}$ models with parallel tooth and parallel slot edges.	77
Figure 4.59 : Air-gap magnetic flux density comparison of $g=0.8\text{mm}$ models with parallel tooth and parallel slot edges.	78
Figure 4.60 : Harmonic amplitude comparison of $g=0.8\text{mm}$ models with parallel tooth and parallel slot edges.	78
Figure 4.61 : Different slot type configurations.	80
Figure 4.62 : Outwards round tooth bottom geometry.	81
Figure 4.63 : Magnetic flux density and equi-flux lines of $g=0.8\text{mm}$ model with outwards rounded tooth bottom.	81
Figure 4.64 : Torque graph comparison of inwards and outwards rounded tooth bottom models.	82
Figure 4.65 : Induced voltage graph comparison of inwards and outwards rounded tooth bottom models.	82
Figure 4.66 : Air-gap magnetic flux density comparison of inwards and outwards rounded tooth bottom models.	83
Figure 4.67 : Harmonic amplitude comparison of inwards and outwards rounded tooth bottom models.	83
Figure 4.68 : Torque graph comparison of the sample and the optimized prototype.	86
Figure 4.69 : Induced voltage graph comparison of the sample and the optimized prototype.	86

Figure 4.70 : Air-gap magnetic flux density comparison of the sample and the optimized prototype.....	87
Figure 4.71 : Harmonic amplitude comparison of the sample and the optimized prototype.....	87
Figure 4.72 : Test setup of the optimized prototype.	89
Figure 4.73 : Current–torque graphs of the optimized prototype.....	90
Figure 4.74 : Current-efficiency graphs of the optimized prototype.....	91
Figure 4.75 : Torque-speed characteristics of sample prototype.	92
Figure 4.76 : Current-Speed characteristics of sample prototype.	92
Figure 4.77 : Torque-speed characteristics of the optimized prototype.....	93
Figure 4.78 : Current-speed characteristics of the optimized prototype.	94
Figure 5.1 : Heat transfer due to temperature difference inside the object [40].	96
Figure 5.2 : Radial and axial view of the sample prototype motor.	100
Figure 5.3 : 3D view of the motor.....	100
Figure 5.4 : Winding and slot configuration.	101
Figure 5.5 : Active power loss settings.	102
Figure 5.6 : Material settings.	103
Figure 5.7 : Interface settings.....	104
Figure 5.8 : Radiation settings.	104
Figure 5.9 : Natural convection settings.....	105
Figure 5.10 : Front and rear end-space settings.	106
Figure 5.11 : Radial view of analytical temperature results of sample prototype...	107
Figure 5.12 : Lumped thermal circuit of the sample prototype.....	108
Figure 5.13 : Axial view of analytical temperature results of sample prototype. ...	109
Figure 5.14 : Slot temperature distribution using FEM.	109
Figure 5.15 : Rotor temperature distribution using FEM.....	110
Figure 5.16 : Axial temperature distribution using FEM.	110
Figure 5.17 : Spinning mode transient settings of the sample prototype.	111
Figure 5.18 : Transient temperature results of the sample prototype.....	112
Figure 5.19 : Loss settings of the optimized prototype.	113
Figure 5.20 : Radial view of the temperature results of optimized prototype.....	113
Figure 5.21 : Lumped thermal circuit of the optimized prototype.	114
Figure 5.22 : Axial view of analytical temperature results of optimized prototype.	115
Figure 5.23 : Slot temperature distribution using FEM.	115
Figure 5.24 : Rotor temperature distribution using FEM.....	116
Figure 5.25 : Axial temperature distribution using FEM.	116
Figure 5.26 : Spinning mode transient settings.	117
Figure 5.27 : Transient temperature results of the optimized prototype.	117
Figure 6.1 : Equivalent stress results of the sample prototype at 13000 min ⁻¹	120
Figure 6.2 : Equivalent elastic strain results of the sample prototype at 13000 min ⁻¹	120
Figure 6.3 : Total deformation results of sample prototype at 13000 min ⁻¹	121
Figure 6.4 : Equivalent stress results of the sample prototype at 563 min ⁻¹	121
Figure 6.5 : Equivalent elastic strain results of the sample prototype at 563 min ⁻¹	122
Figure 6.6 : Total deformation results of the sample prototype at 563 min ⁻¹	122
Figure 6.7 : Equivalent stress results of the optimized prototype at 13000 min ⁻¹ ...	123
Figure 6.8 : Equivalent elastic strain results of optimized prototype at 13000 min ⁻¹	123
Figure 6.9 : Total deformation results of optimized prototype at 13000 min ⁻¹	124

Figure 6.10 : Equivalent stress results of optimized prototype at 563 min^{-1} 124
Figure 6.11 : Equivalent elastic strain results of optimized prototype at 563 min^{-1} .
..... 125
Figure 6.12 : Total deformation results of optimized prototype at 563 min^{-1} 125





A PERFORMANCE IMPROVEMENT STUDY OF A PERMANENT-MAGNET ASSISTED SYNCHRONOUS MOTOR USED IN WASHERS

SUMMARY

Everyday more, synchronous reluctance motors are becoming one of the most preferred type of electric motors used in different applications. Their simple, light and easily maintainable rotor structure have made many researches to continue their work on the optimization of the nowadays synchronous reluctance motors. Another issue considered in the area of motor design, is the use of permanent magnets in these motors. Such modification of synchronous reluctance machines has changed their performance drastically, resulting in another type of electric motor nowadays called as permanent magnet assisted synchronous reluctance motor. Permanent magnet assisted synchronous reluctance motors have become the comparable reluctance motors to the conventional induction and brushless DC motors, if not even replacing them in several industrial and home appliances.

The complete structure of synchronous reluctance motors and permanent magnet assisted ones (PMaSynRM), is composed of a multiphase stator, similar to those of induction or permanent magnet synchronous motors. All of their advantages over other motors come from the special rotor structure, having no windings and simple structure. The special rotor structure includes flux barriers that guide the magnetic flux coming from the stator to flow from one to another pole of the rotor. Such flux guidance is possible due to the reluctance difference in different axes of the rotor. The low reluctance axis is called as the direct or d-axis, whereas the high reluctance axis is called as quadrature or q-axis. When currents flow in the stator, the magnetic flux coming into the rotor tends to pass through minimum reluctance, thus it tries to align the rotor axes accordingly. Thus, a rotating magnetic field induces a constant torque on the rotor trying to align by following it at the same rotating speed. The main purpose of the flux barriers is actually the minimization of reluctance in the d-axis and maximization of the reluctance in the q-axis. The inductance values on these axes would be vice-versa, meaning the d-axis inductance should be as high as possible, whereas the q-axis inductance should be as low as possible. In literature, there are many methods presented related to the optimization of inductance values of the synchronous reluctance motors. One way of doing this, is the positioning of permanent magnets inside the flux barriers in such way that they will decrease the q-axis inductance by opposing the flux on this axis, whereas they will increase the d-axis inductance by supporting the flux on this axis. Increasing the difference between the d- and q-axis inductances means that the motor of the same size will be able to induce larger torque than that without permanent magnets. Permanent magnets inside the flux barriers are placed in different configurations and sizes. The location of magnets and many other parameters related to the rotor design, including number of flux barriers and size of the segments are optimized when the performance of permanent magnet synchronous reluctance motor is to be improved. On the stator

size, number of slots, slot shape and tooth shape are the parameters that are change during optimization of synchronous reluctance machines.

On this thesis, the washer's sample motor taken from another thesis, is further optimized to get better performance on both washing and spinning mode operations. The optimization work is started with the decrease of the air-gap length without increasing the torque ripple too much. The effect of the distance between third rotor barriers is also observed to see whether the desired performance is possible with lower magnet volume compared to the sample motor. After the air-gap and the magnet location is defined, having in consideration the maximum slot fill factor, the stator yoke and tooth optimization is done such that the magnetic flux density in these parts remains under pre-defined limits. When general dimensions of the stator are defined, detailed optimization of the stator slot including slot shape, slot opening height and width are done to see whether they have effect on the performance of the motor. All of the analysis are simulated using finite element method solving software Maxwell 2D. After the optimized prototype is selected, it is produced and tested according to several electrical motor standards. Further, its thermal analysis is performed using Motor-CAD, and then compared to that of the sample motor to see the thermal advantages of the new prototype. Mechanical analysis of both the optimized prototype and the sample motor are performed in ANSYS Static Structural module to see the mechanical integrity of the rotor at high speed spinning mode operations.

KALICI MIKNATIS DESTEKLİ SENKRON RELÜKTANS MOTORLARDA PERFORMANS ARTIRMAYA YÖNELİK BİR ÇALIŞMA

ÖZET

Elektrik motorları kullanan farklı endüstriyel uygulamalar ve ev gereçleri gün geçtikçe daha yüksek performansa sahip ve daha verimli motorlara ihtiyaç duymaktadır. Bu ihtiyaç, yüksek verimli ve yüksek performanslı motor tasarımı konusunu, tüm dünyada yaygın bir araştırma konusu haline getirmiştir. Günümüzde bir çok çeşit elektrik makinesi görece yüksek verimlerde işletilebilmektedir. Dolayısı ile yenilikçi ve daha yüksek verimli makine tasarımı, tasarım mühendisleri için gün geçtikçe daha zor ve çaba gerektiren bir konu olmuştur. Bu tip yenilikçi ve yüksek performans hedeflerine sahip çalışmalarda en sık rastlanan motorlardan biri senkron relüktans motorlarıdır. Senkron relüktans motorları, bir çok uygulamada en çok tercih edilen motorlardan biri haline gelmektedir. Senkron relüktans motorlarını diğer motorlardan ayıran basit, hafif ve bakım gerektirmeyen rotor yapısı; araştırmacıları bu motorların rotorları üzerine bir çok eniyileme yapmaya itmiştir. Senkron Relüktans Motorlarının Jaroslav Kostko tarafından 1923’de tanıtılmasından itibaren geçen sürede motorun hem stator hem rotor yapısının iyileştirilmesi hem de performansının artırılmasına dair üzerine sayısız çalışma literatüre kazandırılmıştır. Bu eniyilemeler motorun çeşitli tiplerde çıkık rotor yapıları, laminasyon tipleri, farklı akı bariyeri tasarımları vb. gibi konuları kapsamaktadır. Bunlarla beraber Senkron Relüktans Motoru eniyilemesinde karşılaşılan bir diğer konu ise sürekli mıknatıslardır. Senkron relüktans motorlarına yapılan sürekli mıknatıs eklemesi, performans üzerinde çok ciddi bir etki yaratmış ve bugünlerde karşımıza çıkan Sürekli Mıknatıs Destekli Senkron Relüktans Motorlarını (PMSynRM) oluşturmuştur. PMSynRM’ler belirli endüstriyel ve ev gereçleri uygulamalarında asenkron motorlar, PMSM ve BLDC’lerin yerini almanın yanında, bu motorlara tüm uygulamalar için çok ciddi bir alternatif olmuştur. PMSynRM’ler sözü edilen bu motorlara kıyasla, iletken kaybindan yoksun bir rotor, çok daha düşük mıknatıs hacmi, fırça kolektör sisteminin olmaması gibi bir çok avantajı beraberinde getirdiğinden daha verimli, bakımı az ve üretimi kolay motorlar olarak öne çıkmaktadırlar.

Senkron Relüktans ve Mıknatıs Destekli Senkron Relüktans Motorlarının yapısı, çok fazlı bir stator ve içerisinde herhangi bir uyarma sargısı bulunmayan bir rotordan oluşmaktadır. Stator yapısı, sıkça karşılaştırıldığı asenkron, senkron ve sürekli mıknatıslı senkron motorlar gibi birçok motor ile aynıdır. Tüm avantajları içerisinde iletken barındırmayan ve basit bir yapıya sahip rotorundan ileri gelmektedir. Bu özel rotor yapısı, stator gelen manyetik akıya yol verecek akı bariyerlerine sahiptir. Bu akıya yön verme davranışı farklı eksenlerde farklı relüktanslara sahip yolları fiziksel olarak oluşturarak moment indükleyecek relüktans farkını yaratır. Düşük relüktansa sahip yol üzerine d-ekseni ve yüksek relüktansa sahip yol üzerine ise q-ekseni adı verilmektedir. Stator sargıları içerisinden akımlar akmaya başladığında, stator alanından gelen akı düşük relüktans yollarını izleme eğilimi gösterecek ve rotorun

düşük relüktans eksenini stator alanını eksenine üzerine getirecek şekilde bir moment indükleyecektir. Dolayısı ile stator tarafında oluşturulan bir döner alan, rotoru da sürekli olarak aynı hızda dönmeye zorlayacaktır. Bu açıdan akı bariyerlerinin amacı, q-ekseni üzerindeki relüktansı en yüksek ve d-ekseni üzerindeki relüktansı da en düşük yapmaktır. Bu yollar üzerindeki indüktans değerleri de tam tersi olacak ve d-ekseni indüktansı, q-ekseni indüktansından büyük olacaktır. Performans bazında ise bu indüktans farkı arttıkça, indüklenen moment de artacaktır. Dolayısı ile eksenler arası indüktans farkının, tasarım sürecinde olabilecek en büyük değerlere getirilmesi hedeflenmektedir. Bu indüktans farkı beraberinde iki önemli tasarım kriterini getirmektedir. Bu tasarım kriterlerinden biri çıkıklık oranı olarak adlandırılan L_d/L_q oranı, diğeri ise indüktans farkı (L_d-L_q)'dur. Bu iki kriteri; bir senkron relüktans motorunun performansını belirleyen en kritik iki parametredir. Indüktans farkı indüklenene maksimum momenti belirlerken çıkıklık oranı da işletmedeki en yüksek güç faktörü üzerinde belirleyici rol oynar. Literatür incelendiğinde, aynı geometri için bu iki parametrenin eniyilemesine dair birçok çalışma görülebilir. Bu çalışmalar incelendiğinde indüktans farkından doğan bu iki tasarım parametresi üzerine etkisi olan tasarım kriterlerinden en önemlileri akı bariyeri sayısı, akı bariyeri genişliği ve şekli ve demir bölüt genişlikleridir. Sürekli Mıknatıs Destekli Senkron Relüktans Motorlarında ise bu indüktans farkını artırmanın yolu, bu parametrelerin eniyilemesinin yanında, mıknatısları stator'dan gelen q-ekseni uyarmasını azaltıcı şekilde ve d-ekseni akısını destekleyici şekilde akı bariyerleri içerisine yerleştirmektir. Bu yöntemlerle d ve q-ekseni indüktans farkını artırmak, aynı boyuttaki bir mıknatıssız bir motora kıyasla daha yüksek moment elde edilebileceği anlamına gelmektedir. Sürekli mıknatısları akı bariyerleri içerisine yerleştirme sırasında mıknatısların akı bariyeri içerisindeki konumu ve hacimleri, motor performansı üzerine büyük etkide bulunur. Elde edilebilecek tüm mıknatıs kombinasyonları arasından mıknatısları mile yakın yerleştirmek, hem göreceli olarak daha iyi bir performans vermekte hem de mıknatıs yerleşim sürecini kolaylaştırmaktadır. Stator tarafında ise oluk sayısı, oluk ve diş şekli, SynRM eniyilemeleri sırasında üzerinde durulan parametrelerdir. Fakat stator tarafı eniyilemelerinin performansa etkisi rotor tarafı eniyilemelerinin etkisi kadar belirgin olmamaktadır. Tüm bu avantajlarının yanında, PMSynRM'lerin dezavantajlarından da bahsetmek gerekir. Bu dezavantajlarının en önemli iki tanesi işletme sırasındaki moment titreşimi ve karmaşık kontrol sistemi gereksinimleridir. Bu motorlardaki moment titreşimi, akı bariyerli ve bölütlü rotorun, stator dişleri altından geçişinde oluşan ve hıza bağlı frekansla değişen farklı relüktans yollarından kaynaklanmaktadır. Bu yollardaki relüktans değişimleri işletme sırasında indüklenen momentin anlık değişimlerine yol açarak moment titreşimlerine sebep olmaktadır. Bu moment titreşimleri ise yüksek hızlarda daha belirgin olmakta ve motorun mekanik titreşimine ve akustik gürültüye sebep olmaktadır. Moment titreşimini azaltmak için birçok çalışma yapılmıştır. Bu çalışmalardan en etkili sonucu veren stator oluk sayısının ve rotor akı bariyeri sayısının belirli kombinasyonlara göre seçilmesidir. PMSynRM'lerin kontrolleri tarafındaki dezavantajı değişken frekanslı bir evirici sistemi gereksinimidir. Bu motorlar; doğrudan şebekeden kalkış yapamamakta, konum algılayıcısı ve değişken frekanslı eviriciler ile kalkış yapabilmekte ve işletmede kalabilmektedirler. Sürücü devresi gereksinimi de bu makinelerin kurulum, işletme ve bakım maliyetlerini artırmaktadır.

Bu tez çalışmasında, referans alınan bir çamaşır makinesi motorunun eniyilenecek yıkama ve sıkma esnasındaki performansının artırılması amaçlanmıştır. Tezin ikinci bölümünde, bu motorların analitik tasarımı ile ilgili belirli tasarım parametreleri,

tanımlar ve denklemler verilmiştir. Bu parametreler arasında, kutup sayısı, izolasyon oranları, akı bariyerlerinin ve demir bölütlerin konumu ve boyutlarının performans üzerindeki etkileri açıklanmıştır. Akı bariyerlerinin ve demir bölütlerin konumlandırması ve boyutlandırılması ile ilgili senkron relüktans motorlardaki rotor tasarımında kullanılan denklemler verilmiştir. Bu denklemlere göre, rotorun dış çapı ve mil çapı gibi boyutları kullanarak, d- ve q- ekseninde tanımlanan izolasyon oranlarına göre, bu eksenlerdeki akı bariyerlerinin ve demir bölütlerin genişliği tanımlanır. Referans olarak alınan motorun izolasyon oranlarının en uygun olduğu varsayıldığından bu tez çalışmasında bu oranlar değiştirilmemiştir. Eniyileme çalışmalara göre çizilen rotorların sadece dış çapları ve mil çapları değiştirilmiştir. Bu denklemlerden elde edilen akı bariyeri ve demir bölüt genişlikleri, tezde verilen d- ve q-ekseni indüktansların hesaplanması için geliştirilen analitik yöntemde kullanılmıştır. Bu yöntemde göre indüktans değerleri, akı yolları belirlenerek ve bu yollar üzerindeki manyeto motor kuvveti denklemleri çözümlenerek hesaplanmaktadır. Bu denklem sisteminin sonucu olarak elde edilen hava aralığındaki manyetik akı yoğunluğu kullanılarak, d- ve q-eksenindeki toplam akı ve indüktanslar hesaplanmaktadır. Eniyileme süreci ise moment titreşimi üzerindeki etkisi de göz önünde bulundurularak hava aralığı azaltılması ile başlamıştır. Devamında, hava aralığı uzunluğu ile rotorun her bir çeyreğindeki üçüncü akı bariyerlerinin arasındaki mesafenin etkisi örnek motora kıyasla aynı performansı sağlayabilecek şekilde incelenmiştir. Ayrıca mıknatısların hacimleri ve akı bariyerleri içerisindeki konumları da bu eniyilemeler sırasında incelenmiş ve sonuçları sunulmuştur. Hava aralığı uzunluğu ve mıknatıs konumlarına karar verildikten sonra, en yüksek oluk doluluk oranı göz önünde bulundurularak stator boyunduruk ve dış eniyilemeleri ön tanımlı doyma değerleri de gözetilerek yapılmıştır. Stator eniyilemeleri, sargı tiplerinin incelenmesi ile devam etmiştir. Tek ve çift tabakalı sargılar deneyerek ortalama moment ve moment titreşimi üzerindeki etkileri belirlenmiştir. Kullanılan malzemeler tarafında ise, iki farklı ferromanyetik malzemenin performansa etkisi incelenmiştir. Stator ve rotorda M700 ve M350 sınıfı silisli çelik kullanarak demir kayıpları üzerinde etkisi araştırılmış ve prototipleme aşaması için uygun olana karar verilmiştir. Stator üzerindeki genel maksatlı eniyilemeler tamamlandıktan sonra geometrinin detaylarındaki eniyilemeler yapılmış stator oluk şekli, oluk açıklığı yüksekliği ve oluk açıklığı genişliği eniyilenecek prototip performansı üzerine etkileri incelenmiştir. Tüm elektromanyetik analizler Maxwell 2D ve Motor-CAD isimli ticari paket programlarında sonlu elemanlar yöntemi ile iki boyutlu olarak modellenmiş ve analiz edilmiştir. Sıkma modu işletmesindeki alan zayıflatma bölgesi de dahil olmak üzere tüm hız aralığında verim haritası Motor-CAD yazılımı ile çıkartılmış ve işletme koşullarına ilişkin akım, moment ve faz açıları gerilim ve akım sınırlı bölgeler için verilmiştir. Tasarım süreci sonunda elde edilen prototip üretilmiş, testleri yapılmış ve deneysel sonuçlar ile benzetim sonuçları karşılaştırılarak uygulanan yöntemin doğruluğu gösterilmiştir. Elektromanyetik analiz ve prototip sonuçlarına göre eniyilenecek prototip motorun ısısal analizi Motor-CAD yazılımı ile yapılmıştır. Elde edilen ısısal analiz sonuçları referans motor ile karşılaştırılarak eniyileme sürecinin olumlu sonuçları sunulmuştur. Isısal analize motorun tüm bölgelerindeki bakır ve demir kayıpları dahil edilmiştir. Isısal analizi mekanik zorlanma analizleri takip etmektedir. Mekanik zorlanmaların ve mekanik bütünlüğün sağlandığını analiz etmek amacı ile prototip ve referans motor ANSYS Statik Yapısal Modül üzerinde hem yıkama hem de sıkma modunda analiz edilmiştir. Yüksek hızlarda yarıçapsal merkezkaç kuvvetinin etkilerinin yol açtığı mekanik bozulmanın boyutları sunulmuştur.



1. INTRODUCTION

Synchronous reluctance machines, since their foundation in 1923 by J. K. Kostko [1], have changed and developed slowly but sustainably with the technology. When they were introduced, they were very disadvantageous compared to other brushless electrical machines because of their high torque ripple, low power factor and efficiency values. After several rotor models and drive mechanisms were introduced, the first usable and applicable synchronous reluctance motors were designed in 1960 [2]. However, their acceptance and usage in industry was low until 1990s. New researches on semiconductor drive mechanisms and rotor designs made the 90s the brightest years for the reluctance machines leading to a drastic increase in the performance of reluctance machines. Thus, improved performance and constructional advantages of reluctance motor designs over the conventional induction and PM motors finally attracted the attention of industry.

Reluctance machines operate and drive the loads by taking advantage of the reluctance torque induced in their rotor. Their stator construction is the same as the stator of induction motors, having laminations and distributed 3-phase windings for developing a constant rotating magnetic field. The reason of using laminated steel is the same as in all electrical machines, to decrease the flowing eddy currents and minimizing iron losses. Depending on the starting and control mechanism, it may have also windings on the rotor for inductive starting. The induced torque of reluctance motors highly depends on the saliency ratio (X_d / X_q) of their rotor. The direct axis reactance (X_d) should be as high as possible, whereas the quadrature axis reactance (X_q) should be as low as possible in order to have a significant and usable induced torque value on the rotor. Since the reactance is directly proportional to inductance, higher inductance in direct axis will allow magnetic flux to pass easily, whereas lower inductance in the quadrature axis will not allow much flux to flow in this axis. This phenomena of different inductance in d- and q-axis, is created by using air-gaps inside the rotor. Obtaining better saliency ratio for better performing reluctance motors became the most important research issue for all researches of this

filed. There are two types of machines working on reluctance torque principle: Switched Reluctance Machine and Synchronous Reluctance Machine.

1.1 Purpose of the Thesis

In the thesis a sample Permanent Magnet Assisted Synchronous Reluctance motor designed and prototyped for washing machine application is optimized with respect to several objectives and limitations. Having into consideration the stator's outer radius and the maximum slot fill factor applicable, optimization analysis of stator, rotor and permanent magnets of the sample motor are given in details with all the measured physical parameters. Initially, referring to the desired output torque and torque ripple, the air-gap is changed to find its optimum length. Air-gap change is followed by stator optimization, magnet type and volume optimization, distance between first barriers (D) optimization, number of winding layers' optimization, type of ferromagnetic material and finally by detailed slot optimization. After the final optimized design is selected, its electromagnetic, thermal and mechanical comparison to the sample motor is given with all measured physical quantities to have better idea for the overall performance advantages of the new design over the sample motor. The geometry of the sample PMASynRM prototype is given in Figure 1.1.

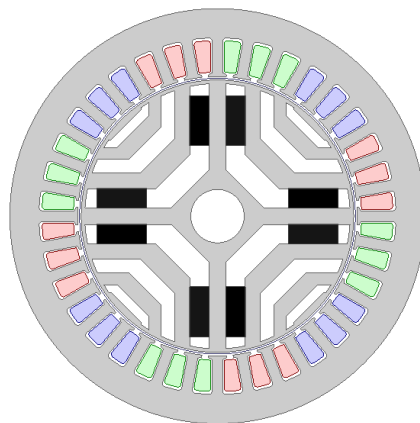


Figure 1.1 : Geometry of the sample PMASynRM [3].

The new motor that is going to be selected at the end of this thesis, aims to have the required torque output at the same current value but with a better efficiency. Input current and the stack length of the motor is going to be kept the same as that of the

sample rotor, whereas winding turns, magnet volume and position may be changed until the aimed output is satisfied.

1.2 Literature Review

Synchronous Reluctance Motors are new electrical machines that have first appeared after the researches, related to “Polyphase reaction synchronous motors”, of J. K. Kostko in 1923. According to Kostko, adapting slits along the d-axis of the rotor would maintain high flux through this axis, whereas it would minimize the flux along the q-axis of the rotor [1]. This rotor configuration became the basis for all the rotor models that would be designed later with flux barriers barrier, segmental rotor and axial lamination structures.

Most of the researches that were done later were related to the rotor structure, because the stator of synchronous reluctance motor was essentially the same as the stator of induction motors. After the foundation of J. K. Kostko, researches done by P.F. Bauer [4] and N. Risch [5] resulted in new rotor structures, which provided more efficient operating motors, that included flux guides/barriers and segments. This kind of segmental rotor designs were further developed by Lawrenson, who is actually known as the father of Switched Reluctance Drive [6]. P. J. Lawrenson rotor designs were made of salient circumferential segments in the rotor periphery divided by non-magnetic material in between that increased the q-axis reluctance and the saliency ratio [7]. Circumferential segments directed the magnetic flux from one pole on the circumference to the other. Flux was not flowing radially any more as in the previous salient rotor designs. Center of segments paths with nonmagnetic material in between increased the saliency ratio more, thus giving a better motor performance. In his paper of “Theory and Performance of Polyphase Reluctance Machines”, he emphasizes that such designs have better torque and power factor performances [8]. Moreover, in one of his papers, Lawrenson emphasized that instead of using starter windings, addition of axial conductor channels inside the rotor segments of the synchronous reluctance motors induced higher pull-out torque relative to the break-down torque of induction machines of the same size, and such designs showed better power factor values than 0.8 [9]. Later, A. F. Cruickshank and A. J. O. Anderson on their work proposed axial laminated rotor structure [10]. According to them, experimental results of motor designs with axial lamination, showed that they had

higher power capabilities and better performance compared to salient pole reluctance motors. Such designs were also comparable to the most advanced motor designs of that time [10]. The most used types of laminations in synchronous reluctance motors are showed in Figure 1.2 and Figure 1.3.

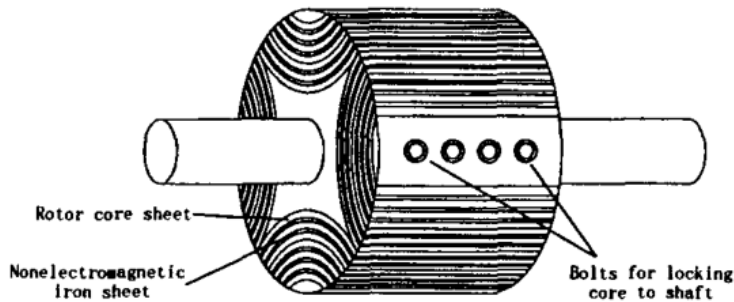


Figure 1.2 : Axially laminated anisotropy rotor [14].

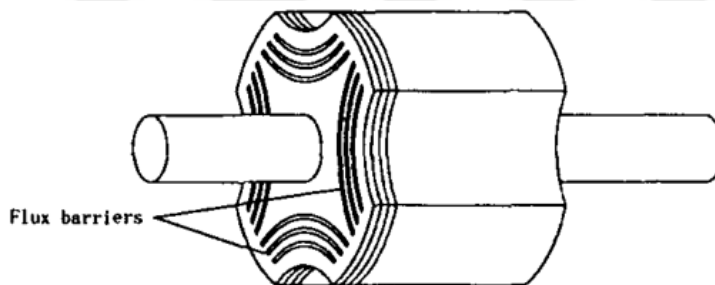


Figure 1.3 : Transversally laminated flux barrier rotor with cut-outs in the q-axis [14].

Considering the magnetic field of rotor, axial lamination shows better performance than the radial lamination type. This advantage, in the research work of Rao related to the axial lamination, was better accepted and patented later in 1978 [11]. In 1972 B. J. Chalmers proposed a rotor design with solid (bulk) ferromagnetic material, that using the eddy currents induced in the core, started as an induction motor and after a while it reached synchronous speed [12]. Later on in 1992, according to A. Fratta it was stated that rotors with axial lamination were more suitable and better in high dynamic application areas [13]. The effect of the flux barriers on the laminated motor's efficiency was better explained later in 1998 by Kiriyama, in a study according to which a synchronous reluctance motor prototype used, when driven by the same inverter drive, it showed to be 6% more efficient than induction machine [14]. Researches of Boglietti later in 2008, emphasized that for the same motor size,

synchronous reluctance motors were capable of inducing 10% to 15% higher rated torque values than induction motors, due to the lack of excessive rotor active losses [15]. Another optimization work on synchronous reluctance motors done by Fratta, included small permanent magnets located inside the stator slots for better flux management. This work showed that such motors can have further improved torque and their performance can be compared to that of PM [16].

In his research work which got him a patent in 1996, A. Vagati came up with an analytical relation between the stator slot number and the number of rotor slots. His work showed that without skewing, the torque ripple of synchronous reluctance motors could be significantly decreased if the following conditions are used for determining the stator slot and rotor segment number:

n_s : Slot number per pole pair

n_r : Rotor slot number per pole pair

- $n_s - n_r \neq 0$ and $n_s - n_r \neq \pm 2$
- $n_r > 6$
- $n_s \neq m \times n_r$, m is a constant
- $n_s - n_r = \pm 4$

These conditions and other design features, including saturable rotor end ribs, barrier bridges and permanent magnet location, are explained in details in his patent [17].

R. R. Moghaddam in the near past, came up with a simple analytical model related to the sizes of segments and flux barriers of synchronous reluctance motors. Considering sinusoidal MMF in the air-gap, he divided the d- and q-axis MMF components and according to this flux distribution he developed expressions that give the width of each segment and barrier inside the rotor [18-20].

When it comes to the control of synchronous reluctance motors, they are controlled by either vector control or scalar control. For simple control applications, direct starting models that have rotor windings are available. Initially they start as induction motors, later they reach synchronization. In most applications, these motors are provided with sensors that are used for position, speed and torque measurements. Another way of sensorless control and estimation of such variables is by instantaneous phase current and voltages [21]. Several switching mechanisms used in

induction motors are also applicable on synchronous reluctance motors in much easier and simpler way because of the lack of slip [22]. In terms of multiphase applications, solid state control mechanisms provide much higher flexibility. 10 switching devices are used to drive a 5-phase synchronous reluctance motor which shows 10% higher torque for the same current value than 3-phase models [23].

Since torque ripple is the primary problem of modern SynRMs, many work is conducted in order to reduce the torque ripple. In 1998, Vagati et. al. proposed a method for reducing torque ripple caused by slot harmonics. In their proposed method they defined separation points between rotor segments which in turn defines how many barriers/slots in rotor and they achieved low torque ripples even with full pitched windings on par with surface mounted PM counterparts [24].

The PMSynRMs are identical to SynRMs in construction but with permanent magnets inserted into the flux barriers so as to cancel out the q-axis excitation flux. This results in better operational performance because SynRM performance depends largely on L_d/L_q , namely saliency ratio.

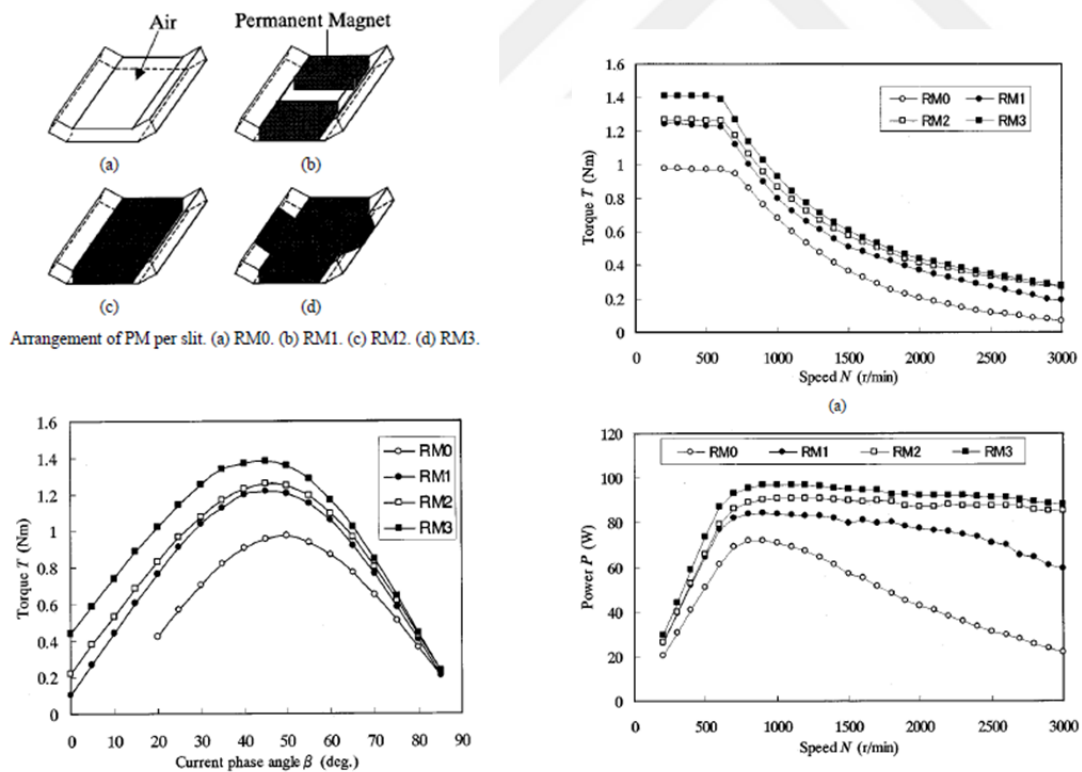


Figure 1.4 : Performance of difference PM insertions [25].

In 2001, S. Morimoto et.al. in their much cited paper, examined PMSynRMs for wide constant-power operation. By properly adding PM inside the flux barriers they

showed that the machine can exhibit large constant-power speed range, high efficiency and high power factor in comparison to normal SynRMs. And adding to that they showed that decrease of efficiency in high speed regions and uncontrolled generator mode operation which occur in conventional PM drives are nor present in PMaSynRMs [25]. Figure 1.4 gives different arrangements of permanent magnets inside the flux barriers. The effect of each configuration on the constant torque and limited voltage and current region it can be seen from the speed-torque characteristics of each arrangement. It is clearly seen that higher magnet volume results in better performance of the motor in all operating regions [25].

In 2004, M. Sanada et.al. proposed asymmetrical barrier configuration to further reduce torque ripple. The motivation behind this is to prevent barrier ends passing under stator slots at the same time, which is causing a torque ripple [26]. In Figure 1.5 results corresponding to three different machines are presented for both symmetrical and asymmetrical arrangements of barriers.

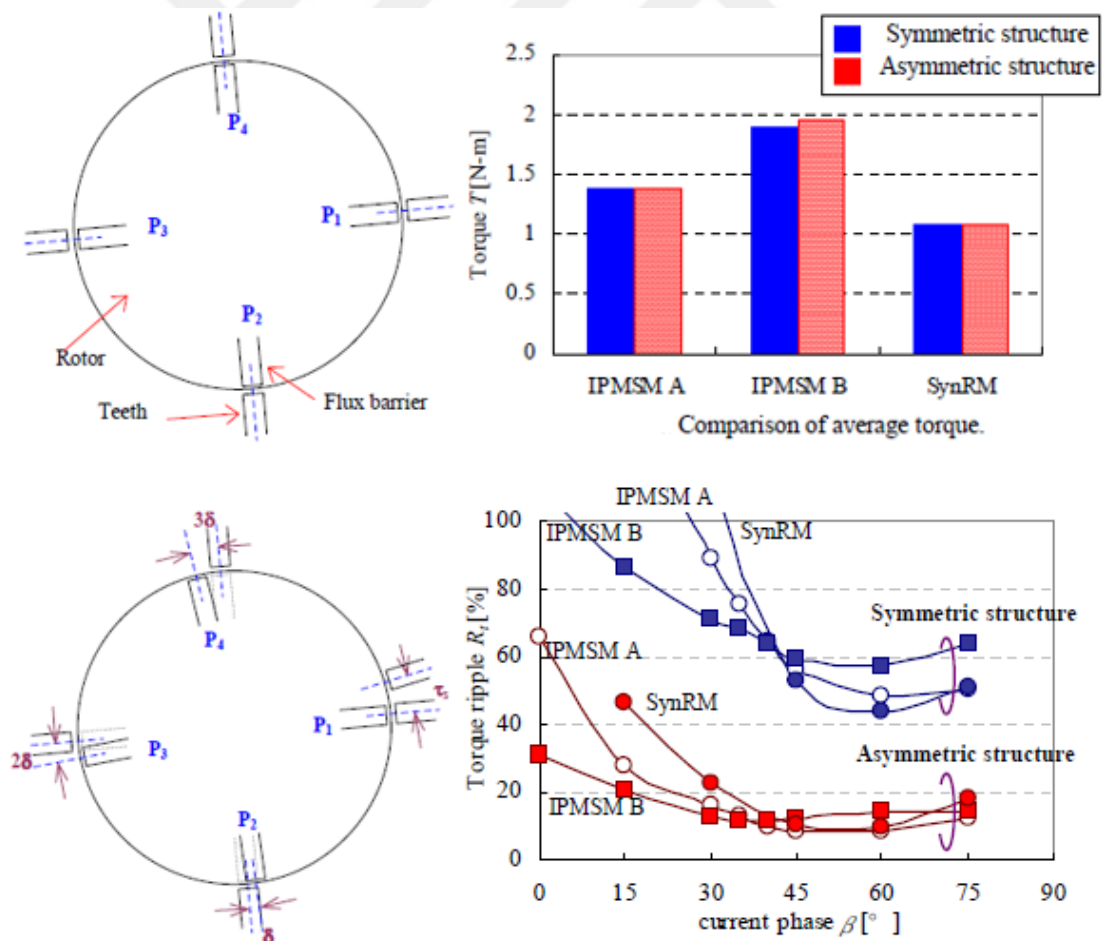


Figure 1.5 : Torque ripple of asymmetric barrier configuration. IPMSM A magnet is 300 kA/m and IPMSM B is 900 kA/m [26].

The torque ripple results, given for different load angle values, show a drastic decrease in the asymmetric arrangement of barriers. The machines used have the same stator, one of them is SynRM and two others are interior permanent magnet synchronous motors (IPMSM) A and B, with permanent magnets having 300kA/m and 900kA/m coercive force, respectively [26].

In 2008, Vagati et.al. inspected the injected plasto-ferrites in order to skew the rotor more efficiently to reduce torque ripple. They filled up the barriers with melted magnet material and then magnetized it for more flexibility in terms of conventional skewing in PM machines which is step skewing [27]. In 2009, N. Bianchi et.al. proposed Romeo & Juliet configuration. Romeo & Juliet type of lamination is given in Figure 1.6.

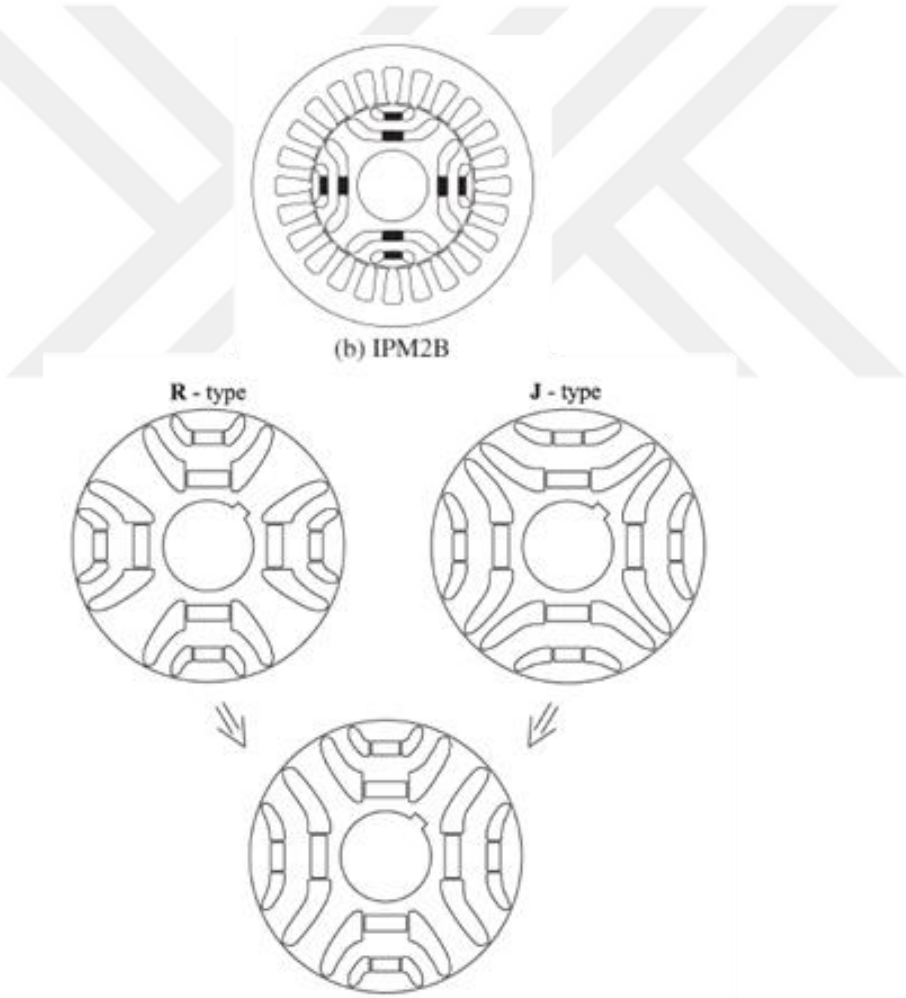


Figure 1.6 : Two barrier conventional PMaSynRM & Evaluation of Machaon from R&J [28].

This involves two set of barrier shapes which are different from each other on different laminations and aligning these laminations in alternating fashion. Also they

proposed a Machaon structure which incorporates these two shapes together on same lamination. Also they skewed the rotor while using these laminations. Results are promising, torque ripple caused by higher order harmonics are suppressed [28].

The induced torque and torque ripple results of the rotor types given in Figure 1.6 are given in Figure 1.7. ‘Romeo & Juliet’ barrier configurations show decrease of both the torque ripple and the average torque value when compared to the conventional PMaSynRM. The Machaon rotor type, however, has the average torque value of a conventional reluctance motor and the low torque ripple of a R&J type rotor.

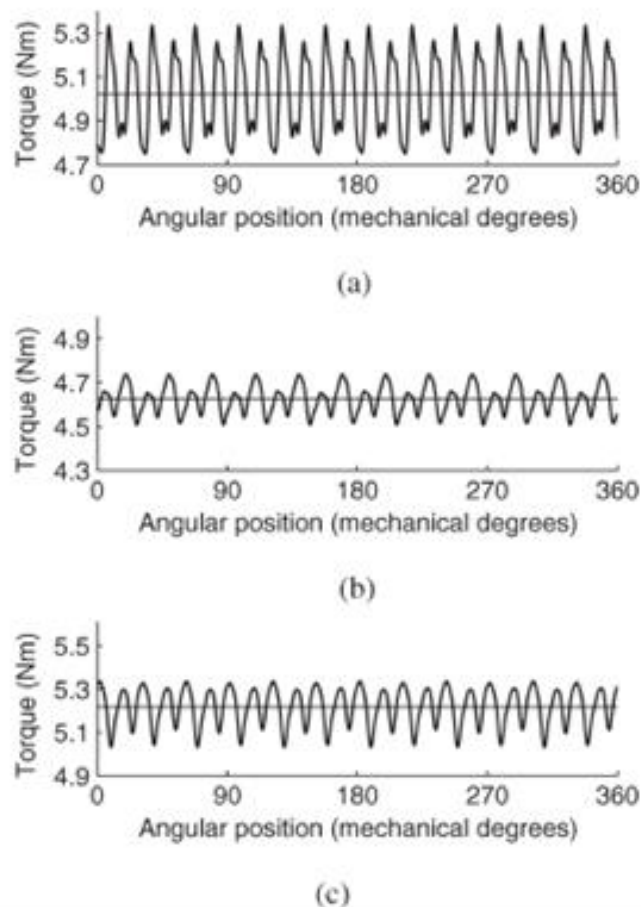


Figure 1.7 : 2 barrier PMaSynRM rotor b) R&J rotor c) Machaon rotor all at $I = 5.3$ A [28].

Since PMaSynRMs incorporate PMs, there has to be some countermeasures regarding PM demagnetization. M. Sanada et.al. proposed a rotor structure for such countermeasures. By altering the barrier ends by some specific geometries, demagnetization can be minimized. Authors compared three different machines, one with conventional barrier shape, two with optimized shapes. By changing the shape of first barrier demagnetization is reduced since the first magnet closest to air-gap is

the most effected from changing fields [29]. The modified flux barrier shapes B-type and C-type being compared with conventional A-type shape are given in Figure 1.8. Due to the reverse magnetic field coming from the stator windings, the resulting percentage demagnetization curves for A-type conventional flux barrier type rotor, B-type rotor with wider first flux barrier and C-type rotor with tapered flux edges are given in Figure 1.9 for different values of excitation current. First layer corresponds to the barrier closest to the air-gap whereas third layer is furthest one form the air-gap.

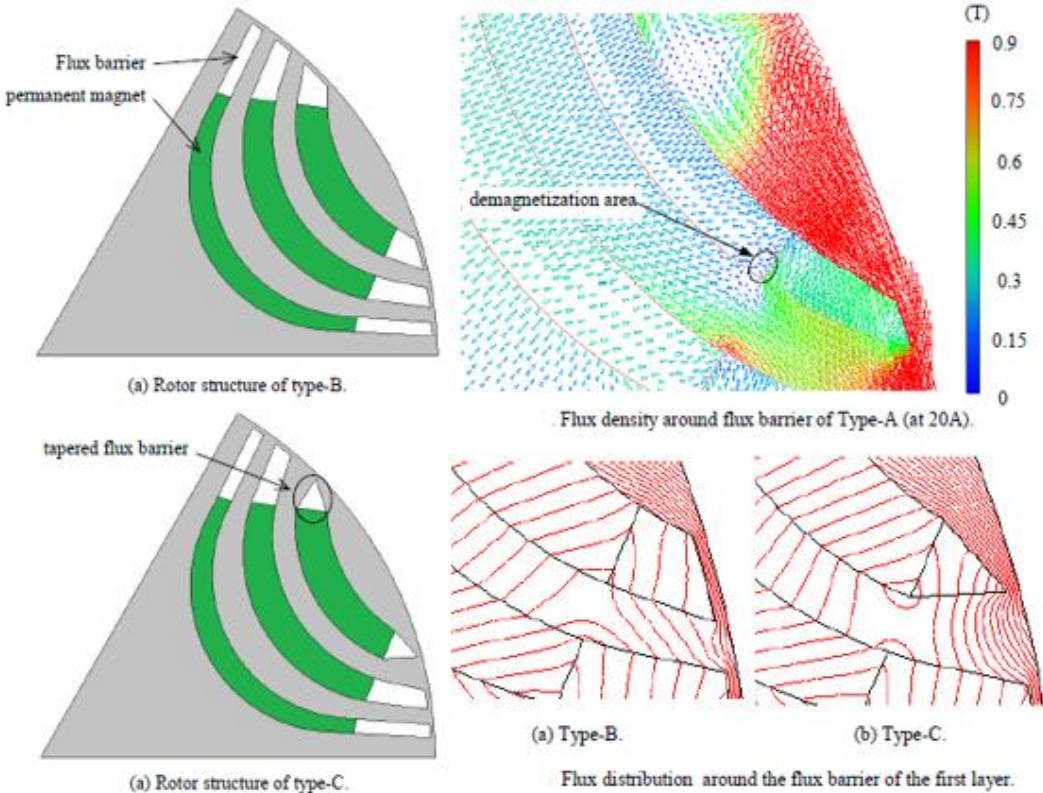


Figure 1.8 : Structures against demagnetization [29].

Concerning the effect of stator winding configuration, authors Bianchi et.al. presented a study detailing the effect of fractional slot or integral winding. Authors separated the PM and reluctance torque components when investigating the machine behavior. They have found out that contrary to common expectations, fractional slot machines exhibit a high reluctance torque. Under overload conditions both PM and reluctance components are reduced. This study concluded that under nominal working conditions there are no differences between fractional and integral slot windings but in overload conditions fractional slot windings exhibit lower average torque and higher torque ripple compared to integral winding machines [30].

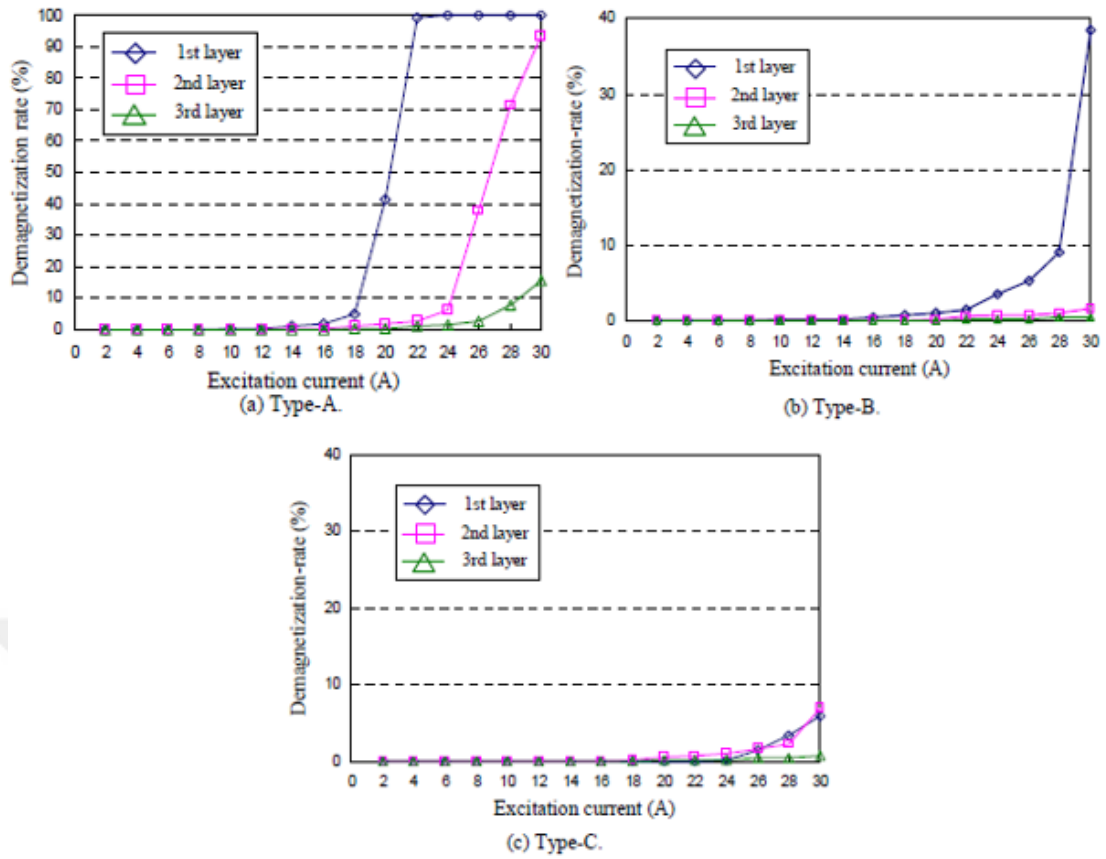


Figure 1.9 : Demagnetization percentages against demagnetizing excitation of different barrier types [29].

In 2010 Vagati et.al. presented a trade-off in their study between the torque ripple and core loss. They presented the optimal slot numbers for both stator and rotor in order to have minimal torque ripple [31]. The results corresponding to the torque ripple for different combinations of stator and rotor slot number are given in Figure 1.10.

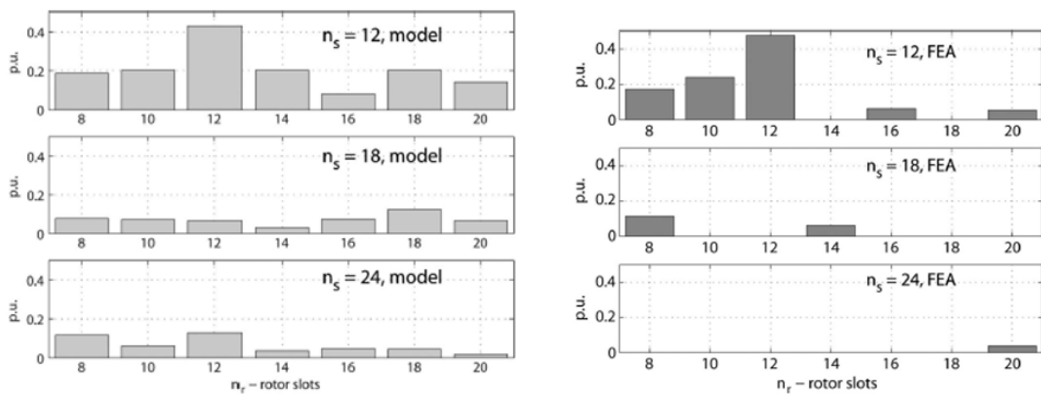


Figure 1.10 : Torque ripple results of analytical model and FEA simulations [31].

Selection of the PM excitation amount is also an important subject. Bianchi et.al. in one of their studies explained the optimal selection of PM flux linkage. Authors stated that for over 0.8 power factor and nominal current, optimal q-axis PM excitation should be three times more than the q-axis flux in that situation. That in turn should correspond to 0.25-0.3 times the nominal flux linkage [32].

1.3 Working Principle and Mathematical Model of SynRM

Reluctance torque is what makes the rotor of a synchronous reluctance motor rotate. The stator of synchronous is the same as that of an induction motor, having three phase distributed windings. The distribution of the three phases is in such way that a rotating constant magnetic field is produced inside the motor. Due to its saliency, the rotor tries to align the low reluctance axis with the magnetic field, thus it continuously rotates following the magnetic field generated from the stator. Beside the stator design, the performance of synchronous reluctance motors is strongly dependent on the design of its rotor. Motor types that can be directly connected to the AC supply are known as line start, and they have a shorted conductor cage structures inside the rotor. The induced currents in the conductor cage help the rotor start as an induction motor until it reaches synchronization. After the motor reaches synchronization, the conductor cage serves as speed fluctuation damper. Another type of synchronous reluctance motors requires to be driven by inverters. They do not contain any conductive cages in the rotor, however, several sensors detect the position of the rotor and then supply the 3-phases to the stator with the required phase angle.

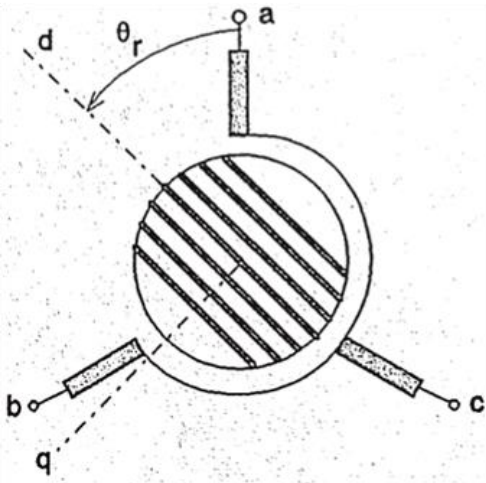


Figure 1.11 : 3 phase 2 pole SynRM [21].

Such motors start simply by the reluctance torque induced initially on their rotor. This flux guidance in inverter fed synchronous reluctance motors is realized with special electronic circuits. Moreover, the directed flow of the magnetic flux through the laminated segments of the rotor, that are divided by the flux barriers and bridges, results in higher torque per volume ratio due to the higher saliency ratio of the rotor. In Figure 1.11 a simple two pole synchronous reluctance motor is given and the mathematical model in the following sections is derived for this type of motor.

For a distributed winding configuration with $q \geq 2$, the MMF distribution with respect to the rotor position is close to sinusoidal waveform. The general 3-phase system will be given first, followed later by its Park's transformation.

$$q = \# \text{ of slots} / (\# \text{ of poles} * \# \text{ of phases}) \quad (1.1)$$

For any phase "a" of the motor, the voltage equation is written as follows:

$$\frac{d\varphi_a}{dt} = V_a - i_a R_s \quad (1.2)$$

Where φ denotes the flux linkage of corresponding phase, V is the phase voltage, i is the phase current and R_s is the phase resistance. Knowing that the flux linkage of each phase is proportional to the phase inductance as a function of rotor position, the flux linkage vector of all three phases is written as:

$$\begin{bmatrix} \varphi_a \\ \varphi_b \\ \varphi_c \end{bmatrix} = |L_{abc}(\theta_{er})| \begin{bmatrix} i_a \\ i_b \\ i_c \end{bmatrix} \quad (1.3)$$

In equation 1.3, θ_{er} denotes the electrical angle of the rotor and $|L_{abc}(\theta_{er})|$ is the inductance matrix containing self and mutual inductance of all three phases, as function of the rotor position.

In the conventional 3-phase system, the induced electrical torque equation is as given in Equation 1.4:

$$T_e = \frac{p}{2} |i_a \ i_b \ i_c| \left| \frac{\partial L_{abc}(\theta_{er})}{\partial \theta_{er}} \right| \begin{bmatrix} i_a \\ i_b \\ i_c \end{bmatrix} \quad (1.4)$$

where p is the number of pole poles, i 's denote the phase currents and L denotes the phase inductances that change with respect to rotor position. Finally, the complete equation representing the dynamics of the rotor is given as:

$$\frac{J}{p} \frac{d\omega_r}{dt} = T_e - T_{load} \quad (1.5)$$

Where ω_r denotes the angular velocity of the rotor defined as given in Equation 1.6:

$$\frac{d\theta_{er}}{dt} = \omega_r \quad (1.6)$$

The currents of all three phases change in time, whereas the phase inductances change with respect to the position of the rotor. Since the multiplication of phase currents and inductances give the flux linkages, their analysis in the phasor reference frame becomes difficult due to the sensitivity on both time and rotor position. Park's transformation is a useful method to simplify the complex 3-phase system into constant direct and quadrature variables. Without giving the computational details, the equations that appear as a result of Park's Transformation, or the $dq0$ equations, are as shown in the following sections.

The equation corresponding to the d-axis voltage:

$$\frac{d\phi_d}{dt} = V_d - i_d R_s + \omega_r \phi_q; \quad \phi_d = L_d i_d; \quad L_d = L_{s\sigma} + L_{dm} \quad (1.7)$$

The equation corresponding to the q-axis voltage;

$$\frac{d\phi_q}{dt} = V_q - i_q R_s + \omega_r \phi_d; \quad \phi_q = L_q i_q; \quad L_q = L_{s\sigma} + L_{qm} \quad (1.8)$$

The derivative of the flux linkage over time is sometimes called as the transformer component, whereas the multiplication of the flux linkage and the angular speed is also known as the speed voltage component.

The equations corresponding to the d-q axes magnetizing inductances:

$$L_{dm} = \frac{3}{2} (L_h + L_0); \quad L_{qm} = \frac{3}{2} (L_h - L_0) \quad (1.9)$$

The induced torque equation on d-q reference frame:

$$T_e = \frac{3}{2}p(L_d - L_q)i_d i_q \quad (1.10)$$

The motor's dynamic equation is the same as in the phasor reference frame:

$$\frac{J}{p} \frac{d\omega_r}{dt} = T_e - T_{load} \quad (1.11)$$

In the $dq0$ equations above, d and q subscripts denote the corresponding axis of the values given. L_m stands for magnetizing inductance, $L_{s\sigma}$ for stator leakage inductance, L_h for magnetizing inductance of stator, L_0 for the sinusoidal varying component of air-gap inductance due to saliency, ω_r for mechanical speed of rotor and again p for pole pairs.

The term $L_d \cdot i_d$ corresponds to the d-axis and it represents the magnetic saturation. Even though there is a transient component in the d-axis inductance, which was neglected in the previous equations, q-axis inductance is constant. However, for higher values of i_q , the effects of the transient d-axis inductance on L_d should be considered as shown in the following equation:

$$L_{dt} = L_d + \frac{\partial L_d}{\partial i_d} i_d \quad (1.12)$$

Consideration of the transient inductance in the d-axis and its substitution in the voltage equations gives the final equations for the d and q axes as follows:

Voltage equation in d-axis:

$$L_{dt} \frac{di_d}{dt} = V_d - i_d R_s + \omega_r L_q i_q \quad (1.13)$$

Voltage equation in q-axis:

$$L_q \frac{di_q}{dt} = V_q - i_q R_s - \omega_r L_d i_d \quad (1.14)$$

Referring to the d- and q-axis voltage equations shown above, the equivalent circuits for both axes are shown in the Figure 1.12 below where “p” indicates the derivative function with respect to time.

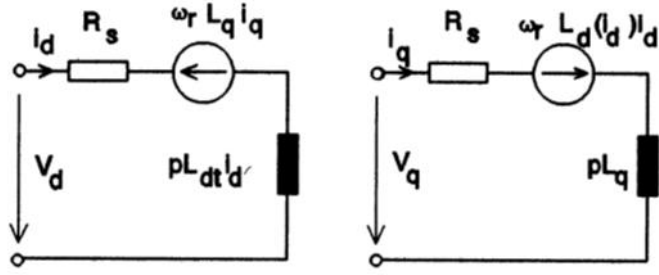


Figure 1.12 : d & q-axis equivalent circuits neglecting core losses [21].

The previous circuits do not account for the iron losses in the stator and the rotor. The core losses corresponding to the stator core, are added parallel to the d- and q-axis induced voltages. Since they are relevant to the q-axis components, the losses arising from the harmonics of the q-axis field are added parallel to the speed voltage component of d-axis and the transformer voltage component of the q-axis. The final equivalent circuits of d- and q-axis voltages, including the iron losses of stator and rotor, are implemented as given in Figure 1.13 below.

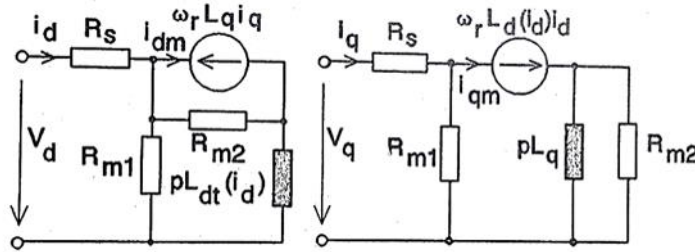


Figure 1.13 : d & q-axis equivalent circuits including core losses [21].

1.3.1 PMaSynRM's mathematical model

The mathematical model of PM assisted synchronous reluctance motor (PMaSynRM) is derived by adding the flux linkage of the permanent magnet λ_m on the final torque as given below in Equation 1.15.

$$T_e = \frac{3}{2} p [(L_d - L_q) i_d i_q + \lambda_m i_d] \quad (1.15)$$

2. ANALYTICAL ROTOR DESIGN AND INDUCTANCE CALCULATIONS

The performance of PMaSynRM, as it was mentioned before, is significantly dependent on the rotor design. Stator design does not have much effect on the overall performance of the motor. Important design parameters on the rotor side include pole number, number of flux barriers and insulation ratio. Depending on these parameters, rotor and shaft radii, the structure of the rotor is designed analytically. Such analytical design defines the location and geometrical dimensions of the flux barriers and segment inside the rotor. Moreover, the segment and barrier dimensions are used in the calculation of the d- and q-axis magnetizing inductances of the rotor. Rotor design parameters and the modified inductance calculation method are explained in details in the following sections.

2.1 Pole Number

In synchronous reluctance machines, the number of poles is determined by the rotor rather than stator. The number of rotor poles in such machines is the same as the number of blocks of flux barrier around the circumference of the rotor. In literature synchronous reluctance machines having 2,4,6 and 8 poles are present. From these structure the one that is most used and preferred is motor with $2p=4$ poles, where p denotes the pole pair number.

Since the PMaSynRM being optimized is used in washing machines, it has a small rotor diameter which is not practical for high pole number constructions. Both numerically and from the literature, it can be clearly seen that small diameter rotors with large number of poles are not suitable designs for synchronous machines. Therefore, in all the following optimization analysis, the optimum pole number is chosen to be as in the prototype $2p=4$.

2.2 Number of Barriers

The overall performance and the induced torque of PMSynRM is strongly related to saliency ratio, which changes significantly with the number of barriers and the air/iron ratio of the rotor. Being one of the most important design parameters of synchronous reluctance motors, the number of barriers has a direct effect on the induced torque. Moreover, the position of these barriers in the rotor has a direct effect on the output torque ripple of the motor.

Number of barriers can be selected independently from the insulation ratio. However, it has a significant effect on the output torque and torque ripple of the motor. Related to the number of barriers, K. Wang and Z. Q. Zhu in their work with a 24 slot motor, have obtained the ripple vs. barrier number results as given in Figure 2.1 [33]. From the plot, it can be clearly seen that 3 barrier designs have the minimum torque. Therefore, the number of barriers in the following optimization analysis is also kept constant as in the prototype motor to be 3.

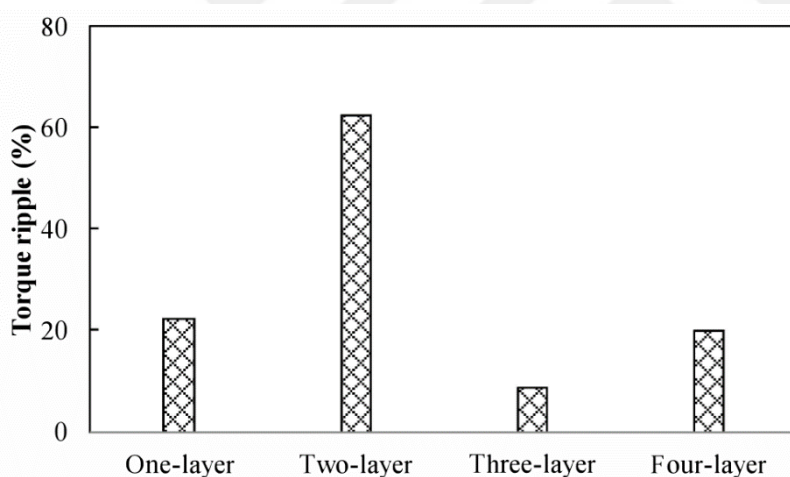


Figure 2.1 : Barrier number effect on torque ripple [33].

2.3 Insulation Ratios

The output performance of synchronous reluctance motors is strictly related to the saliency ratio, which is determined by the air barriers in the rotor. Special design of the air barriers, their location and size directly effects the output torque, torque ripple and other electromagnetic parameters of the motor.

The parameters that define the saliency ratio of the rotor are the insulation ratios in the q- and d-axis of the rotor. The insulation ratio in the q-axis determines the ratio of

the total barrier width to the total width of the flux segments of the rotor in the q-axis, whereas the insulation ratio in d-axis, determines the total barrier width to the total segment width perpendicular to that axis of the rotor. The selection of the q- and d-axis directions and their insulation ratios will be explained in details in the following sections. The insulation ratio is defined as given in Equation 2.1.

$$k_{wq,d} = \frac{\text{Total barrier air length on } q, d - \text{axis}}{\text{Total segment iron length on } q, d - \text{axis}} \quad (2.1)$$

Selection of the insulation ratios for synchronous reluctance motors is related to the motor's geometry also. According to A. O. Dulanto's thesis, the q-axis insulation that gives the largest inductance difference between L_d and L_q is between 0.3 and 0.6, as shown in Figure 2.2 [34].

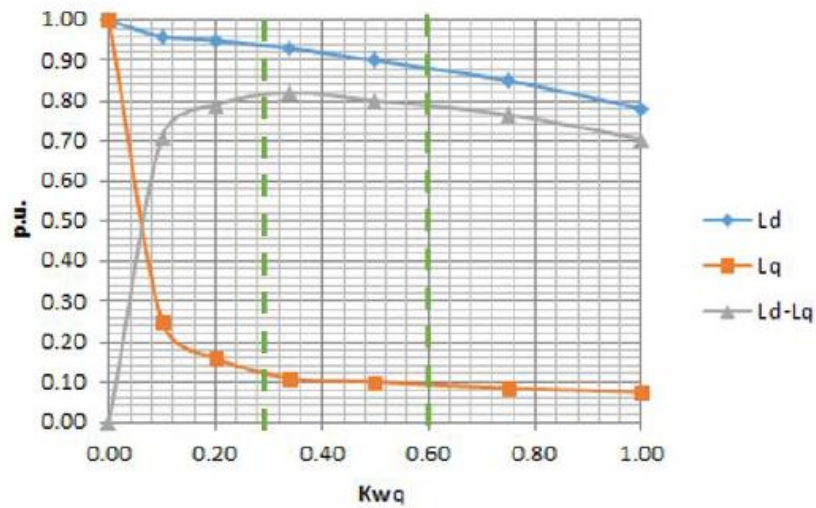


Figure 2.2 : Change of inductance values with respect to q-axis insulation ratio [34].

2.4 Positioning of Barriers and Segments

While positioning the barriers and the segments constant slot pitch is used as a general method. According to this method, the angle between two adjacent segment ends is kept constant. The barriers in between the segments are considered as slots, and in order to minimize the torque ripple, their midpoint position is adjusted with respect to the stator slot number. Equation 2.2 gives the angle between two adjacent segments in the constant slot pitch method [35].

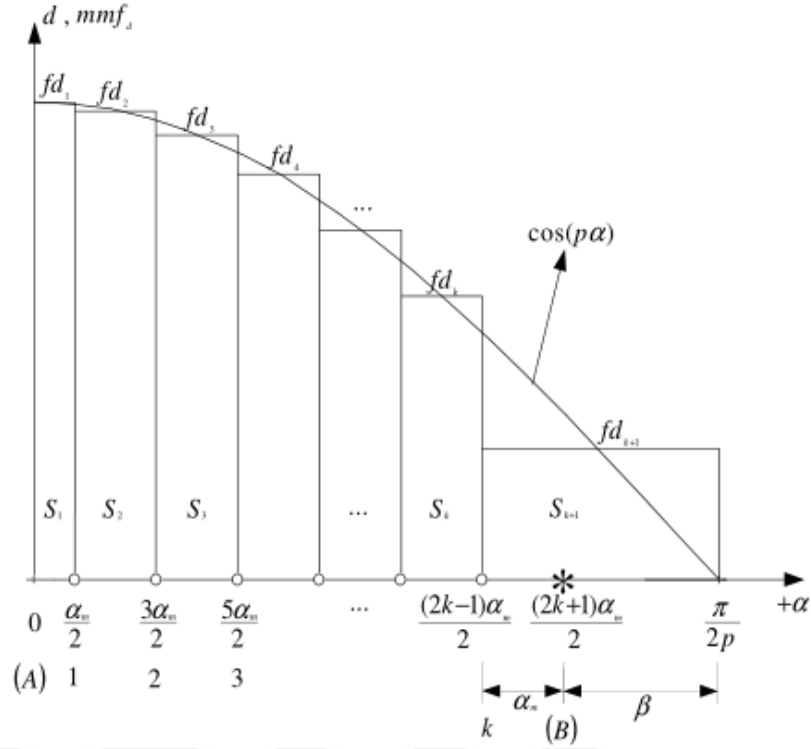


Figure 2.4 : P. u. MMF distribution in the d-axis [35].

Referring to the MMF distribution above, the width of the segments in d-axis can be determined using the following Equation 2.3 and 2.4 [32].

$$fd_h = \frac{\int_{\frac{2h-3}{2}\alpha}^{\frac{2h-1}{2}\alpha} \cos(p\alpha) d\alpha}{\alpha} = \frac{\sin\left(p\frac{2h-1}{2}\alpha\right) - \sin\left(p\frac{2h-3}{2}\alpha\right)}{p\alpha}, h = 1, \dots, k \quad (2.3)$$

$$fd_{k+1} = \frac{\int_{\frac{2k-1}{2}\alpha}^{\frac{\pi}{2p}} \cos(p\alpha) d\alpha}{\alpha + \beta} = \frac{1 - \sin\left(p\frac{2k-1}{2}\alpha\right)}{p(\alpha + \beta)} \quad (2.4)$$

In these equations fd_h represents the per unit MMF coming out from the h^{th} segment. Equation 2.4 is used for calculation of the per unit MMF of the last segment. If the segment width is kept constant on both axes, d-axis segment width is determined by the total iron width between the shaft and rotor radius, and the insulation ratio in the q-axis. However, if they are to be different, the segments width in the d-axis can be calculated and positioned along l_d according to the insulation ratio k_{wd} . Equation 2.5 gives the proportions for calculating the width of each segment using p.u. MMF values.

$$\frac{2S_1}{S_2} = \frac{fd_1}{fd_2}, \quad \frac{S_h}{S_{h+1}} = \frac{fd_h}{fd_{h+1}}, \quad h = 2, \dots, k \quad (2.5)$$

2.6 Flux Barrier Width in Q-axis

The MMF distribution in the q-axis is also assumed to have a sinusoidal form. Taking the d-axis as reference, the sinusoidal distribution of per-unit MMF block in the q-axis is given in Figure 2.5.

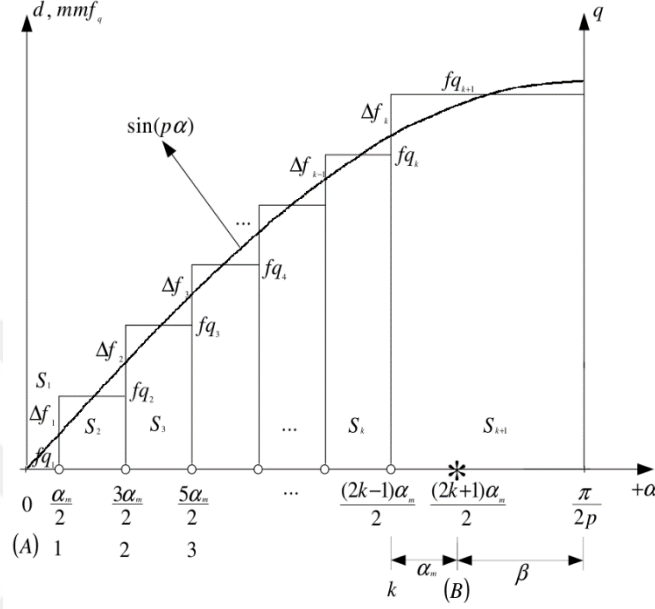


Figure 2.5 : P. u. MMF distribution in the q-axis [35].

As it can be seen from the figure, the difference of MMF values Δf_k between two adjacent segments can be calculated and used for the calculation of the optimum barrier width in q-axis [35]. The following equations are used for calculation of the per-unit MMF values in the q-axis.

$$f_{q_1} = 0, h = 2, \dots, k \quad (2.6)$$

$$f_{q_h} = \frac{\int_{\frac{2h-3}{2}\alpha}^{\frac{2h-1}{2}\alpha} \sin(p\alpha) d\alpha}{\alpha} = \frac{\cos\left(p\frac{2h-3}{2}\alpha\right) - \cos\left(p\frac{2h-1}{2}\alpha\right)}{p\alpha} \quad (2.7)$$

$$f_{q_{k+1}} = \frac{\int_{\frac{2k-1}{2}\alpha}^{\frac{\pi}{2p}} \sin(p\alpha) d\alpha}{\alpha + \beta} = \frac{\cos\left(p\frac{2k-1}{2}\alpha\right)}{p(\alpha + \beta)} \quad (2.8)$$

Equations 2.6-2.8 are used for calculation of the p.u. MMF values of each flux block in the q-axis.

The difference between two adjacent MMF blocks is given by Equation 2.9-2.10 [35].

$$\Delta f_1 = f_{q_2} - f_{q_1} = \frac{\cos\left(\frac{p\alpha}{2}\right) - \cos\left(\frac{3p\alpha}{2}\right)}{p\alpha} \quad (2.9)$$

$$\Delta f_{h-1} = \frac{(2\alpha + \beta)\cos\left(p\frac{2k-1}{2}\alpha\right) - (\alpha + \beta)\cos\left(p\frac{2k-3}{2}\alpha\right)}{p\alpha(\alpha + \beta)} \quad (2.10)$$

The ratio of the barrier width is equated to the square of the corresponding MMF difference ratios, and calculated as given in Equation 2.11 [35].

$$\frac{W_{1h}}{W_{1h+1}} = \left(\frac{\Delta f_h}{\Delta f_{h+1}}\right)^2, h = 1, \dots, k-1 \quad (2.11)$$

2.7 Barrier Width in D-axis

While defining the barrier width in d-axis, it is very important to select the right perpendicular axis to it. The position of this perpendicular axis is directly related to the magnitude of the imaginary angle β . In this thesis, in order to define l_d , the total length available in the d-axis, the angle β is equated to $\alpha/2$. Thus, the new slot pitch angle α' is calculated as given in Equation 2.12.

$$\alpha' = \alpha|_{\beta=\frac{\alpha}{2}} = \frac{\frac{\pi}{2p}}{k+1} \quad (2.12)$$

Therefore, the width of the complete d-axis l_d given in Figure 2.6, stretches from the center of d-axis to point C which is at angular distance of $(\frac{3}{4})\alpha$ away from the q-axis. The length of l_d is calculated as given in Equation 2.13 [4].

$$l_d = \left(\frac{D_s}{2} - g\right) * \sin\left(\frac{\pi}{2p} - \frac{3\alpha'_m}{4}\right) \quad (2.13)$$

In Equation 2.13, D_s denotes the inner diameter of the stator, g is the air-gap length and p is the number of pole pairs. Since l_d is the total width of the d-axis, it does not give any idea related to the width of the barriers in this axis. By keeping the ratio of the barrier widths in d-axis the same as the ratio of those in q-axis, the following

$$F_{qm} = \frac{4}{\pi} \times \frac{m}{2} \times \frac{\sqrt{2} I_q N k_w}{P} \quad (2.16)$$

In the previous equations, m represents the number of phases, k_w defines the winding factor and P is the total pole number of the model.

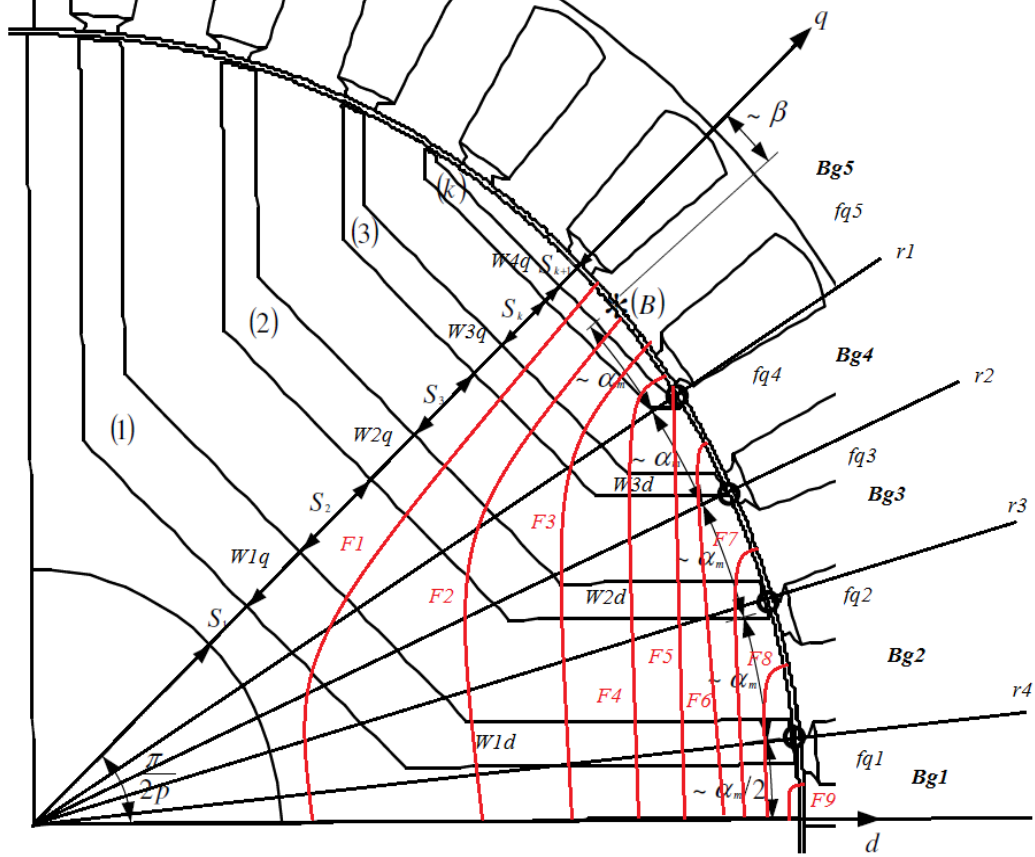


Figure 2.7 : Magnetic flux lines in the q-axis [35].

Multiplication of the maximum MMF values with its per unit calculated under each segment, gives the real value of the MMF at that portion. Following the flux lines in the q-axis as defined in Figure 2.7 and assuming that the ferromagnetic material has infinite permeability, the MMF in the air-gap would be equal to the sum of MMF values in the barriers through which the corresponding flux line passes. Thus, the equation corresponding to line F_1 is as given in Equation 2.17.

$$B_{1c} W_{1q} + B_{2c} W_{2q} + B_{3c} W_{3q} + B_{4c} W_{4q} + B_{g5} g_5 = F_{qm} \times f_{q5} \times \mu \quad (2.17)$$

B_{g5} is the air-gap magnetic flux density between q and r_1 axes, whereas B_{1c} , B_{2c} , B_{3c} and B_{4c} are the magnetic flux density in the center part of the barriers. W_{iq} represents

the width of the i^{th} barrier in the q -axis. Moreover, f_{q5} defines the per-unit MMF value between q and r_1 axes as defined in equation. Multiplying this variable with the maximum F_{qm} gives the real time MMF on that portion of the air-gap.

The MMF equation corresponding to line F_2 is written as given in Equation 2.18.

$$B_{1s}W_{1d} + B_{2c}W_{2q} + B_{3c}W_{3q} + B_{4c}W_{4q} + B_{g5}g_5 = F_{qm} \times f_{q5} \times \mu \quad (2.18)$$

B_{1s} defines the magnetic field density at the side part of the first barrier, whereas W_{1d} is the width of the first barrier in the d -axis. In the same manner MMF equations for the remaining lines ($F_3 \dots F_8$) are written following the corresponding lines. At last, the equation corresponding to line F_9 is written as given in Equation 2.19.

$$B_{g1}g_1 = F_{qm} \times f_{q1} \times \mu \quad (2.19)$$

Furthermore, by equating the MMF in a single flux barrier with the MMF on the air-gap in such way that they make up a closed loop, “ k ” more equations can be defined to make the system of equations solvable for the required variables.

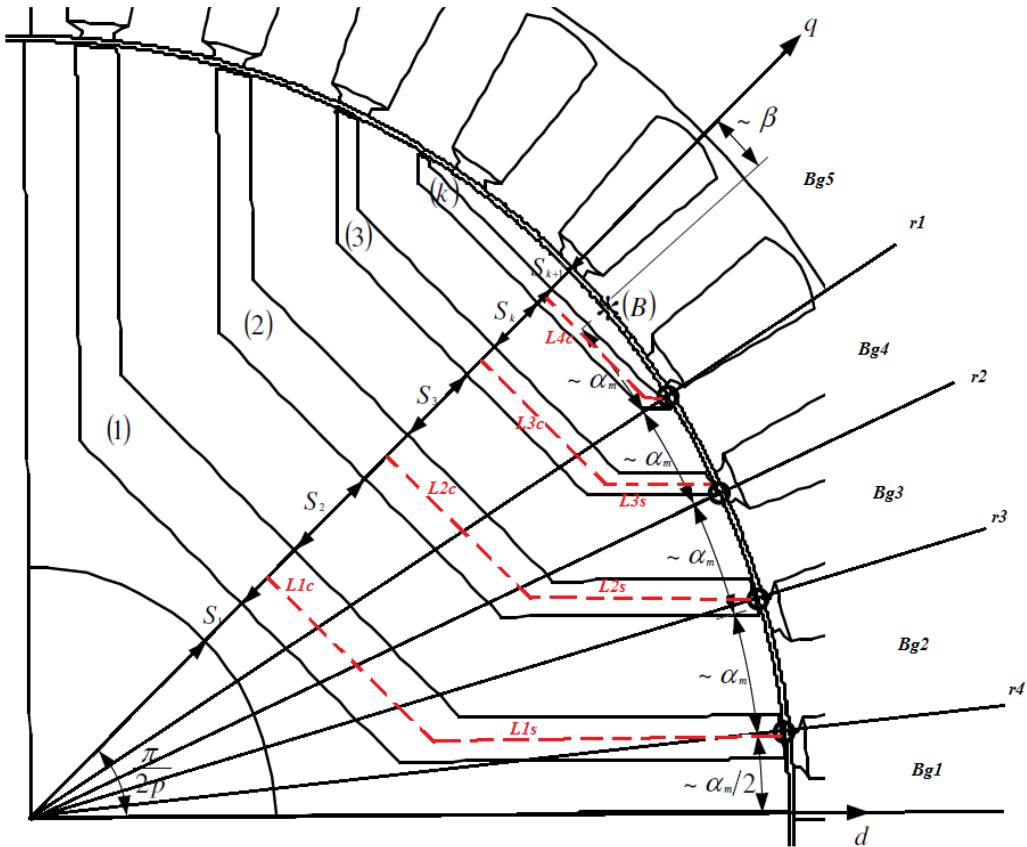


Figure 2.8 : MMF lines along the flux barriers [35].

Referring to Figure 2.8, the equation corresponding to the 4th barrier is as given in Equation 2.20.

$$\left(\frac{D_s - g}{2}\right) \left[\int_{7\alpha_m/2}^{\pi/4} B_{g5} d\theta \right] = L_{4c} \times B_{4c} + L_{4s} \times B_{4s} \quad (2.20)$$

L_{4c} defined the length of the center part whereas L_{4s} defines the length of the side part of the 4th barrier. Similarly, the equations for the barrier 3 is written as given in Equation 2.21.

$$\left(\frac{D_s - g}{2}\right) \left[\int_{7\alpha_m/2}^{\pi/4} B_{g5} d\theta + \int_{5\alpha_m/2}^{7\alpha_m/2} B_{g4} d\theta \right] = L_{3c} \times B_{3c} + L_{3s} \times B_{3s} \quad (2.21)$$

In these equations, D_s is the stator inner radius, whereas g is the air-gap length. The equations for the third and fourth barriers are written in the same way by equation the MMF along the barrier to the corresponding MMF sum in the air-gap.

With the least equations written the number of variables and the number of independent equations is equal. Solution of this system, gives the magnetic field density at the center and side part of barriers and the magnetic field density under each segment in the air-gap as a function of the quadrature axis I_q current. The total flux in the q-axis ϕ_q using the magnetic field densities calculated above is calculated with the following Equation 2.22.

$$\phi_q = 2 \frac{D_s}{2} L \int_0^{\pi/4} B_q d\theta \quad (2.22)$$

Total flux calculated above is a function of I_q current whereas L is the stack length of the motor. The flux linkage ψ_{mq} in the same axis is given in Equation 2.23.

$$\psi_{mq} = k_w N \phi_q = \sqrt{2} L_{mq} I_q \quad (2.23)$$

Replacing the flux equation in the flux linkage equation, the inductance in the q-axis is calculated with the following Equation 2.24.

$$L_{mq} = \frac{\psi_{mq}}{\sqrt{2} I_q} = \frac{k_w N \phi_q}{\sqrt{2} I_q} \quad (2.24)$$

In Equation 2.23 and Equation 2.24 k_w is the winding factor, N is the total number of turns per phase. For calculating the direct axis inductance, we again assume that the permeability of the ferromagnetic material is infinite, therefore we neglect the MMF in the flux segments and we consider only that in the air-gap. According to the flux lines defined in Figure 2.9, equating the MMF in the air-gap with the calculated value using the maximum and the per-unit MMF under each segment, the equation becomes as given in Equation 2.25.

$$B_{di} g = F_{dm} \times f_{di} \times \mu \tag{2.25}$$

$i=1 \dots 5$ defines the number of the corresponding segment. The variables calculated from the system of equations are the magnetic flux densities in the air-gap under each segment and they are calculated as a function of I_d .

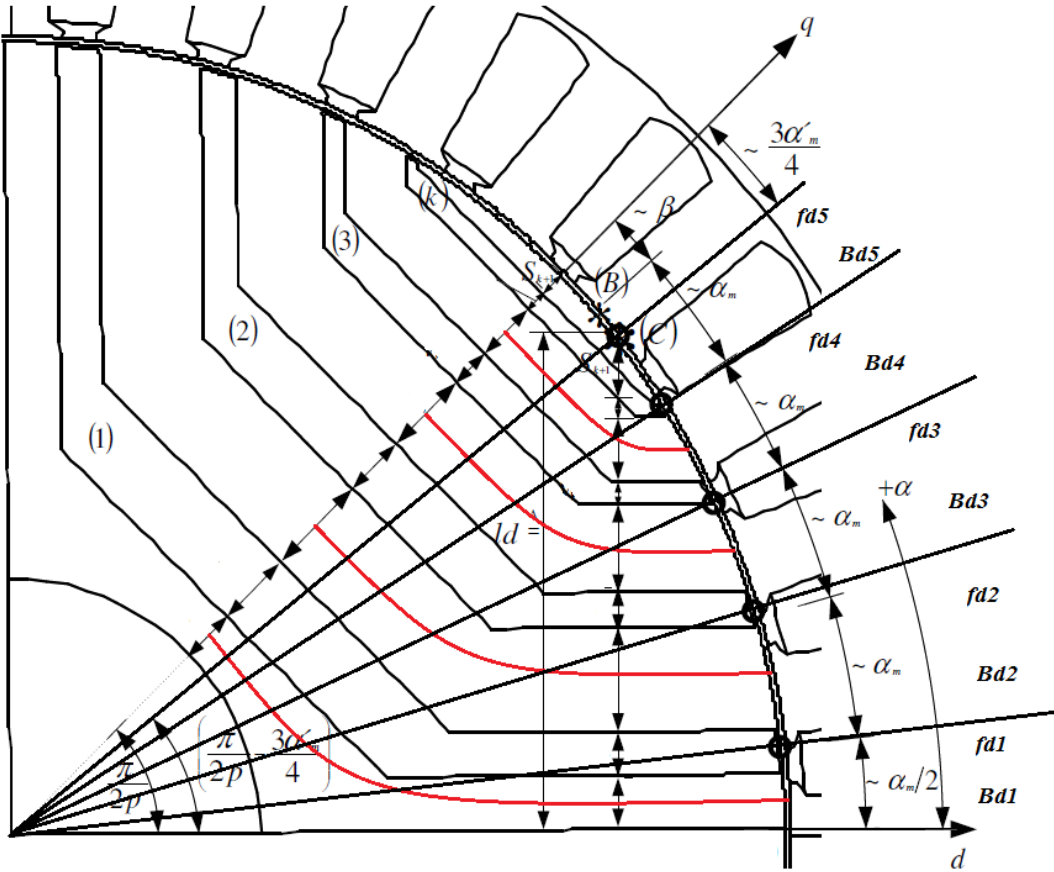


Figure 2.9 : MMF lines along the flux segments [35].

Similar to the q-axis flux, the total flux in the d-axis as a function of I_d current is calculated by summing the magnetic flux density under each segment multiplied by

the corresponding section area under that segment. The total flux in the d-axis ϕ_d is calculated as given in Equation 2.26.

$$\phi_d = 2 \frac{D_s}{2} L \int_0^{\pi/4 - 3\alpha/4} B_d d\theta \quad (2.26)$$

The flux linkage for the calculated total flux in the d-axis ψ_{md} is calculated using Equation 2.27.

$$\psi_{md} = k_w N \phi_d = \sqrt{2} L_{md} I_d \quad (2.27)$$

Replacing the flux equation in the flux linkage equation, the inductance in the d-axis is calculated with the following Equation 2.28.

$$L_{md} = \frac{\psi_{md}}{\sqrt{2} I_d} = \frac{k_w N \phi_d}{\sqrt{2} I_d} \quad (2.28)$$

Using the analytic method explained above, the d- and q-axis inductances for the sample and the optimized prototype models are calculated and recorded in Table 2.1 below. The given inductance values are in unit of [mH].

Table 2.1 : Inductance values and saliency ratios.

Model	L_{md}	L_{mq}	Saliency Ratio- ξ
Sample Prototype	113.4	10.9	10.4
Optimized Prototype	156.3	12.3	12.45



3. FINITE ELEMENT METHOD

Finite Element Method is a numerical analysis method developed in 1940 by Courant for solving mechanical and stability problems [37]. In the following years this method was used in solving problems related to airplane designs, elasticity problems, structural analysis, fluid dynamics and electromagnetic field problems. Such analysis method, is based on discretization of the model being analyzed into small parts, and solving the relative physical equations (thermal, mechanic, electromagnetic) for each part separately. In this thesis, the electromagnetic analysis is done using the finite element method solving software package known as ANSYS Maxwell, and all models are analyzed in the two dimensional module.

3.1 Maxwell Equations

The finite element solution of an electromagnetic model whose boundary conditions are defined, is related to solution of the Maxwell Equations over the same model. This set of equations explained the macroscopic behavior of all electromagnetic phenomena. Developed firstly by James Clerk Maxwell, these equations were later detailed in the research work of Michael Faraday, Andre Marie Ampere and Carl Friedrich Gauss, explaining the behaviors of electromagnetism very close to the real one. The following equations give the derivatives of the Maxwell equations:

$$\nabla \times \mathbf{E} = -\frac{\partial \mathbf{B}}{\partial t} \quad (3.1)$$

$$\nabla \times \mathbf{H} = \frac{\partial \mathbf{D}}{\partial t} + \mathbf{J} \quad (3.2)$$

$$\nabla \cdot \mathbf{D} = \rho \quad (3.3)$$

$$\nabla \cdot \mathbf{B} = 0 \quad (3.4)$$

In equations 3.1 to 3.4, E [V/m] is the electric field intensity, D [C/m] is the electric field density, H [A/m] is the magnetic field intensity and B [T] denotes the magnetic

field density. When the derivative of the fields with respect to time becomes zero for electrostatic and magneto-static field cases, the equations are changed as follows:

$$\nabla \times \mathbf{E} = 0 \quad (3.5)$$

$$\nabla \times \mathbf{H} = \mathbf{J} \quad (3.6)$$

$$\nabla \cdot \mathbf{J} = 0 \quad (3.7)$$

In this case, it is obvious that there is no relation between electric and magnetic fields. Therefore, in case of unchanging fields with respect to time, electric and magnetic field are independent of each other.

The equations 3.1 to 3.3 are known as the basic Maxwell Equations. However, since there is larger number of unknowns than the number of equations, it is still an undefined system of equations. When the equalities given in equations 3.8 to 3.10 are replaced, Maxwell Equations become definite.

$$\mathbf{D} = \epsilon \mathbf{E} \quad (3.8)$$

$$\mathbf{B} = \mu \mathbf{H} \quad (3.9)$$

$$\mathbf{J} = \sigma \mathbf{E} \quad (3.10)$$

In equations 3.8 to 3.10 ϵ , μ and σ denote the material dielectric [F/m], magnetic permeability [H/m] and conductivity [S/m], respectively.

3.2 Boundary Conditions and Periodicity

To be able to analyze a system using the finite element methods, it is required to define the boundary conditions of the system. In finite element analysis, the boundary conditions that are most met are the Dirichlet and Neumann boundary conditions. Dirichlet boundary condition is an indispensable condition for the solution of the problem, because it defines the value of the variable at the boundary of the solution space. For electromagnetic analysis, this variable is the magnetic flux. Neumann boundary condition defines the value of the derivative of variable at the boundary, which in all is equal to zero. If Dirichlet boundary condition is defined, Neuman condition is automatically satisfied during the solution of the problem.

Another issue that requires attention in finite element method analysis is the periodicity of the model. If the model to be solved is a periodical model, except the boundary conditions, the symmetry axes are defined for the smallest repeating part of the model. Thus, the model becomes smaller, the number of equations to be solved and the solving time are decreased.

3.3 Discretization of Model and Mesh Structure

As it was mentioned above, finite element analysis is realized on models that are discretized into small parts. The discretization process or meshing, divides the model in numerous small subspaces called as elements. Optimum meshing of the models is very important regarding the solving time and the data stored during solution. A model having large number of elements gives better results, however solving time of such model last longer and require larger data storage capacities.

The elements resulting from the meshing process of a model, come up in different forms depending on the number of model dimensions. For example, dividing a regular two dimensional rectangles into smaller rectangles and dividing an irregular geometry into small triangles would give the optimum solution for an optimum solving time. Figure 3.1 gives different element geometries used in model meshing. In single dimensional geometries nodes and lines, in two dimensional geometries surface triangles and rectangles, whereas in three dimensional models volumic pyramids, triangle or rectangle prisms are used as meshing elements.

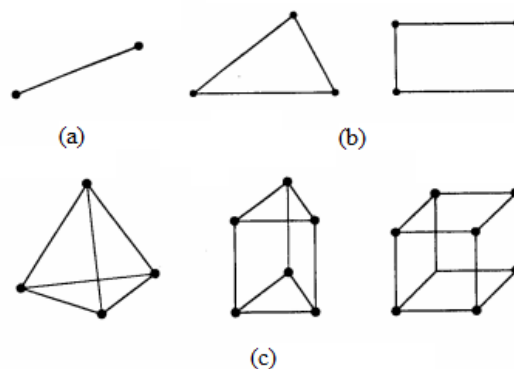


Figure 3.1 : (a) Single dimension (b) Two dimension (c) Three dimensional mesh element geometries [37].

The structure of the mesh and the number of elements built inside it have a significant effect on the accuracy of the solution and solving time. A denser mesh

will give more accurate solution, however in regions of the model where the physical parameters do not change much dense mesh is unnecessary. For example, while modelling a synchronous machine, the mesh on the stator and the air-gap should be dense because the magnetic field changes direction and magnitude more frequently, whereas in the stator the field is nearly constant and smaller number of elements would be enough. Thus, both accuracy and optimum solving time are satisfied while analyzing the model. The electromagnetic optimization analysis in the following section are all performed using finite element method solving software Maxwell 2D.



4. OPTIMIZATION ANALYSIS OF THE SAMPLE PROTOTYPE

The sample prototype that is optimized in the following sections, as it was mentioned before, is designed for washing machine applications. It has two different operating speeds, washing and spinning mode operation. During washing mode operation the motor operates at constant torque region with a rotating speed of 563 min^{-1} , whereas at spinning mode the motor reaches up to 13000 min^{-1} at voltage and current limited regions. At voltage and current limited region operation the magnetic field is weakened, therefore the most critical electromagnetic design is the constant torque operation where the magnetic field is higher. The geometrical and electromagnetic characteristics together with the output performance of the sample motor at washing mode rated current are given in Table 4.1.

Table 4.1 : Characteristics of the sample prototype [3].

Parameter	Value
Turns/phase	420
Phase Resistance [ohms]	6.7
Slot Fill Factor [%]	40
Air-gap [mm]	1
Outer Diameter [mm]	120
Stack Length [mm]	32
Magnet Volume [cm^3]	19.16
Washing Speed [min^{-1}]	563
Current [A]	1.62
Torque [Nm]	0.9

The purpose in the following sections is to increase the output torque of the motor for the same rated current to target value of 1.2 Nm. The outer diameter, stack length and the slot fill factor are limited so they will not change during optimization work also. All other parameters including air-gap length, magnet type, magnet volume, turn number etc. may change if required. The combination of stator slot and rotor barrier number is also kept the same as the prototype motor, meaning that the stator will have 36 slots and the rotor will have three flux barriers per pole. The ferromagnetic material used in the following analysis is SURA M700 50A type,

whose magnetizing curve is given in Figure 4.1, and the maximum saturation value of the final selected model should not pass 1.3 T.

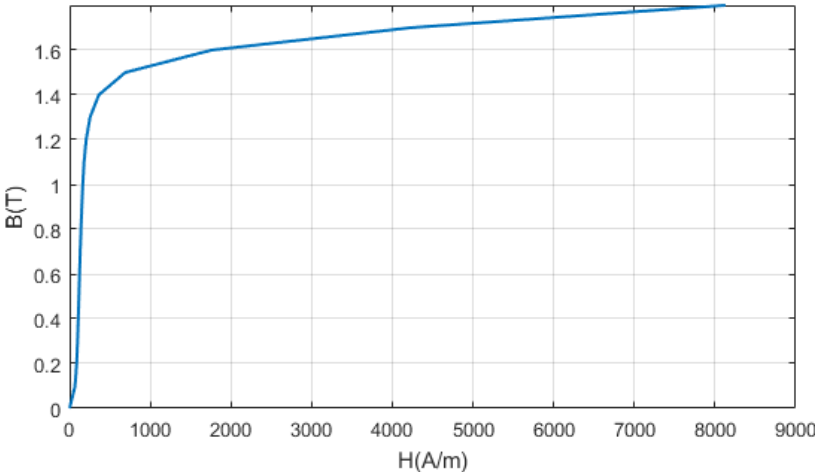


Figure 4.1 : Magnetizing curve of M700 ferromagnetic material [38].

4.1 Analysis of Air-gap Length’s Effects

Keeping all the parameters the same and changing only the rotor diameter, the effect of the air-gap length has been observed by solving the prototype model using FEM in Maxwell software. Stator structure, teeth, yoke, magnet volume and turn number are kept constant during this investigation.

4.1.1 Motor model with g=1mm

Motor model with air-gap length of g=1 mm is the prototype itself. To have a better comparison analysis, the prototype simulation and results are given in this section also. Its geometry is given in Figure 4.2.

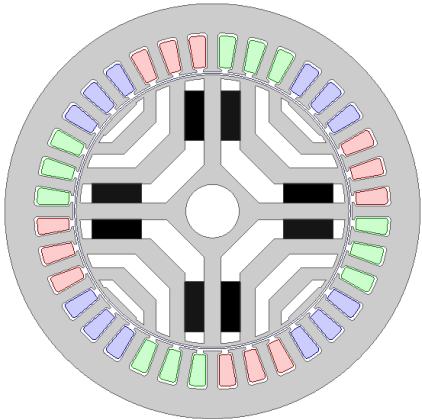


Figure 4.2 : Geometry of prototype model with g=1 mm.

The simulation results including magnetic flux and the equi-flux lines of the prototype motor are given in Figure 4.3.

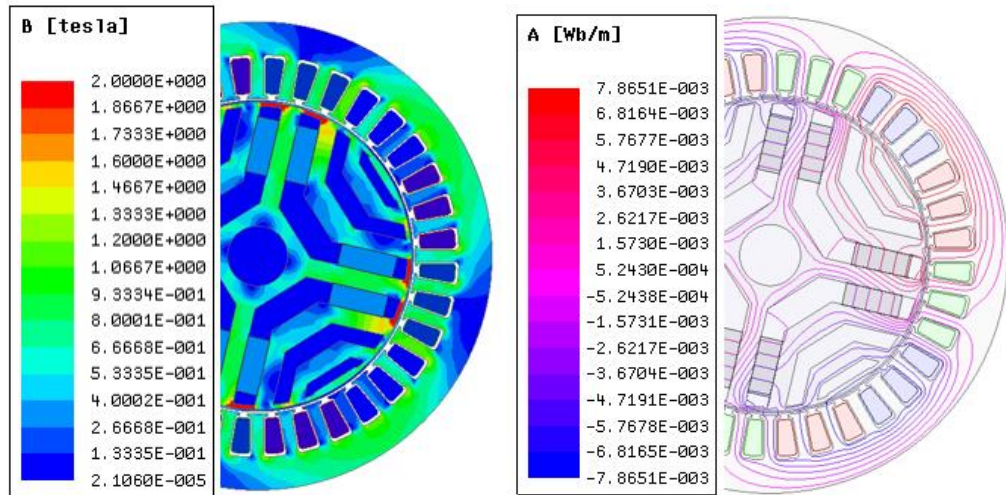


Figure 4.3 : Magnetic flux density and equi-flux lines of model prototype model with $g=1$ mm.

4.1.2 Motor model with $g=0.9$ mm

In this model the air-gap length is decreased by 0.1 mm by increasing the rotor diameter. The simulation results of magnetic flux density and equi-flux lines of the model having air-gap length of $g=0.9$ mm are given in Figure 4.4.

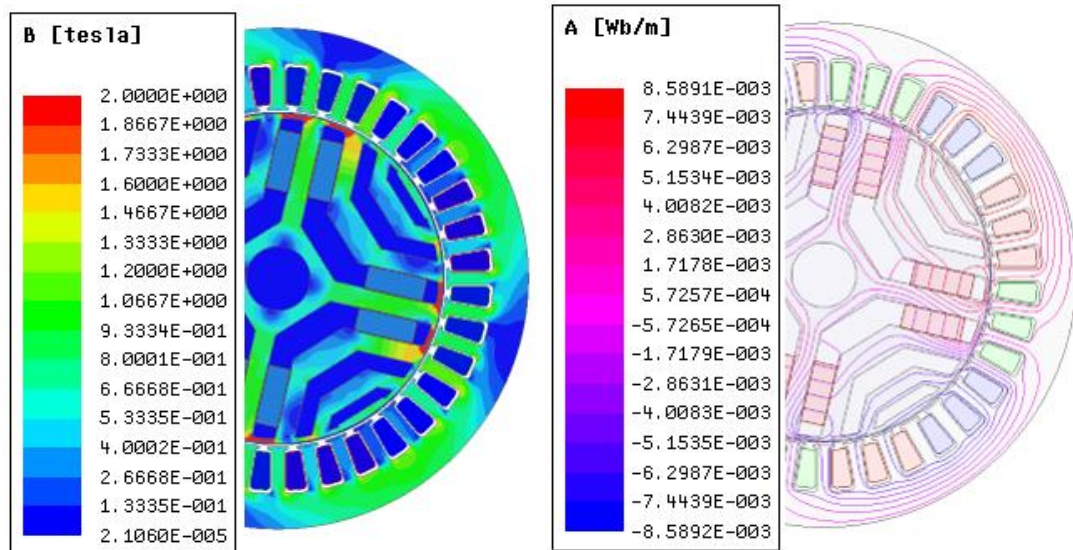


Figure 4.4 : Magnetic flux density and equi-flux lines of model prototype model with $g=0.9$ mm.

Decrease of the air-gap length, as it was expected, resulted in higher saturation of the motor ferromagnetic material.

4.1.3 Motor model with $g=0.8\text{mm}$

Similarly, the air-gap is further decreased to a value of $g=0.8\text{ mm}$. The magnetic flux density and equi-flux lines of the model having air-gap length of $g=0.8\text{ mm}$ are given in Figure 4.5.

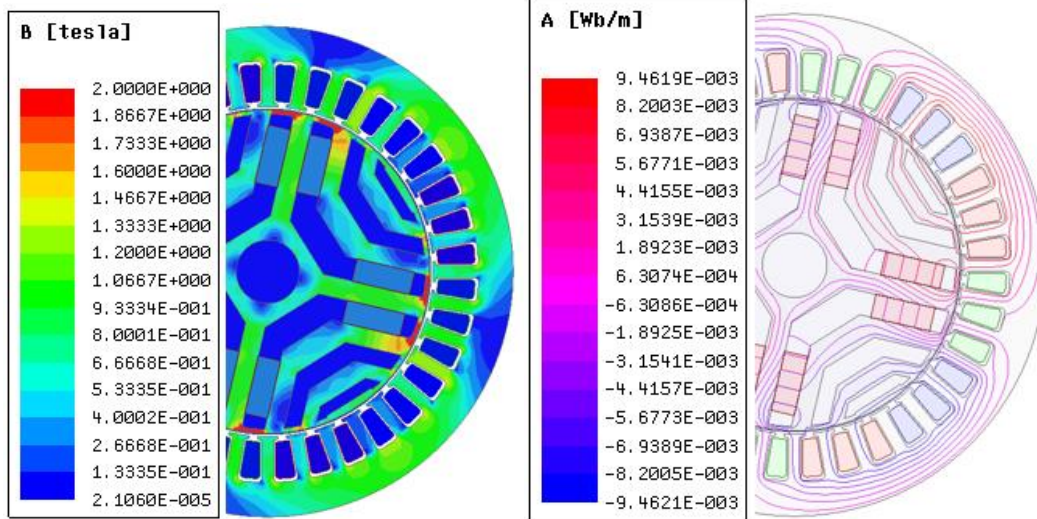


Figure 4.5 : Magnetic flux density and equi-flux lines of model prototype model with $g=0.8\text{ mm}$.

4.1.4 Motor model with $g=0.7\text{mm}$

The magnetic flux density and equi-flux lines of the model having air-gap length of $g=0.7\text{ mm}$ are given in Figure 4.6.

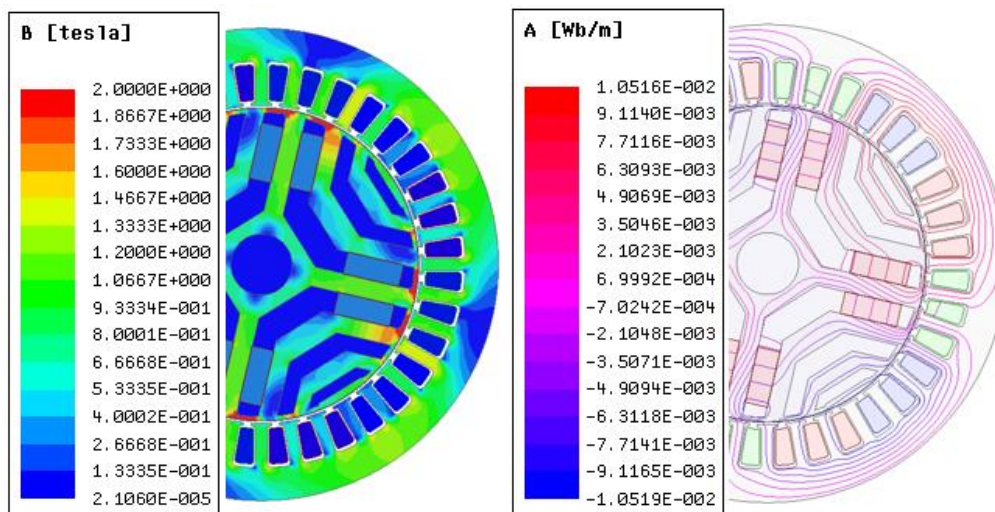


Figure 4.6 : Magnetic flux density and equi-flux lines of model prototype model with $g=0.7\text{ mm}$.

4.1.5 Motor model with $g=0.6\text{mm}$

The magnetic flux density and equi-flux lines of the model having air-gap length of $g=0.6\text{ mm}$ are given in figure 4.7. The saturation of the stator teeth due to narrow air-gap length has resulted in saturation of the ferromagnetic material over the knee region of the magnetizing curve.

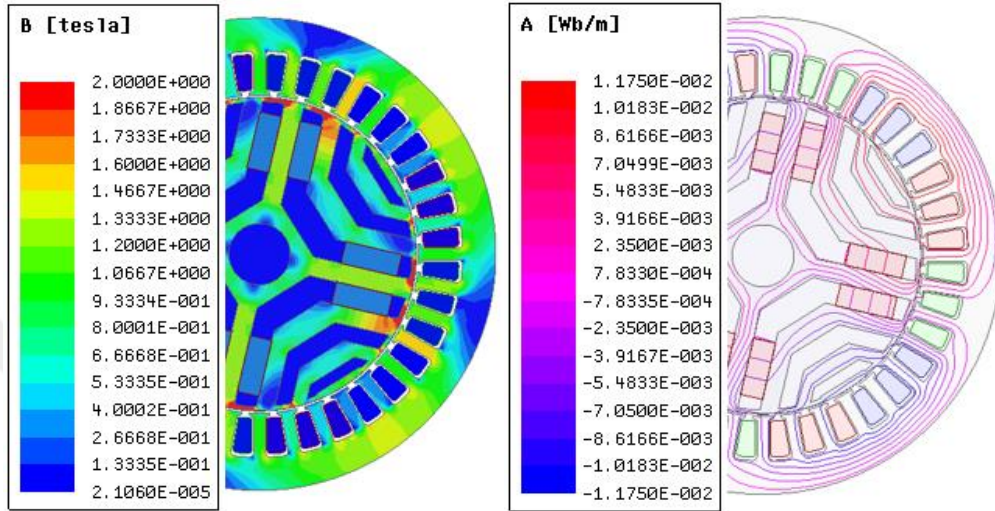


Figure 4.7 : Magnetic flux density and equi-flux lines of model prototype model with $g=0.6\text{ mm}$.

4.1.6 Motor model with $g=0.5\text{mm}$

The magnetic flux density and equi-flux lines results of the model having air-gap length of $g=0.5\text{ mm}$ are given in Figure 4.8. Saturation on both teeth and yoke has passed the knee region magnetic flux density.

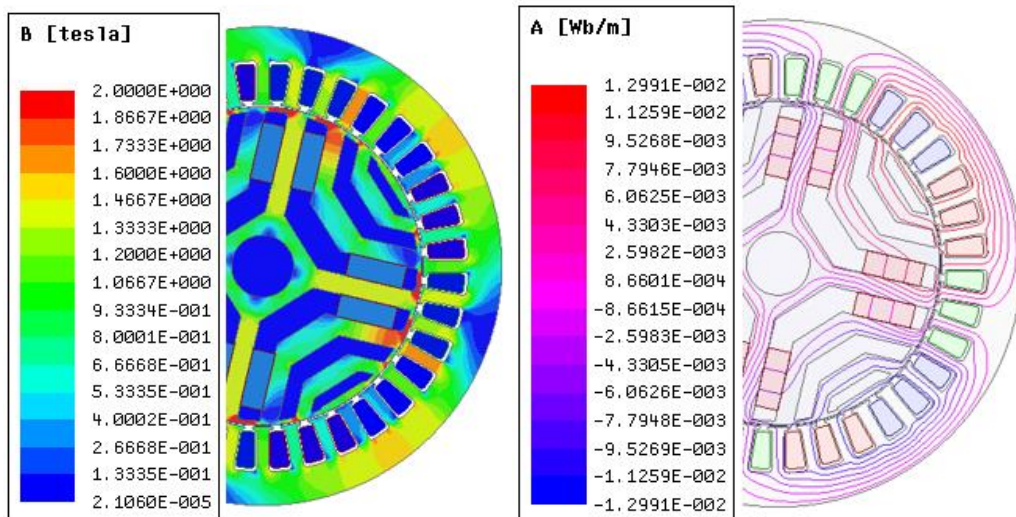


Figure 4.8 : Magnetic flux density and equi-flux lines of model prototype model with $g=0.5\text{ mm}$.

4.1.7 Comparison results and analysis

The simulation results observed from the FEM analysis of the previous models are given in this section. The induced torque graphs for all the models with different air-gap lengths are given in Figure 4.9. Decrease of the air-gap increases the induced torque. However, at the same time it increases the torque ripple which is not desirable in washing machine applications.

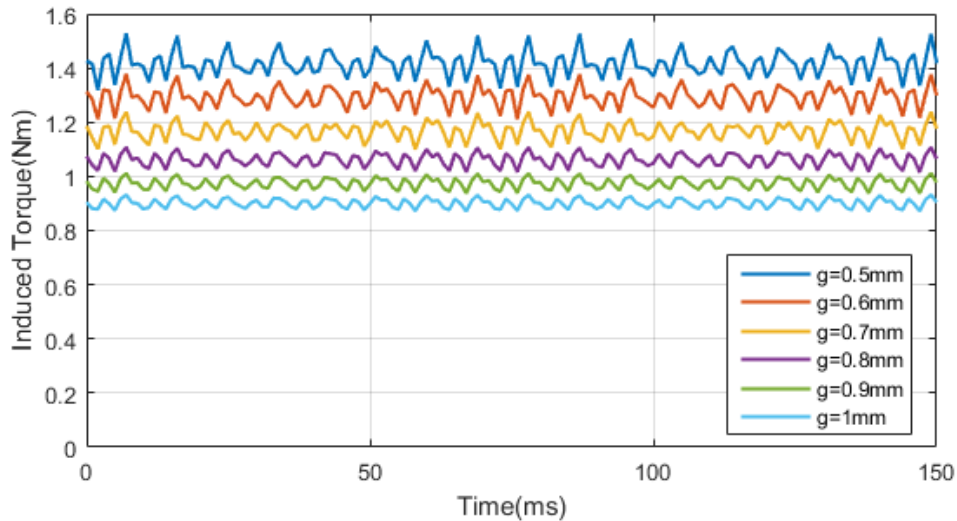


Figure 4.9 : Torque graph comparison for different air-gap lengths.

As the air-gap length decreases, the increase of the magnetic field rotating in the stator of the motor induces higher voltages in the motor windings, thus increasing the output power of the motor. The induced voltage graphs for all models with different air-gap length are given in Figure 4.10.

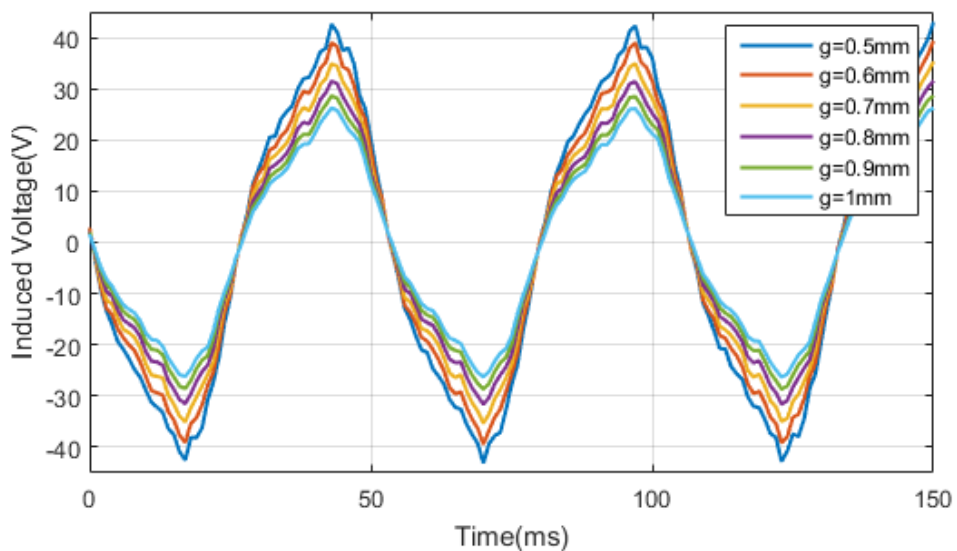


Figure 4.10 : Induced voltage graph comparison for different air-gap lengths.

Another physical quantity that is helpful to be investigated is the magnetic field density distribution in the air-gap. Ideally, this should be as close as possible to a perfect sinusoidal waveform. However, real time air-gap flux densities have a lot of harmonics causing torque ripple and noisy operation. The air-gap magnetic field density for all the models with different air-gap length are given in Figure 4.11.

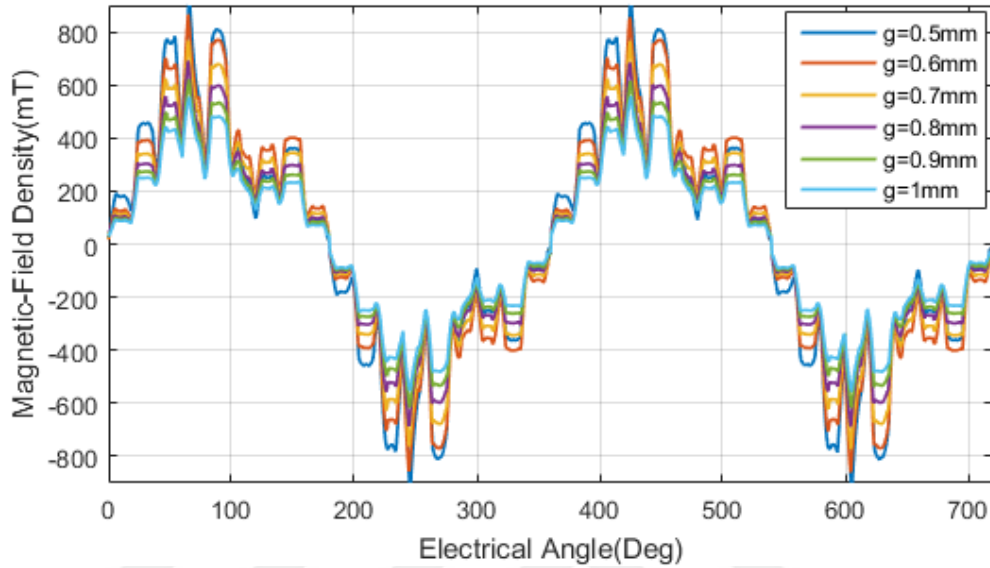


Figure 4.11 : Air-gap magnetic flux density comparison for different air-gap lengths. The harmonic amplitude for the models having air-gap length of 0.5, 0.8 and 1 mm are given in Figure 4.12. The complete harmonic amplitudes for all the models are given in Table 4.2.

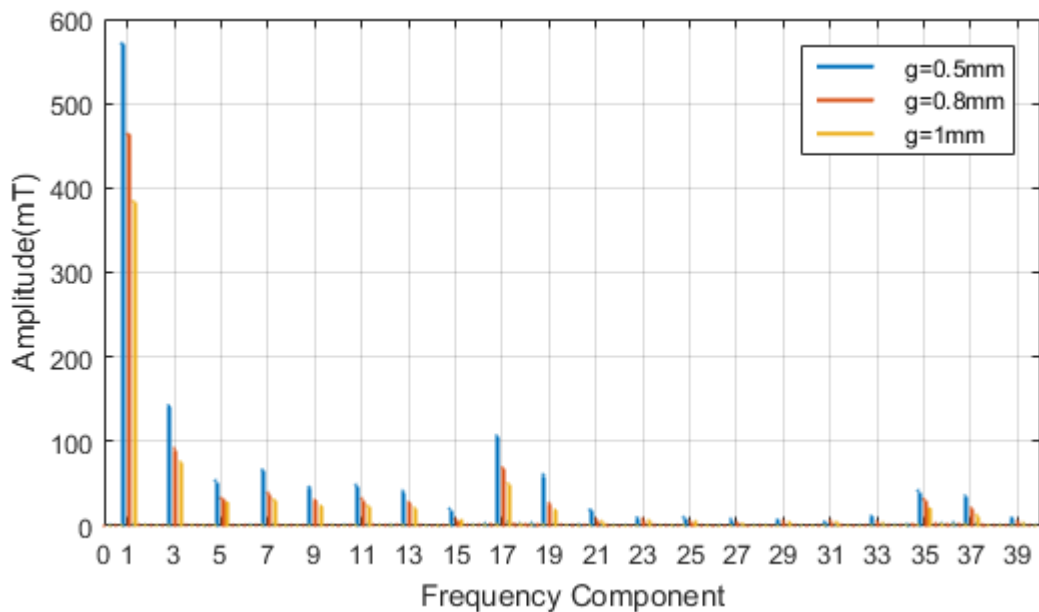


Figure 4.12 : Harmonic amplitude comparison for different air-gap lengths.

Table 4.2 : Harmonic component amplitudes for different g.

Frequency Component	Amplitude [mT]					
	g=1mm	g=0.9mm	g=0.8mm	g=0.7mm	g=0.6mm	g=0.5mm
1	383.9	420.6	463.8	515.7	575.0	630.2
3	75.4	82.4	91.3	100.9	112.5	125.0
5	27.4	29.9	32.6	36.9	41.9	46.3
7	30.9	34.4	38.6	44.1	51.0	57.3
9	23.5	26.5	30.3	34.6	38.9	40.1
11	23.6	27.2	31.9	38.1	45.2	50.4
13	20.8	23.5	27.3	31.9	37.4	40.2
15	6.3	7.1	7.7	9.0	10.5	12.9
17	50.0	58.4	68.9	82.4	99.1	119.2
19	18.8	21.9	26.5	32.3	41.1	54.4
21	5.1	6.2	7.6	9.7	12.7	16.7
23	6.0	7.2	8.1	9.5	11.0	11.9
25	5.0	5.0	5.5	6.0	7.1	8.5
27	2.5	3.1	3.6	4.7	6.1	8.8
29	4.1	4.9	5.7	5.8	6.0	3.7
31	4.3	5.1	5.9	6.4	6.8	4.5
33	3.2	4.0	4.6	6.1	7.9	9.6
35	20.4	25.7	31.6	38.4	45.7	45.9
37	12.6	16.2	20.9	26.4	33.3	35.4
39	3.1	4.1	5.1	6.6	8.1	7.0

Complete comparison of the physical quantities analyzed in this section are given in Table 4.3. The model having air-gap length of $g=0.6$ mm has reached the target output torque. However, the maximum saturation and the torque ripple for this model are high, therefore it makes unsuitable for selection. The maximum saturation value is required to not pass 1.3 T and torque ripple should not be too high. As a result, it is insufficient to modify the prototype by only changing the air-gap length. Thus, the following sections other parameters will be optimized to obtain the target output under the pre-defined limitations.

Table 4.3 : Average and RMS data comparison for different g.

Air-gap Length [mm]	B_{rms} [T]	Induced Torque [Nm]	Induced Voltage _{rms} [V]	Teeth B_{max} [T]	Torque Ripple [%]
0.5	0.472	1.417	27.4	1.65	14.75
0.6	0.43	1.29	24.86	1.56	12.9
0.7	0.383	1.17	22.3	1.43	11.8
0.8	0.343	1.06	20.1	1.3	8.5
0.9	0.31	0.97	18.26	1.18	7.5
1	0.282	0.9	16.7	1.08	6.67

4.2 Selection of the Magnet Type and Dimensions

In this part of the thesis, the effect of the magnet volume placed in the side section of first flux barrier of the PMASynRM is investigated. Keeping the stator structure the same, the motor is simulated for cases with different magnet volume and air-gap lengths. The results, including those of the sample prototype, are given in Table 4.4.

Table 4.4 : The effects of magnet volume and air-gap length on the induced torque.

Turn Number /Slot	Air-gap Length [mm]	Magnet Volume [cm ³]	Induced Torque [Nm]	Torque Ripple [%]
70	1 (prototype)	19.2	0.9	6.67
	1	25.34	1.04	6.73
	0.9	25.34	1.12	8.04
	0.8	25.34	1.21	8.26
	0.7	25.34	1.31	9.92

In the two models having air-gap length of 0.8 and 0.7 mm, the target output torque of 1.2 Nm is satisfied. In both cases the side of the first barrier is completely filled with magnet, resulting in an increased magnet volume to 25.34 cm³. Even though the target torque is reached, the torque ripple is also increased due to the decrease in the air-gap length. In the following parts of the thesis, optimization of techniques will tend to decrease the torque ripple as much as possible. The magnetic field density and the equi-flux lines results of the model with g=0.8 mm and a magnet volume of 25.34 cm³ is given in Figure 4.13.

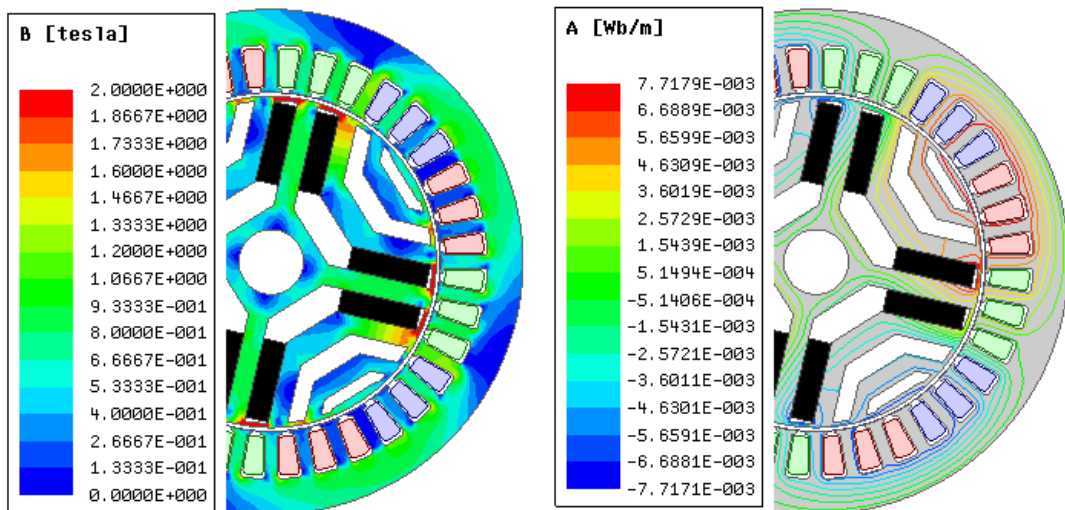


Figure 4.13 : Prototype motor with increased magnet volume.

The type of the magnet used in the prototype is ferrite magnet. Considering the effect of the magnet volume, two types of magnet including ferrite and NdFeB are used in the following investigation. Both types of magnet are used in models with air-gap length of $g=1\text{mm}$ as the prototype and $g=0.8\text{mm}$ as the model which induced the target output torque of 1.2 Nm. The results for the models with ferrite magnet in Table 4.5, whereas of those with NdFeB magnet given in Table 4.6. In the same tables, considering the maximum slot fill factor of 40% in the sample prototype, two different conductor sizes 0.6 mm and 0.7 mm have been used, resulting in a maximum turn number per slot of 70 and 52 turns, respectively. The geometry cross section of the models with different magnet volume are given in Figure 4.14.

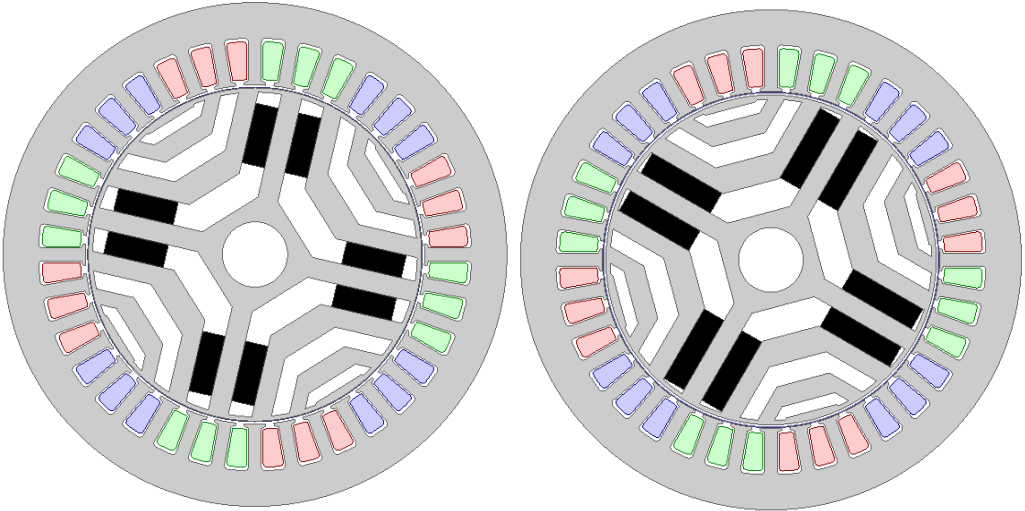


Figure 4.14 : Prototype motor with 19.2 cm³ (left) and 25.34 cm³ (right) volume of magnet.

The simulation results for different air-gap lengths and magnet volume for models using ferrite magnet are given in Table 4.5 whereas of those using NdFeB are given in Table 4.6.

Table 4.5 : Air-gap length and magnet volume’s effects using ferrite magnet.

Conductor Diameter [mm]	Turn Number /Slot	g [mm]	Mag. Vol. [cm ³]	Torque [Nm]	Absolute Ripple [Nm]	Ripple [%]
0.6	70	1	19.2	0.9	0.06	6.67
		1	25.34	1.04	0.07	6.73
		0.8	25.34	1.21	0.1	8.26
0.7	52	1	19.2	0.57	0.038	6.67

Table 4.6 : Air-gap length and magnet volume’s effects using NdFeB magnet.

Conductor Diameter [mm]	Turn Number /slot	g [mm]	Mag. Vol. [cm ³]	Torque [Nm]	Absolute Ripple [Nm]	Ripple [%]
0.6	70	1	19.2	1.688	0.317	18.78
		1	25.34	1.96	0.33	16.84
		0.8	25.34	2.11	0.438	20.76
0.7	52	1	19.2	1.16	0.26	22.41

The target output torque has been reached by decreasing the air-gap length and the ferrite magnet volume, therefore the use of NdFeB type of magnet in such application is unnecessary and disadvantageous due to high price and high saturation of the ferromagnetic material. Therefore, ferrite magnet is decided to be the type of magnet for the oncoming optimization analysis.

4.3 The Effects of Distance Between First Barriers “D”

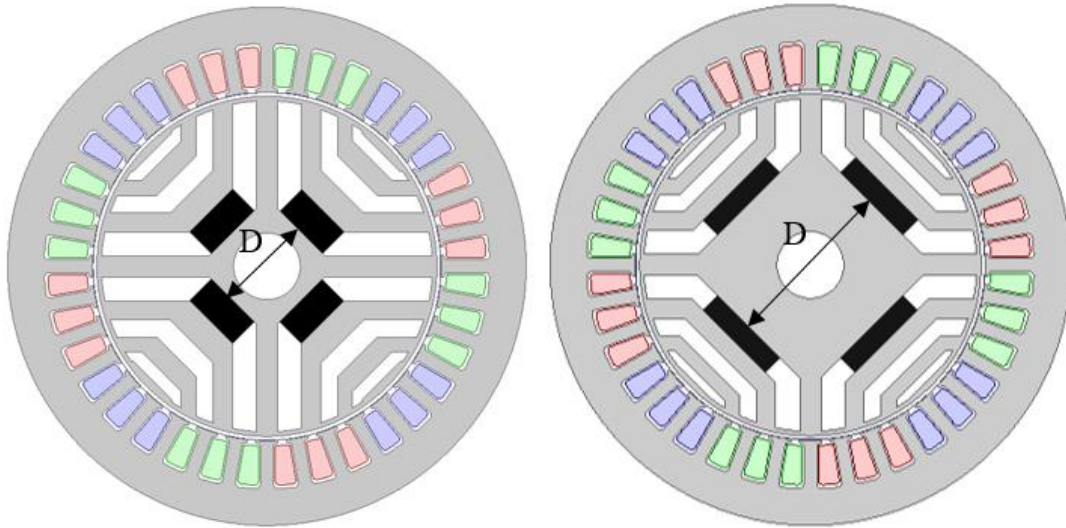


Figure 4.15 : Distance between first flux barriers ”D”.

To analyze the effect of the distance between first barriers on the induced torque and ripple, parameter D has been changed as given in Figure 4.15. During this analysis, the shaft diameter of the motor, and the insulation ratios on the d- and q-axis are kept constant by redrawing the flux segments and barriers accordingly. The results of this analysis are given in Table 4.7.

Table 4.7 : Effect of distance “D” on the induced torque and ripple.

D [mm]	Magnet Volume [cm ³]	Air-gap Length [mm]	Induced Torque [Nm]	Torque Ripple [%]
22.1	12.16	1	0.617	8.27
39.66	12.16	1	0.748	8.56

As it can be seen from Table 4.7, placing the magnets closer to the air-gap results in higher induced torque for the same magnet volume. Therefore, as an upcoming task, this effect is required to be analyzed for different magnet location and volume.

4.3.1 Magnet volume, air-gap length and “D” length’s effects

The effect of the distance D with different magnet configurations and different air-gap length is analyzed and the results are given in Table 4.8. The table includes the cross sectional view of the models simulated, torque data and the maximum magnetic field density occurring in the stator teeth for each model. The models that give an output of 1.2 Nm and higher are highlighted with green color. From Table 4.8 it can be seen that the model with $g=0.7$ mm and $D=39.66$ mm that gives the target torque has several disadvantages over the model having $g=0.8$ mm and $D=22.1$ mm, like higher torque ripple and different magnet dimensions. Different permanent magnet dimensions are problematic during production because they increase the production cost.

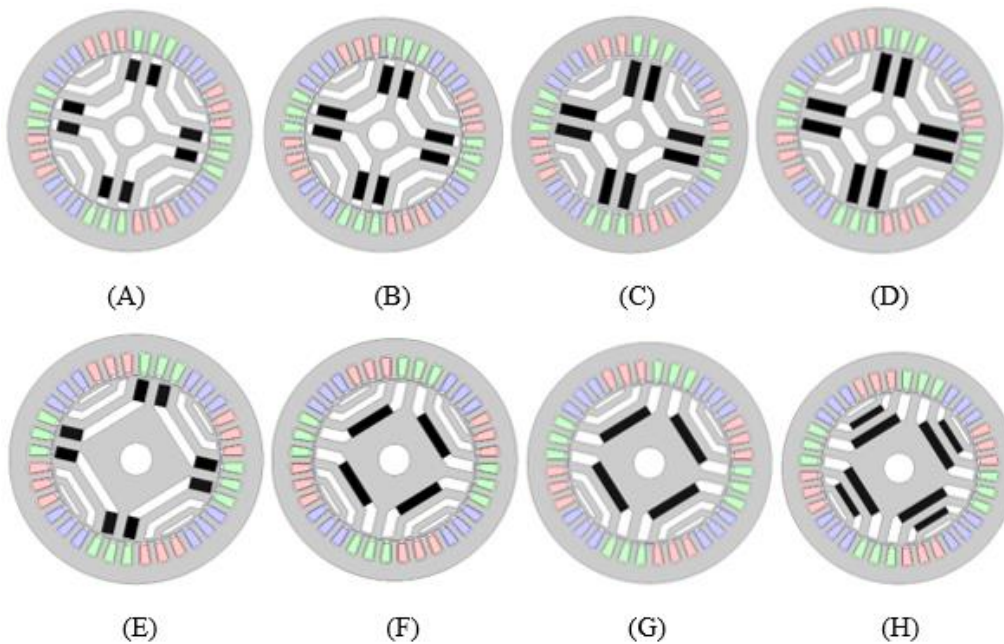


Figure 4.16 : Cross sectional view of models with different D and magnet volume.

Table 4.8 : Effects of D, magnet volume and air-gap length on the average torque and ripple.

D [mm]	Model	Magnet Volume [cm ³]	g [mm]	Torque [Nm]	Absolute Ripple [Nm]	Ripple [%]	B _{max} [T]
22.1	A	14.08	1	0.758	0.053	6.99	0.99
			0.9	0.83	0.064	7.71	1.08
			0.8	0.92	0.078	8.48	1.2
			0.7	1.02	0.12	11.76	1.34
	B	19.35	1	0.9	0.06	6.67	1.08
			0.9	0.974	0.07	7.19	1.18
			0.8	1.06	0.09	8.49	1.3
	C	24.5	0.7	1.16	0.14	12.07	1.43
			1	1.02	0.074	7.25	1.18
			0.9	1.095	0.089	8.13	1.28
	D	25.34	0.8	1.18	0.107	9.07	1.4
			0.7	1.286	0.135	10.50	1.52
1			1.04	0.07	6.73	1.2	
39.66	E	14.08	0.9	1.124	0.084	7.47	1.3
			0.8	1.21	0.11	9.09	1.4
			0.7	1.31	0.135	10.31	1.53
			1	0.763	0.056	7.34	0.997
	F	14.08	0.9	0.837	0.069	8.24	1.1
			0.8	0.923	0.083	8.99	1.21
			0.7	1.04	0.108	10.38	1.36
	G	16.12	1	0.813	0.056	6.89	1.03
			0.9	0.888	0.072	8.11	1.13
			0.8	0.976	0.09	9.22	1.24
	H	24.5	0.7	1.088	0.11	10.11	1.37
			1	0.88	0.058	6.59	1.076
0.9			0.952	0.08	8.40	1.17	
H	24.5	0.8	1.04	0.1	9.62	1.28	
		0.7	1.14	0.12	10.53	1.41	
		1	0.985	0.085	8.63	0.96	
H	24.5	0.9	1.06	0.098	9.25	1.05	
		0.8	1.16	0.11	9.48	1.16	
		0.7	1.28	0.15	11.72	1.29	

Referring to the table results, changing distance D is not suitable for this application since the space for placement of magnets in the first barrier decreases and the second barrier should be filled up with magnet also to satisfy the target torque value. Thus, for further optimization the distance D is decided to remain as in the prototype motor (D=22.1mm). In the following sections detailed analysis of the highlighted models is given including magnetic field density, equi-flux lines, induced torque and voltage.

4.3.1.1 Motor model with $g=0.8\text{mm}/D=22.1\text{mm}$

As it was mentioned before, all the structure except the air-gap length and the magnet dimensions of the prototype are kept constant for this model. The air-gap length is decreased to $g=0.8\text{mm}$ and the magnet dimensions are increased so that the side of the first barrier is filled completely. The magnetic field density and the equi-flux lines of this model are given in Figure 4.17.

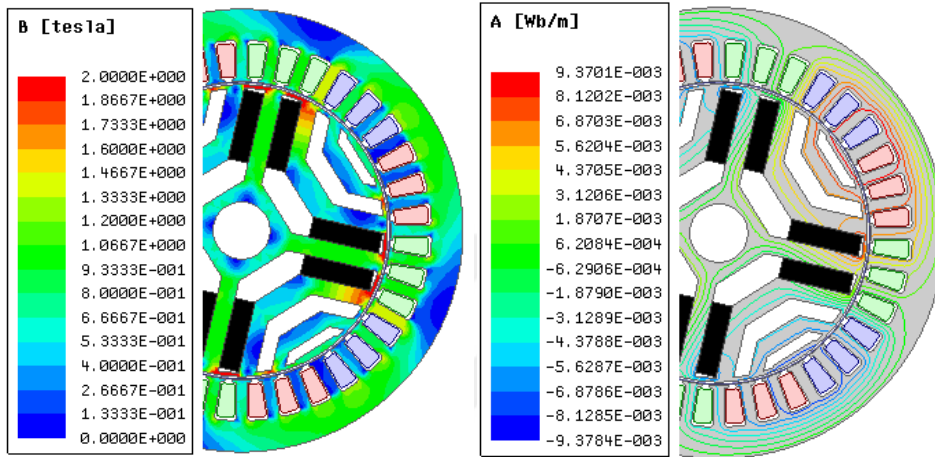


Figure 4.17 : Magnetic flux density and equi-flux line of model with $g=0.8\text{mm}/D=22.1\text{mm}$.

4.3.1.2 Motor model with $g=0.7\text{mm}/D=22.1\text{mm}$

Similarly, for this model the air-gap length of the prototype is further decreased to $g=0.7\text{mm}$ and all the remaining structure is kept constant. Its FEM results are given in Figure 4.18.

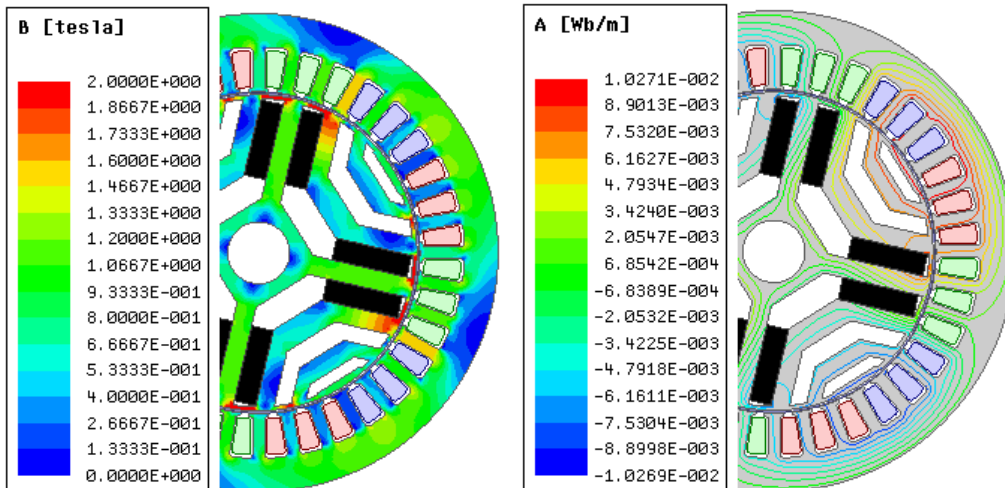


Figure 4.18 : Magnetic flux density and equi-flux line of model with $g=0.7\text{mm}/D=22.1\text{mm}$.

4.3.1.3 Motor model with $g=0.7\text{mm}/D=39.66\text{mm}$

The following results correspond to the model in which the parameter D has been changed from 22.1 to 39.66 mm by keeping the insulation ratios and other parameters constant. Drawing of such model is done by increasing the shaft radius value in the equations corresponding to the analytical design procedure given in section two of this thesis. After the flux barriers have been drawn using the enlarged shaft radius, the shaft radius is decreased again to its initial value. Decrease of the shaft radius after the barriers are pushed towards the air-gap, increases the total length of the magnetic iron in the q -axis, thus decreasing the insulation ratio on this axis. On the other hand, the magnetic flux does not penetrate too much towards the center of the rotor, therefore the model having enlarged shaft radius and the model having small shaft radius do not differ too much in their induced torque value. For comparison, the model having the same shaft radius as the sample prototype is selected. Its air-gap is 0.7mm and the magnets are placed in the center part of the first and the second barrier. The magnetic field density and equi-flux lines results of the corresponding model are given in Figure 4.19.

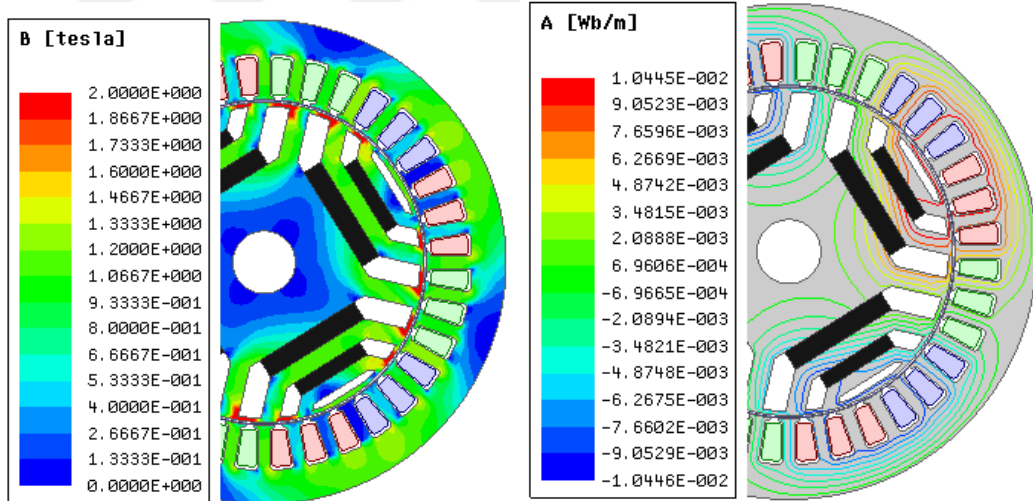


Figure 4.19 : Magnetic flux density and equi-flux line of model with $g=0.8\text{mm}/D=22.1\text{mm}$.

4.3.1.4 Comparison of results and analysis

The comparison of the FEM results of the models given in Table 4.8 above that showed the target performance is given in the following section. The models are compared with respect to the induced torque graph, induced voltage, air-gap magnetic field density and its harmonics. The torque graphs of all the models are

given in Figure 4.20. All three models have average torque around 1.2 Nm, however the models having air-gap length of $g=0.7$ mm have slightly higher average torque and torque ripple.

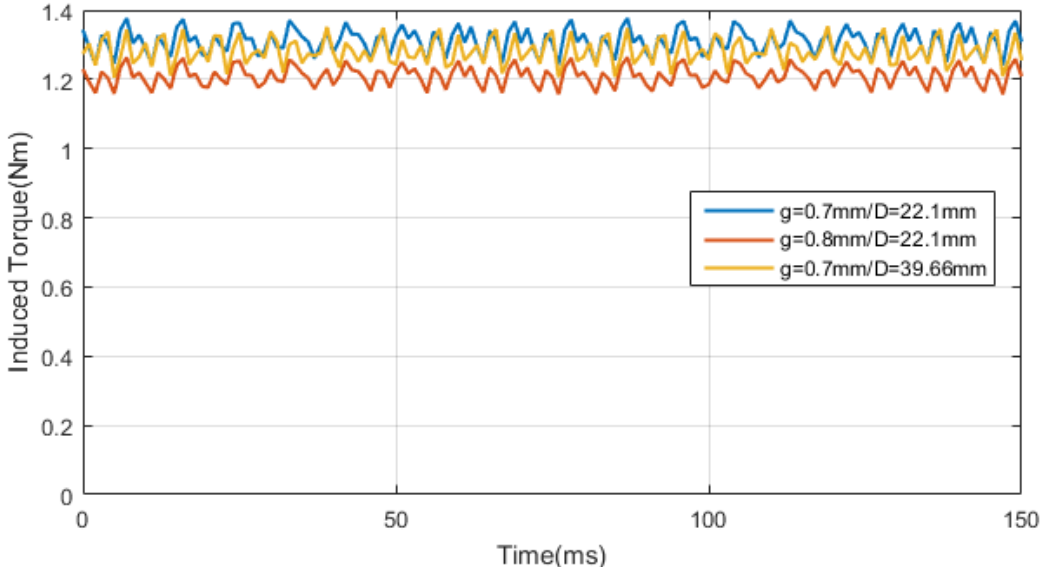


Figure 4.20 : Torque graph comparison for different g and D values.

The induced voltage graphs for a single phase of the highlighted models are given in Figure 4.21. Similarly, the models having air-gap length of $g=0.7$ mm have larger magnetic field passing through the air-gap, thus the induced voltage is higher.

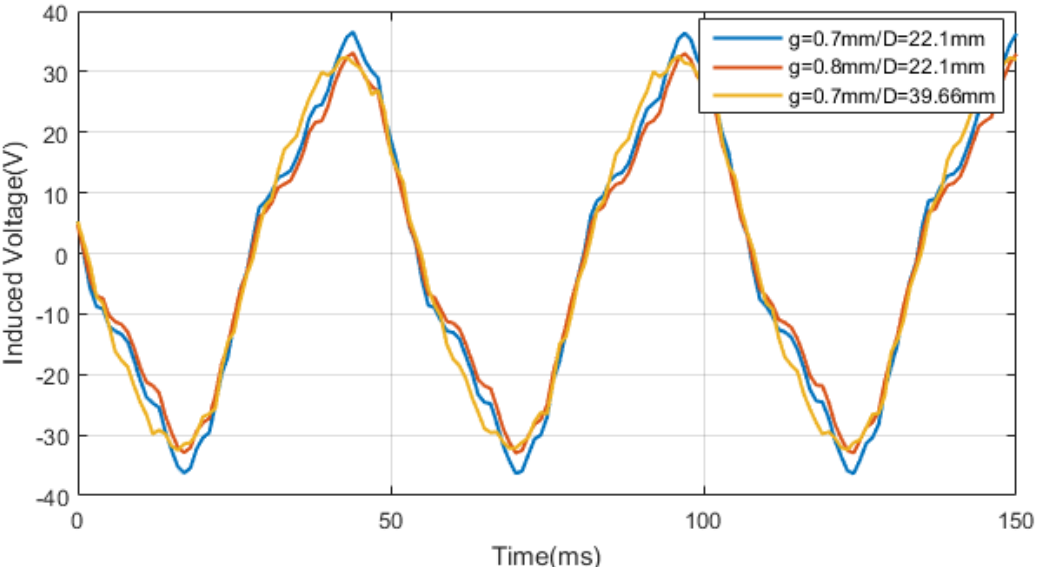


Figure 4.21 : Induced voltage graph comparison for different g and D values.

Another physical quantity that has been considered in this section is the air-gap magnetic field density. The magnetic field density distribution for all the models are given in Figure 4.22.

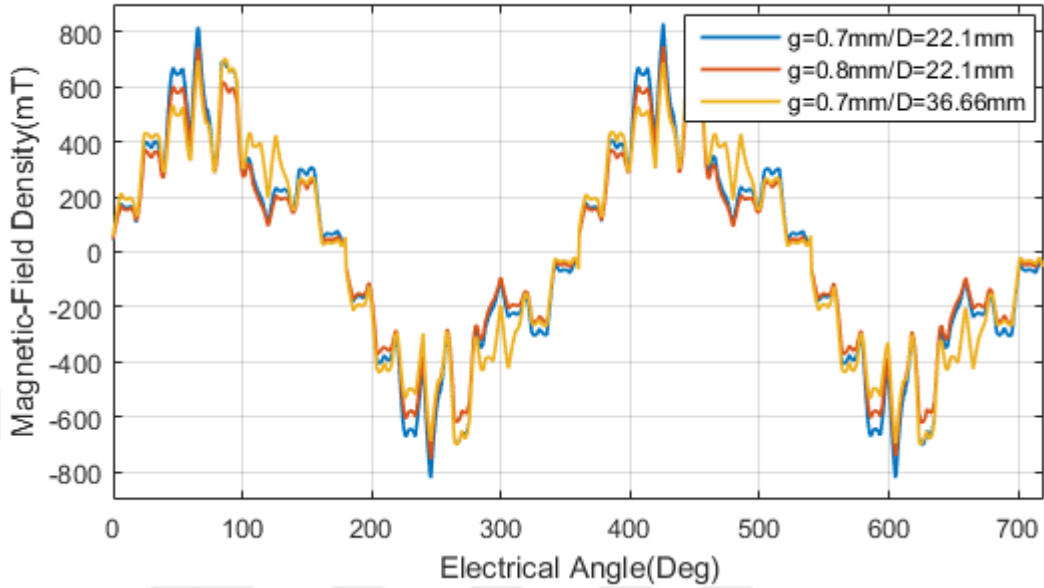


Figure 4.22 : Air-gap magnetic flux density comparison for different g and D values.

The air-gap magnetic density is desirable to have as close as possible a sinusoidal waveform, however, single layer windings generate a harmonic magnetic flux density in the air-gap. The harmonic amplitude comparison for the magnetic flux densities of the three models being analyzed are given in Figure 4.23.

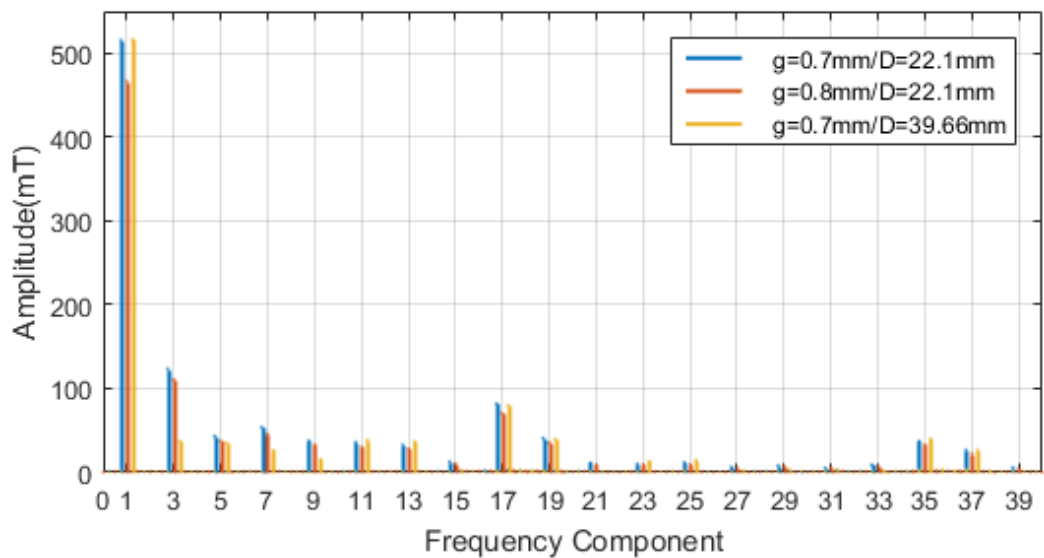


Figure 4.23 : Harmonic amplitude comparison for different g and D values.

The complete harmonic content of the models with numerical values up to 39th harmonics are given in Table 4.9.

Table 4.9 : Harmonic component amplitude for different g and D values.

Frequency Component	Amplitude [mT]		
	g=0.7mm D=22.1mm	g=0.8mm D=22.1mm	g=0.7mm D=39.66mm
1	515.3	466.5	516.1
3	123.4	110.5	36.9
5	42.9	37.2	34.8
7	53.7	45.3	26.0
9	37.2	32.9	15.4
11	35.7	29.9	38.5
13	32.7	28.4	36.8
15	12.6	10.1	2.7
17	81.7	70.1	79.7
19	40.6	34.8	39.1
21	11.3	8.6	0.8
23	9.9	8.7	13.0
25	11.6	9.6	14.4
27	6.1	5.3	1.8
29	7.9	7.3	3.3
31	5.3	4.9	3.3
33	8.5	6.9	1.5
35	36.8	32.8	39.5
37	26.2	22.3	26.6
39	5.6	4.6	0.6

Complete comparison of the physical quantities analyzed in this section are given in Table 4.10. All models satisfy the target torque value, however models having D=22.1 mm that have low torque ripple, have high tooth saturation over 1.3 T. The model having lower tooth saturation lower than 1.3 T and D=39.66 mm has high torque ripple and different magnet dimensions. Therefore, the distance D for the following analysis will be kept the same as that of the prototype motor.

Table 4.10 : Average and RMS data comparison of the three selectable models.

Model	B _{rms} [T]	Induced Torque [Nm]	Induced Voltage _{rms} [V]	Teeth Magnetic Field Density B _{max} [T]	Torque Ripple [%]
g=0.7mm/ D=22.1mm	0.387	1.31	22.3	1.53	10.31
g=0.8mm/ D=22.1mm	0.349	1.21	20.2	1.4	9.1
g=0.7mm/ D=39.66mm	0.376	1.28	22.4	1.29	11.72

4.4 Stator Yoke and Teeth Optimization

The optimization analysis that were shown until now, are performed by keeping the prototype stator structure unchanged. Decrease of the air-gap length and increase in the magnet volume used in the rotor, have caused magnetic field density in the stator to increase significantly and saturate the ferromagnetic material. Therefore, it is required that the tooth and yoke width are optimized such that the ferromagnetic material will be magnetized and demagnetized in the linear region. For different air-gap lengths (0.5-1 mm) the stator is optimized such that the maximum tooth and yoke magnetic field density remains between 1.2 and 1.3 T. The slot fill factor is 45%, and as the air-gap length is decreased, the turn number per slot is decreased by trial and error such that the output torque of each model is over the target value of 1.2 Nm. For each model, the FEM results including induced torque, induced voltage, magnetic field density, equi-flux lines, air-gap flux density and its harmonics are recorded and analyzed.

4.4.1 Motor model with $g=0.5\text{mm}$

The stator tooth and yoke width are changed according to the maximum magnetic field density so that it remains within the pre-specified limits. The magnetic field density and equi-flux lines results corresponding to this model are given in Figure 4.24.

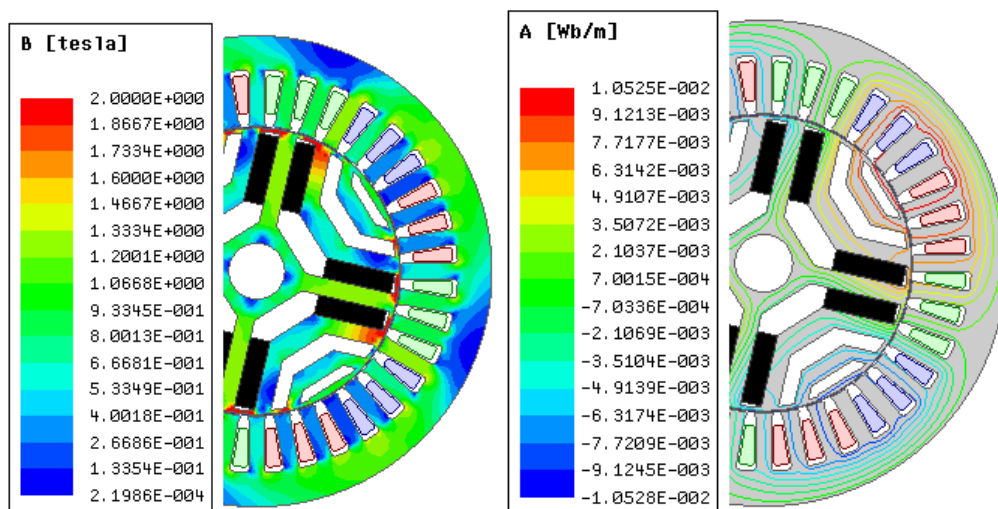


Figure 4.24 : Magnetic flux density and equi-flux lines of model with $g= 0.5\text{ mm}$.

4.4.2 Motor model with $g=0.6\text{mm}$

Similarly, the stator tooth and yoke width are changed according to the maximum magnetic field density so that it remains under the specified limits. The magnetic field density and equi-flux lines corresponding to this model are given in Figure 4.25.

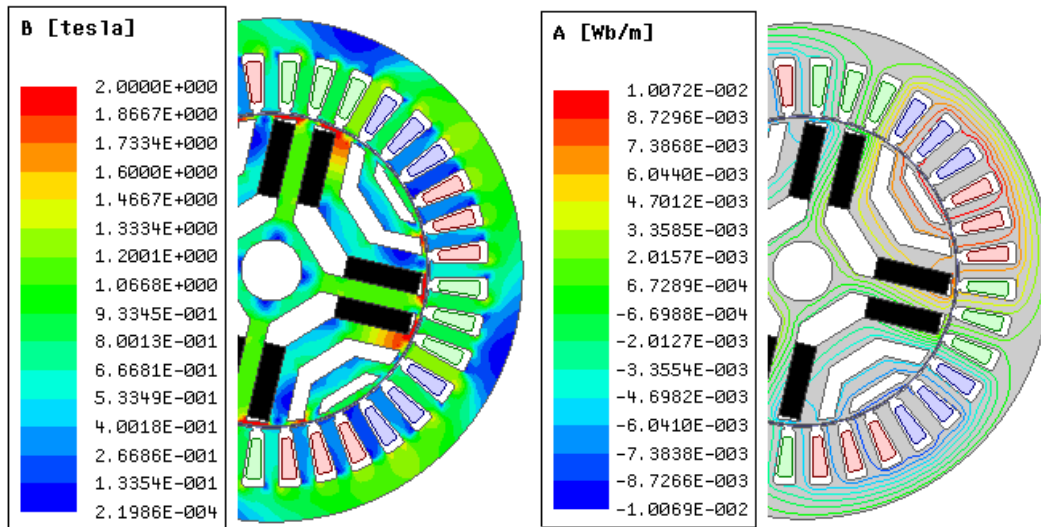


Figure 4.25 : Magnetic flux density and equi-flux lines of model with $g=0.6\text{ mm}$.

4.4.3 Motor model with $g=0.7\text{mm}$

The stator tooth and yoke width for this model are changed according to the maximum magnetic field density so that it remains under the limit. The magnetic field density and the equi-flux lines corresponding to this model are given in Figure 4.26.

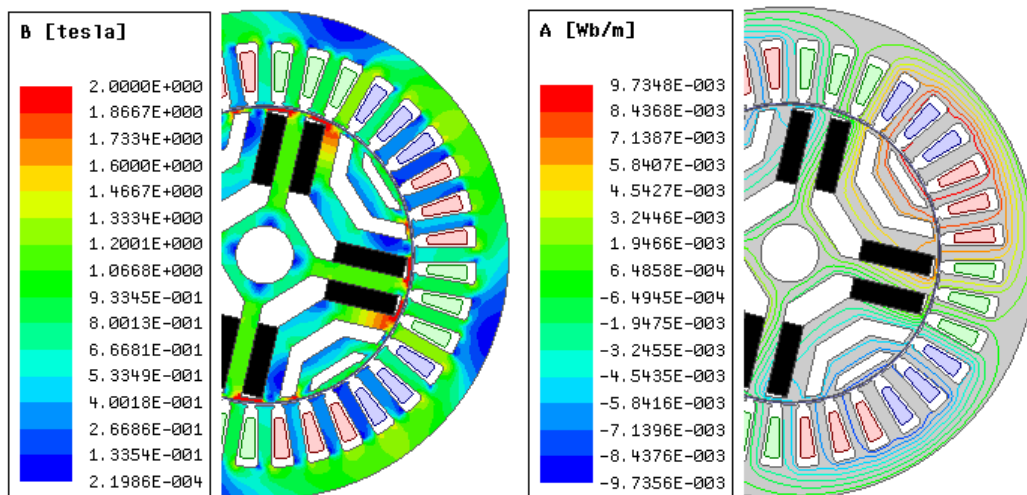


Figure 4.26 : Magnetic flux density and equi-flux lines of model with $g=0.7\text{ mm}$.

4.4.4 Motor model with $g=0.8\text{mm}$

The stator tooth and yoke width are changed according to the maximum magnetic field density so that it remains under the pre-specified limits. The magnetic field density and equi-flux lines results corresponding to this model are given in Figure 4.27.

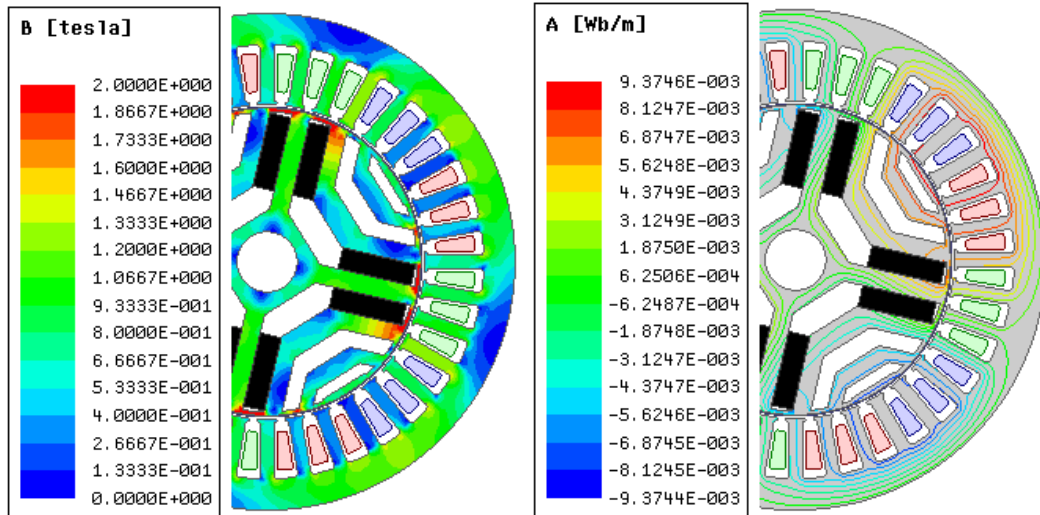


Figure 4.27 : Magnetic flux density and equi-flux lines of model with $g= 0.8 \text{ mm}$.

4.4.5 Motor model with $g=0.9\text{mm}$

The stator tooth and yoke width for this model are changed so that the maximum magnetic field density does not violate the specified limit. The corresponding magnetic field density and the equi-flux lines are given in Figure 4.28.

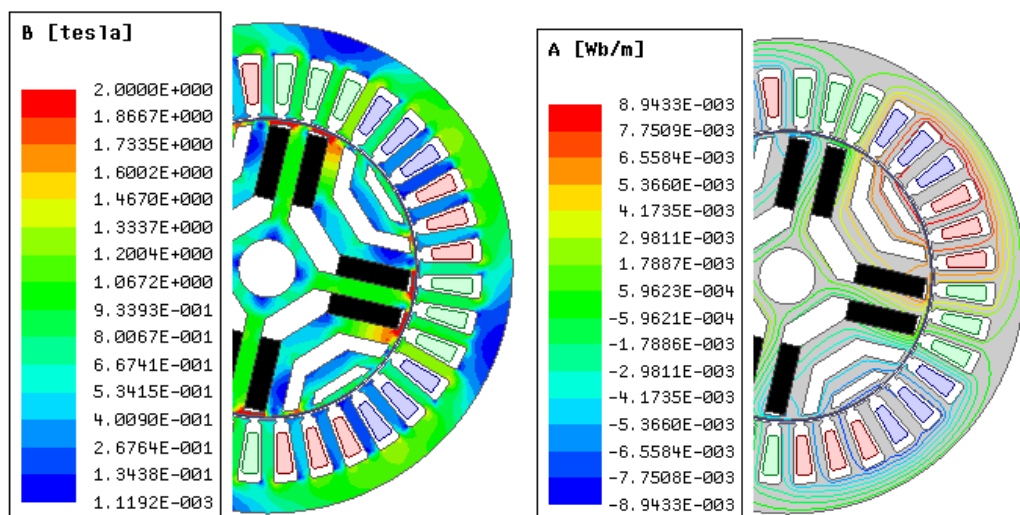


Figure 4.28 : Magnetic flux density and equi-flux lines of model with $g= 0.9 \text{ mm}$.

4.4.6 Motor model with $g=1\text{mm}$

Similarly, the stator tooth and yoke width are changed according to the maximum magnetic field density so that it does not violate the upper saturation limit. The magnetic field density and equi-flux lines corresponding to this model are given in Figure 4.29.

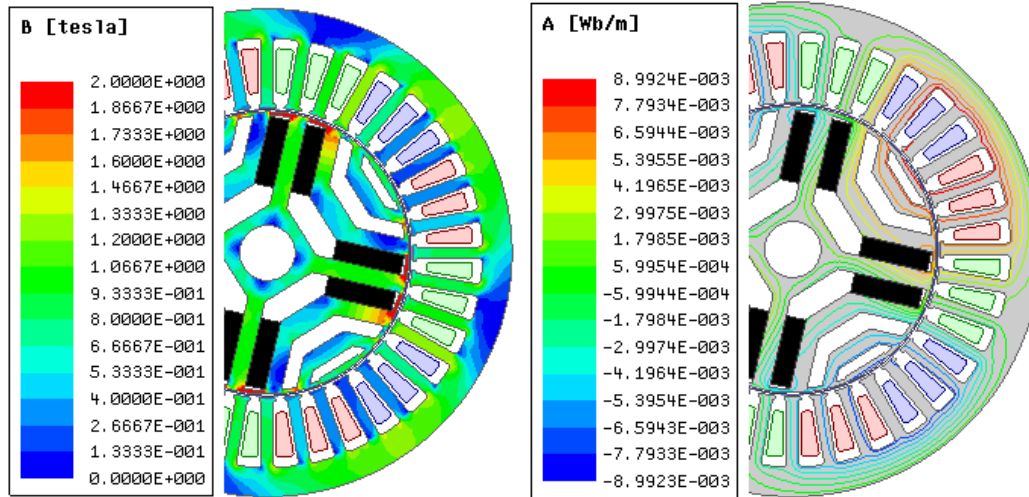


Figure 4.29 : Magnetic flux density and equi-flux lines of model with $g= 1\text{ mm}$.

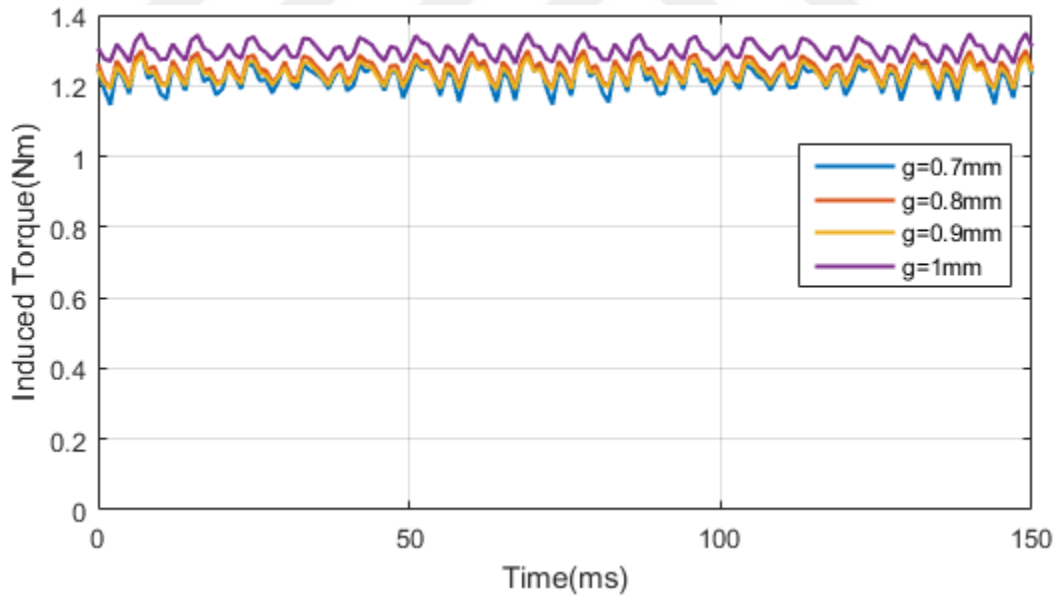
4.4.7 Comparison of results and analysis

The result obtained from FEM analysis of the previous models are summarized in Table 4.11. Each model is simulated using two different magnet volumes, and they are compared with respect to induced torque, torque ripple, efficiency and the maximum magnetic field density values in the stator. All the models have been driven at the rated washing mode current of the prototype. However, to maintain the target output torque, as it can be seen from the table, increase in the air-gap length is replaced with increase of number of winding turns. The models which have reached the target output torque of 1.2 Nm, are highlighted with bold font. Even though all the highlighted models show similar performance, due to geometrical and efficiency advantages the most suitable model that shows the required performance is chosen to be the one having an air-gap length of $g=0.8\text{mm}$, turn number per slot 75 and ferrite magnet volume of 21.5 cm^3 . The following analyzes will be performed on this model for further optimization of its performance.

Table 4.11 : Stator yoke and tooth optimization results.

Turn Number/Slot	g [mm]	Magnet Volume [cm ³]	Induced Torque [Nm]	Torque Ripple [%]	Efficiency [%]	B _{max} tooth [T]	B _{max} yoke [T]
90	1	14.9	1.13	6.37	55.98	1.21	1.287
		19.76	1.3	6.54	59.40	1.3	1.27
80	0.9	16.25	1.072	7.28	57.49	1.18	1.255
		21.5	1.23	7.32	60.81	1.28	1.24
75	0.8	17	1.087	8.65	59.34	1.21	1.3
		22.6	1.245	8.67	62.50	1.31	1.27
72	0.7	16.2	1.09	11.47	60.35	1.27	1.28
		21.45	1.22	11.97	63.01	1.2	1.3
65	0.6	22.6	1.18	16.44	64.51	1.28	1.29
60	0.5	21.7	1.13	20.88	65.27	1.25	1.25

Graphical comparison of the models satisfying the target output torque including torque, induced voltage, air-gap flux density and its harmonics, is given in the following sections. The graphs of the induced torque for all highlighted models are given in Figure 4.30. All the models have similar average torque, however torque ripple increases as the air-gap length decreases.

**Figure 4.30** : Torque graph comparison at different air-gap values for the optimized tooth and yoke.

Since the magnetic field in all the models is nearly the same, induced voltage of all the models is also similar. The induced voltage graphs for all the models that satisfy the target output torque are given in Figure 4.31. The air-gap magnetic field density distribution for all the highlighted models above is given in Figure 4.32.

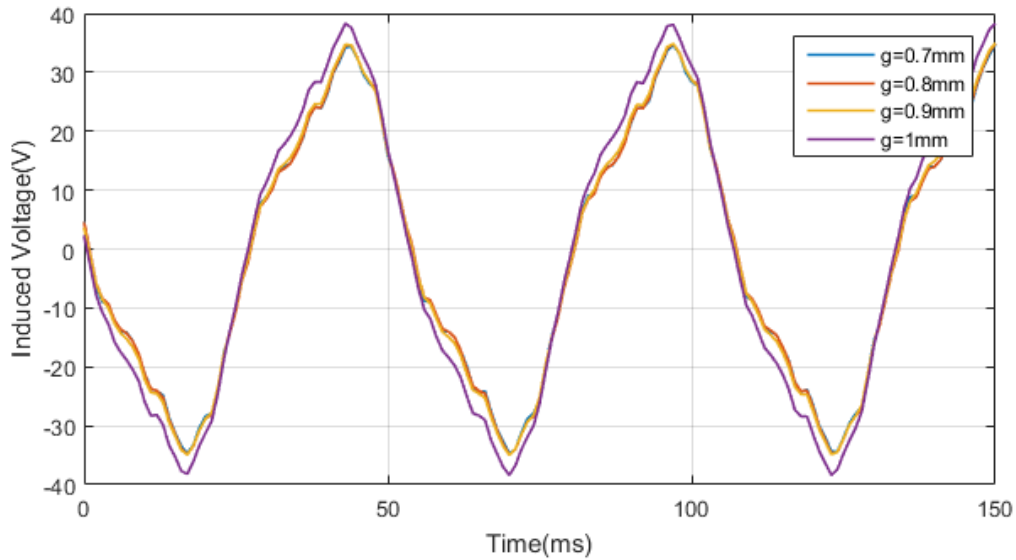


Figure 4.31 : Induced voltage graph comparison at different air-gap values for the optimized tooth and yoke.

As expected, all the models have similar magnetic field density distribution in the air-gap. However, there is a slight increase in the peak magnetic field density as the air-gap length decreases.

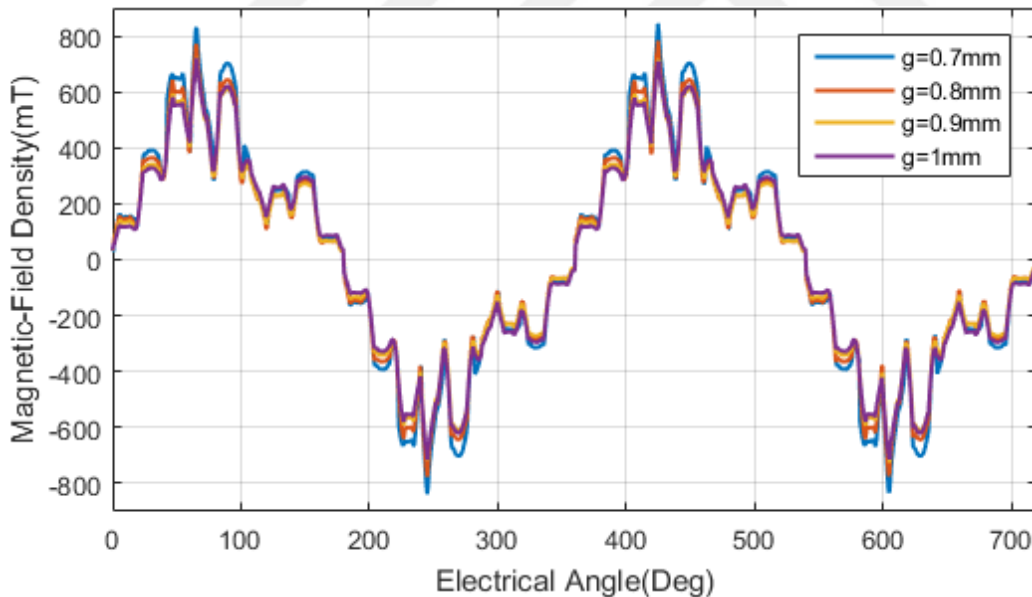


Figure 4.32 : Air-gap magnetic flux density comparison at different air-gap values for the optimized tooth and yoke.

The comparison of the harmonic amplitudes for the previous models is given in Figure 4.33. As the air-gap increases the harmonic amplitudes decrease, except the fundamental component. The model having air-gap length of $g=0.9$ mm has the lowest fundamental component of air-gap magnetic flux density, and that is related to the magnetic field induced inside that model.

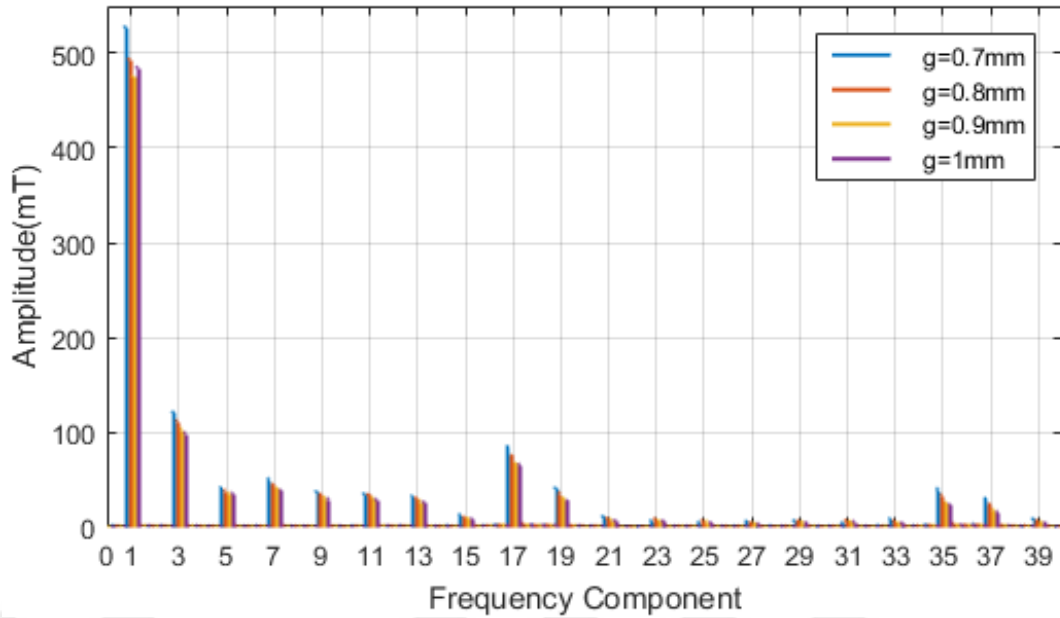


Figure 4.33 : Harmonic amplitude comparison at different air-gap values for the optimized tooth and yoke.

The numerical values of the amplitudes for the harmonics are given in Table 4.12.

Table 4.12 : Harmonic component amplitudes at different air-gap values for the optimized tooth and yoke.

Frequency Component	Amplitude [mT]			
	g=0.7mm	g=0.8mm	g=0.9mm	g=1mm
1	528.4	494.1	475.5	485.3
3	120.8	111.7	103.1	98.8
5	41.2	38.0	35.6	35.3
7	50.5	44.7	40.6	38.4
9	37.1	34.2	31.0	29.1
11	34.9	33.8	30.3	28.5
13	32.1	30.3	27.0	25.9
15	12.6	10.1	9.0	8.3
17	84.8	75.0	66.6	65.7
19	40.9	35.7	30.2	27.3
21	10.6	8.9	7.4	6.5
23	5.9	7.9	6.7	6.0
25	4.7	6.0	5.4	4.5
27	5.6	4.5	3.4	2.8
29	6.3	5.8	4.9	4.5
31	3.9	6.7	5.5	5.1
33	8.0	5.9	4.4	3.8
35	40.0	33.4	25.3	23.4
37	29.7	23.8	17.7	15.7
39	7.9	6.5	4.6	4.0

A complete and final comparison of the models is given in Table 4.13. Since the magnetic fields of all the models are nearly the equal, air-gap magnetic field density, induced voltage and induced torque are also similar to each other. However, there is significant increase in the torque ripple as the air-gap length of the models is decreased.

Table 4.13 : Average and RMS data comparison for different improved models.

Air-gap Length [mm]	B_{rms} [T]	Induced Torque [Nm]	Induced Voltage $_{rms}$ [V]	Teeth Magnetic Field Density B_{max} [T]	Torque Ripple [%]
0.7	0.396	1.22	21.47	1.2	11.97
0.8	0.369	1.245	21.6	1.31	8.67
0.9	0.352	1.23	21.87	1.28	7.32
1	0.358	1.3	24.48	1.3	6.54

4.5 Analysis of Multilayer Winding's Effects

The design of the stator windings in electric motors, requires that the MMF waveform produced by each winding is as close as possible to sinusoidal waveform. However, the MMF waveforms of electric motors are not sine waveforms, therefore they contain several harmonics, which cause unwanted rotating magnetic fields induced in the air-gap. These unwanted rotating magnetic fields have negative effect and reduce the MMF of the main field. They also cause excess torque ripple and iron losses. To minimize such negative effects, stator windings in motors should be distributed in a sinusoidal manner, thus resulting in a sinusoidal MMF distribution. However, distribution of the conductors in a sinusoidal manner is problematic during production. One other method of sinusoidal distribution is by changing the coil pitch angle by shifting half of the distributed winding turns such that the MMF waveform gets closer to sine wave. Depending on the harmonic of the air-gap magnetic field that is to be reduced, half of the winding may be shifted accordingly. This is possible by dividing the turns in a slot into fractions making several layers of winding.

During the optimization analysis of this thesis, the model that was selected in the stator and yoke optimization, one having air-gap length of $g=0.8\text{mm}$, has been simulated with double layer distributed winding with 20 and 40 degree shift of the coil pitch angle. To be comparable to other models, the turn number per slot is kept constant, only divided into two fractions. The FEM results obtained and recorded

during this analysis show the effect of double layer windings on the induced torque and the torque ripple of the motor. Looking at the theoretical MMF distribution of the single and double layer models given in Figure 4.34, it is clear that as the shift angle increases the MMF waveform gets closer to sinusoidal form.

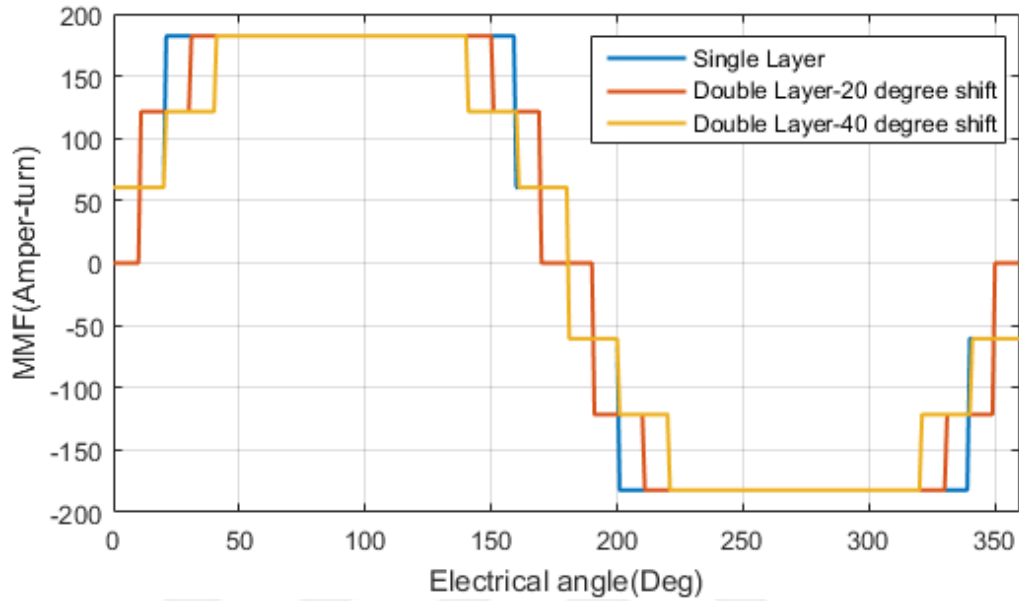


Figure 4.34 : Theoretical MMF of single and double layer models.

FFT analysis of theoretical MMF distributions gives the winding factors corresponding to each harmonic component. The winding factor k_{wi} of the i^{th} harmonic component is calculated as given in Equation 4.1.

$$k_{wi} = \frac{P \times \pi \times F_{peaki} \times i}{4 \times N \times I} \quad (4.1)$$

In this equation, i is the harmonic contents index, P denotes the pole number, N is the number of phase windings, F_{peaki} is the amplitude of the i^{th} harmonic content calculated in the FFT analysis of the theoretical MMF distribution. The calculated winding factors of the 1st, 5th, 7th, 11th and 17th harmonics are given in Table 4.14.

Table 4.14 : Winding factors for single and double layer models.

Harmonic Factor	Single Layer	Double Layer 20° shift	Double Layer 40° shift
k_{w1}	0.957	0.944	0.901
k_{w5}	0.188	0.118	0.039
k_{w7}	0.203	0.100	0.135
k_{w11}	0.136	0.028	0.135
k_{w17}	0.986	0.955	0.901

The analysis results of the selected model show that the 11th harmonic of the model with 20° shifted layer and the 5th harmonic of the model with 40° shifted layer are the harmonic contents mostly suppressed. The winding factor of the fundamental harmonic also decreases as the angle shift of the winding layer increases.

4.5.1 Motor model with 20° shifted winding layer

The cross sectional view of this model is given in Figure 4.35. The magnetic field density and equi-flux lines results corresponding to this double layer model are given in Figure 4.36.

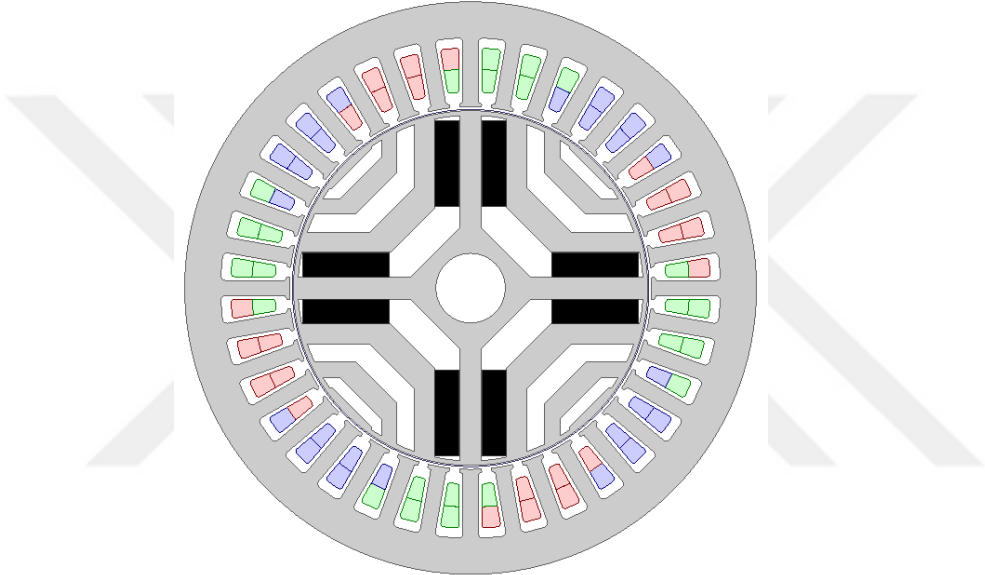


Figure 4.35 : Geometry of the double layer-20° shifted model with $g= 0.8\text{mm}$.

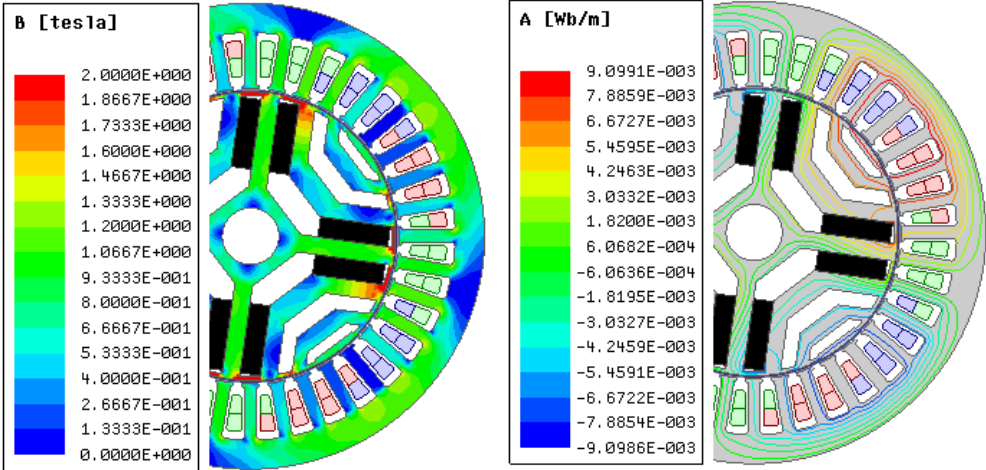


Figure 4.36 : Magnetic flux density and air-gap flux density of the double layer-20° shifted model with $g= 0.8 \text{ mm}$.

4.5.2 Motor model with 40° shifted winding layer

The geometry of this double layer model is given in Figure 4.37. The corresponding magnetic field density and equi-flux lines results are given in Figure 4.38.

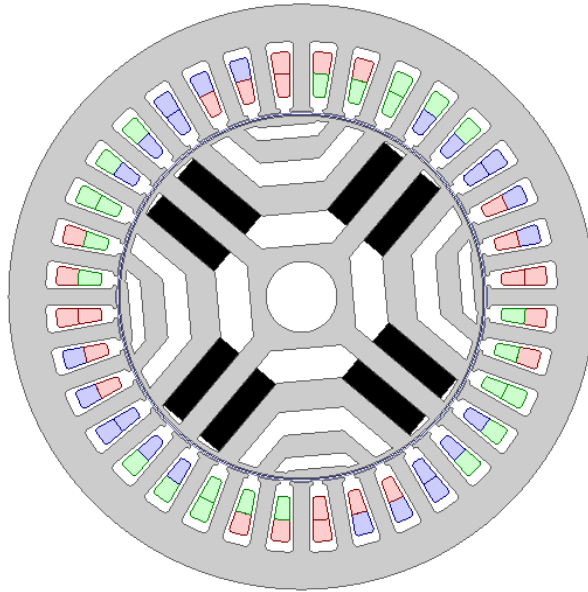


Figure 4.37 : Geometry of the double layer-40° shifted model with $g= 0.8\text{mm}$.

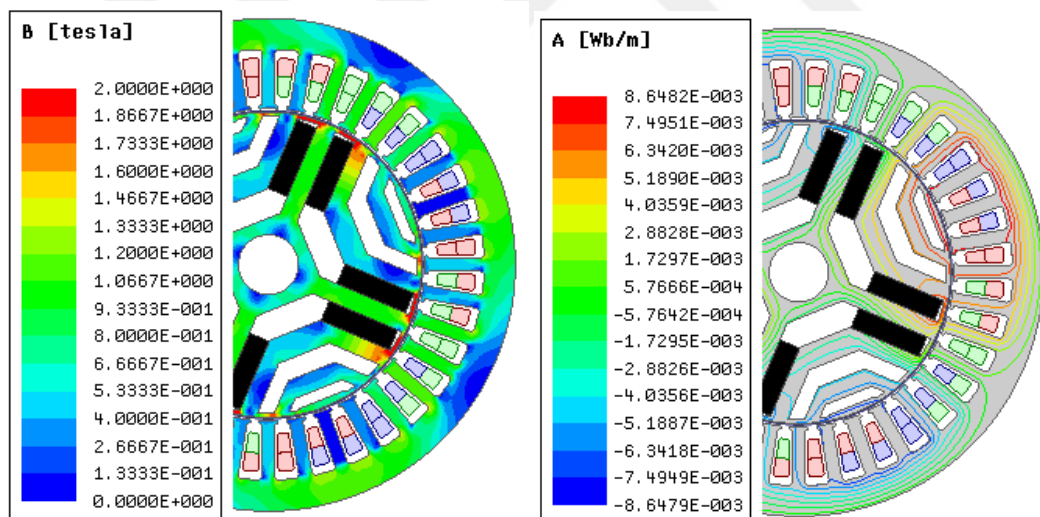


Figure 4.38 : Magnetic flux density and air-gap flux density of the double layer-40° shifted model with $g= 0.8\text{ mm}$.

4.5.3 Comparison results and analysis

In this section of thesis, single and double models are compared to each other based on the induced torque graphs, induced voltage graphs, air-gap field density and its harmonics. Including also the single layer winding model, the comparison of the induced torque graphs is given in Figure 4.39. Single layer and the model having 20°

shifted layer have nearly the same average torque, however the torque ripple for the double layer model is clearly decreased. As it was expected, the model having 40° shifted layer has lower average torque due to lower amplitude of the fundamental MMF component.

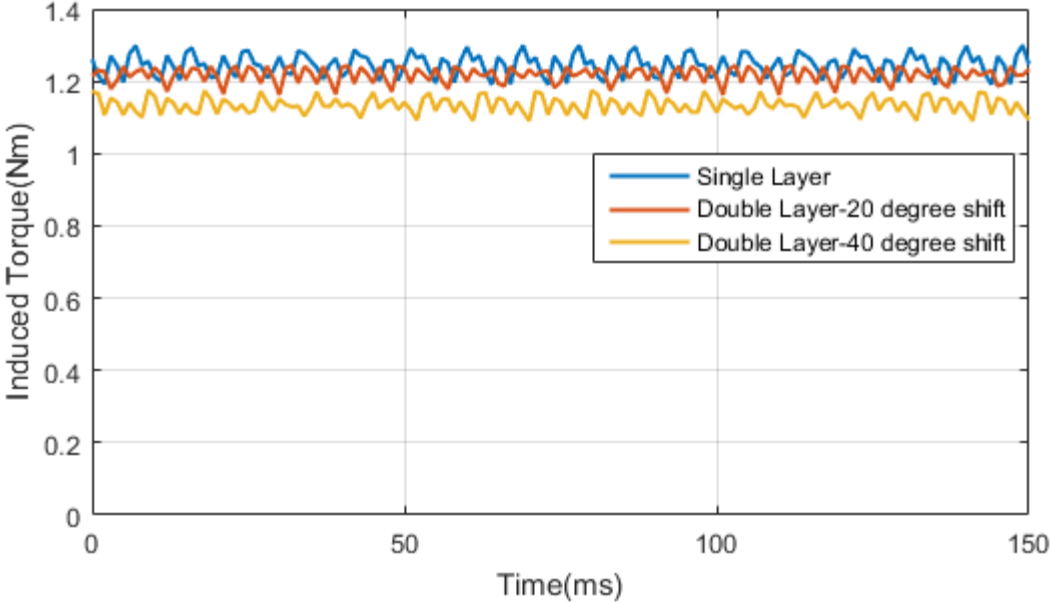


Figure 4.39 : Torque graph comparison of single and double layer models.

The induced voltage for each model is given in Figure 4.40. Decrease in the fundamental MMF component of the double layer models decreases also the induced phase voltage, thus decreasing the output power of the model.

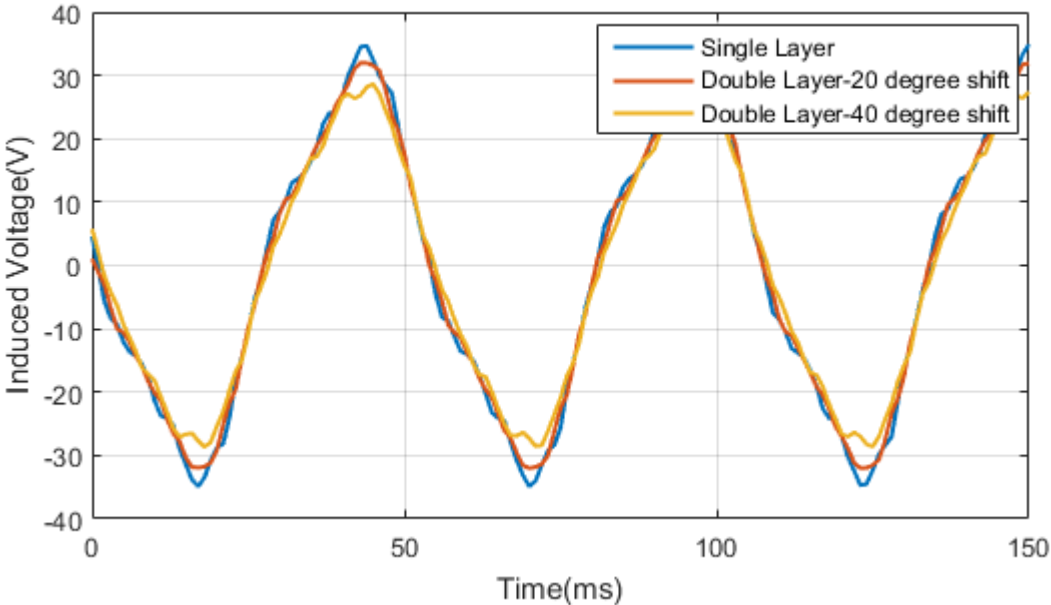


Figure 4.40 : Induced voltage graph comparison of single and double layer models.

The air-gap magnetic flux density of the single and double layer models is given in Figure 4.41. All three models have similar air-gap magnetic flux distribution, therefore its helpful to perform FFT analysis and to check the frequency components of each model.

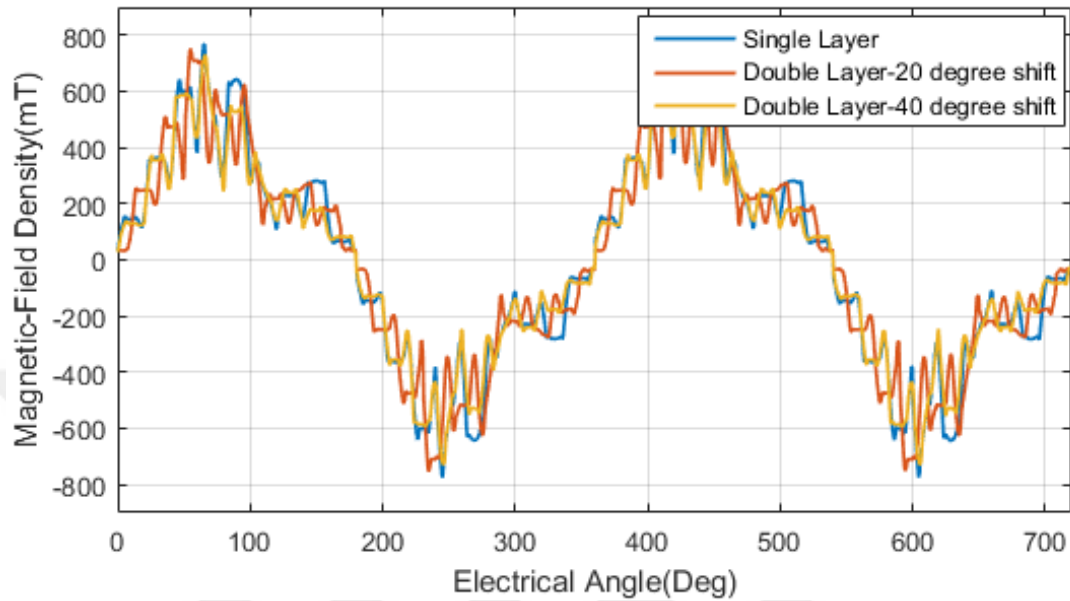


Figure 4.41 : Air-gap magnetic flux density comparison of single and double layer models.

The amplitudes of frequency components observed from the FFT analysis of the air-gap magnetic flux density are given and compared in Figure 4.42. Their complete numerical values are given in Table 4.15.

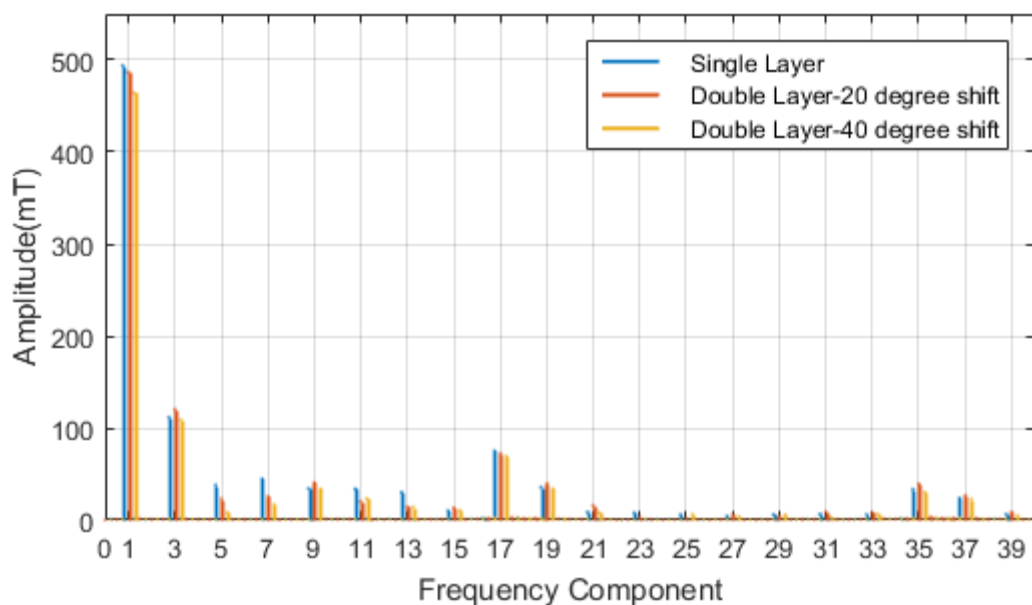


Figure 4.42 : Harmonic amplitude comparison of single and double layer models.

As it was predicted from the FFT analysis of the theoretical MMF distribution and the harmonic winding factors, single slot shift resulted in light decrease of the 11th harmonic whereas double slot shift resulted in significant decrease of the 5th harmonic.

Table 4.15 : Harmonic component amplitudes for single and double layer models.

Frequency Component	Amplitude [mT]		
	Single Layer	Double Layer 20° shift	Double Layer 40° shift
1	494.1	486.5	464.2
3	111.7	120.2	109.0
5	38.0	22.8	8.4
7	44.7	25.4	16.8
9	34.2	40.4	33.8
11	33.8	20.1	23.2
13	30.3	14.3	14.1
15	10.1	13.2	10.7
17	75.0	72.2	69.3
19	35.7	39.4	34.0
21	8.9	15.5	8.1
23	7.9	2.8	0.9
25	6.0	1.7	6.1
27	4.5	5.7	3.7
29	5.8	4.5	5.7
31	6.7	9.2	2.8
33	5.9	7.7	6.3
35	33.4	39.4	30.6
37	23.8	26.6	22.8
39	6.5	8.4	4.7

A complete and final comparison of the single and double layer models is given in Table 4.16. The model having a 40° shifted layer has both low average torque and high torque ripple, making it unsuitable for selection.

Table 4.16 : Average and RMS data comparison for single and double layer models.

Layer No:	B_{rms} [T]	Induced Torque [Nm]	Induced Voltage _{rms} [V]	Teeth Magnetic Field Density B_{max} [T]	Torque Ripple [%]
1	0.369	1.245	21.6	1.31	8.67
2 [20° shift]	0.363	1.216	20.83	1.18	6.7
2 [40° shift]	0.344	1.13	18.96	1.16	7.4

The FEM results of the double layer model having 20° shifted layer show that this method can be used for reduction of the induction torque ripple by suppressing specific harmonic contents of the air-gap flux density and not decreasing average torque too much. However, the decrease of the average torque value, non-significant decrease in the torque ripple and production difficulty makes the use of double winding in this application not useful. Therefore, further optimization process will continue using single layer winding.

4.6 Effects of the Ferromagnetic Material

All the analysis that have been performed until now are done using M700 type of ferromagnetic material. Another material that is available for production of the new prototype is M350 type. The magnetizing graph of M700 and M350 are quite similar as it is shown in Figure 4.43. However, when it comes to the core losses, M350 has significant lower W/kg losses compared to M700. The loss graphs at 50Hz for both materials are given in Figure 4.44. The following optimization analysis of the previously selected model of 0.8 mm air-gap length is done using M350 material. The FEM results obtained from this analysis are recorded and analyzed below, they are also compared with the results of M700 material with respect to the induced torque, induced voltage, air-gap flux density and its harmonics.

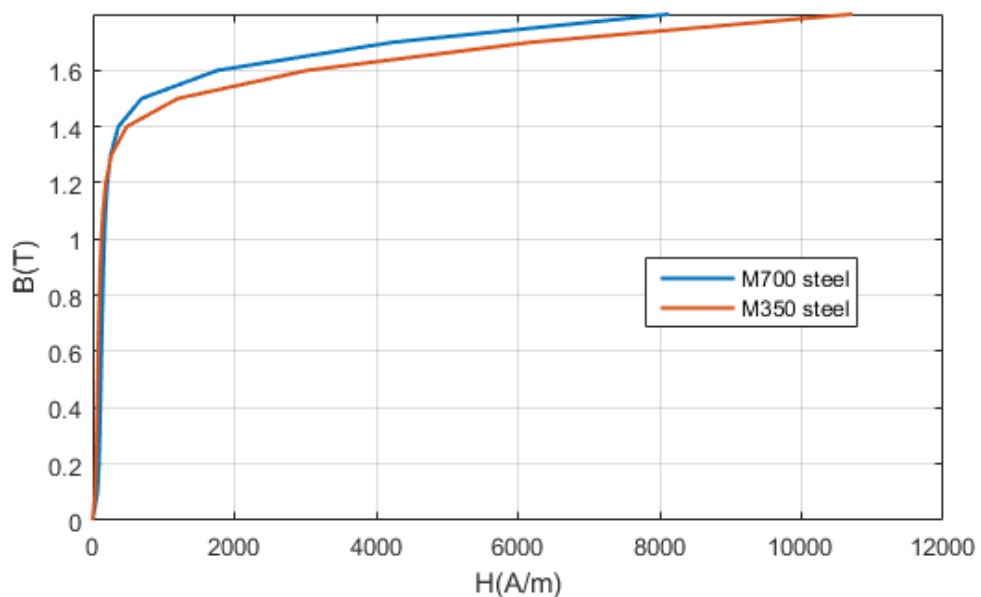


Figure 4.43 : Magnetizing graphs of M700 and M350 ferromagnetic materials [38,39].

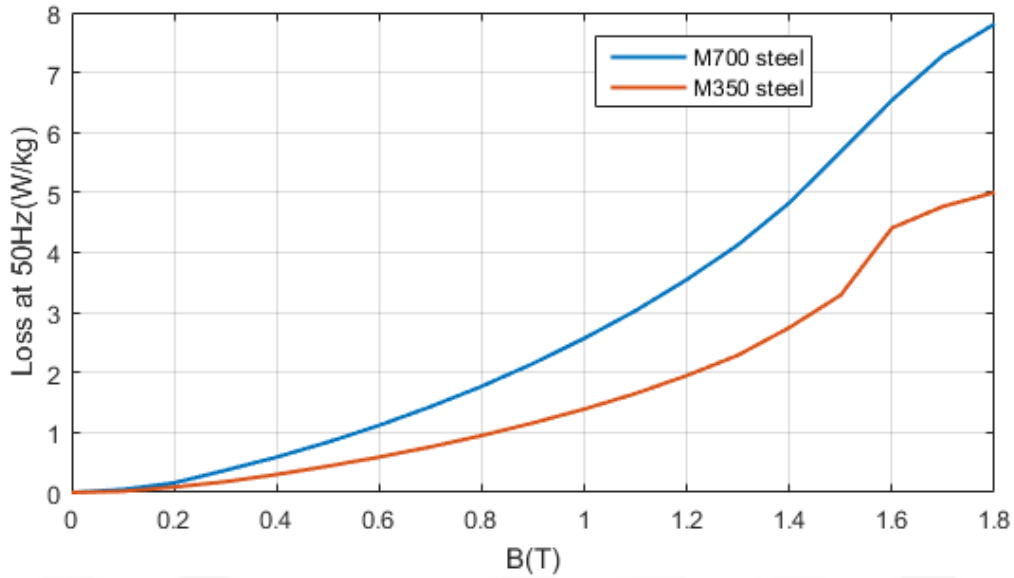


Figure 4.44 : Loss graphs of M700 and M350 ferromagnetic materials at 50 Hz [38,39].

The magnetic flux density and equi-flux lines results corresponding to the model with M350 ferromagnetic material are given in Figure 4.45. These results are quite similar to those of the model with M700 material.

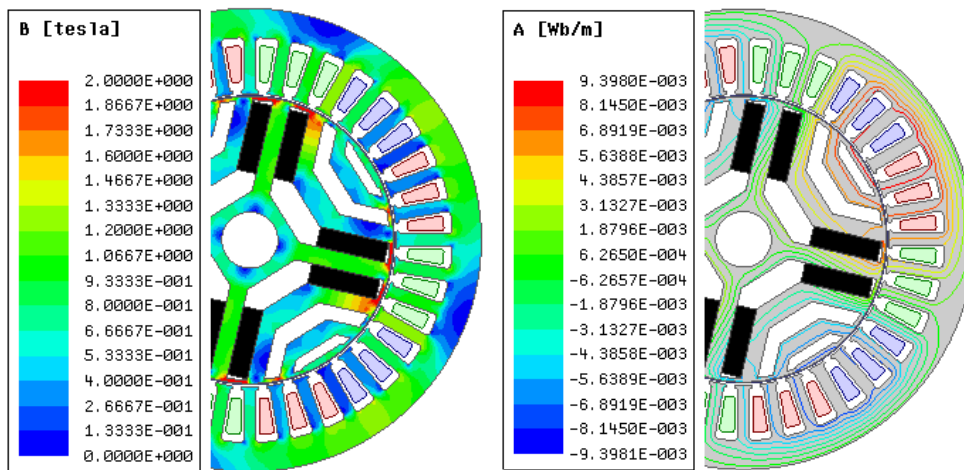


Figure 4.45 : Magnetic flux density and equi-flux lines of $g=0.8\text{mm}$ model with M350 ferromagnetic material.

As it was observed from the B-H curve of the different ferromagnetic materials, electromagnetically they are quite similar. Therefore, the induced torque, induced voltage and air-gap magnetic flux density are quite similar for both models. Average and RMS comparison of the electromagnetic parameters for different materials are given in Table 4.17.

Table 4.17 : Average and RMS data comparison for different materials.

Material Type	B_{rms} [T]	Induced torque [Nm]	Induced Voltage $_{rms}$ [V]	Teeth Magnetic Field Density B_{max} [T]	Torque Ripple [%]
M700	0.369	1.24	21.6	1.31	8.64
M350	0.369	1.26	21.6	1.32	9.5

The induced torque graphs for both models are given in Figure 4.46.

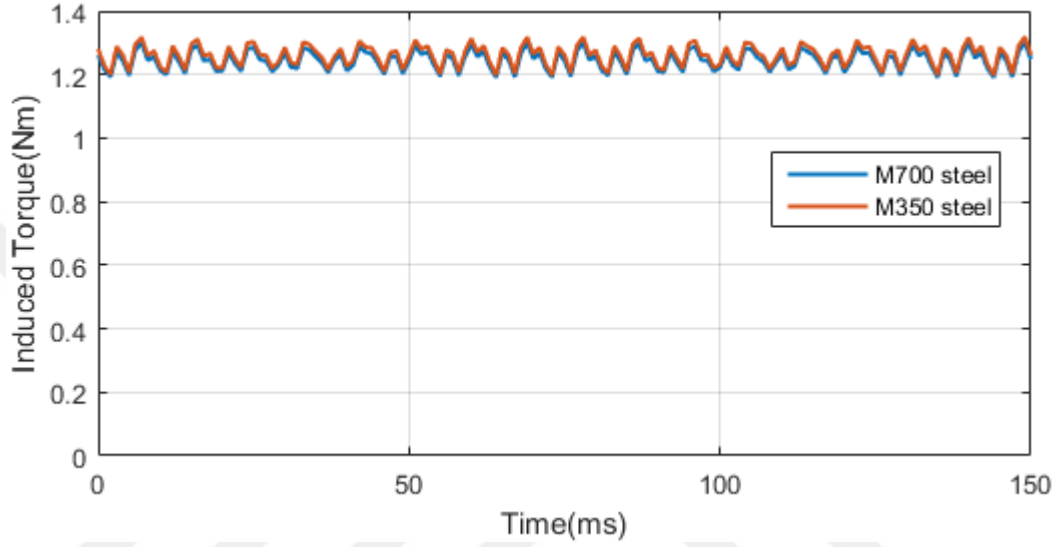


Figure 4.46 : Torque graph comparison of models with M700 and M350.

The air-gap magnetic field density distribution for both models is nearly the same, and their comparison is given in Figure 4.47.

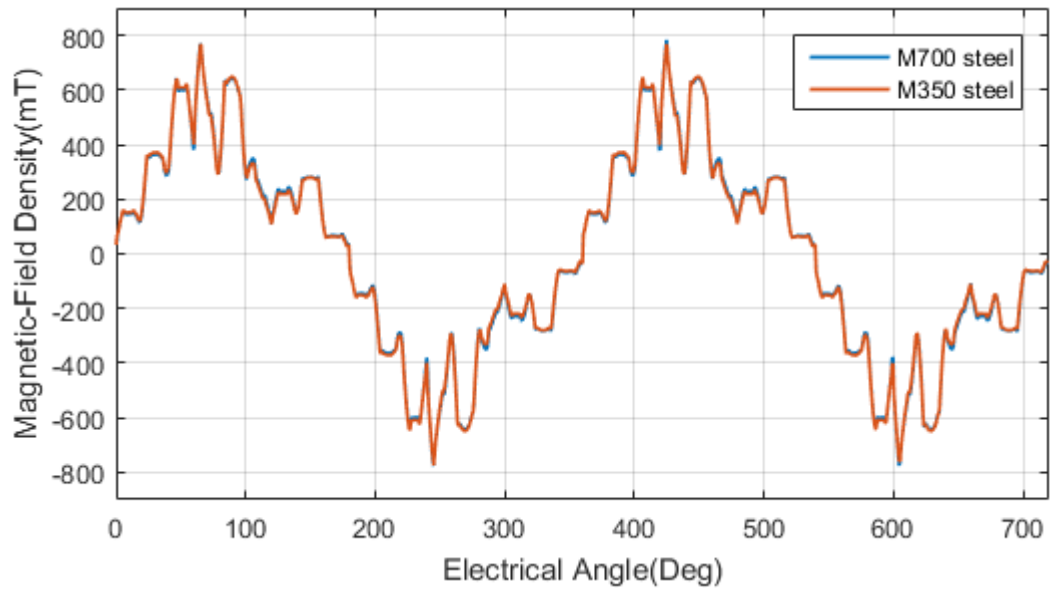


Figure 4.47 : Air-gap magnetic flux density of models with M700 and M350.

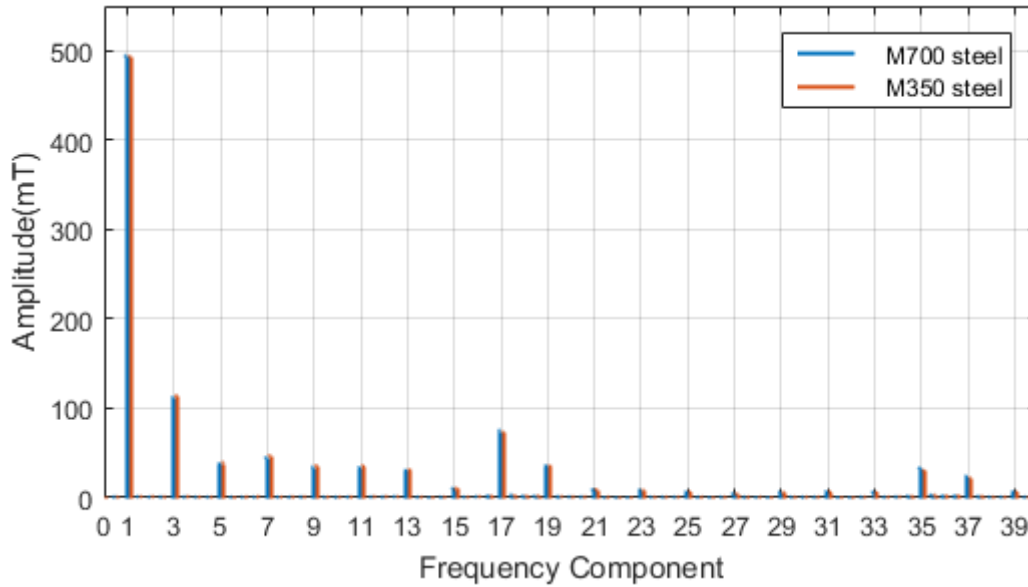


Figure 4.48 : Induced voltage graph comparison of models with M700 and M350.

The similarity of the electromagnetic parameters can be seen also from the similarity of the air-gap magnetic flux density harmonics. The fundamental and other harmonics are nearly the same when compared, as it can be seen in Figure 4.48. However, if the efficiency of the motor is considered, lower iron losses of the model with M350 ferromagnetic material result in better efficiency than the model with M700 material. The core losses and the efficiency values for both models are given in Table 4.17. For the final prototype both materials may be used, however there is not a significant change in the efficiency of the motor. This efficiency advantage of M350 would be much more significant for higher power motors.

Table 4.18 : Effect of ferromagnetic material on core loss and efficiency.

Material Type	Induced Torque [Nm]	Core Loss [W]	Efficiency [%]
M700	1.24	1.53	62.50
M350	1.26	0.97	63.17

4.7 Analysis of the Slot Opening Dimensions' Effects

Regarding the slot opening geometry and its effects on the performance of PMSynRM, slot opening width and slot opening height's effect have been investigated in this section. This investigation has been done for different slot opening and height measures.

4.7.1 Slot opening width

The effect of the slot opening width on the efficiency, induced torque and the torque ripple is analyzed in this section. Narrowing the slot opening width too much increases the leakage flux between stator teeth, whereas its widening increases the reluctance between the stator and the rotor, therefore the results in decrease of the total flux passing through the air-gap. The model with 0.8 mm air-gap that was selected in the previous analysis, has a slot opening width of 2 mm. In this analysis, different slot opening widths, 1 mm, 1.5 mm, 2 mm, 2.5 mm and 3 mm have been simulated and analyzed. For each case, the FEM results including induced torque, torque ripple, magnetic field density and efficiency have been recorded and given in Table 4.17.

Table 4.19 : The effect of the slot opening width on torque, core loss and efficiency.

Slot Opening Width [mm]	Induced Torque [Nm]	Torque Ripple [%]	B_{tooth} [T]	B_{yoke} [T]	Core Loss [W]	Efficiency [%]
1	1.32	6.81	1.41	1.38	1.75	63.95
1.5	1.29	7.5	1.36	1.33	1.65	63.42
2	1.24	8.7	1.31	1.26	1.51	62.50
2.5	1.2	9.9	1.25	1.17	1.39	61.72
3	1.15	11.08	1.18	1.1	1.27	60.71

The magnetic flux density on the tooth and yoke of the model having slot opening of 1 mm is given in Figure 4.49.

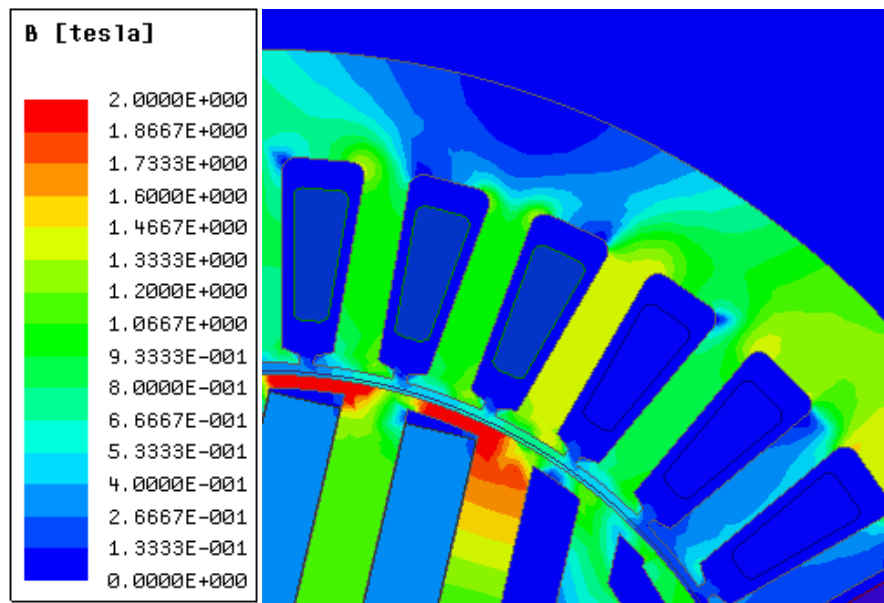


Figure 4.49 : Stator yoke and tooth magnetic flux density of model with slot opening of 1 mm.

The magnetic flux density on the tooth and yoke of the model having slot opening of 1.5 mm is given in Figure 4.50.

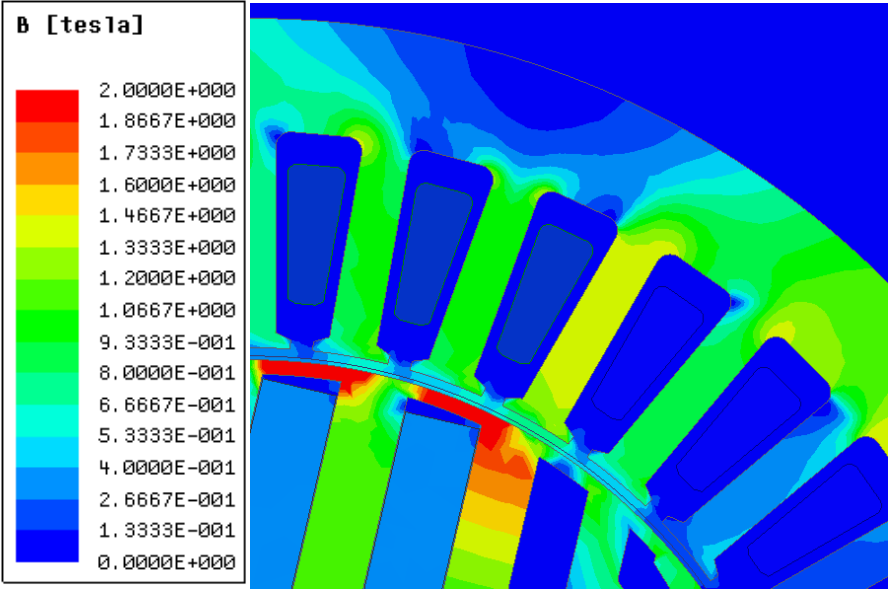


Figure 4.50 : Stator yoke and tooth magnetic flux density of model with slot opening of 1.5 mm.

The magnetic flux density on the tooth and yoke of the model having slot opening of 2 mm is given in Figure 4.51.

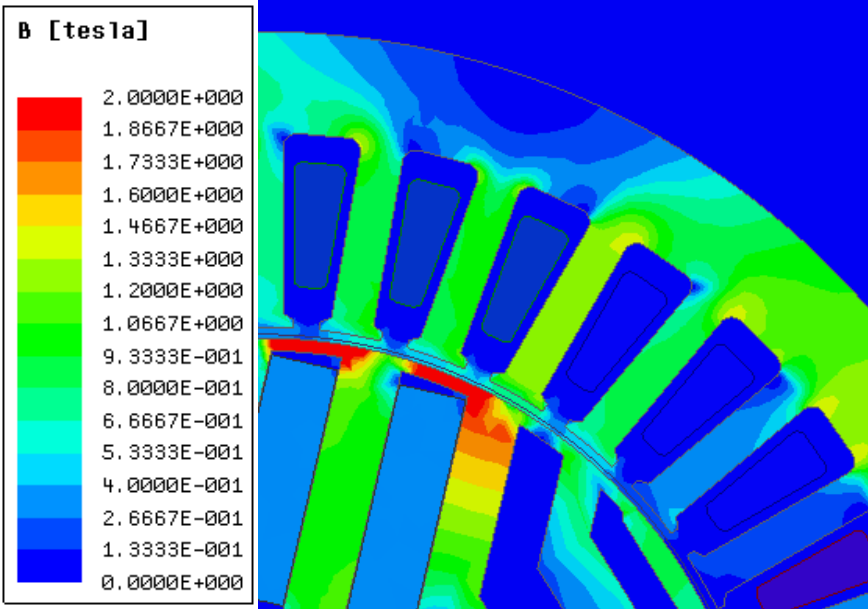


Figure 4.51 : Stator yoke and tooth magnetic flux density of model with slot opening of 2 mm.

The magnetic flux density on the tooth and yoke of the model having slot opening of 2.5 mm is given in Figure 4.52.

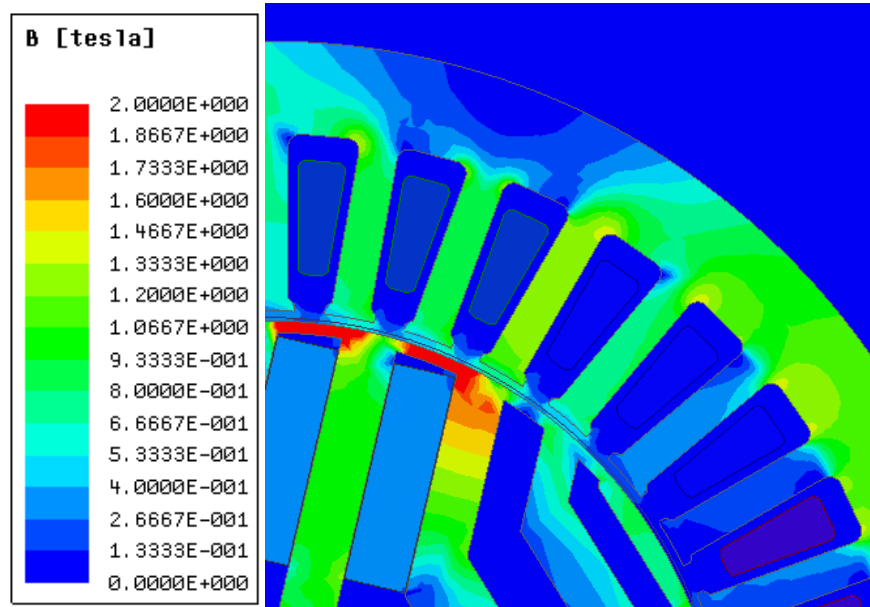


Figure 4.52 : Stator yoke and tooth magnetic flux density of model with slot opening of 2.5 mm.

The magnetic flux density on the tooth and yoke of the model having slot opening of 3 mm is given in Figure 4.53.

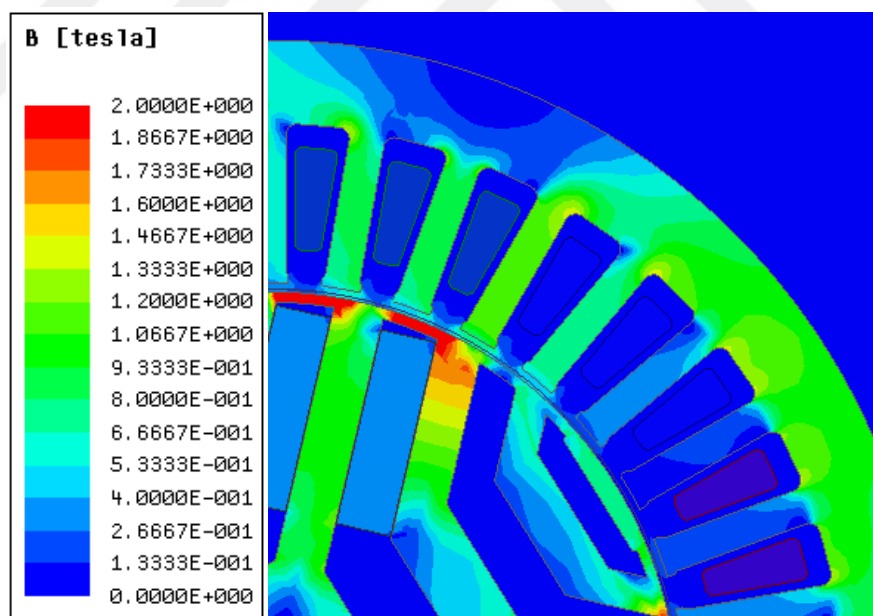


Figure 4.53 : Stator yoke and tooth magnetic flux density of model with slot opening of 3 mm.

The model having slot opening of 1 mm shows the best electromagnetic performance, however insertion of the winding conductor through this opening makes production of the motor problematic. Therefore, the slot opening width is kept at 2 mm.

4.7.2 Slot opening height

The optimization analysis of the prototype continues with the analysis of the effect of slot opening height (H) shown in Figure 4.54. The previous prototype has a slot opening height of $H=0.6\text{mm}$. To get an idea of its effect, H is changed from 0.2 to 1 mm, and simulated on different models.

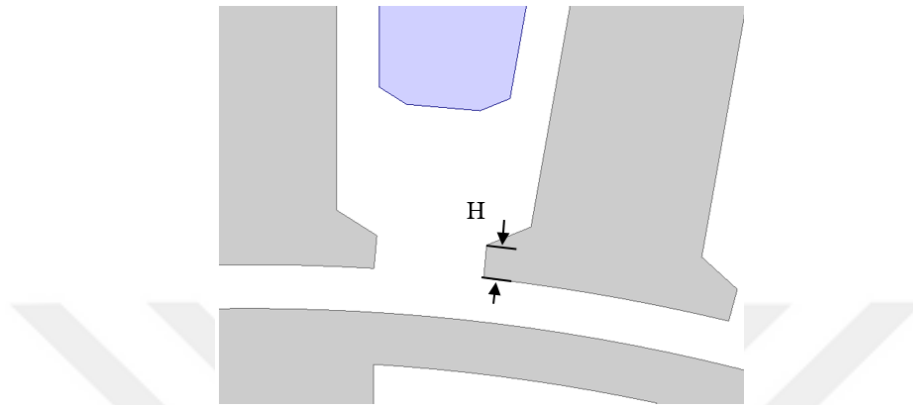


Figure 4.54 : Geometrical definition of slot opening height “H”.

The FEM results obtained from the analysis of different slot opening heights are given in Table 4.20.

Table 4.20 : Effect of slot opening height on the average torque and ripple.

Slot Opening Height [mm]	Induced Torque [Nm]	Torque Ripple [%]
0.2	1.235	9.2
0.4	1.242	8.9
0.6	1.245	8.7
0.8	1.246	8.7
1	1.246	8.7

Form the results given in Table 4.19 it can be clearly seen that the slot opening height does not have a significant effect on the induced torque and torque ripple of small motors. Therefore, the slot opening height of the previous prototype will not be changed in the following optimization analysis.

4.8 Analysis of the Slot Shape's Effects

4.8.1 Effect of parallel tooth edges and parallel slot edges

Depending on the size and the output power of the electrical machines, the types of slots that may be used are parallel slot edge or parallel tooth edge slots. Larger power machines are constructed with parallel slot edges for better placement of the strip conductors, whereas in smaller machines parallel tooth edge slots are used for better usage and minimization of the stator structure. The disadvantage of the parallel slot edge slots in small electrical machines is because of the decrease of the inner stator radius and ineffective usage of the ferromagnetic material. Decrease in the stator inner radius means decrease of the rotor radius, thus the output torque of the motor decreases also. Ineffective usage of the ferromagnetic material means that the magnetic field density is not constant through the stator tooth. When thin part of the teeth is avoided from saturation, the magnetic field density on the wide part is lower. On the other side, parallel tooth slots have larger available slot area for the same stator inner radius. The thickness of the teeth is constant, therefore there is no difference in the magnetic field density throughout one tooth. As a result, with larger rotor radius the motor may induce larger output torque. However, for larger slot area with larger number of turns, production of small machines becomes difficult as the slot opening gets narrower.

During the optimization of the prototype, in order to see the effect of the parallel slot edge type of slot, the slot area is changed according to the slot fill factor of 45% and turn number/slot of 75. Keeping the air-gap length constant ($g=0.8$ mm) the rotor radius is decreased due to decrease of the inner stator radius. The FEM results, including induced torque, induced voltage, air-gap flux density and its harmonics are recorded and analyzed below. The geometry of the model with parallel slot edges is given in Figure 4.55. In the following sections, FEM results corresponding to the model with parallel slot edges are given including magnetic field density, induced torque graph, induced voltage and air-gap magnetic field density. By looking at the geometry it can be clearly seen that for the same number of turns per slot, the rotor radius for parallel slot edge model is smaller, therefore the induced torque is also lower. Moreover, the magnetic field density near the slot openings takes values higher than the pre-defined maximum limit of 1.3 T.

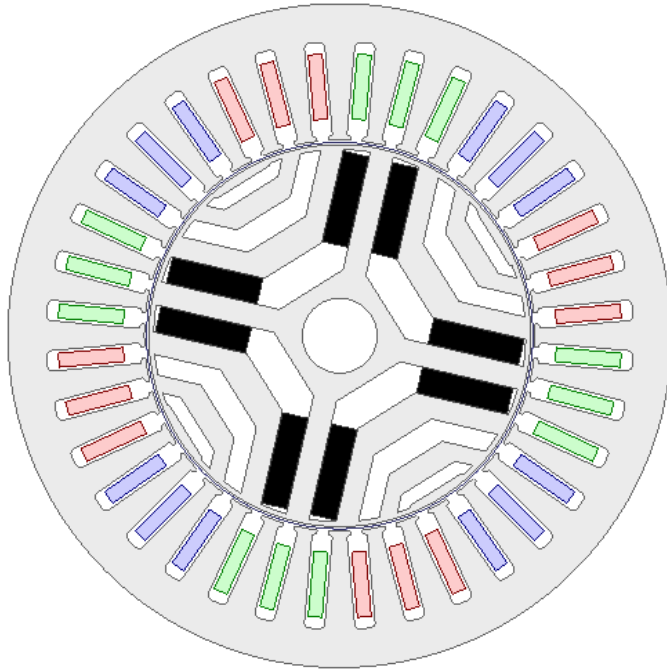


Figure 4.55 : Geometry of $g=0.8\text{mm}$ model with parallel slot edges.

The magnetic field density and the equi-flux lines results of the model with parallel slot edges are given in Figure 4.56.

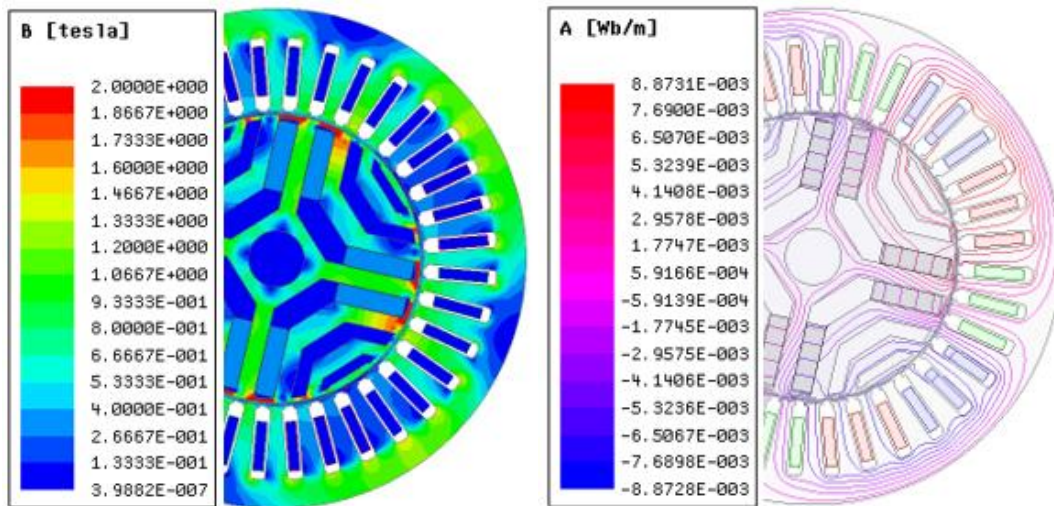


Figure 4.56 : Magnetic flux density and equi-flux lines of $g=0.8\text{mm}$ model with parallel slot edges.

To be comparable to the previous model, the slot opening in this model is also kept the same width of 2 mm. The induced torque graphs for both models, with parallel tooth edges and parallel slot edges, are given in Figure 4.57. Even though the number of turns/slot and air-gap length are kept the same, decrease of the rotor radius has decreased the average torque under the target torque value.

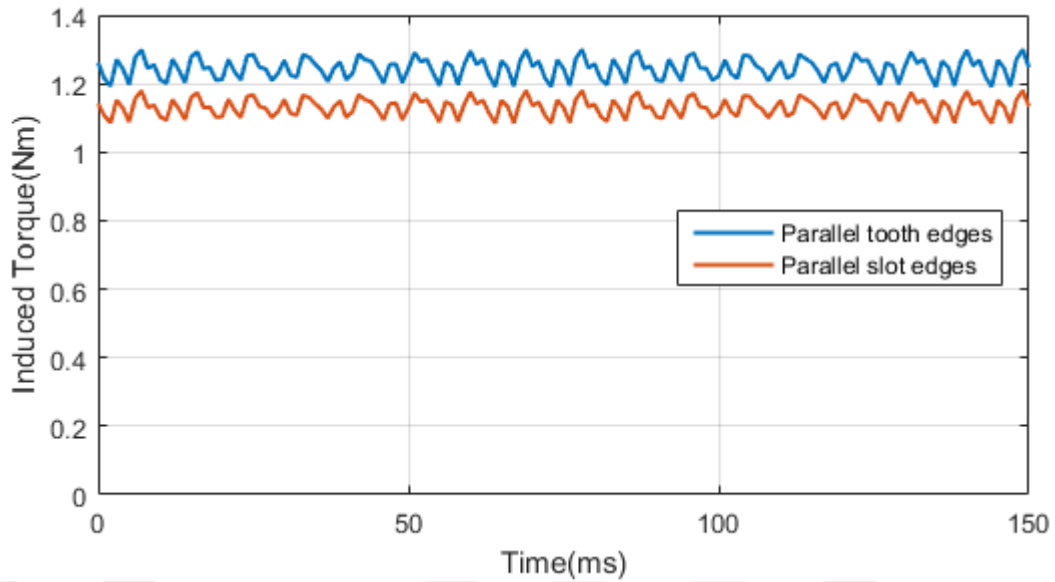


Figure 4.57 : Torque graph comparison of $g=0.8\text{mm}$ models with parallel tooth and parallel slot edges.

The induced phase voltages of both models are given in Figure 4.58. Narrower stator yoke and longer teeth increases the reluctance through which the magnetic field passes. Therefore, with lower magnetic flux, the induced voltage in the model having parallel slot edges is lower.

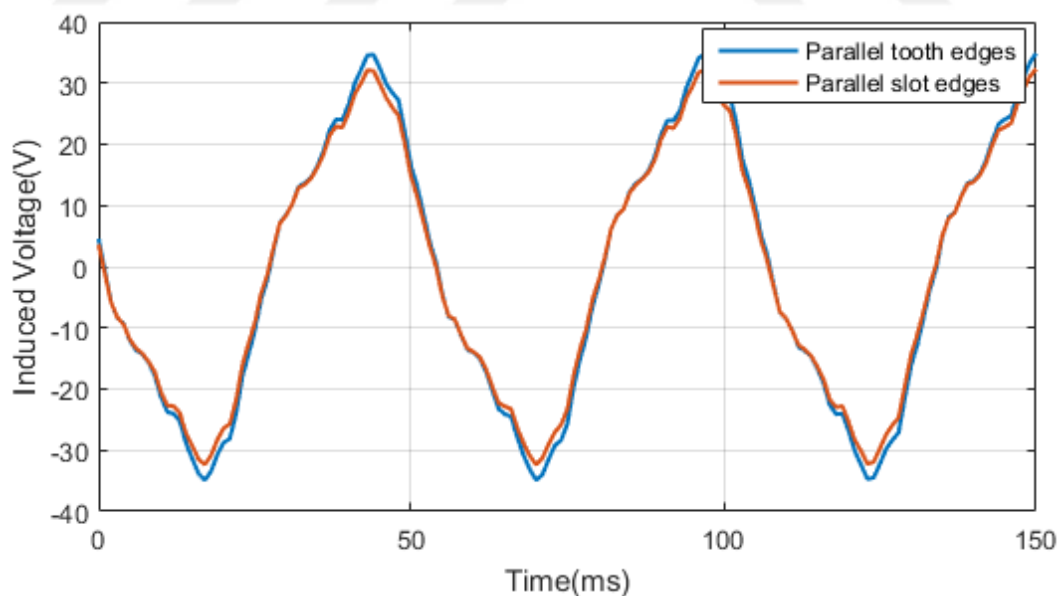


Figure 4.58 : Induced voltage graph comparison of $g=0.8\text{mm}$ models with parallel tooth and parallel slot edges.

The air-gap magnetic flux density for both models is given in Figure 4.59. As it was expected, the air-gap magnetic flux density of the model having parallel slot edges is slightly lower than the original model.

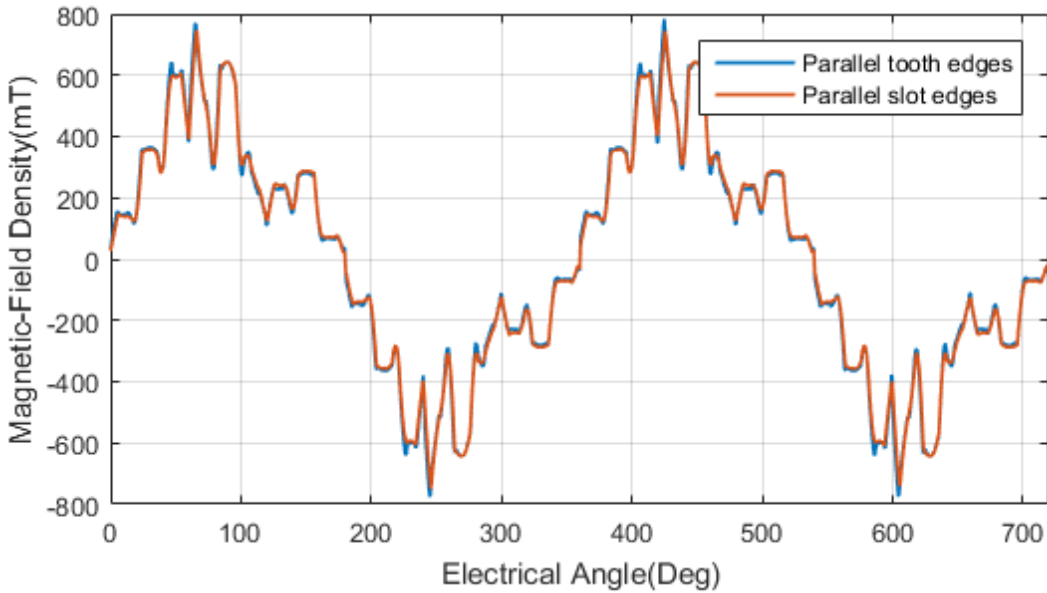


Figure 4.59 : Air-gap magnetic flux density comparison of $g=0.8\text{mm}$ models with parallel tooth and parallel slot edges.

The fact that the total magnetic flux is lower in the model with parallel slot edges is clearly seen also from the frequency components of the air-gap magnetic field density. The fundamental component and the majority of other components have lower amplitude than the model having parallel tooth edges. The comparison of the frequency component amplitudes is given in Figure 4.60. Their complete numerical values can be observed from Table 4.21.

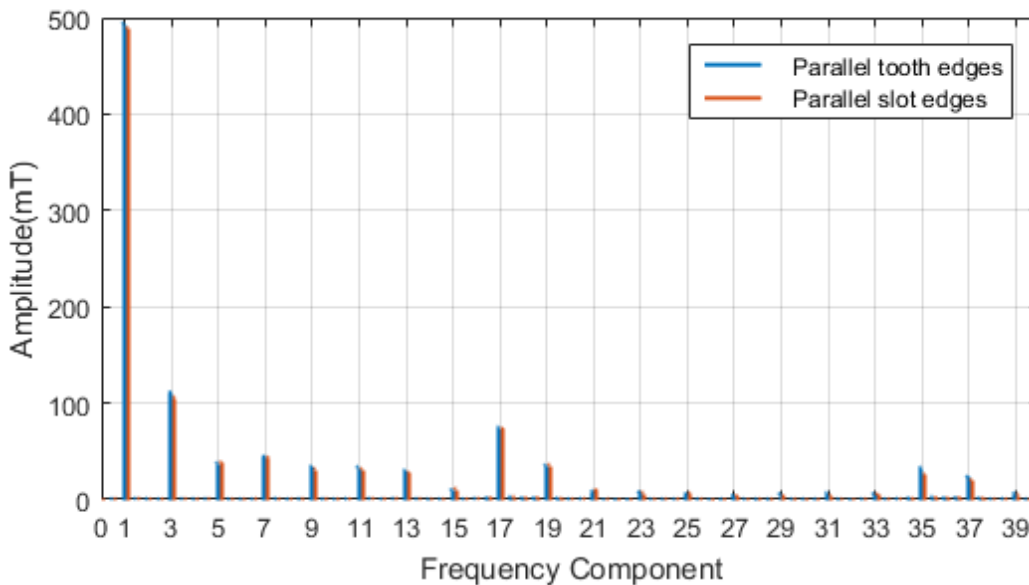


Figure 4.60 : Harmonic amplitude comparison of $g=0.8\text{mm}$ models with parallel tooth and parallel slot edges.

Table 4.21 : Harmonic component amplitudes for different slot types.

Frequency Component	Amplitude [mT]	
	Parallel Tooth Edge	Parallel Slot Edge
1	494.1	489.8
3	111.7	106.1
5	38.0	38.5
7	44.7	44.0
9	34.2	32.0
11	33.8	31.9
13	30.3	28.1
15	10.1	11.2
17	75.0	74.0
19	35.7	36.1
21	8.9	10.1
23	7.9	7.1
25	6.0	6.7
27	4.5	4.4
29	5.8	4.1
31	6.7	3.7
33	5.9	5.6
35	33.4	26.3
37	23.8	20.8
39	6.5	5.1

Since the induced torque of the parallel slot edge model is lower than the target output torque, this type of slot is not useful for the optimization of the prototype, therefore the optimization will be continued using parallel tooth edges type of slot. The results of the final comparison are given in Table 4.22.

Table 4.22 : Comparison results of parallel tooth and parallel slot edge models.

Model	B_{rms} [T]	Magnet Volume [cm ³]	Induced Torque [Nm]	Induced Voltage _{rms} [V]	Torque Ripple [%]	B_{max} tooth	B_{max} Yoke
Parallel Tooth Edge	0.369	22.6	1.245	21.6	8.67	1.31	1.27
Parallel Slot Edge	0.364	19.5	1.13	20.22	8.3	1.3	1.32

4.8.2 Effect of slot's inner wall

Considering the fact that the inner wall form of the slot affects the flow of the flux lines in the stator, in the following optimization analysis simulations of four different slot wall types are performed for the parallel tooth edge model selected previously. The FEM results for each model are recorded and analyzed comparing the induced

torque and the torque ripple for each configuration. Figure 4.61 shows the four types of inner slot walls that have been considered in this analysis.

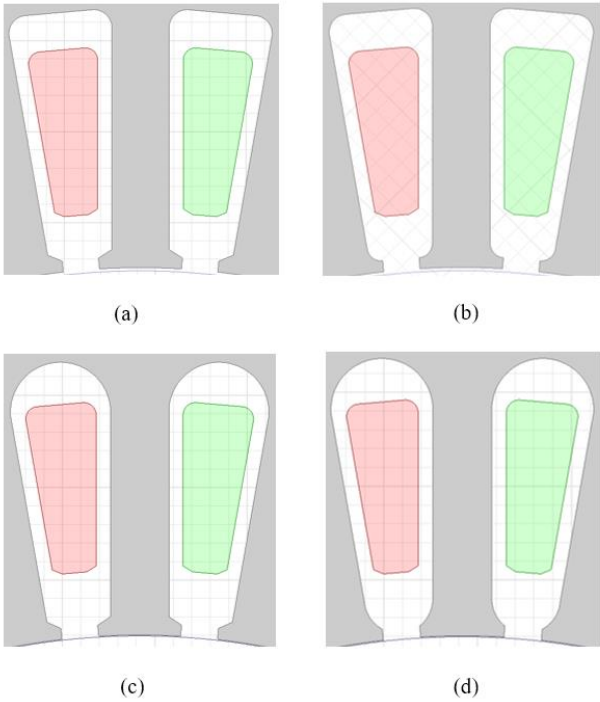


Figure 4.61 : Different slot type configurations.

The results obtained from the simulation of the four models are given in Table 4.23. Models are compared with respect to average induced torque and torque ripple.

Table 4.23 : Effect of slot’s inner wall on average torque and ripple.

Slot Model	Torque [Nm]	Absolute Ripple [Nm]	Torque Ripple [%]
A	1.24	0.108	8.71
B	1.25	0.105	8.4
C	1.21	0.113	9.3
D	1.21	0.112	9.3

Even though there is not a significant difference between the results, the optimum slot inner wall would be the B type. The model with the B type inner wall shows better performance on both average torque and torque ripple.

4.9 Effects of Tooth Bottom’s Shape

One of the techniques to reduce the torque ripple in electrical machines is to make the tooth bottoms rounded outwards the stator by keeping the average air-gap length

constant. Generally, this technique is used in motors having small number of slots and concentrated windings. The following analysis is performed to see how does outwards round tooth bottom affects the induced torque and ripple.

The air-gap length of the optimized model after last analysis is 0.8 mm, therefore to keep the average air-gap length constant, in the model with outwards round tooth bottom the air-gap length at the closest point is chosen as 0.7 mm whereas at the furthest point is chosen as 0.9 mm. The geometry and the zoomed view of the stator teeth of this model are given in Figure 4.62.

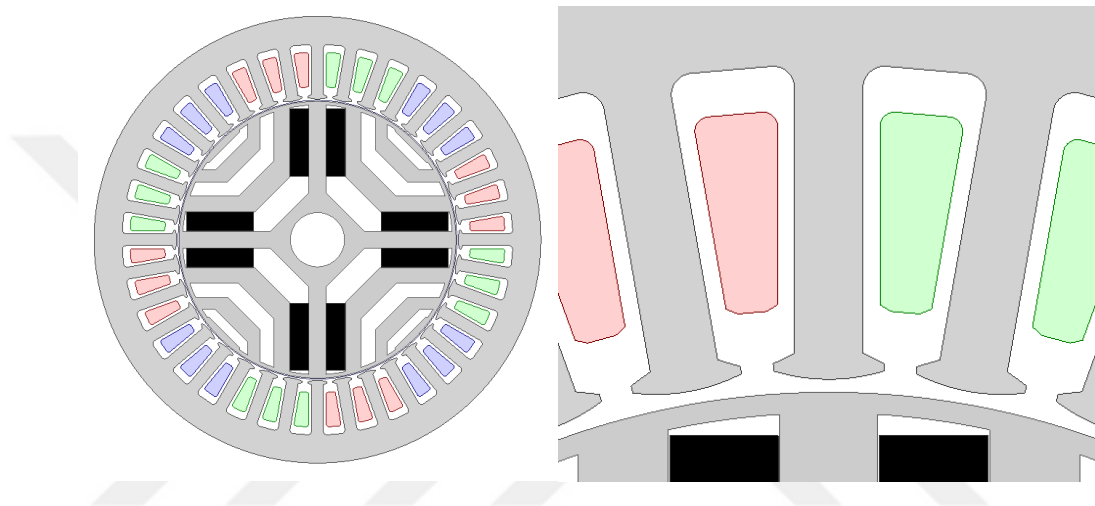


Figure 4.62 : Outwards round tooth bottom geometry.

The magnetic field density and the equi-flux lines results for the model having outwards tooth bottom are given in Figure 4.63.

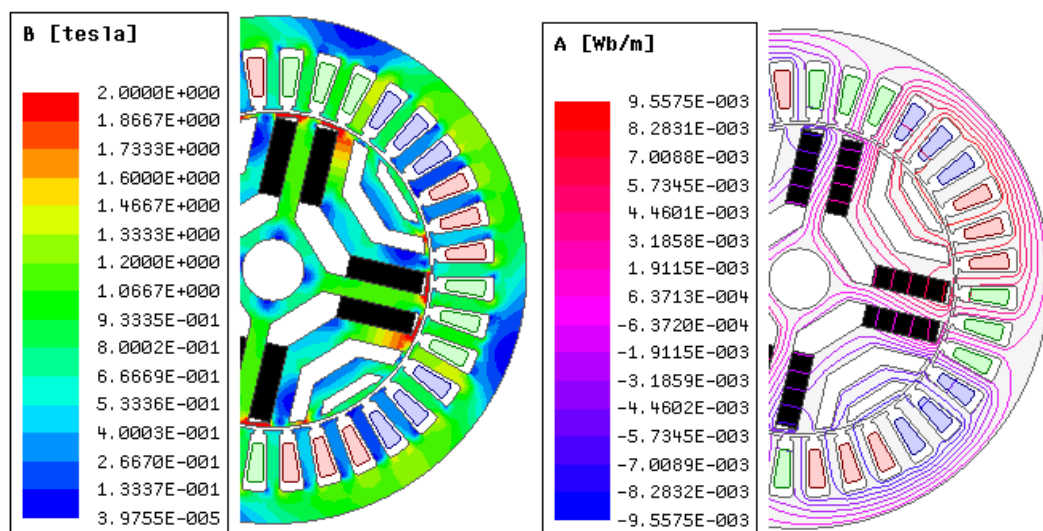


Figure 4.63 : Magnetic flux density and equi-flux lines of $g=0.8\text{mm}$ model with outwards rounded tooth bottom.

The induced torque graphs of both models having inwards and outwards tooth bottom are given and compared in Figure 4.64. The equivalent reluctance faced by the magnetic flux in the model having outwards tooth bottom is lower, therefore the magnetic flux passing through the air-gap is higher. Thus, the induced torque of this model is slightly higher than the previous model.

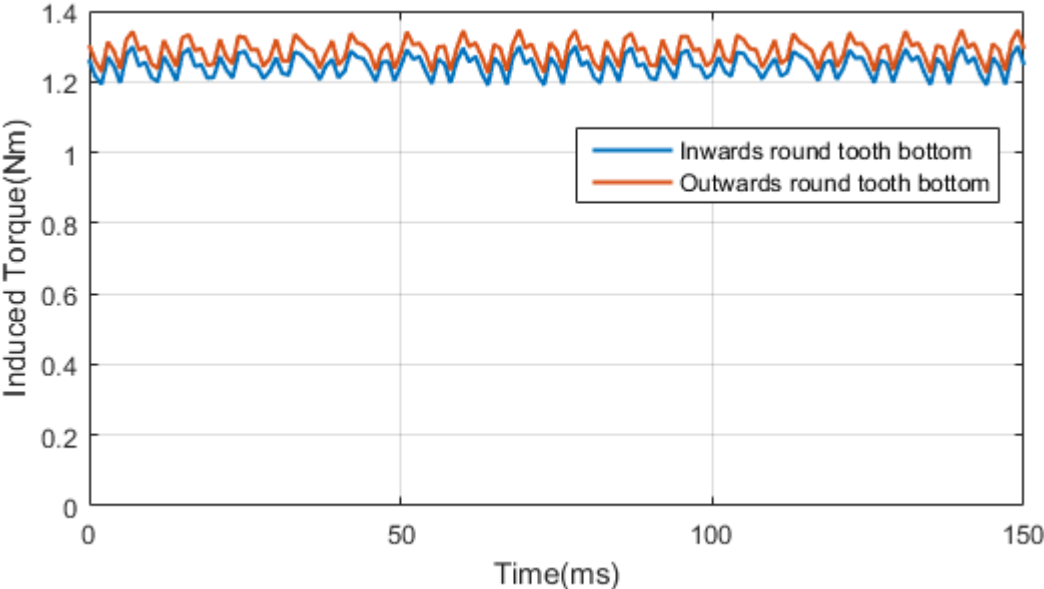


Figure 4.64 : Torque graph comparison of inwards and outwards rounded tooth bottom models.

Higher magnetic field passing through the air-gap induces higher voltages in the motor windings. The induced voltages in both models are given in Figure 4.65.

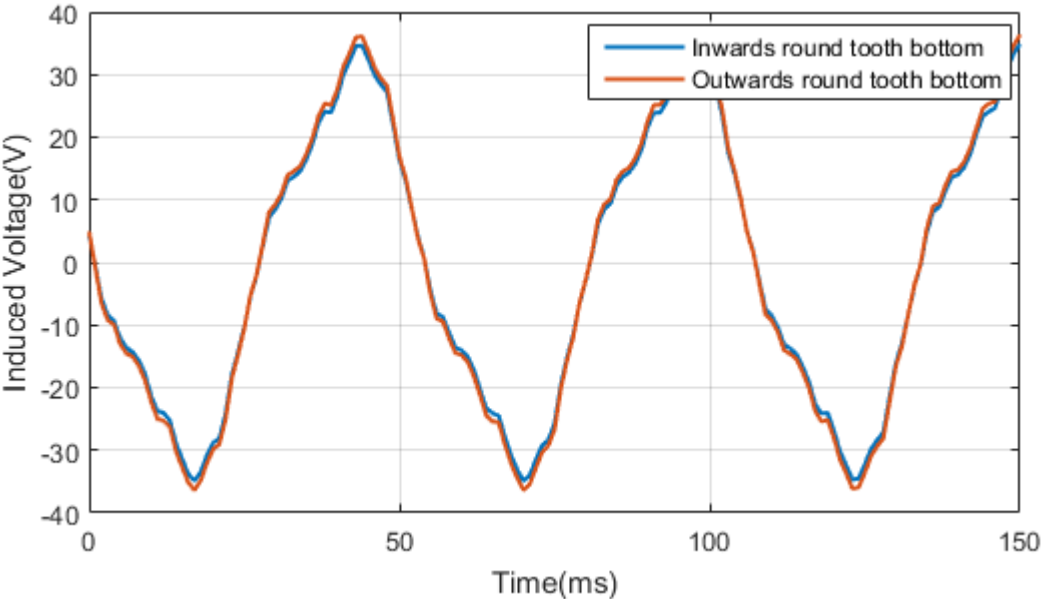


Figure 4.65 : Induced voltage graph comparison of inwards and outwards rounded tooth bottom models.

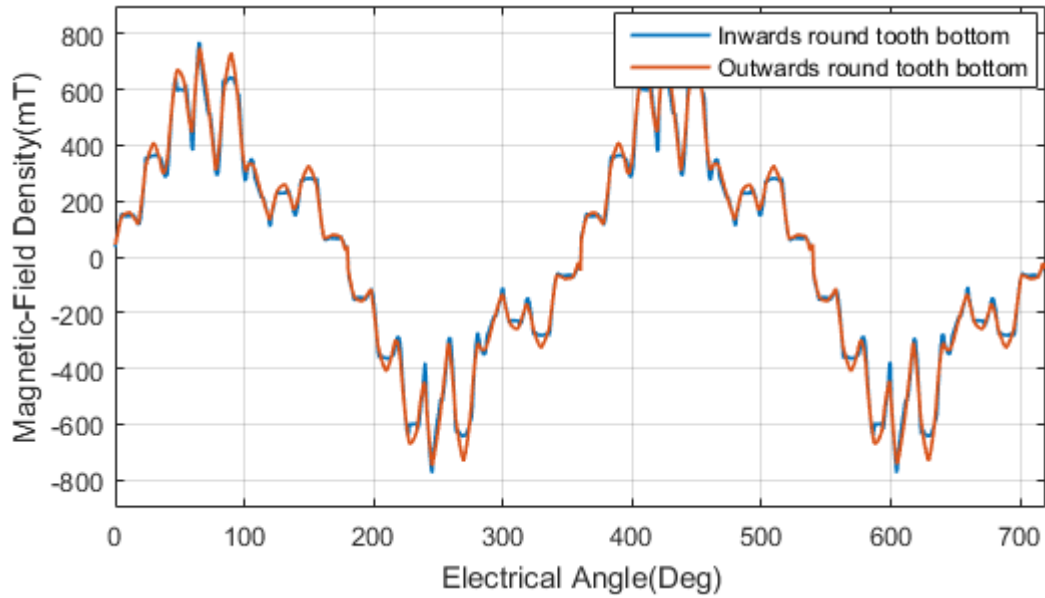


Figure 4.66 : Air-gap magnetic flux density comparison of inwards and outwards rounded tooth bottom models.

The air-gap magnetic flux density distributions of the models being compared are given in Figure 4.66. Due to the minimum air-gap length of 0.7 mm under each tooth, the magnetic flux density makes sharp peaks. These peaks cause that the fundamental component and the majority of the harmonic amplitudes of the model having outwards tooth bottom are higher than the original model. The comparison of the frequency components is given in Figure 4.67.

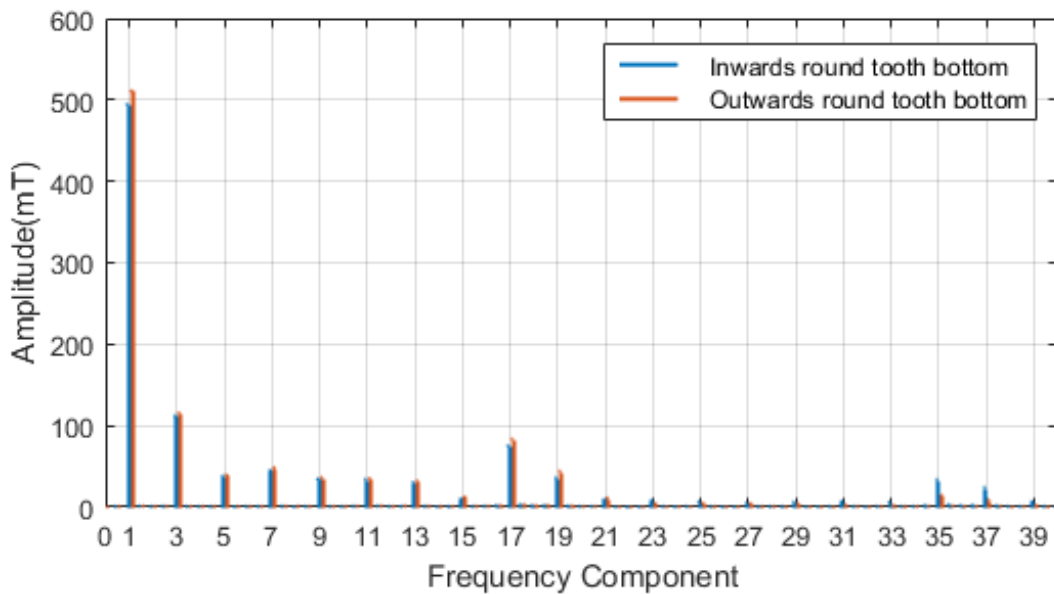


Figure 4.67 : Harmonic amplitude comparison of inwards and outwards rounded tooth bottom models.

The numerical values for all the frequency component amplitudes is given in Table 4.24.

Table 4.24 : Harmonic component amplitudes for different tooth bottom.

Frequency Component	Amplitude [mT]	
	Inwards Round Tooth Bottom	Outwards round Tooth Bottom
1	494.1	511.0
3	111.7	115.8
5	38.0	39.2
7	44.7	48.4
9	34.2	36.1
11	33.8	35.2
13	30.3	31.9
15	10.1	12.5
17	75.0	83.3
19	35.7	43.6
21	8.9	11.0
23	7.9	4.3
25	6.0	5.1
27	4.5	4.5
29	5.8	4.2
31	6.7	3.0
33	5.9	2.6
35	33.4	14.6
37	23.8	8.3
39	6.5	2.4

The final and complete comparison with respect to torque of both models having different tooth bottom is given in Table 4.25. Sharp peaks in the air-gap magnetic field density of the model with outwards tooth bottom increases its torque ripple. Even though the average torque for the outwards round tooth model is slightly higher, the torque ripple increase for about 1.6% makes this model unsuitable for selection. Therefore, the previous model with inwards tooth bottom is chosen as the optimum one for further optimization.

Table 4.25 : Effect of tooth bottom shape on induced torque.

Tooth Bottom Model	Induced Torque [Nm]	Torque Ripple [%]
	1.26	10.3
	1.25	8.64

Other parameters for the models being compared are given in Table 4.26. Slightly higher magnetic field in the model with outwards tooth bottom results in higher teeth saturation and higher induced phase voltages.

Table 4.26 : Average and RMS data comparison for different tooth bottom.

Model	B_{rms} [T]	Induced Voltage $_{rms}$ [V]	Teeth Magnetic Field Density B_{max} [T]
Inwards Round Tooth Bottom	0.369	21.6	1.31
Outwards Round Tooth Bottom	0.381	22	1.34

4.10 Final Electromagnetic Comparison

The final and complete electromagnetic comparison of the FEM results of the sample and optimized prototypes is given in Table 4.27. For the same input current of $I=1.62$ A, the optimized prototype satisfies the target output torque of 1.2 Nm and has better efficiency than the sample prototype. The higher magnetic field induced inside the optimized prototype due to smaller air-gap length and higher number of turns per phase, can be observed from its higher induced voltage and RMS value of the air-gap magnetic field density values. The phase resistance value of the optimized prototype used in calculating its efficiency is 5.375 ohms, which was predicted by Motor-CAD.

Table 4.27 : Electromagnetic comparison of the sample and optimized prototype.

Model	Sample Prototype	Optimized Prototype
Speed [min^{-1}]	563	563
Current [A_{rms}]	1.62	1.62
Induced Voltage [V_{rms}]	16.73	21.7
Induced Torque [Nm]	0.9	1.245
B_{rms} [T]	0.283	0.369
Efficiency [%]	49.6	62.7

The induced torque graphs for both models are given in Figure 4.68. Increase in the average torque has also increased the torque ripple of the optimized prototype. Beside the air-gap magnetic field density, decrease in the air-gap length has also significant effect on the torque ripple increase.

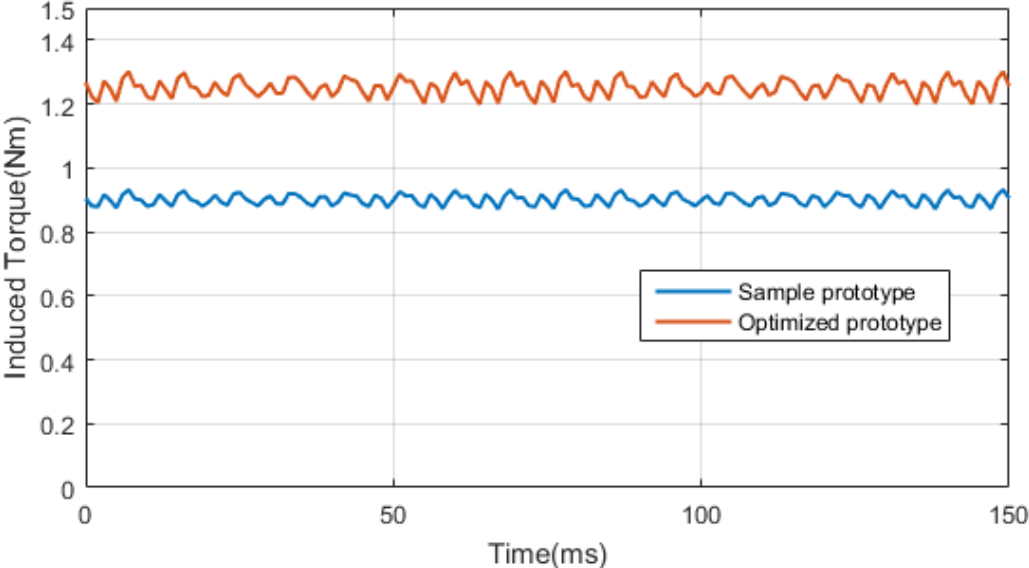


Figure 4.68 : Torque graph comparison of the sample and the optimized prototype.

The induced phase voltages for the sample and optimized prototypes are given in Figure 4.49. Higher peak values of the induced voltage in the optimized prototype are another sign that the induced magnetic field inside it is higher compared to that of the sample prototype.

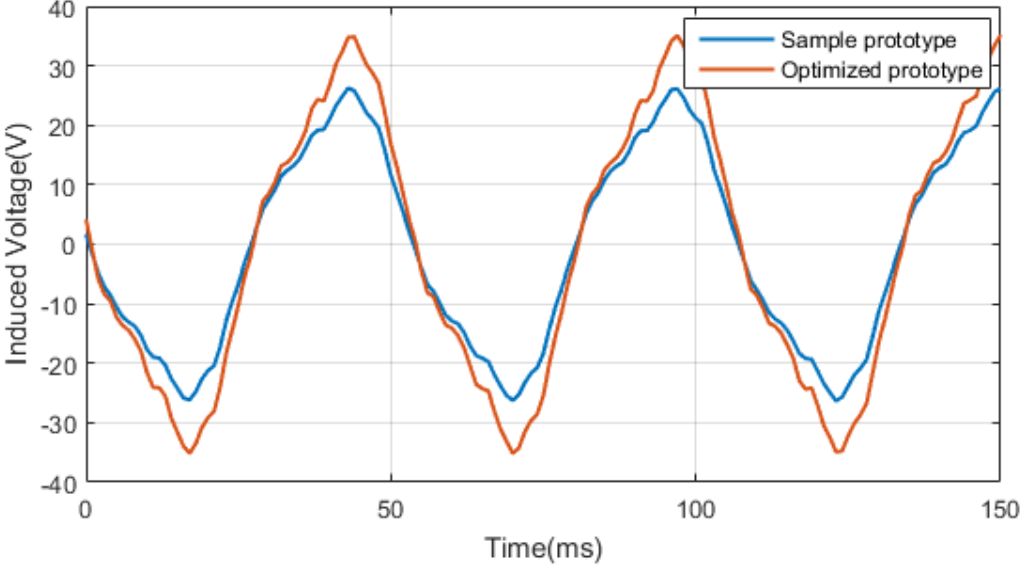


Figure 4.69 : Induced voltage graph comparison of the sample and the optimized prototype.

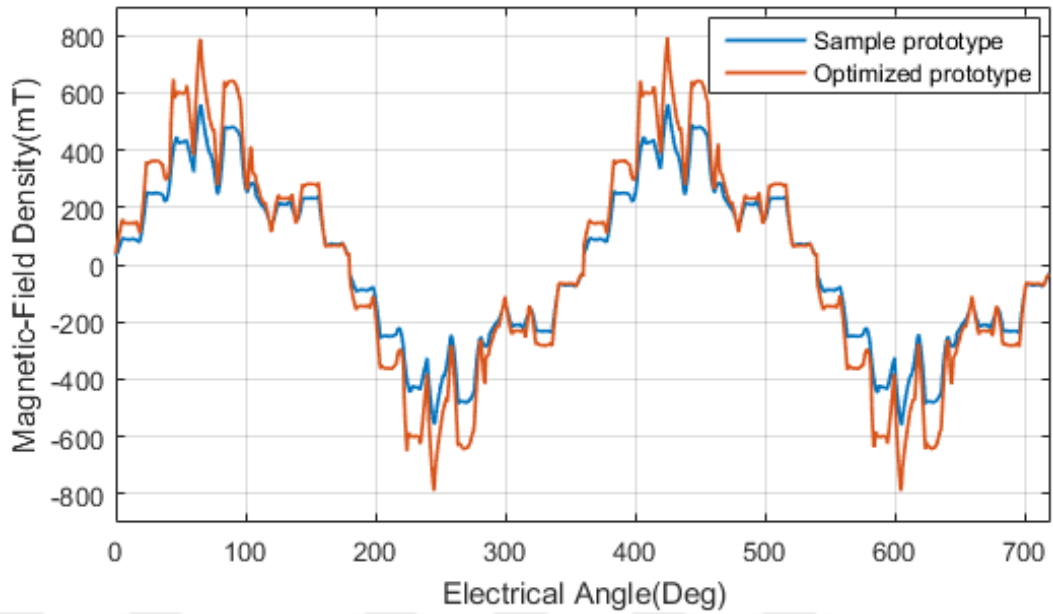


Figure 4.70 : Air-gap magnetic flux density comparison of the sample and the optimized prototype.

The air-gap magnetic field of the optimized prototype is much denser than the air-gap of the sample prototype. The comparison of the air-gap magnetic field of both models is given in Figure 4.70. The amplitudes of the frequency components are given and compared in Figure 4.71. Having the same components, optimized prototype has higher amplitudes than the sample prototype due to higher magnetic field.

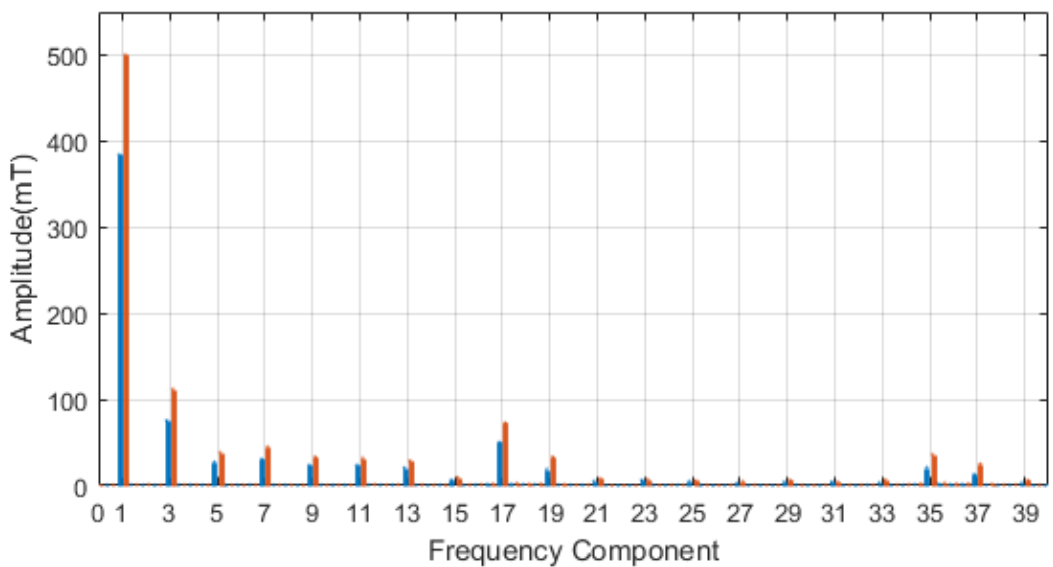


Figure 4.71 : Harmonic amplitude comparison of the sample and the optimized prototype.

The complete numerical values for all the components up to 39th one, are given in Table 4.28.

Table 4.28 : Sample and optimized prototype's air-gap flux density harmonics.

Frequency Component	Amplitude [mT]	
	Sample Prototype	Optimized prototype
1	384.2	500.1
3	75.4	112.1
5	27.4	38.3
7	30.8	44.9
9	23.5	33.3
11	23.5	31.7
13	20.8	28.9
15	6.3	9.7
17	50.4	72.7
19	18.8	33.3
21	5.1	7.8
23	6.1	7.3
25	4.8	5.6
27	2.5	4.9
29	4.2	6.3
31	4.5	4.3
33	3.3	6.9
35	21.1	36.1
37	13.0	25.2
39	3.3	6.3

4.11 Test Results of the Optimized Prototype Motor

The final optimized motor has been produced and tested according to IEC 60034-2-1 and IEC 60034-18-41 standards. In this section, test results of the optimized motor have been compared to the FEM results obtained in optimization analysis. Due to limitations in the inverter side, test results are taken only for washing mode operation at 563 min⁻¹. The test setup, as it can be seen from the Figure 4.72, it includes the prototype motor, inverter and the load. During the test, the speed of the motor is kept constant at 563 min⁻¹ and the load is increased gradually. For different load torque values the input current of the motor is observed and recorded. On the other side, for the same current values, simulations in Maxwell 2D are run to observe the induced torque for each case and later compare them to the test results.

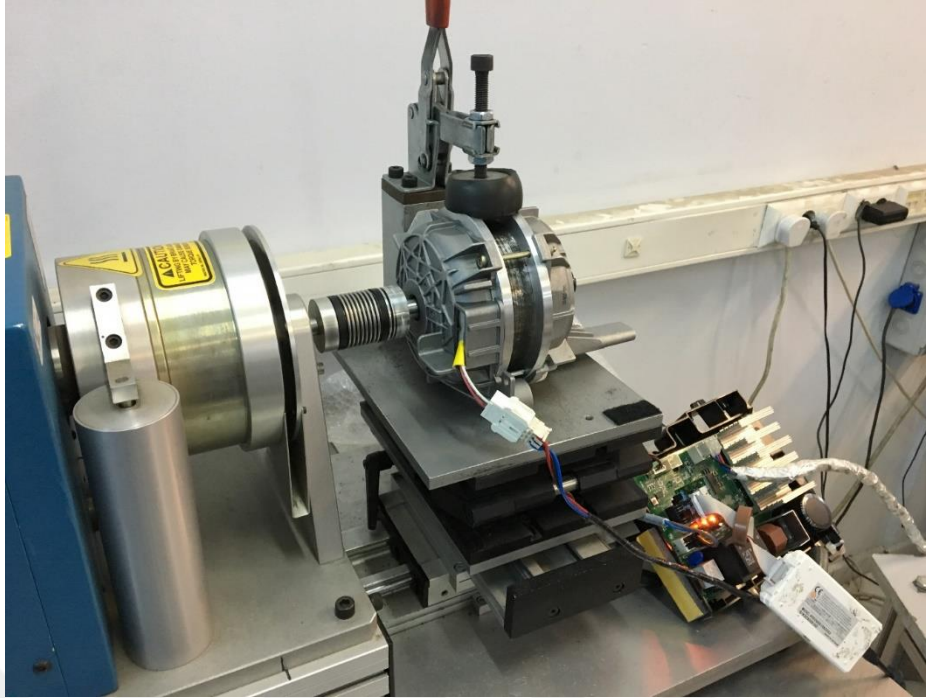


Figure 4.72 : Test setup of the optimized prototype.

The current and torque values for the washing mode test are given in Table 4.29. Referring to the torque comparison graph, it is clearly seen that the test and FEM torque values are quite close to each other with a maximum error of 8.57%. This error is due to the small value of the output torque, whereas for higher output torque values the error drops to very small values. Such small error values show that the FEM analysis performed earlier during the optimization of the sample prototype is highly accurate.

Table 4.29 : Test and simulation torque values of the optimized prototype for different input current.

I [A]	T [Nm] (Test)	T [Nm] (Simulated)	Error [%]
0.71	0.35	0.38	8.57
0.83	0.45	0.47	4.44
0.96	0.55	0.58	5.45
1.04	0.65	0.65	0.00
1.15	0.75	0.75	0.00
1.24	0.85	0.84	1.18
1.33	0.95	0.93	2.11
1.48	1.05	1.09	3.81
1.54	1.15	1.16	0.87
1.6	1.25	1.23	1.60
1.68	1.35	1.32	2.22

The graphical comparison of the torque values for different input current values is given in Figure 4.73.

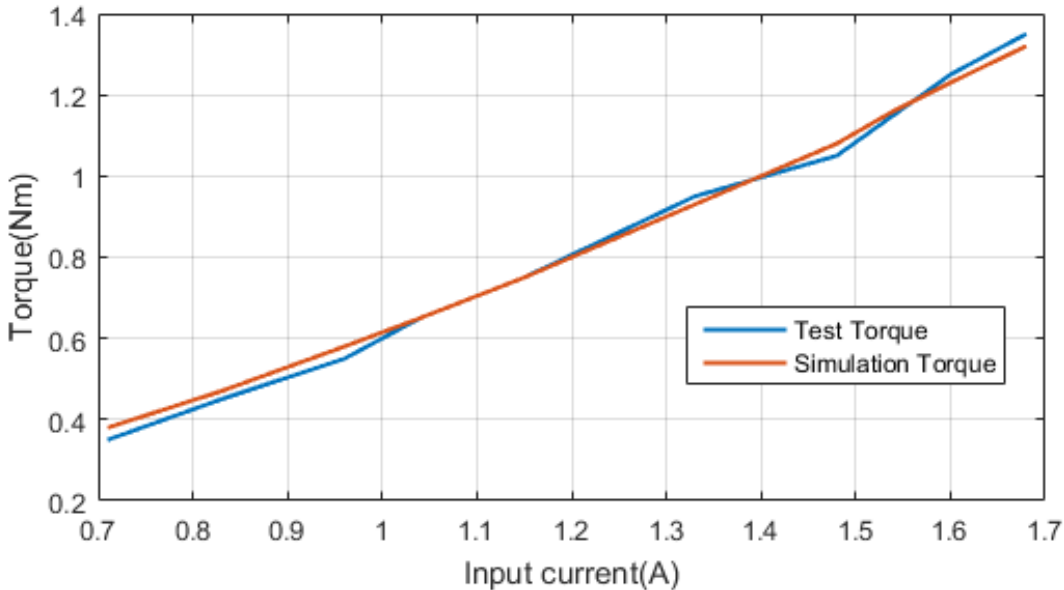


Figure 4.73 : Current–torque graphs of the optimized prototype.

Similar to the torque values, the test efficiency of the prototype is compared to the efficiency calculated by FEM. The results are recorded in Table 4.30.

Table 4.30 : Test and simulation efficiencies of the optimized prototype for different input current.

I [A]	Efficiency [%] (Test)	Efficiency [%] (Simulation)	Difference [%]
0.71	62.50	72.35	9.85
0.83	61.67	70.45	8.78
0.96	61.15	68.85	7.70
1.04	59.85	67.88	8.04
1.15	59.72	66.65	6.93
1.24	58.93	65.85	6.92
1.33	58.31	65.00	6.68
1.48	57.29	63.77	6.48
1.54	56.47	63.38	6.91
1.60	55.80	62.98	7.17
1.68	55.24	62.36	7.11

The graphical representation of the efficiency values is given and compared for both cases in Figure 4.74. The efficiency difference given in Table 4.30, having a maximum value of 9.85%, is due to the difference in the winding resistance which was predicted to be 5.375 ohms, however, the calculated resistance of the produced

prototype appeared to be 6 ohms. Moreover, in FEM analysis, the windage and friction losses of the motor are not included, since mechanical transients are excluded from FEM solutions.

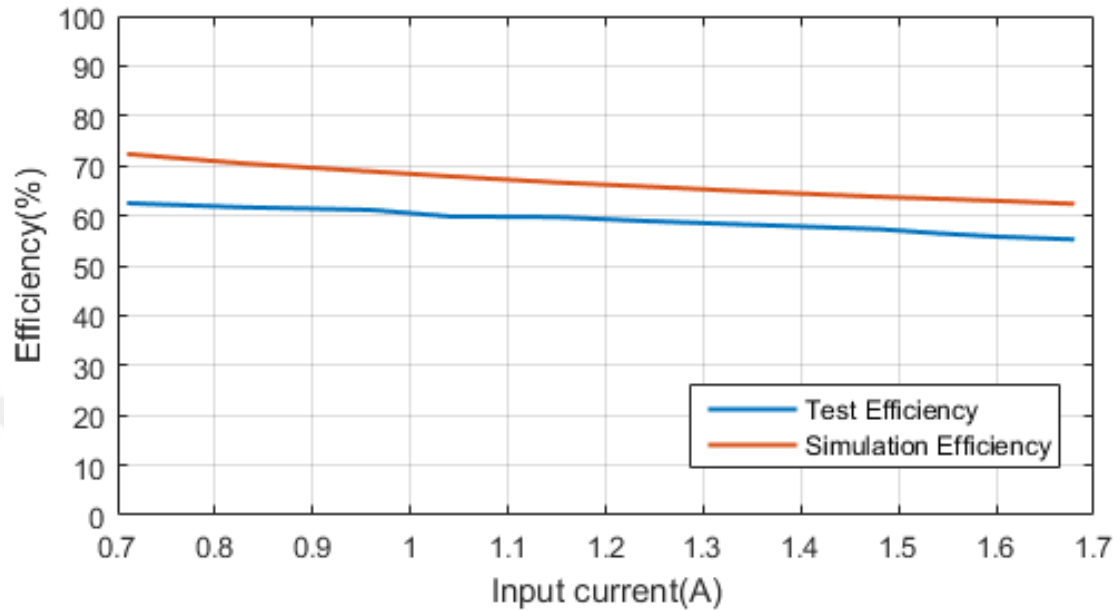


Figure 4.74 : Current-efficiency graphs of the optimized prototype.

4.12 Complete Performance of Sample and Optimized Prototype

The complete torque-speed and current-speed characteristics of both models have been modelled in Motor-LAB module of Motor-CAD. Both models have been driven by a maximum peak current of $I_{\text{peak}}=3$ A and a peak line voltage of $V_{\text{peak}}=311$ V. The main purpose of this analysis is determination of the motor performance during spinning mode operation at 13000 min^{-1} . During high speed operation the magnetic field is weakened by changing the load angle of the motor up to 90° electrically. Increase of the load angle increases the reluctance of the flux path, thus the motor's output torque decreases while it reaches high speeds under limited current and voltage values.

The operation modes of the model can be clearly seen from the torque-speed characteristics of the sample prototype is given in Figure 4.75. The first mode defines the current limited region, where the motor operates at constant current and constant load angle. This mode continues until the motor reaches its base speed, and the current and the voltage reach their limits.

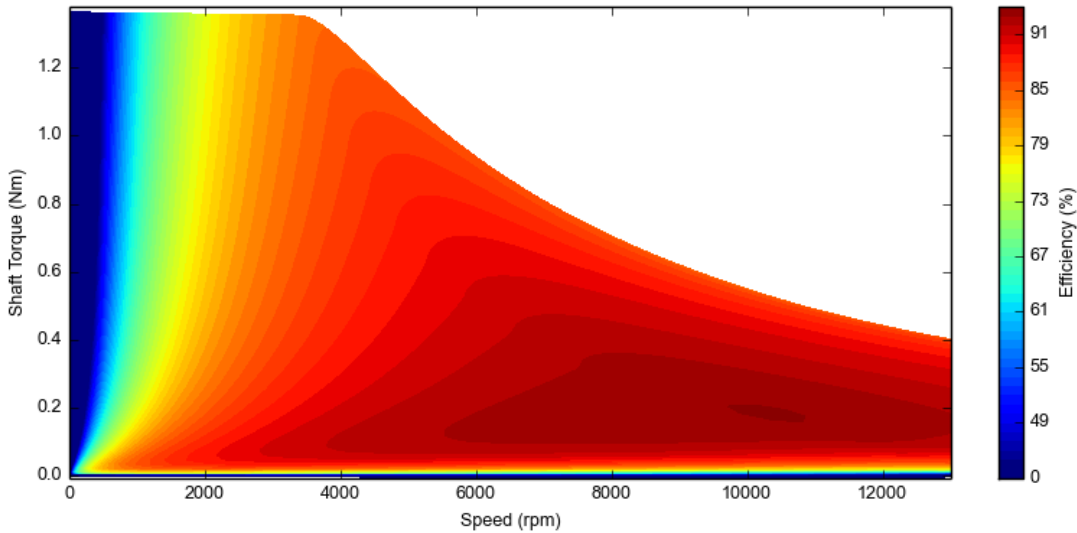


Figure 4.75 : Torque-speed characteristics of sample prototype.

After the base speed, the motor enters current and voltage limited region. In this region the output torque decreases by increasing the load angle, whereas the current remains constant. The third region is the voltage limited region, where the voltage remains at its maximum but the current decreases to further weakening the magnetic field.

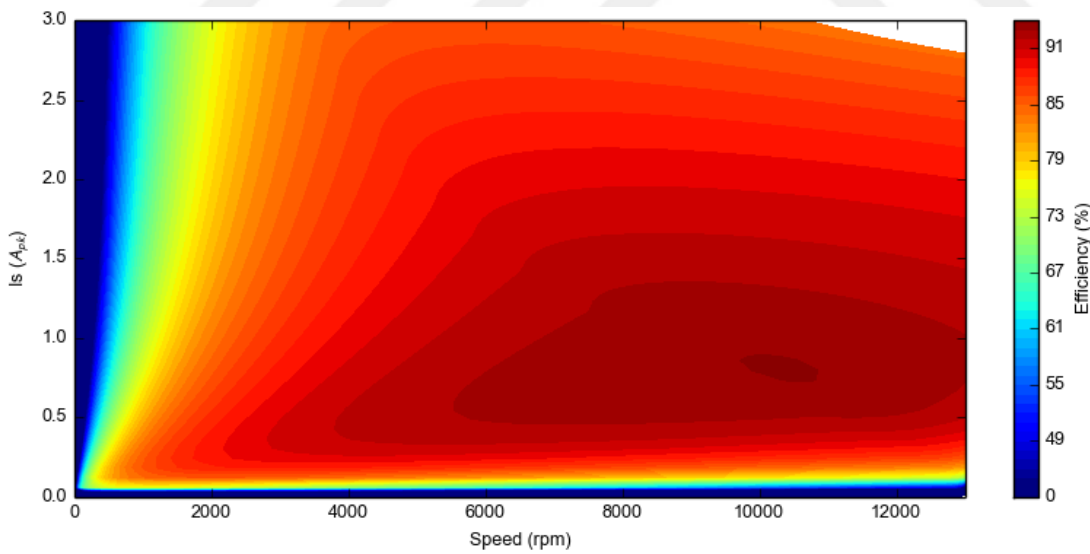


Figure 4.76 : Current-Speed characteristics of sample prototype.

From current-speed characteristics of the sample prototype given in Figure 4.76, it is clearly seen that this model undergoes operation through all three regions until it reaches the spinning speed of 13000 min^{-1} . If the sample prototype was to be used for the same application with output torque of 1.2 Nm , the parameters for both washing

and spinning modes would be as given in Table 4.31. The copper and iron losses given in this table are later used in the thermal analysis of the sample prototype.

Table 4.31 : Complete parameter values for sample prototype.

Operation Mode	Washing	Spinning
Speed [min^{-1}]	563	13000
Current [A]	1.99	1.98
Torque [Nm]	1.25	0.4
DC Copper Losses [W]	79.6	77.97
Iron Losses [W]	0.9	28.86
Efficiency [%]	47.5	83.6

Similar to the sample prototype, the torque-speed characteristics of the optimized prototype are obtained in Motor-LAB module. The characteristics are obtained for the same maximum peak current and line voltage as given in Figure 4.77 and Figure 4.78.

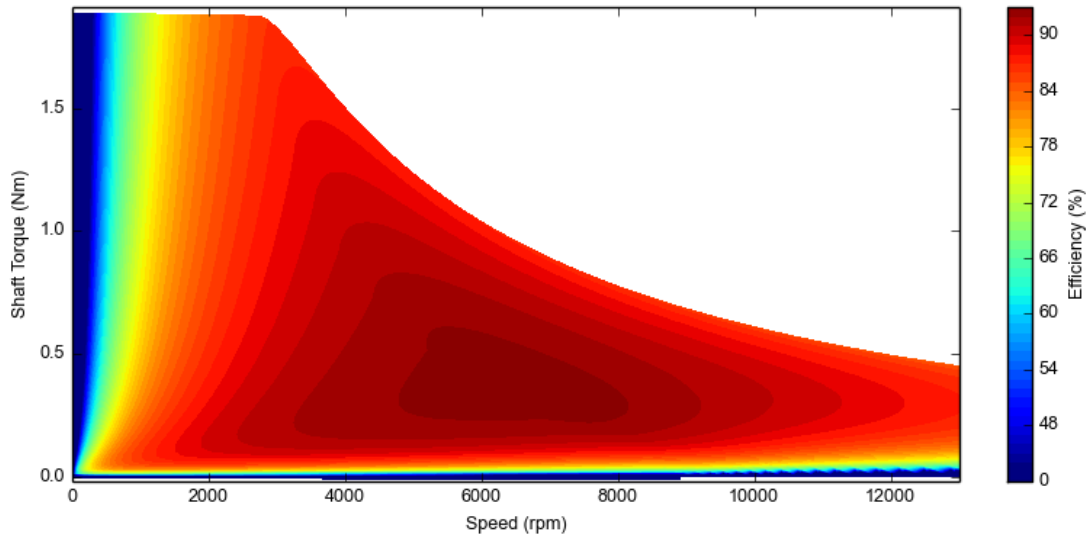


Figure 4.77 : Torque-speed characteristics of the optimized prototype.

Lower phase resistance makes the optimized prototype more efficient at lower speed values. The maximum efficiency region seen in Figure 4.77 is wider and corresponds to lower speed values compared to that of the sample prototype. Moreover, the model does not enter too much in the voltage limited region of operation where the current is decreased for further field weakening. From the current-speed characteristics of the optimized prototype it can be seen that to reach a speed of 13000 min^{-1} the motor undergoes a slight decrease of the current in the voltage limited region. Thus the induced torque at this speed is higher than that of the sample prototype.

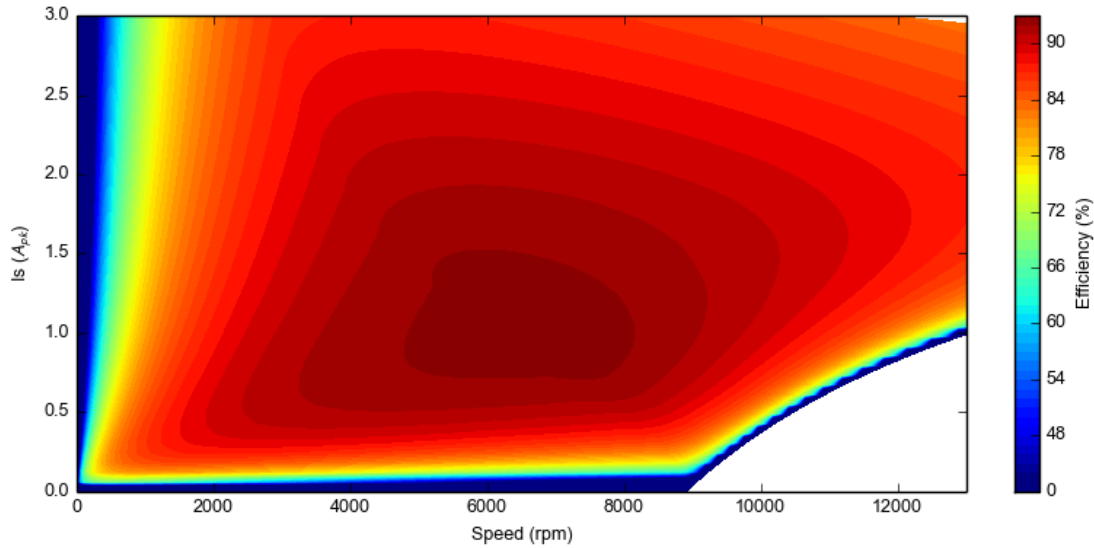


Figure 4.78 : Current-speed characteristics of the optimized prototype.

The complete parameters for washing and spinning modes for the optimized prototype are given in Table 4.32. As it can be seen, the optimized prototype has better efficiency in both operation modes. The copper and iron losses of the optimized prototype are later used in its thermal analysis.

Table 4.32 : Complete parameter values for optimized prototype.

Operation Mode	Washing	Spinning
Speed [min^{-1}]	563	13000
Current [A]	1.62	2.1
Torque [Nm]	1.24	0.45
DC Copper Losses [W]	47.24	78.31
Iron Losses [W]	1.08	51.8
Efficiency [%]	60.2	82.46

5. THERMAL ANALYSIS

One of the most important stages of an electrical motor design is its thermal analysis. The heat that is generated inside the motor windings due to its copper losses is transmitted through other parts of the motor to the outside medium. Considering this heat transfer, thermal analysis determines the temperature values of different parts of the motor and it defines the required insulation class of the winding isolator. Therefore, it is very important thermal analysis of electric motors to be performed right and accurately. In literature, there are two different thermal models of electric motors used in such analysis. First one are the models that use finite element methods. Such models perform thermal analysis by dividing the motor geometry into small parts and solving the heat transfer equations for each part. However, this method requires high data storage capabilities and its calculations last for long periods. The second method includes analytical solutions of thermal circuits defined by dividing the motor in several parts. Each of these parts corresponds to a node where the temperature is going to be measured. Between motor nodes, depending on the geometry and the material characteristics, thermal resistances are calculated for further calculation of the heat transfer from the windings to the outside medium. Thus, depending on the thermal resistance values, the temperature values at each node is calculated as a result of the heat transfer through the thermal circuit. The majority of the active losses in electric motors occur in stator or rotor windings, therefore the maximum thermal stress occurs at these parts. Calculating the temperature values of the windings, the insulation class should be chosen accordingly so that the motor will operate for longer times without damaging the winding insulation. In order to keep the temperature values inside an electric motor within pre-defined limits, different cooling methods like natural convection, self-ventilation cooling, housing water jackets, wet rotor, spray cooling and radiation can be applied. All these methods can also be modeled analytically.

5.1 Heat Transfer

Heat transfer occurs as a result of temperature difference between two points in the same or different media. Depending on the surrounding conditions, heat may be transferred through different ways and with different speed.

Heat is transferred through:

- Conduction
- Convection
- Radiation

5.1.1 Conduction

If there is a difference (gradient) in temperature values between two points of an object, the heat inside is flows from the part where the temperature is higher to the parts where the temperature is lower, as given in Figure 5.1. This kind of heat transfer is known as conduction. The amount of heat transferred Q is directly proportional to the cross sectional area A and the normal temperature gradient.

$$Q = -kA \frac{\partial T}{\partial x} \quad (5.1)$$

Here, $\frac{\partial T}{\partial x} = \frac{T_2 - T_1}{L}$ is the temperature gradient in the heat transfer direction. The factor k in the equation is known as the conduction constant and it depends on the material characteristics of the object. The negative sign in the equation results due to the second law of thermodynamics. The unit of the conduction constant k is [W/m°C] whereas the unit of heat transfer Q is [W].

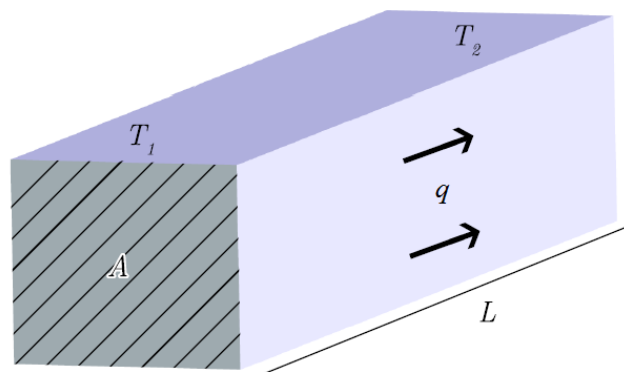


Figure 5.1 : Heat transfer due to temperature difference inside the object [40].

While designing the thermal circuit of any object, for each node inside the object the equation of energy conservation can be written as:

$$\text{Entering heat energy} + \text{generated heat energy} = \text{change in the stored energy} + \text{leaving heat energy}$$

Mathematically, the energy conversion equation is defined as follows.

Entering heat energy:

$$Q_x = -kA \frac{\partial T}{\partial x} \quad (5.2)$$

Generated heat energy:

$$Q' A dx \quad (5.3)$$

Change in the stored energy:

$$\rho c A \frac{\partial T}{\partial \tau} dx \quad (5.4)$$

Leaving heat energy:

$$Q_{x+dx} = -kA \frac{\partial T}{\partial x} \Big|_{x+dx} = -A \left[k \frac{\partial T}{\partial x} + \frac{\partial}{\partial x} \left(k \frac{\partial T}{\partial x} \right) dx \right] \quad (5.5)$$

In the above equations, Q' is the generated heat energy in unit volume [W/m³], c is the material specific heat capacity [J/kg°C] and ρ is the material density [kg/m³].

The node equation of energy conversion equation is written as given in Equation 5.6.

$$-kA \frac{\partial T}{\partial x} + Q' A dx = \rho c A \frac{\partial T}{\partial \tau} dx - A \left[k \frac{\partial T}{\partial x} + \frac{\partial}{\partial x} \left(k \frac{\partial T}{\partial x} \right) dx \right] \quad (5.6)$$

This is a single dimension heat transfer equation. For a multidimensional model, energy conversion over a unit volume should include the energy transfer through conduction in each direction. In such cases, the equation becomes,

$$Q_x + Q_y + Q_z + Q_{generated} = Q_{x+dx} + Q_{y+dy} + Q_{z+dz} + dE / d\tau \quad (5.7)$$

where:
$$\frac{dE}{d\tau} = \rho c dx dy dz \frac{\partial T}{\partial \tau} \quad (5.8)$$

5.1.2 Convection

Convection is the heat transfer from any object occurring as a result of the motion of the fluids around them. The simplest example of such heat transfer is the faster cooling of a hot metal object with a fan put in front of it. The heat energy from the metal object is said to be transferred through convection. The change of the temperature values during convection is directly proportional to the transfer rate of the fluid transferring the heat. For example, faster flowing fluids result in greater temperature changes.

To define the effect of the convection, Newton's cooling law is used. Thus, the equation is written as:

$$Q = h_c A (T_w - T_\infty) \quad (5.9)$$

The value of heat transfer Q depends on the temperature values of the object and the fluid, the contact sectional area and the material characteristics of the transferring fluid. In the equation, h_c is the convection constant and it depends on the transferring fluid. A is the contact sectional area between the object and the transferring fluid, whereas T_w and T_∞ are the temperature values of the object being cooled and the transferring fluid, respectively.

While calculating the constant h_c , some systems use analytical solutions. However, in more complex systems, this constant is determined experimentally. Its unit is $[\text{W}/\text{m}^2\text{C}]$ dir. Moreover, the heat transfer through convection is also dependent on the thermal characteristics of the transferring fluid, like thermal conductivity, specific heat capacity and density.

5.1.3 Radiation

In conduction and convection, the heat transferred through a medium or between two media that are in contact. However, the heat can be also transferred when there is no transfer medium around the cooling object. This kind of heat transfer occurs as a result of electromagnetic radiation. According to the results obtained from thermodynamic researches, the heat being radiated from a perfect radiative object, is directly proportional to the fourth power of the objects temperature and its sectional area A .

$$Q_{radiated} = \sigma AT^4 \quad (5.10)$$

In Equation 5.10, the constant σ is known as the Stefan-Boltzmann constant, and its value is 5.669×10^{-8} [W/ m²K⁴]. According to the equation above, the net radiation between two different surfaces is directly proportional to the fourth power of the temperature difference between them (T_1 and T_2). Mathematically the net radiation between two surfaces it takes the following form.

$$\frac{Q_{radiated}}{A} \approx \sigma(T_1^4 - T_2^4) \approx \sigma(T_1^4 - T_2^4) \quad (5.11)$$

5.1.4 Motor-CAD software

Motor-CAD is a software developed by Motor Design Ltd. for electromagnetic and thermal analysis of electric motors and generators. The software used both analytical and finite element methods for thermal analysis whereas it uses only finite element methods for electromagnetic analysis. This software has several motor models for analysis including brushless permanent-magnet motors (BPM), outside rotor motors, induction motors, permanent magnet DC motors, etc. Moreover, for all type of motor models, different cooling systems like natural convection, self-ventilation cooling, housing water jackets, wet rotor, spray cooling and radiation can be modelled and analyzed [41]. It is accepted that the development and the high accuracy of the thermal models of electric motors is more difficult than their electromagnetic models. In Motor-CAD, instead of using motor drawings from other software, the geometry of the motor is obtained by changing several numerical parameters defined in the software interface. Such software plays a significant role and are becoming more and more important in designing more efficient and compact electrical machines by performing fast and accurate thermal analysis for different operating and cooling conditions.

5.2 Thermal Analysis of the Sample Prototype

In this section of thesis, thermal analysis of the sample prototype is performed in Motor-CAD. The steps how the motor is modeled in Motor-CAD software is explained only for the sample prototype motor, later the thermal results are compared for both sample and optimized motors.

5.2.1 Geometry settings

In the software used for thermal analysis, the geometry of the motor is defined by changing the parameters given corresponding to the geometry settings. The geometry settings and the defined geometry is given in Figure 5.2. The stator of the first design defined in Motor-CAD is exactly the same as the geometry defined in Maxwell. However, as a result of limited parameter number in the rotor side, the defined geometry is an approximation of the original one. The magnet length is changed by a single parameter, therefore, the magnet volume in the Motor-CAD geometry is distributed in three barriers with the same ratio as in the original geometry.

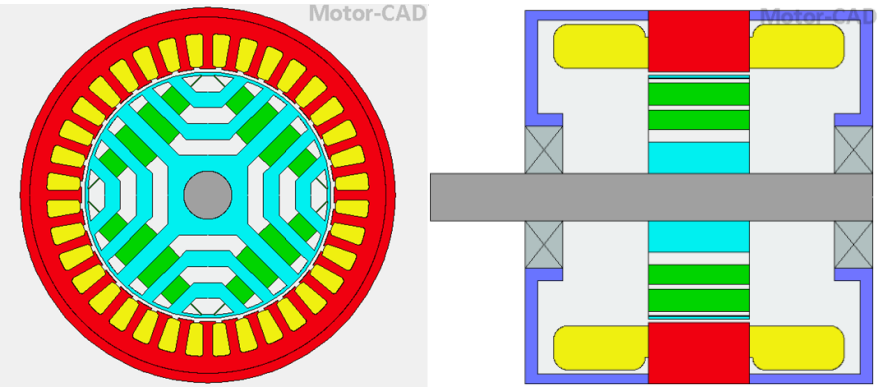


Figure 5.2 : Radial and axial view of the sample prototype motor.

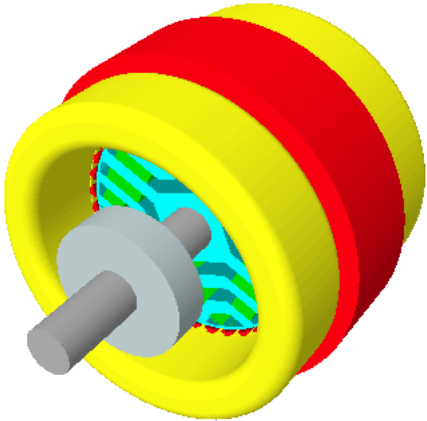


Figure 5.3 : 3D view of the motor.

5.2.2 Windings settings

In the winding settings, the available parameters include the winding type, slot fill factor and conductor diameter. In the performed analysis, the conductor number/slot is chosen as 70. ''Ewdg MLT'' factor defined the ratio of the winding length that remains outside the stack length. Since the motor's stack length is small and the

winding is distributed, the end-winding mean length is calculated to be 200 mm. The conductor configuration in a single slot is given in Figure 5.4.

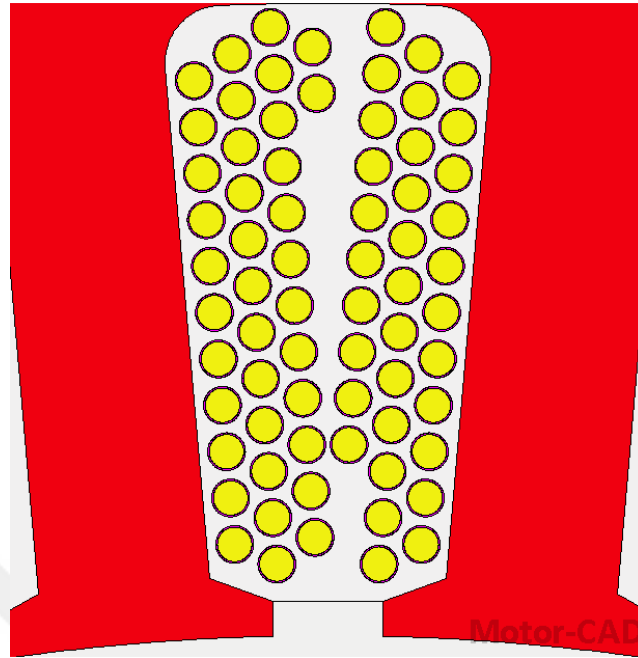


Figure 5.4 : Winding and slot configuration.

5.2.3 Loss parameters

The sample prototype at 1.62 A induces a torque of 0.9 Nm. At this current value, this motor is not usable for washing application due to low output torque. Therefore, to make the sample prototype comparable to the final optimized motor, its input current is increased to $I=2$ A, value at which the sample prototype induces the target output torque of 1.2 Nm. Using this current value, the losses of the motor calculated in Motor-CAD at 563 min^{-1} are as given below:

- Copper losses: $P_{Cu}=79,6 \text{ W}$
- Stator yoke core losses: $P_{yoke}=0,4856 \text{ W}$
- Stator tooth core losses: $P_{tooth}=0,378 \text{ W}$
- Rotor core losses: $P_{rotor}=0,021 \text{ W}$

The copper losses do not vary with speed. They only vary with temperature, and the temperature at which the copper losses are calculated is defined in the settings. However, the core losses are directly proportional to the rotational speed of the motor, and at any speed they are calculated with the following equation [42].

$$P_{speed}=P_{input} \times \left(\frac{\text{Shaft Speed}}{\text{Reference speed}} \right)^{1.5} \quad (5.12)$$

The reference speed is actually the washing mode speed of the motor. Since the shaft and the reference speed are equal in this thermal model, the iron losses will remain the same as the entered values. The detailed window showing the losses settings is given in Figure 5.5. The change of the copper losses with temperature is selected to take into account the change of the winding resistance as the temperature values increase. The copper losses are inserted for 20°C.

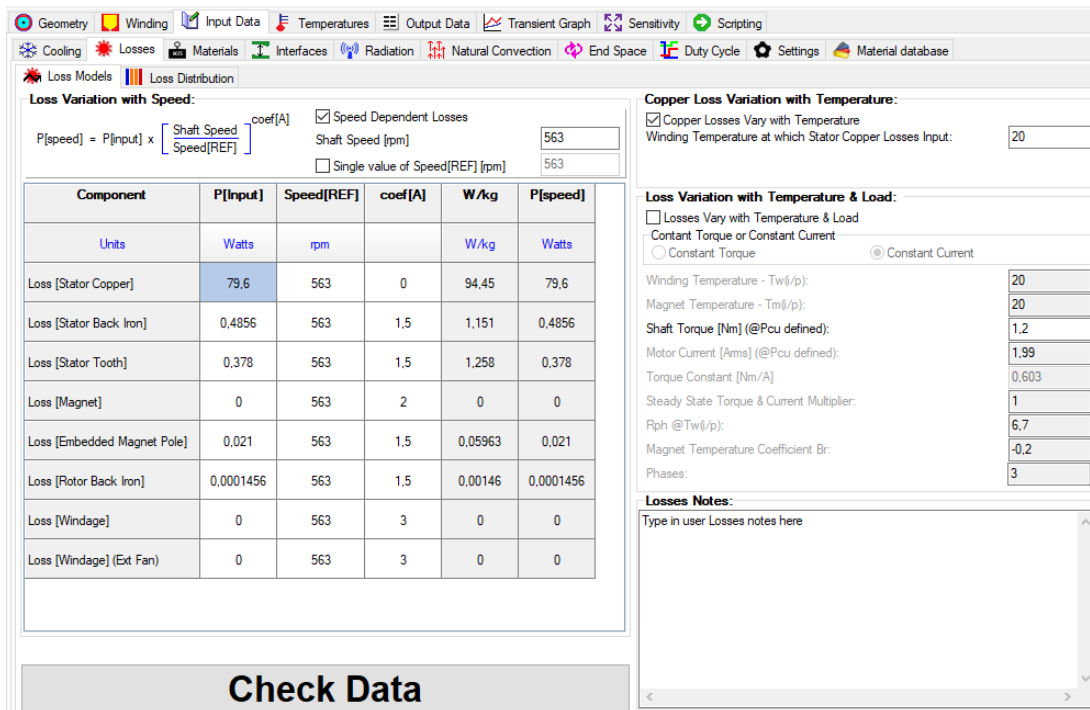


Figure 5.5 : Active power loss settings.

5.2.4 Material settings

In the performed thermal analysis, the material for each part of the motor is defined as show in the settings window in Figure 5.6. Motor-CAD has registered in its database the properties of each material, therefore is enough only to select the type of the material for each corresponding part of the motor. The most important parts and their material are given as follows:

- Stator and rotor: M700 ferromagnetic steel
- Front and rear endcaps: aluminum
- Stator winding: Copper
- Shaft: Steel
- Magnet: Y30H-2 (Ferrite magnet)

Component	Material from Database	Thermal Conductivity	Specific Heat	Density	Weight Internal	Weight Multiplier	Weight Addition	Weight Total
Units		W/m/C	J/kg/C	kg/m3	kg		kg	kg
Stator Lam (Outer)	cogentM700	30	460	7650	0,2574	1	0	0,2574
Inter Lam (Outer)	cogentM700	30	460	7650	0,00796	1	0	0,00796
Endcap [Front]	Aluminium (Alloy 195 Cast)	168	833	2790	0,2239	1	0	0,2239
Endcap [Rear]	Aluminium (Alloy 195 Cast)	168	833	2790	0,2239	1	0	0,2239
Stator Lam (Back Iron)	cogentM700	30	460	7650	0,4219	1	0	0,4219
Inter Lam (Back Iron)		0,02723	1007	1,127	1,922E-06	1	0	1,922E-06
Stator Lam (Tooth)	cogentM700	30	460	7650	0,3006	1	0	0,3006
Inter Lam (Tooth)		0,02723	1007	1,127	1,369E-06	1	0	1,369E-06
Stator Lamination					0,9878			0,9878
Winding [Active]	Copper (Pure)	401	385	8933	0,2026	1	0	0,2026
Winding [Front End-Wdg]	Copper (Pure)	401	385	8933	0,3201	1	0	0,3201
Winding [Rear End-Wdg]	Copper (Pure)	401	385	8933	0,3201	1	0	0,3201
Winding [Total]					0,8428			0,8428
Wire Ins. [Active]		0,21	1000	1400	0,006865	1	0	0,006865
Wire Ins. [Front End-Wdg]		0,21	1000	1400	0,008961	1	0	0,008961
Wire Ins. [Rear End-Wdg]		0,21	1000	1400	0,008961	1	0	0,008961
Wire Ins. [Total]					0,02479			0,02479
Impreg. [Active]		0,2	1700	1400	0	1	0	0
Impreg. [Front End-Wdg.]		0,2	1700	1400	0	1	0	0
Impreg. [Rear End-Wdg.]		0,2	1700	1400	0	1	0	0
Impreg. [Total]					0			0
Slot Liner		0,21	1000	700	0	1	0	0
Magnet	Y30H-2 femite	2,9	800	5000	0,1425	1	0	0,1425
Inter Magnet Gap		30	460	7650	0,1116	1	0	0,1116
Rotor Lam (Back Iron)	cogentM700	30	460	7650	0,09969	1	0	0,09969
Rot Inter Lam (Back Iron)		0,02723	1007	1,127	4,542E-07	1	0	4,542E-07
IPM Magnet Pole	cogentM700	30	460	7650	0,3522	1	0	0,3522
Rotor Lamination [Total]					0,5634			0,5634
Shaft [Active]	Mild Steel	25	450	7800	0,04499	1	0	0,04499
Shaft [Front]	Mild Steel	25	450	7800	0,09702	1	0	0,09702
Shaft [Rear]	Mild Steel	25	450	7800	0,05484	1	0	0,05484
Shaft [Total]					0,1969			0,1969
Bearing [Front]		30	460	7800	0,132	1	0	0,132
Bearing [Rear]		30	460	7800	0,132	1	0	0,132
Motor Weight [Total]					3,47			3,47

Figure 5.6 : Material settings.

5.2.5 Interface settings

Between any two different parts of the motor, there is a remaining interface that affects the heat flow negatively. The empty space remaining as a result of imperfections between the surfaces of motor parts decreases the heat flow and causes the temperature of inner parts of the motor to take higher values. The interfaces in this model are all chosen as average quality interfaces, and the completed and detailed interface settings of the sample prototype are given in Figure 5.7.

Component	Gap	Details	Resistance @T=100,0C	Conductance @T=100,0C
Units	mm		m2.C/W	W/m2/C
Stator Lam - Endcap[F]	0,005	Metal-Metal - Average surface Contact	0,0001577	6343
Stator Lam - Endcap[R]	0,005	Metal-Metal - Average surface Contact (0,005)	0,0001577	6343
Magnet - Rotor Lam	0,005	Metal-Metal - Average surface Contact (0,005)	0,0001577	6343
Rotor Lam - Shaft	0,005	Metal-Metal - Average surface Contact	0,0001577	6343
Bearing Effective Gap [F]	0,4	High Effective Gap [Torino Testing]	0,01261	79,29
Bearing Effective Gap [R]	0,4	High Effective Gap [Torino Testing]	0,01261	79,29
Bearing - Endcap [F]	0,0112	Stainless-Stainless - Medium surface Contact	0,0003531	2832
Bearing - Endcap [R]	0,0073	Stainless-Aluminium - Medium surface Contact	0,0002302	4344
Bearing - Shaft [F]	0,0112	Stainless-Stainless - Medium surface Contact	0,0003531	2832
Bearing - Shaft [R]	0,0112	Stainless-Stainless - Medium surface Contact	0,0003531	2832

Figure 5.7 : Interface settings.

5.2.6 Radiation settings

The heat transfers between the inner parts of the motor due to radiation is neglected in our model, therefore radiation is effective only between the motor and the outer medium. The motor parts that have the emissivity factor defined are those that are in contact with the outer medium, including stator outer surface, end and front endcaps. For all these parts, an approximate emissivity value equal to that of grey color is inserted as 0.9 [42]. The detailed settings corresponding to radiation are given in Figure 5.8.

Component	Emissivity	View Factor	hr @dT=100,0C	Area	Rt @dT=100,0C
Units			W/m2/C	mm ²	C/W
Housing [Active]	0,9	1	8,791	1,186E04	9,589
Endcap [Front] - Radial Area	0,9	1	8,791	1,446E04	7,868
Endcap [Front] - Axial Area	0,9	1	8,791	1,076E04	10,58
Endcap [Rear] - Radial Area	0,9	1	8,791	1,446E04	7,868
Endcap [Rear] - Axial Area	0,9	1	8,791	1,094E04	10,4

Figure 5.8 : Radiation settings.

5.2.7 Natural convection settings

The majority of the heat transfer between the electric motors without fans and the outer medium occurs through natural convection. Having no forced air circulation, natural convection transfers heat only by the natural motion of the air around the motor. In the natural convection settings in Motor-CAD include a dT temperature change is inserted for the software to calculate the h_{nc} heat transfer factors and thermal resistances. Any dT value can be inserted, however the software uses the real time dT values of the model for calculating the thermal resistances and the heat transfer factors during the thermal analysis. The detailed natural convection settings for $dT=10$ are given in Figure 5.9 below.

Component	Input h?	Convection Correlation	h[input] or h[adjust]	h _{nc} @ dT=10.0C	Area	R _t @ dT=10.0C
Units			W/m ² /C	W/m ² /C	mm ²	C/W
Housing [Active]	<input type="checkbox"/>	Horizontal Cylinder	1	4,049	1,186E04	20,82
Endcap [Front] - Radial Area	<input type="checkbox"/>	Horizontal Cylinder	1	4,049	1,446E04	17,08
Endcap [Front] - Axial Area	<input type="checkbox"/>	Vertical Flat Plate	1	4,55	1,045E04	21,04
Endcap [Rear] - Radial Area	<input type="checkbox"/>	Horizontal Cylinder	1	4,049	1,446E04	17,08
Endcap [Rear] - Axial Area	<input type="checkbox"/>	Vertical Flat Plate	1	4,55	1,094E04	20,1

Figure 5.9 : Natural convection settings.

5.2.8 Front and rear end-space

In the front and rear end-spaces of the motor, air flow occurs due to the rotation of the rotor. The parameter that affects the air motion in end-space is the type of the rotor which is defined in end-space settings. In this analysis, the type of the rotor is selected to be normal one, with a medium end-space velocity multiplier. According to the rotor type, the software calculates a reference air speed on the end-spaces, and using this reference speed, for all the motor parts separately that are in contact with the end-space air, it calculates the air speed flowing around them. To calculate the air speed around each part in the end-spaces, the software uses k_1 , k_2 and k_3 constants. Using these constants, the heat transfer factor in the end-space (h), is calculated using the reference air speed with the following Equation 5.13.

$$h = k_1 \times [1 + k_2 \times vel \times k_3] \quad (5.13)$$

In this equation, “*vel*” is the reference speed in the end-space. This reference speed is only used for the stationary parts of the motor. The air speed around the rotating parts is calculated according to their rotational velocity and their average distance(radius) from the shaft center.

Different researches give different values for the, k_1 , k_2 and k_3 constants. However, all researches give similar results while implementing the thermal circuit of the motor. In the Scuber’s researches, the constants used for induction motor thermal analysis are $k_1=15$, $k_2=0.4$ and $k_3=0.9$ [42]. Because induction motor end-space is similar to the synchronous reluctance motor end-space, the same constants are used in this model’s thermal analysis also. The endcaps are completely closed, therefore endcap ventilation is selected as closed, meaning that there is no air exchange between the outer medium and the motor’s end-space. Details for the end-space settings are given in Figure 5.10 below.

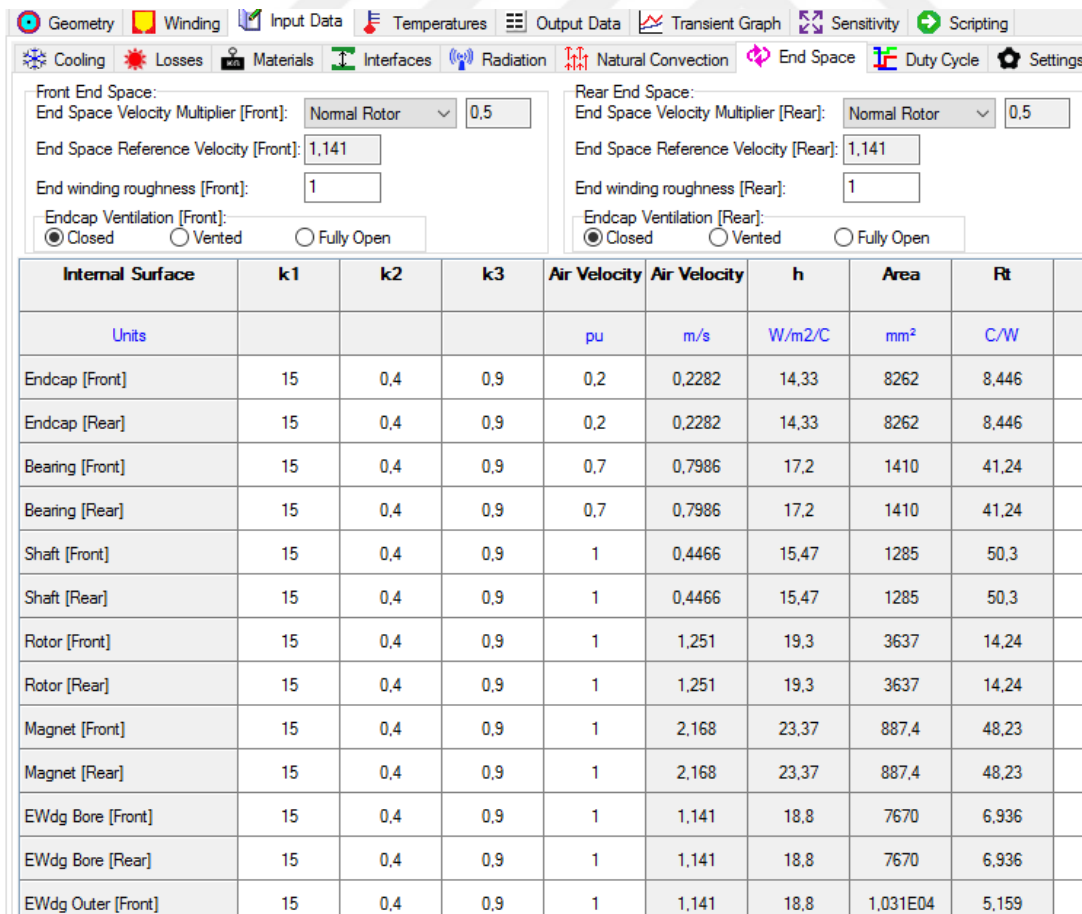


Figure 5.10 : Front and rear end-space settings.

5.2.9 Washing mode thermal results of the sample prototype

After the settings related to the geometry and the thermal model are finished, the software implements the lumped thermal circuit corresponding to the sample prototype, giving the temperature results at each node of the motor. As it was expected, the maximum thermal stress occurs in the stator windings. Referring to the thermal circuit, radial and axial view of the motor, it can be concluded that the maximum temperature value seen in the stator is 156.8°C , the maximum winding temperature is 169.6°C whereas the maximum magnet temperature is 154.9°C . Figure 5.11 gives the radial view of the motor geometry and the distribution of the temperature values. The thermal circuit implemented by the software including all the node temperature of the motor is given in Figure 5.12. In the thermal circuit implemented analytically, the flow of the heat from the winding nodes where is generated to the nodes representing the outer medium is realized through the thermal resistances between nodes. The key symbols used in the lumped thermal circuit are thermal resistances of specific motor parts, interface resistances, convection and radiation resistances, power loss sources and node labels. For each symbol, the resistance, power flow and the temperature drop values are observable.

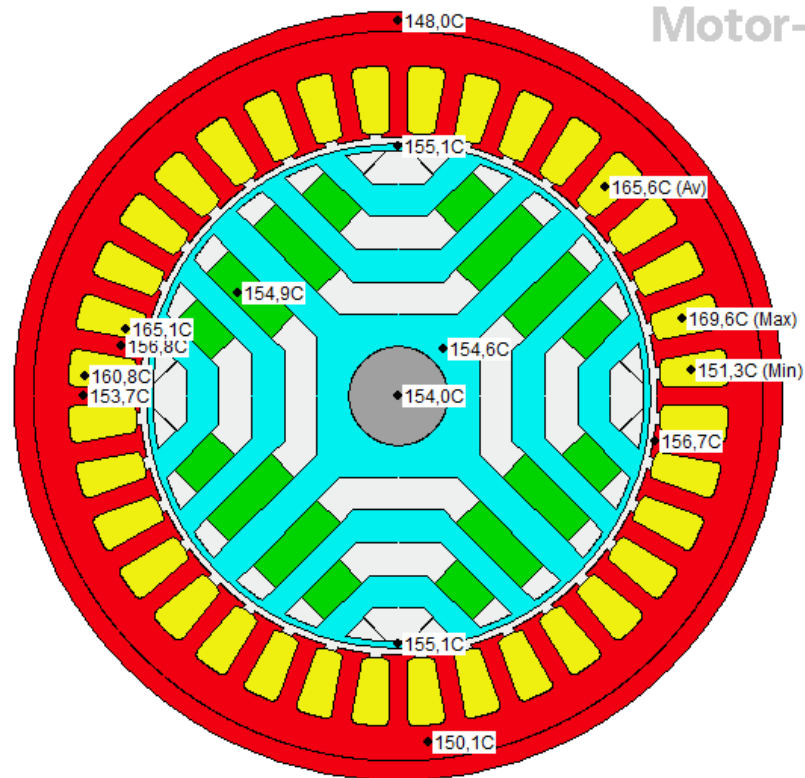


Figure 5.11 : Radial view of analytical temperature results of sample prototype.

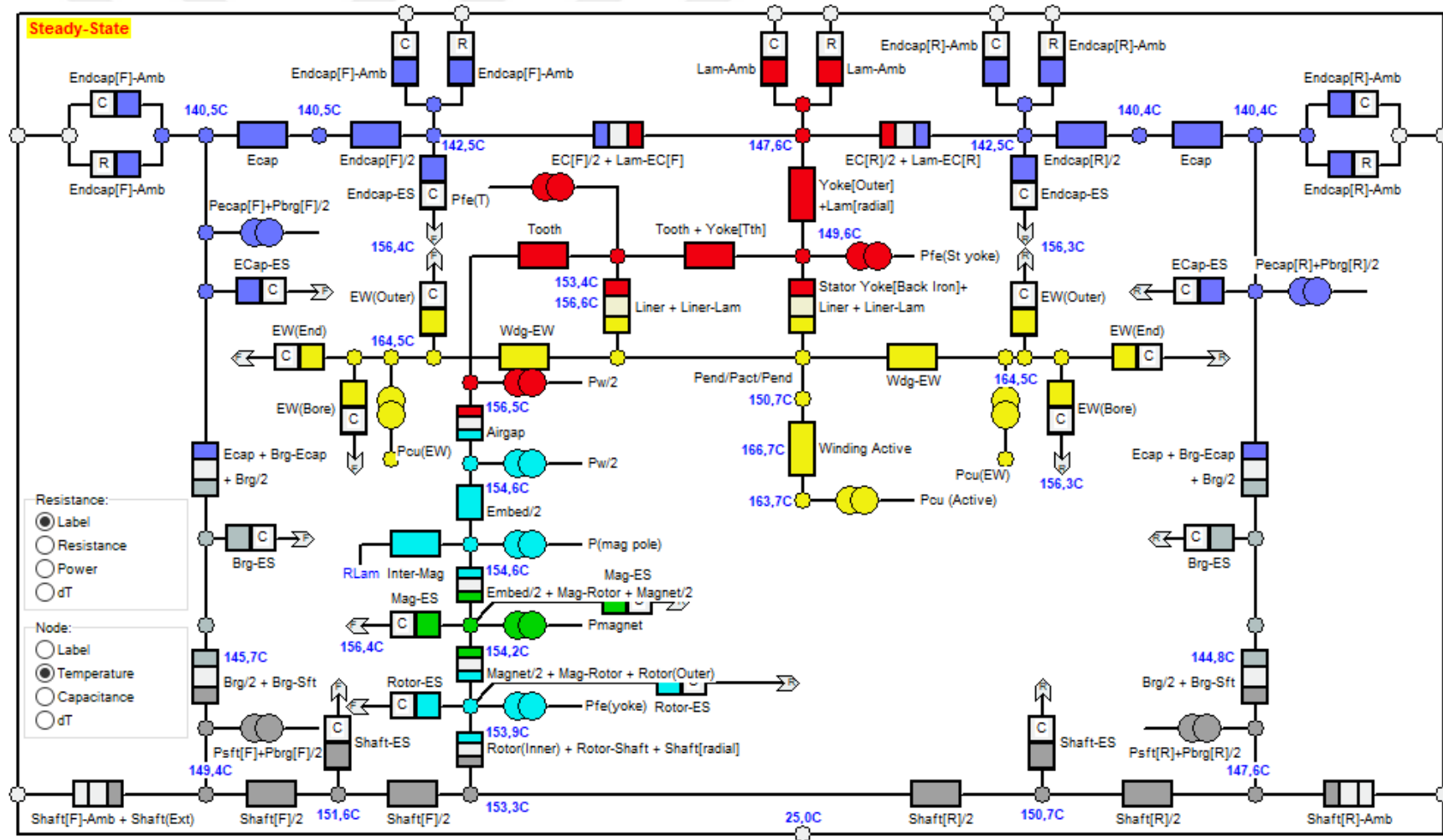


Figure 5.12 : Lumped thermal circuit of the sample prototype.

The axial view of the temperatures calculated analytically is given in Figure 5.13.

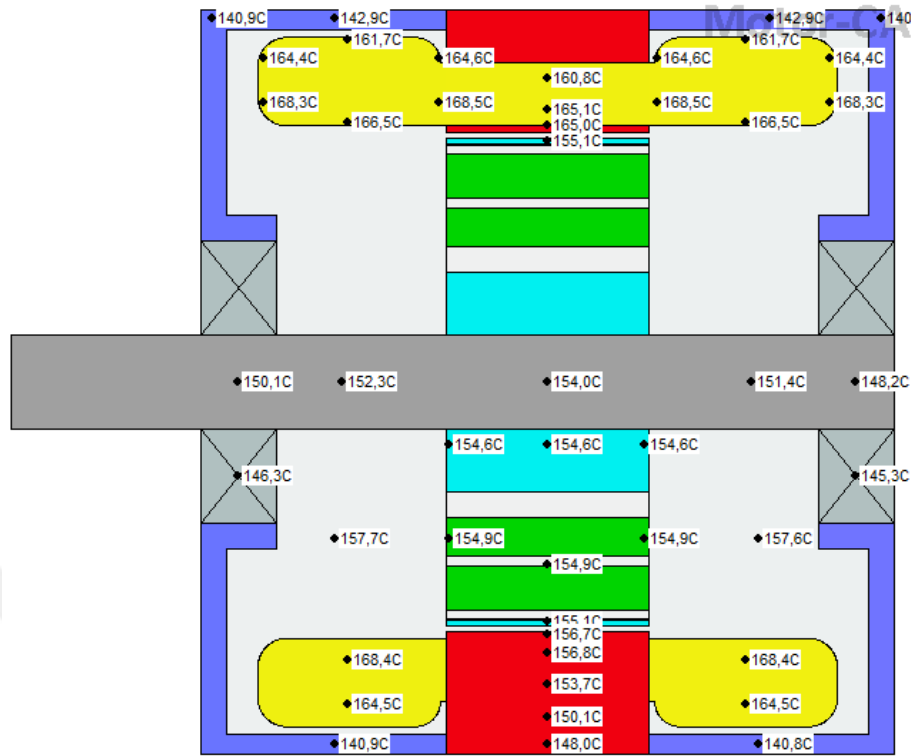


Figure 5.13 : Axial view of analytical temperature results of sample prototype.

To make sure that the analytical model of the sample prototype is accurate, thermal analysis is performed using FEM also. The slot temperature distribution calculated using FEM for the sample prototype is given in Figure 5.14.

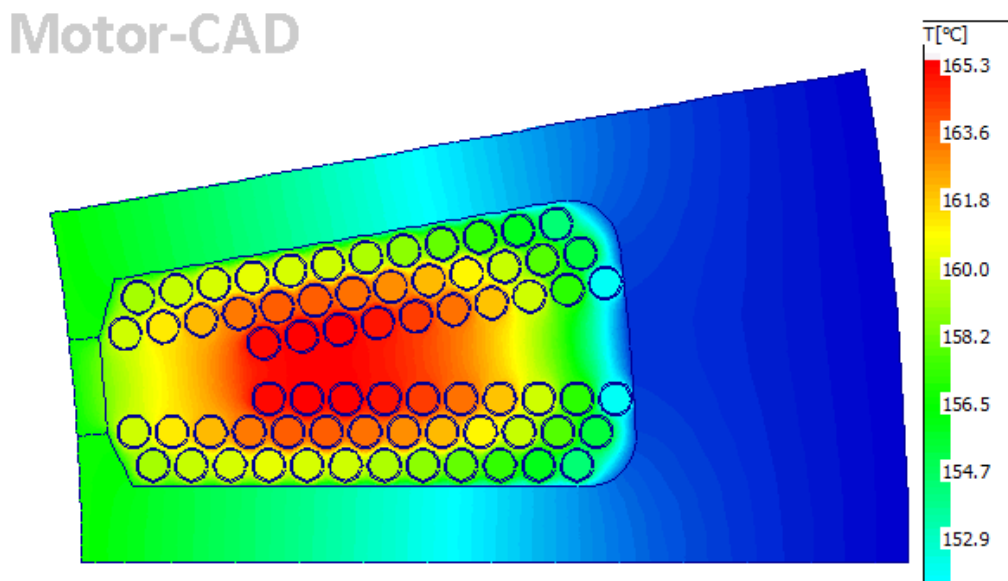


Figure 5.14 : Slot temperature distribution using FEM.

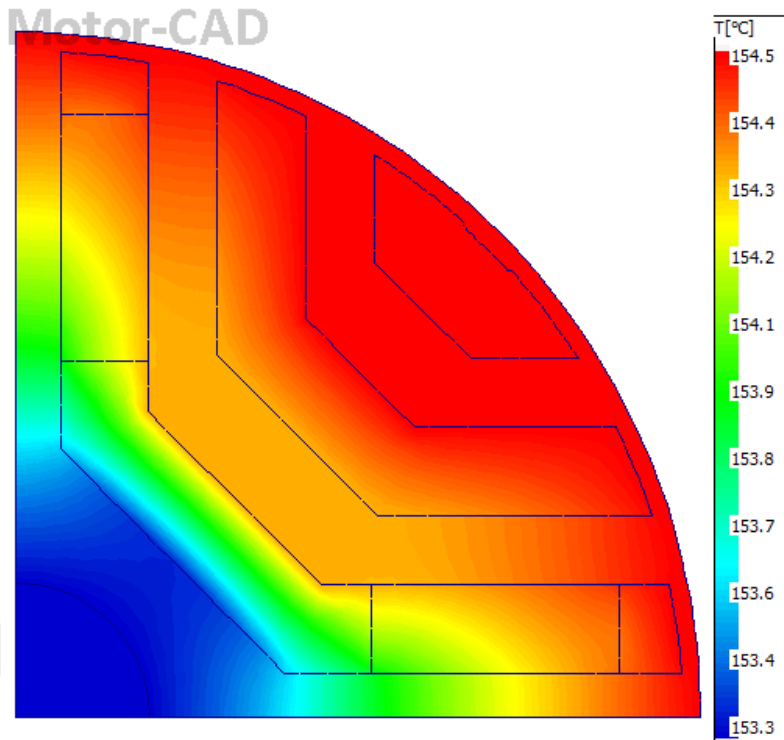


Figure 5.15 : Rotor temperature distribution using FEM.

The rotor and axial temperature distributions calculated via FEM are given in Figure 5.15 and Figure 5.16, respectively. FEM results are fairly close to the analytical ones, meaning that the analytical model of the sample prototype is accurate.

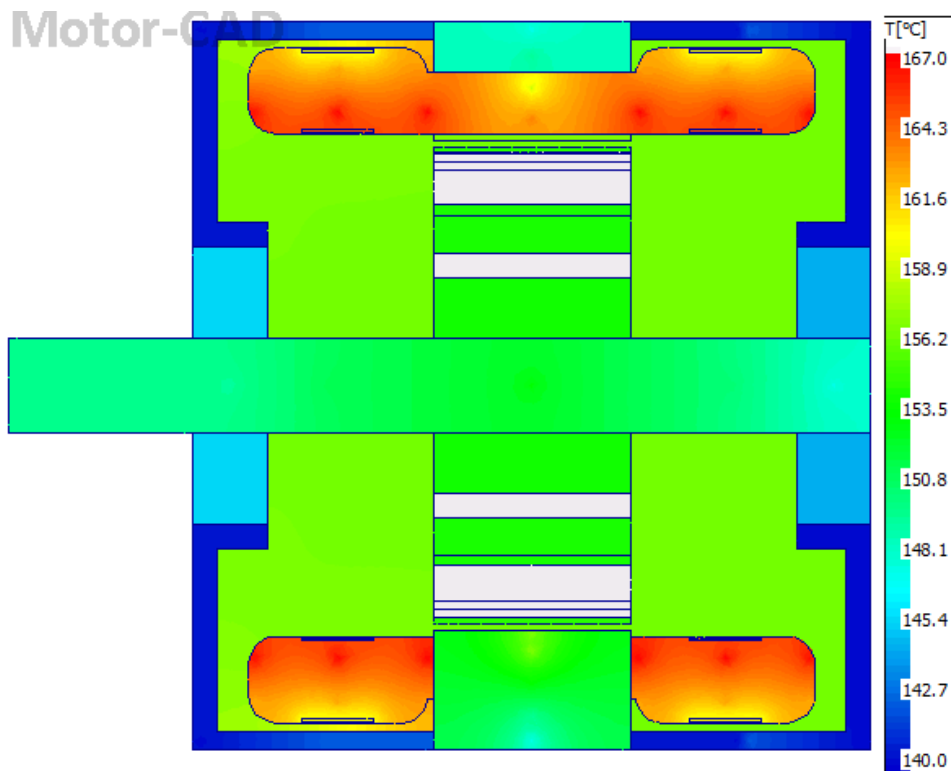


Figure 5.16 : Axial temperature distribution using FEM.

5.2.9.1 Spinning mode thermal results of the sample prototype

The electric motors used in washing machines operate at spinning mode for short periods of time, generally around 3 minutes. Depending on the motor and the washing machine type, the spinning mode speed and time may be different. In this thesis, the spinning mode speed of the sample prototype is 13000 min^{-1} and the average spinning time period is taken as 3 minutes. Since the sample prototype's input current and the core losses are different at spinning mode operation, they are calculated in Motor-LAB module and given as shown below:

- Copper losses: $P_{Cu}=77.97 \text{ W}$
- Stator yoke core losses: $P_{yoke}=15.87 \text{ W}$
- Stator tooth core losses: $P_{tooth}=12.41 \text{ W}$
- Rotor core losses: $P_{rotor}=0.577 \text{ W}$

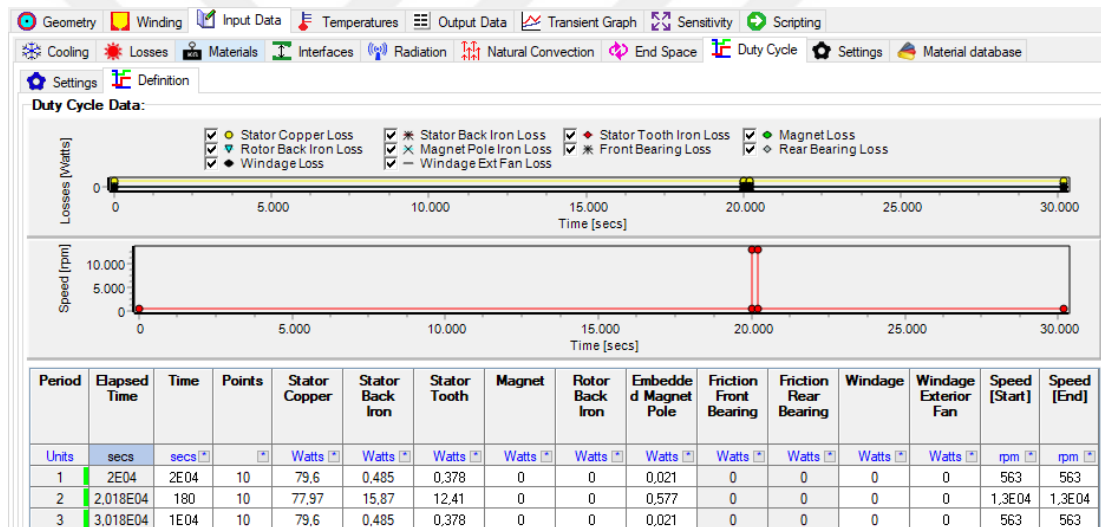


Figure 5.17 : Spinning mode transient settings of the sample prototype.

In the transient settings shown in Figure 5.17, the losses of the model are changed for 3 minutes to calculate the spinning mode temperatures. Assuming that the model operates initially at washing mode long enough so that it reaches steady-state washing mode temperatures, the losses of the motor are changed accordingly to their spinning mode values for 180 seconds, simulating the motor's change of operations. The transient change of the temperatures is given graphically in Figure 5.18. During the spinning mode operation, the maximum winding temperature reaches 170°C at the end of 3-minute period. To observe the temperature's drop to the previously calculated washing mode values as the motor's speed decreases again, the speed and the losses of the model are decreased accordingly for another period of 10^4 seconds.

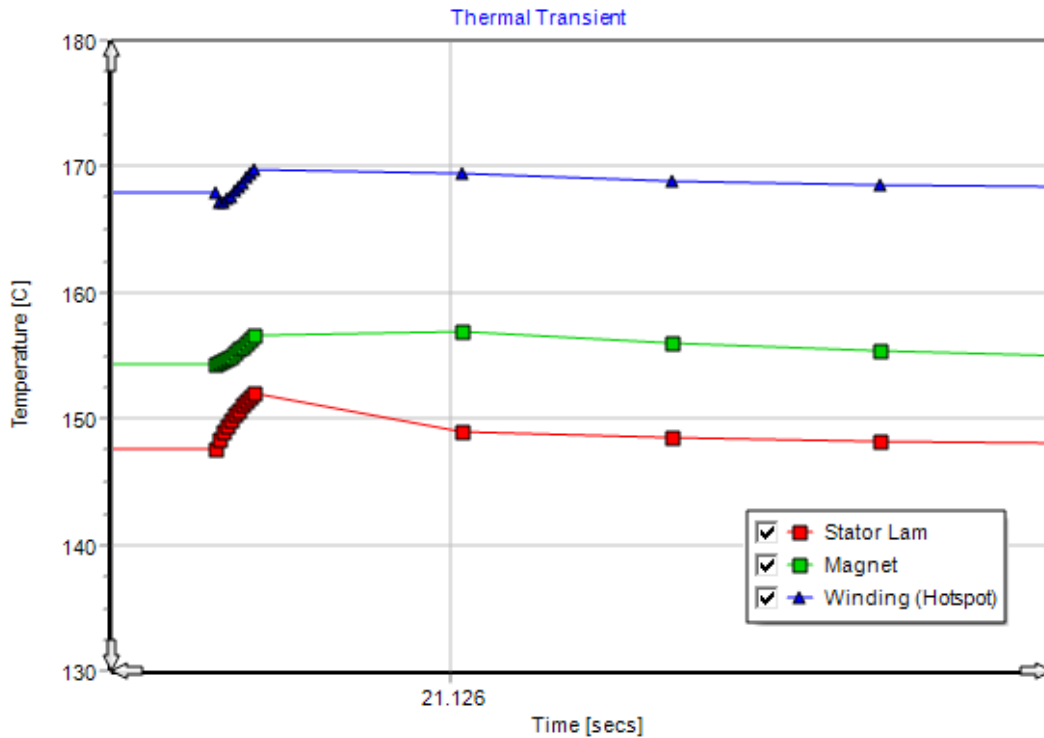


Figure 5.18 : Transient temperature results of the sample prototype.

As a results, looking at the maximum values of temperatures during washing and spinning mode operations, the necessary thermal class of the winding insulation for this model would be H class that can withstand temperatures up to 180°C [43].

5.3 Thermal Analysis of the Optimized Prototype

The optimized prototype is modelled similarly as the sample one in Motor-CAD. The differences between the models are the geometry and the windings. Both models are cooled down only by natural convection and radiation. The losses of the optimized model are calculated using Motor-LAB module as given below:

- Copper losses: $P_{Cu}=47.24$ W
- Stator yoke core losses: $P_{yoke}=0.459$ W
- Stator tooth core losses: $P_{tooth}=0.606$ W
- Rotor core losses: $P_{rotor}=0.018$ W

The loss settings window of the optimized prototype is given in Figure 5.19. The copper and losses are entered accordingly and the change of the copper losses with temperature is activated so that the model encounters the phase resistance change as the winding temperature increases.

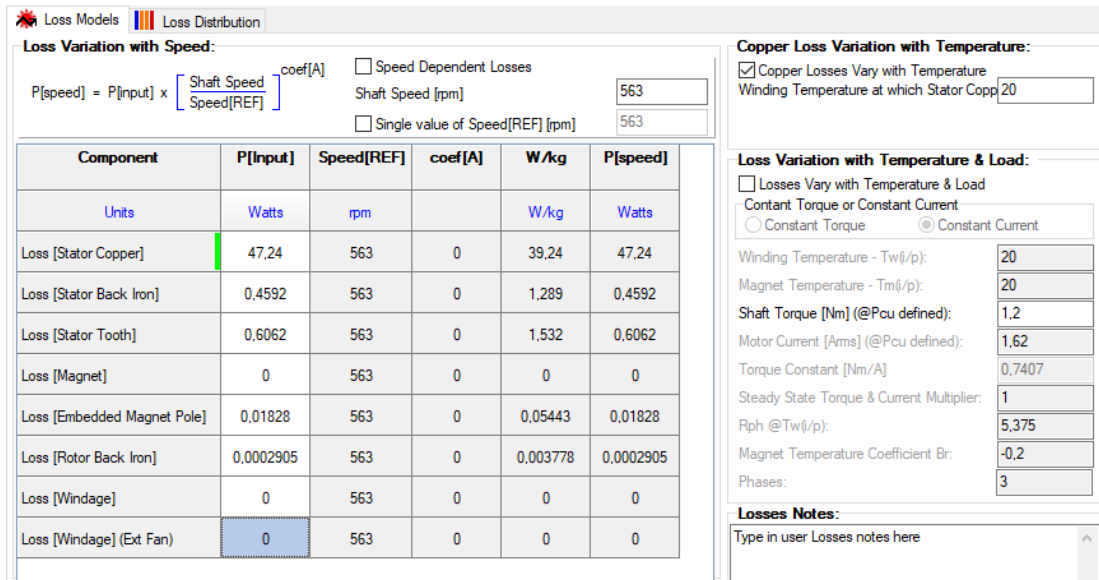


Figure 5.19 : Loss settings of the optimized prototype.

5.3.1 Washing mode thermal circuit and thermal results

After the settings related to the geometry and thermal model are finished, the software implements the thermal circuit corresponding to the optimized prototype giving the temperature results at each node of the motor. Figure 5.20 gives the radial view of the geometry temperature values calculated analytically for the optimized prototype.

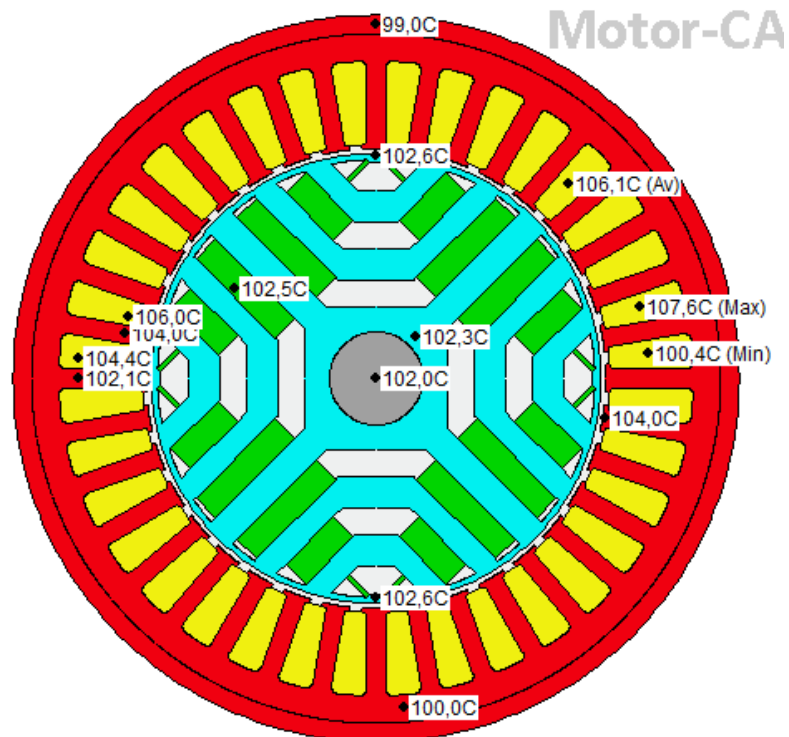


Figure 5.20 : Radial view of the temperature results of optimized prototype.

The thermal circuit implemented by the software including all the node temperature of the optimized prototype is given in Figure 5.21. In the thermal circuit implemented analytically, the flow of the heat from the winding nodes where is generated to the nodes representing the outer medium is realized through the thermal resistances between the nodes. The axial view of the temperature values calculated analytically is given in Figure 5.22.

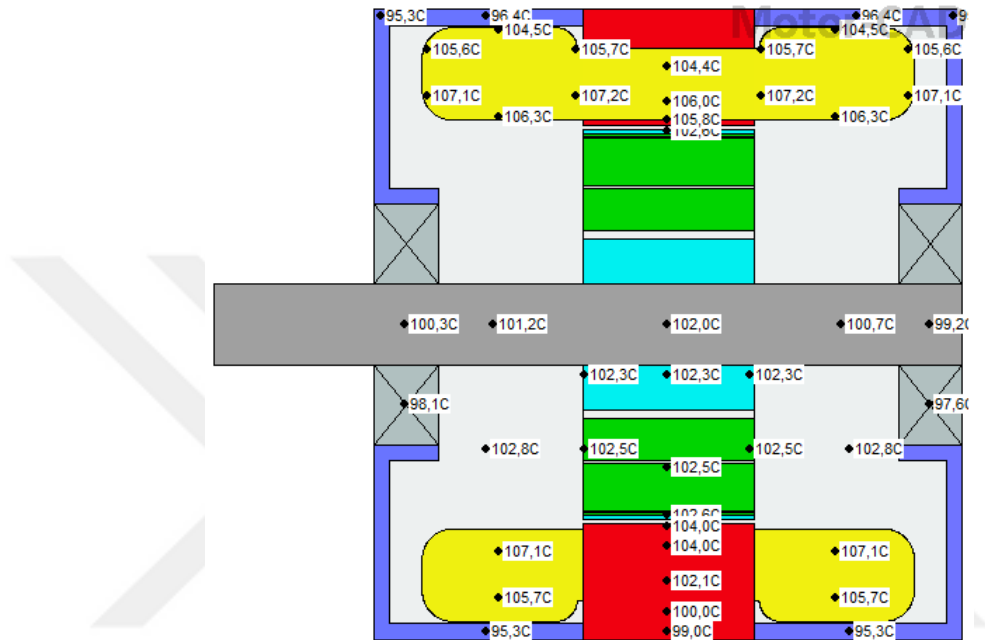


Figure 5.22 : Axial view of analytical temperature results of optimized prototype.

To check if the analytical model of the sample prototype is accurate, thermal analysis is performed using FEM also. The slot temperature distribution calculated using FEM for the sample prototype is given in Figure 5.23.

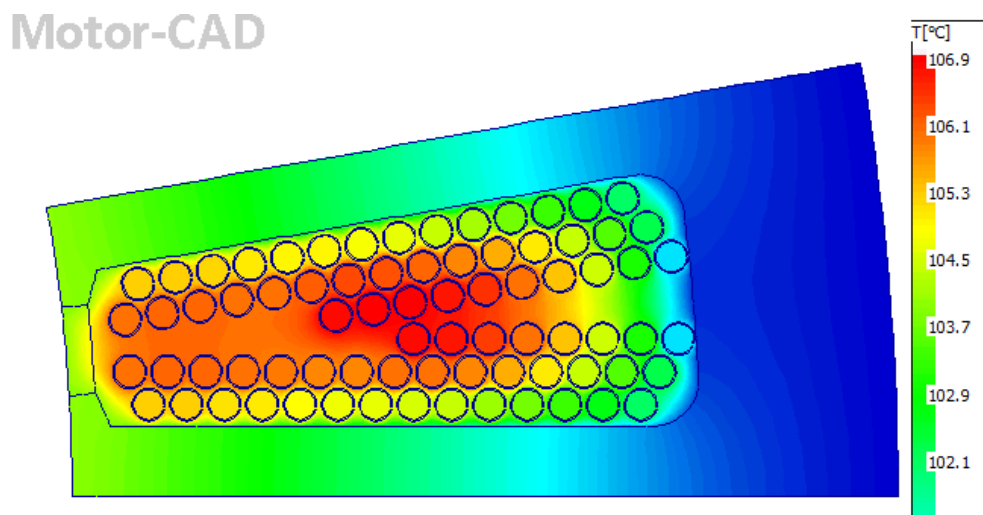


Figure 5.23 : Slot temperature distribution using FEM.

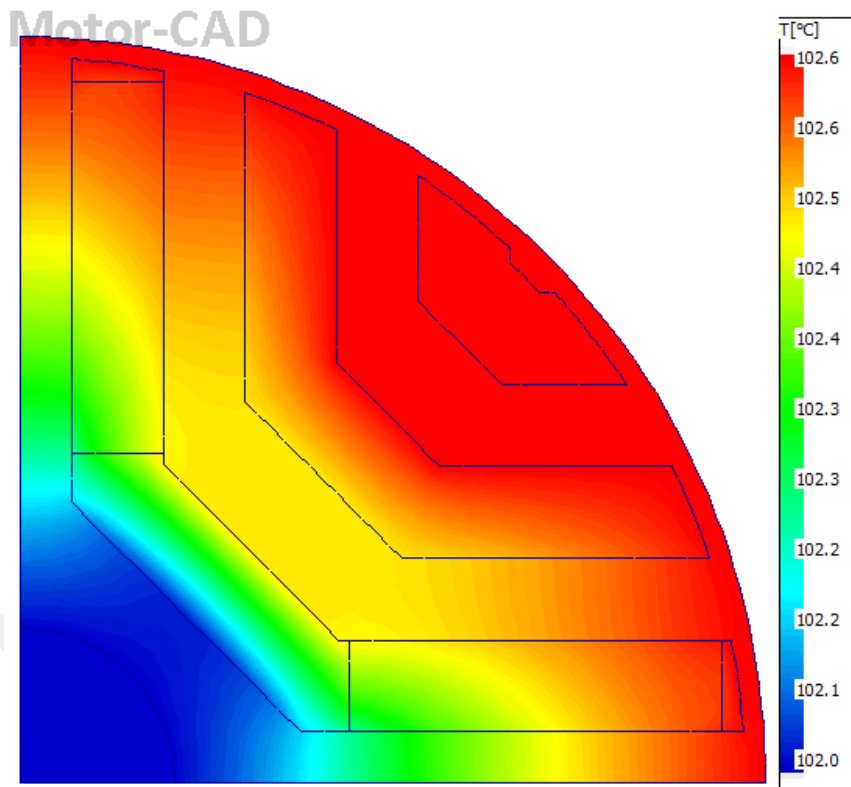


Figure 5.24 : Rotor temperature distribution using FEM.

The rotor and axial temperature distributions calculated via FEM are given in Figure 5.24 and Figure 5.25, respectively. FEM results are fairly close to the analytical ones, meaning that the analytical model of the sample prototype is accurate.

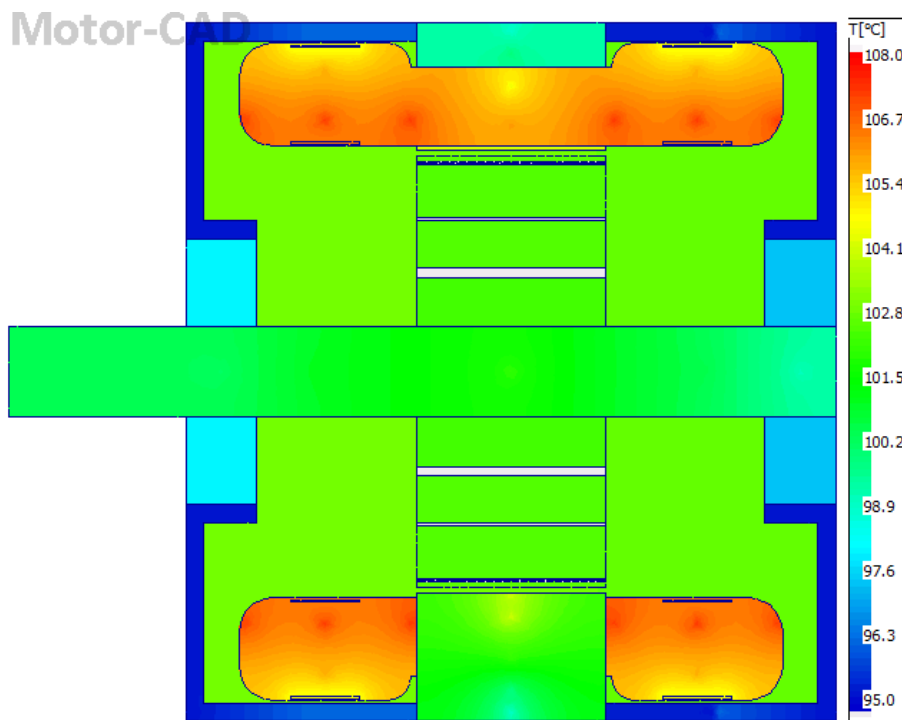


Figure 5.25 : Axial temperature distribution using FEM.

5.3.2 Spinning mode thermal analysis

The spinning mode losses of the optimized prototype are calculated in Motor-LAB module as below:

- Copper losses: $P_{Cu}=78.31$ W
- Stator yoke core losses: $P_{yoke}=23.83$ W
- Stator tooth core losses: $P_{tooth}=27.19$ W
- Rotor core losses: $P_{rotor}=0.777$ W

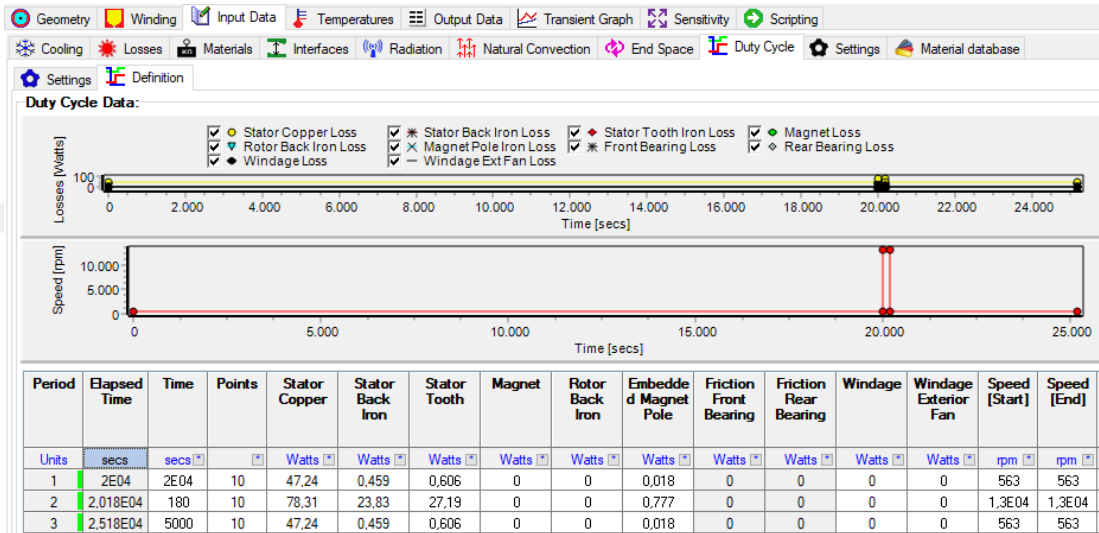


Figure 5.26 : Spinning mode transient settings.

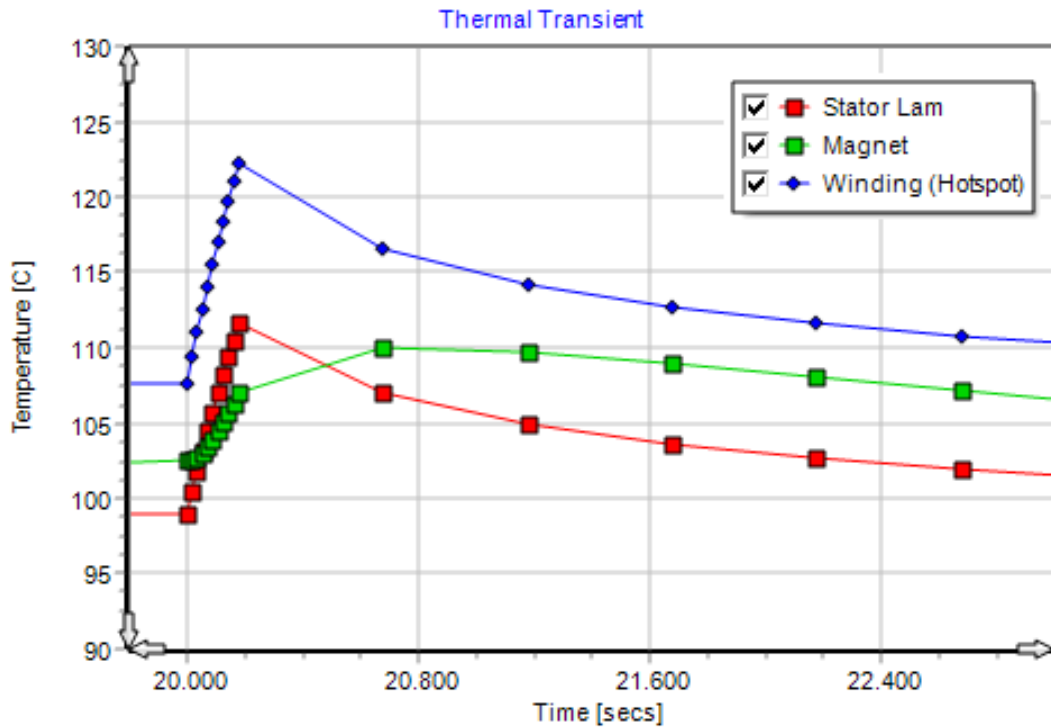


Figure 5.27 : Transient temperature results of the optimized prototype.

In the transient settings shown in Figure 5.26, the losses of the model are changed for 3 minutes to calculate the spinning mode temperatures. Similar to the sample prototype, the model operates initially at washing mode, and then for 180 sec changes its operation to spinning mode. During the spinning mode period the losses of the model are changed accordingly. The transient change of the temperatures is given in Figure 5.27. During the spinning mode operation, the maximum winding temperature reaches 122°C at the end of 3-minute period. After the speed is decreased again to washing mode speed of 563 min⁻¹, losses and temperatures drop again to the previously calculated washing mode values.

5.4 Comparison of Thermal Analysis Results

The final results of the thermal analysis are given in Table 5.1. Looking at the maximum values of winding temperatures of both motors, it is clearly seen that the sample motor undergoes larger thermal stresses than the optimized motor. Its insulation class of the winding is required to be H class that can withstand temperatures up to 180°C [43]. On the other hand, the optimized motor has much lower losses and it undergoes lower thermal stresses during washing and spinning mode operation. Insulation class B, withstanding temperatures up to 130°C, is enough for this motor [43]. Considering the demagnetization of the ferrite magnet due to temperature change, the remanent magnetic field of these magnets decreases by 0.2% for each degree Celsius temperature increase [44].

Table 5.1 : Thermal analysis final results.

Model	Sample Motor	Optimized Motor
Max. Winding Temp. [°C]	164.2	122
Insulation Class	H	B
Magnet Temp. [°C]	153.6	102.5
Ferrite Br. [T]	0.294	0.334
Max. Torque Capability [Nm]	1.11	1.18

Having a remanent magnetic flux density of $B_r=0.4T$ at 20°C, at steady state temperatures obtained above, the B_r values of the sample and optimized prototype are calculated in Motor-CAD to be 0.294T and 0.334T. This decrease of the remanent magnetic flux density decreases the capability of the prototypes to induce torque at steady-state temperatures. The maximum torque capabilities of the sample and optimized prototype, calculated in Motor-CAD are also given in Table 5.1.

6. MECHANICAL STRESS ANALYSIS

Mechanical analysis of electric motors is another important issue to be considered during their designs, especially for those that operate at high speed values. Electric motors that are used in washing machines, at spinning mode operation get speed values up to 13000 min^{-1} . At such high speed values, the mechanical stresses resulting from the centrifugal force acting on the parts of the rotor cause deformations. If these deformations are not limited, they may lead to the total failure and breakage of the rotor. In order to determine whether the motor's mechanical integrity will be sustained, in this section the stress analysis of the sample and optimized motors are simulated and analyzed in ANSYS' Static Structural module. The simulations are performed separately for washing (563 min^{-1}) and spinning mode (13000 min^{-1}) for both models. The mechanical characteristics of the materials composing the rotor are given in Table 6.1.

Table 6.1 : Mechanical characteristics of rotor materials.

Parameters	M700	Ferrite
Mass Density [kg/m ³]	7800	5000
Young Modulus [GPa]	210	180
Poisson Coefficient	0.31	0.28
Tensile Stress Limit [MPa]	405	34

6.1 Spinning Mode Test of the Sample Prototype

The mechanical test during spinning mode is performed to see the total deformation and the equivalent stress on the rotor under constant rotational speed of 13000 min^{-1} . The centrifugal force acting on the flux segments at high speed operations deforms the rotor ribs as the segments are pushed outwards the center of the rotor. After the mechanical properties are defined for the sample prototype, the model is solved for the equivalent stress, equivalent elastic strain and the total deformation. The equivalent stress simulation results are given in Figure 6.1, the equivalent elastic strain simulation results are given in Figure 6.2 and the total deformation simulation results are given in Figure 6.3.

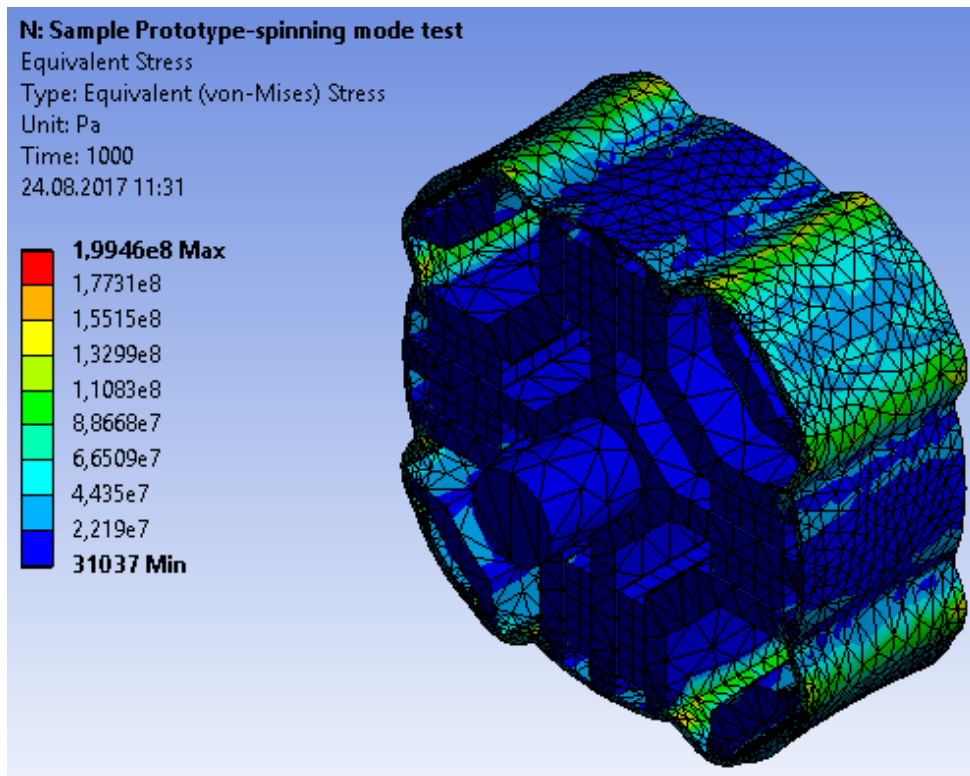


Figure 6.1 : Equivalent stress results of the sample prototype at 13000 min⁻¹.

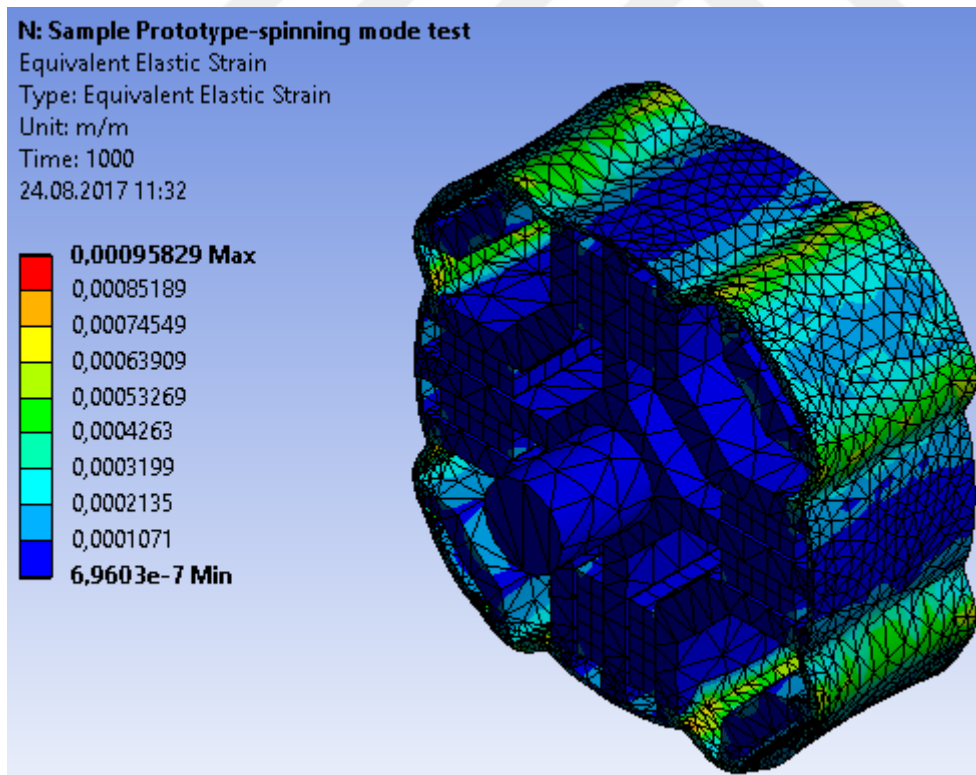


Figure 6.2 : Equivalent elastic strain results of the sample prototype at 13000 min⁻¹.

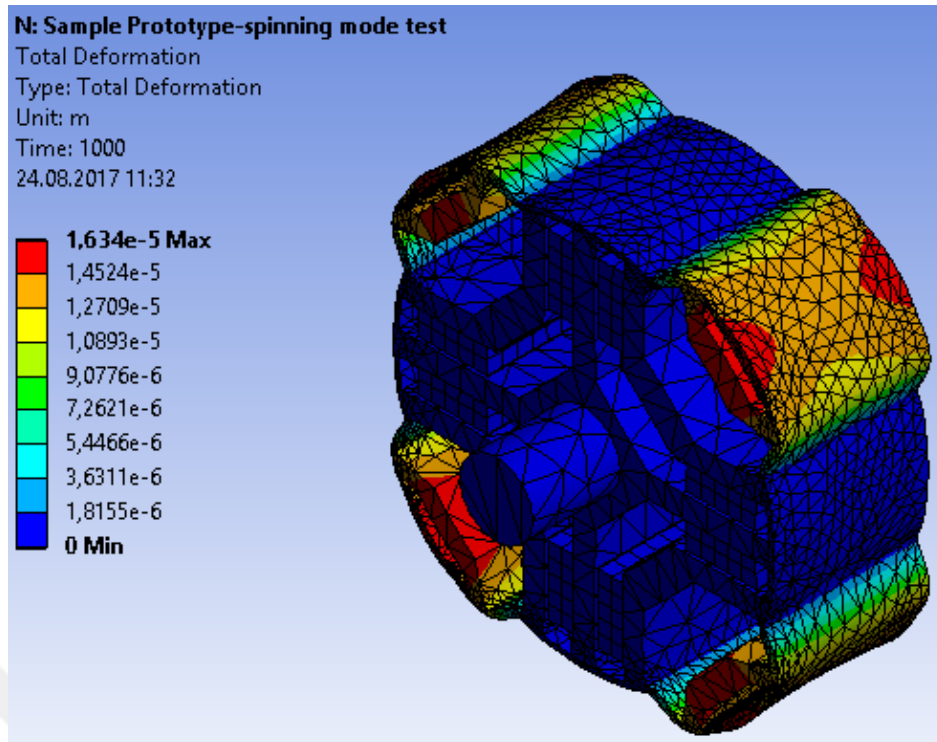


Figure 6.3 : Total deformation results of sample prototype at 13000 min⁻¹.

6.2 Washing Mode Test of the Sample Prototype

For the washing mode operation, the mechanical stress analysis of the sample is done to observe the total torsion on the rotor under constant load of 1.2 Nm.

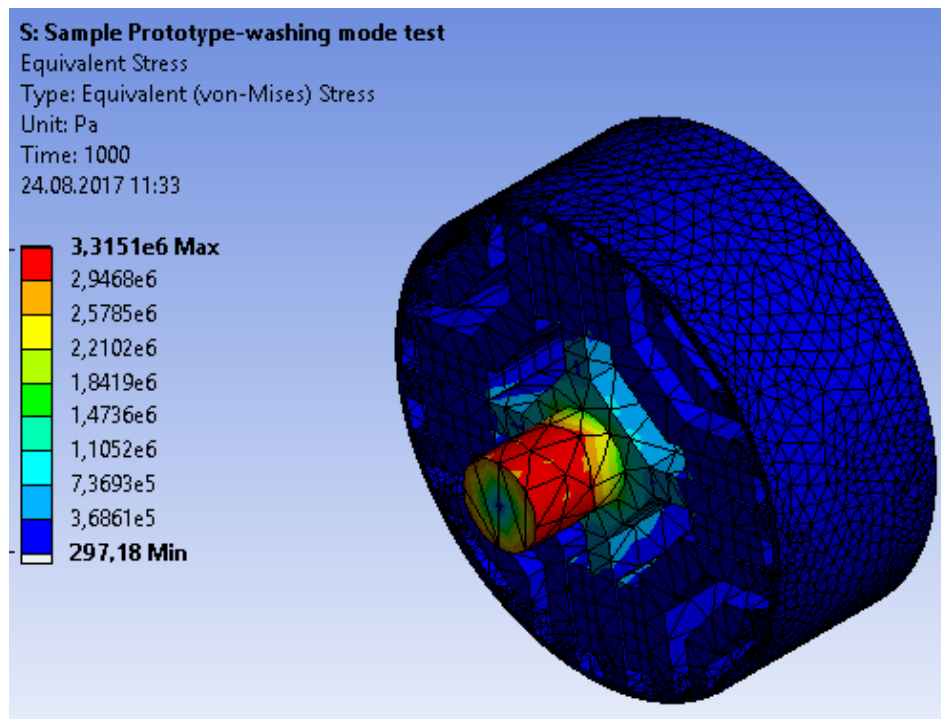


Figure 6.4 : Equivalent stress results of the sample prototype at 563 min⁻¹.

Similarly, the model is solved for equivalent stress given in Figure 6.4, Equivalent elastic strain given in Figure 6.5 and total deformation given in Figure 6.6.

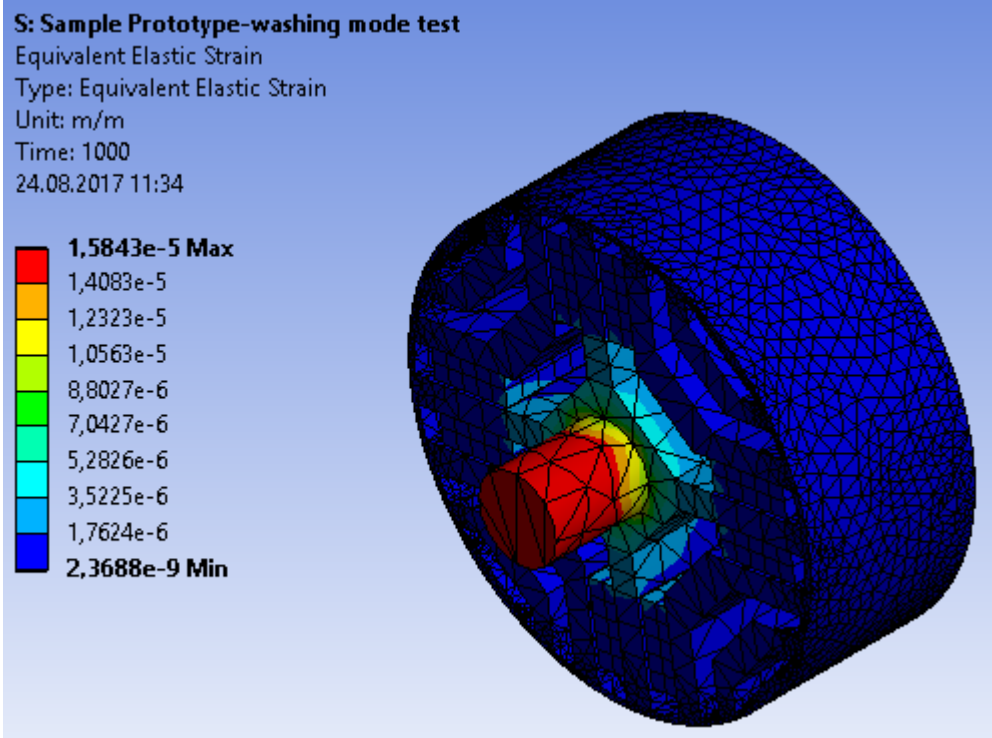


Figure 6.5 : Equivalent elastic strain results of the sample prototype at 563 min⁻¹.

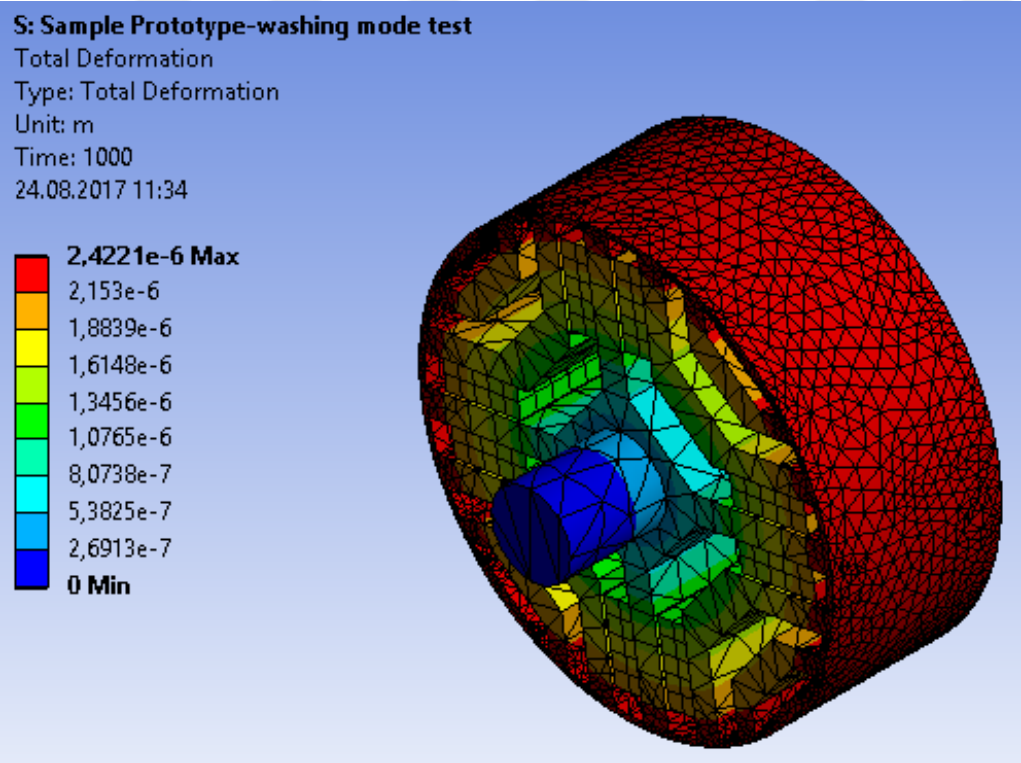


Figure 6.6 : Total deformation results of the sample prototype at 563 min⁻¹.

6.3 Spinning Mode Test of the Optimized Prototype

The spinning mode equivalent stress results for the optimized prototype are given in Figure 6.7.

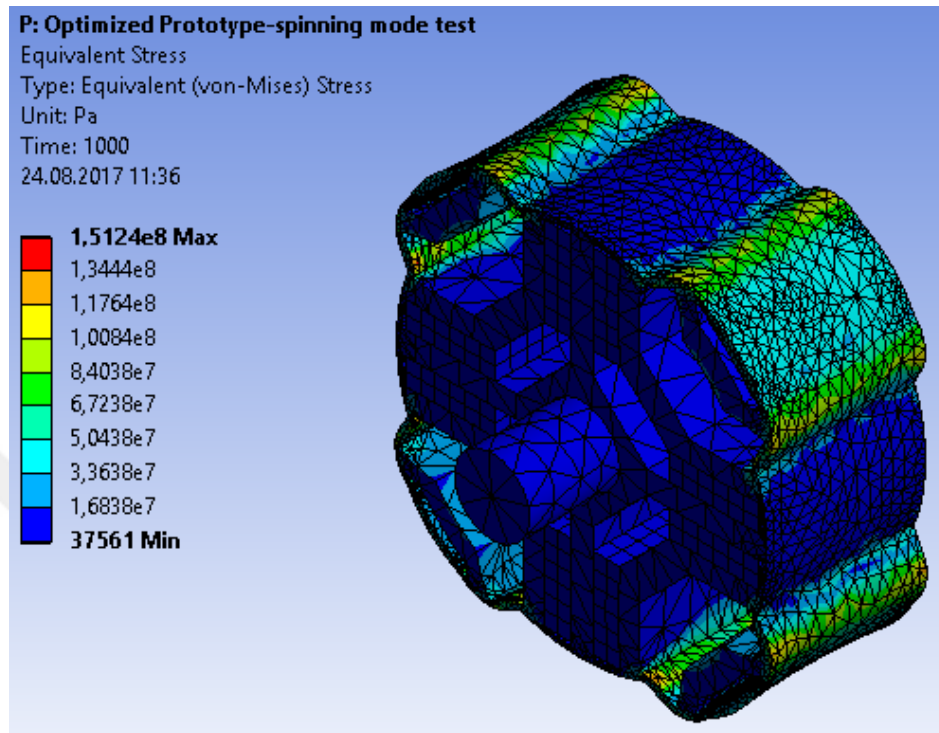


Figure 6.7 : Equivalent stress results of the optimized prototype at 13000 min^{-1} .

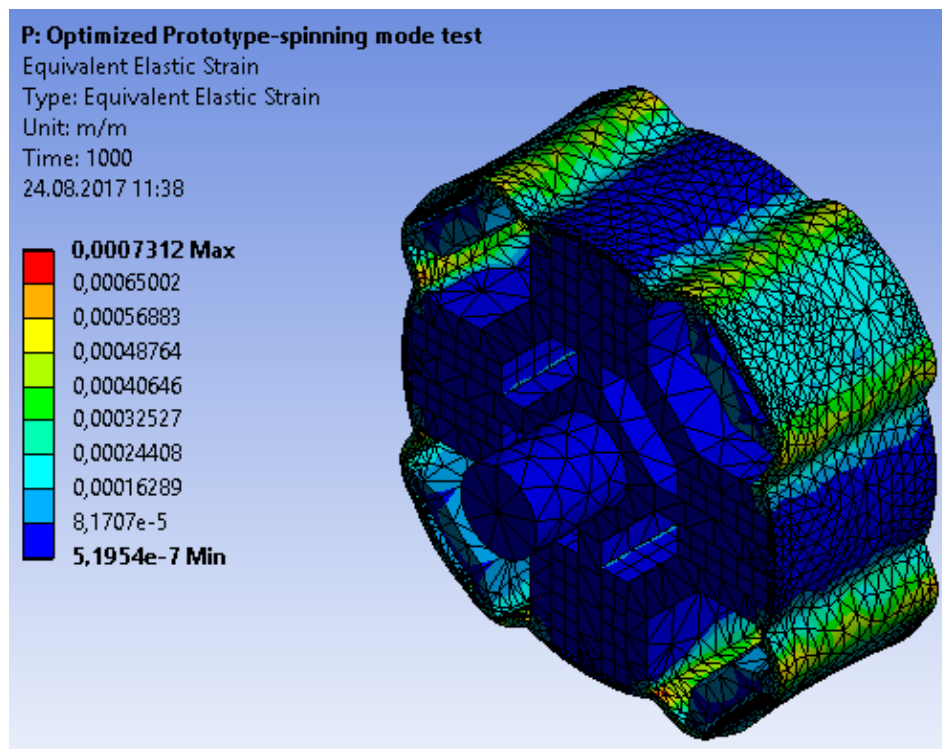


Figure 6.8 : Equivalent elastic strain results of optimized prototype at 13000 min^{-1} .

The equivalent elastic strain and total deformation results for spinning mode of the optimized prototype are given in Figure 6.8 and Figure 6.9, respectively.

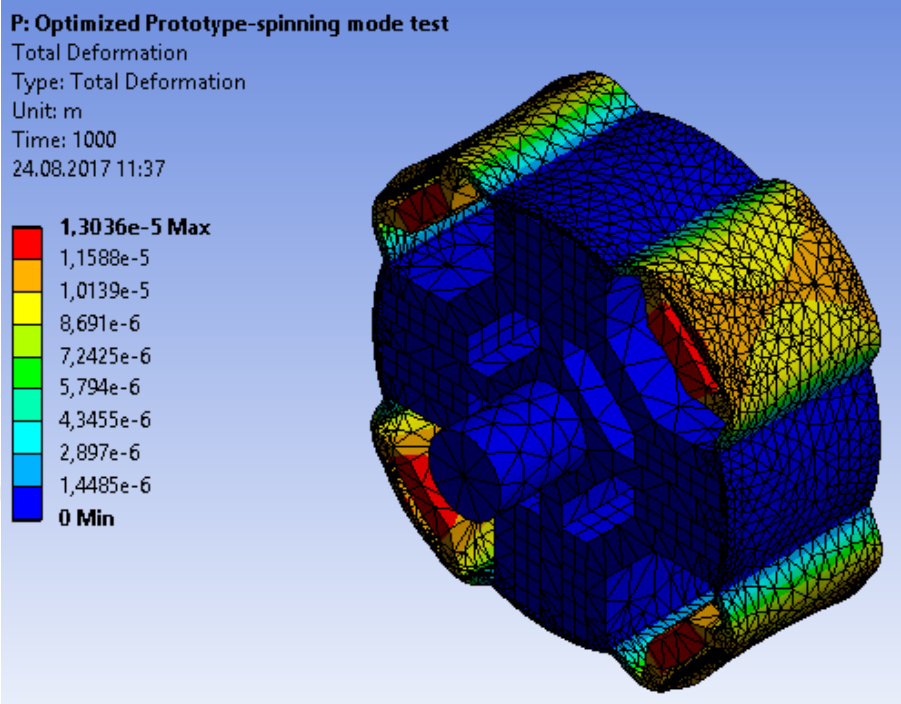


Figure 6.9 : Total deformation results of optimized prototype at 13000 min⁻¹.

6.4 Washing Mode Test of the Optimized Prototype

The equivalent stress results for the optimized prototype are given in Figure 6.10.

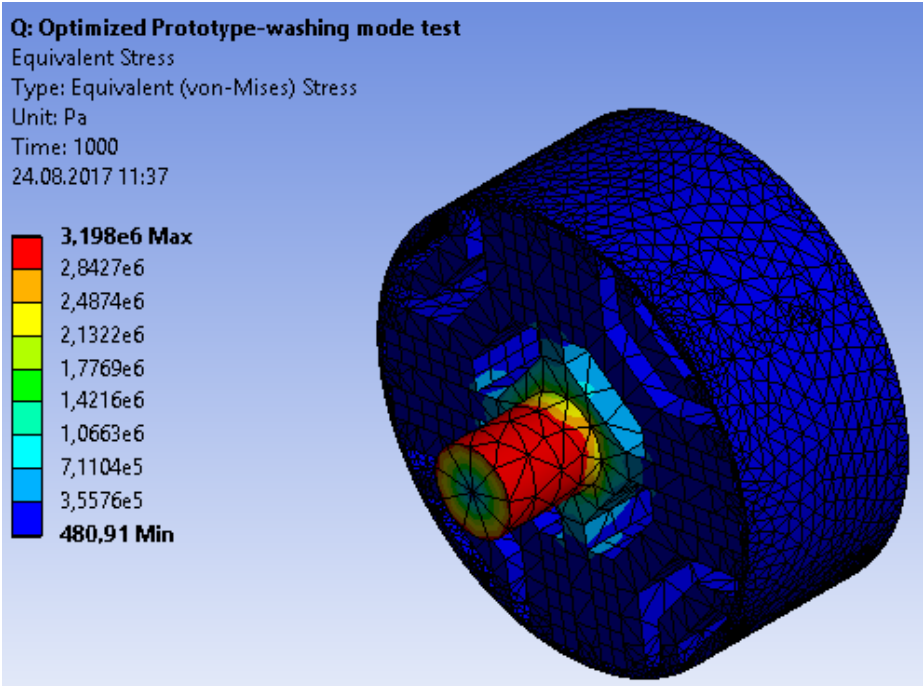


Figure 6.10 : Equivalent stress results of optimized prototype at 563 min⁻¹.

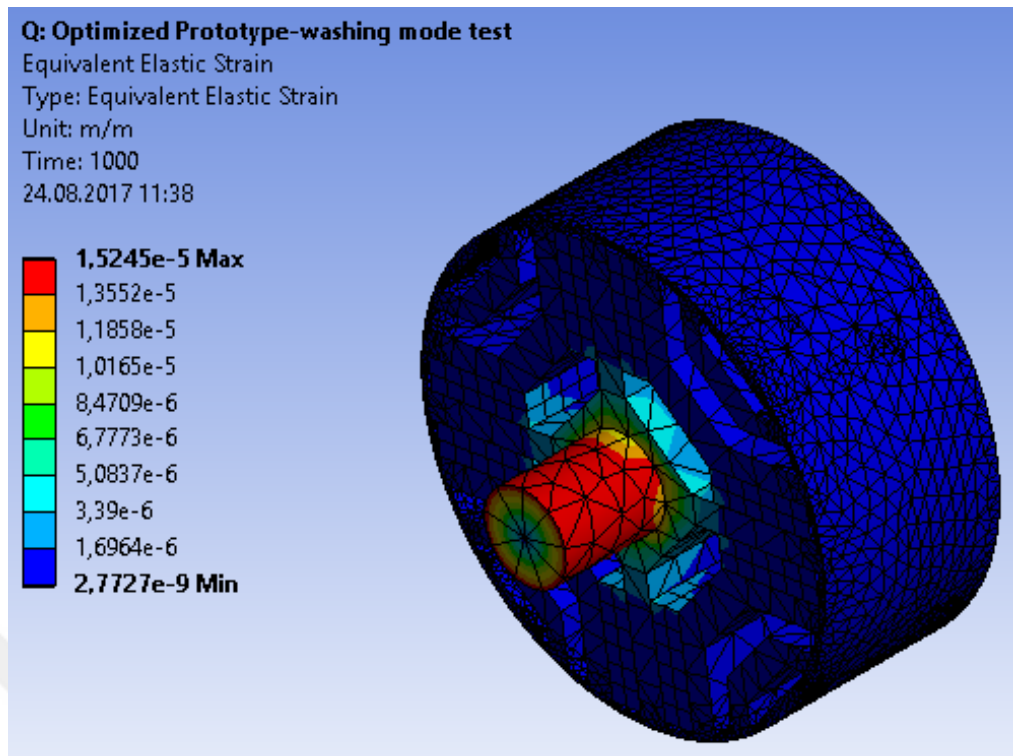


Figure 6.11 : Equivalent elastic strain results of optimized prototype at 563 min^{-1} .

The washing mode equivalent elastic strain and total deformation of the optimized prototype are given in Figure 6.11 and Figure 6.12, respectively.

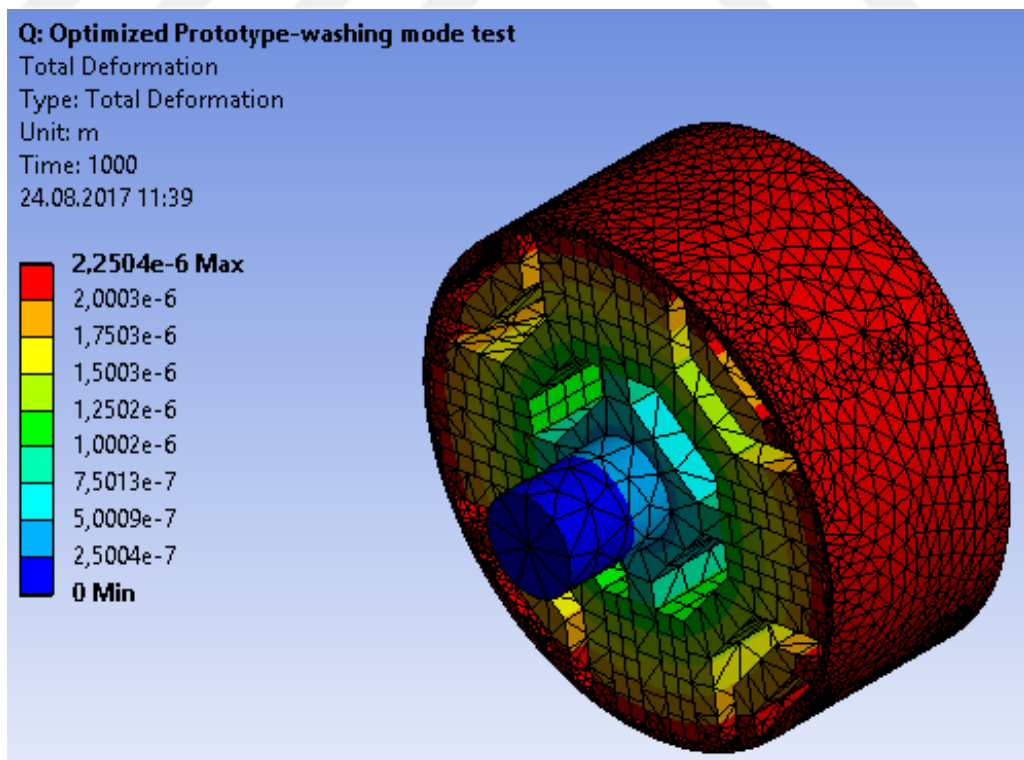


Figure 6.12 : Total deformation results of optimized prototype at 563 min^{-1} .

6.5 Comparison of Mechanical Stress Analysis Results

The comparison of the maximum mechanical stress values for both models are given in Table 6.2.

Table 6.2 : Mechanical stress analysis maximum results.

Model Test	Sample Prototype		Optimized Prototype	
	Spinning	Washing	Spinning	Washing
Equivalent Stress [MPa]	199.46	3.31	151.2	3.2
Equivalent Elastic Strain [m/m]	0.00095	15.84e-06	0.00073	15.24e-06
Total Deformation [μm]	16.34	2.42	13.03	2.25

Referring to the mechanical analysis results, glue that is used between the magnets and the ferromagnetic material has a significant positive effect on the rotor deformation. Making the rotor more compact, the stresses and the maximum deformation are reduced. Moreover, from the mechanical results in Table 6.2 it is clearly seen that the optimized motor is advantageous also in mechanical aspect. Larger magnets and smaller rotor radius, makes the optimized motor's rotor better than the sample motor. Maximum deformation of the optimized motor 13.03 μm , which is negligibly small.

7. RESULTS AND RECOMMENDATIONS

In this thesis, the performance optimization analysis of a sample PMSynRM, designed for washing machine application, is done so that the output torque is increased to the target value for the same rated current of the sample prototype at washing mode. The optimization work has been started from the air-gap length. Decrease of the air-gap has a significant effect on the output torque. However, at the same time the saturation of the stator and the torque ripple increases as the air-gap length is decreased. Together with the air-gap length, permanent magnet volume and position, and distance D effect is analyzed as further optimization work. Increasing distance D increases the output torque of the motor. However, for applications where larger volume of permanent magnet is required such method is not suitable since it narrows the barriers and decrease the available space for placing the magnets. Therefore, from this work it is concluded that the optimum D and magnet location is the same as those in the sample prototype. Further analysis includes the stator yoke and tooth optimization. This optimization work is done such that the output torque of the motor is kept around the target value of 1.2 Nm, and the magnetic field density of the stator yoke and tooth does not pass the limit of 1.3 T. For different air-gap length different number of turns/phase are used in the models analyzed in this section. The optimum model is chosen to be that with air-gap length of $g=0.8$ mm and number of turns/phase of $N=450$. Further optimization on this selected model includes the multilayer winding effect, ferromagnetic material type, slot opening, slot type and tooth bottom form analysis. Referring to the results of multilayer winding effect, such application does not prefer multilayered windings due to small space and difficult production. The type of ferromagnetic materials considered are M700 and M350 having quite similar B-H curves. However, the difference in the iron losses makes the model having M350 slightly more efficient. Considering the slot form, decreasing the slot opening decreases the reluctance between the stator and rotor therefore the output torque of the motor increases. However, since the minimum value of the slot opening acceptable is the diameter of the conductor used, for easier production the slot opening is kept the same as that of the sample prototype. Slot

opening height does not have a significant effect on the output torque of the motor, therefore this parameter is also kept the same as that of the sample prototype. The inner slot wall effect is also analyzed and seen to not have a significant effect on the output torque. Finally, the effect of outwards and inwards tooth bottom is analyzed and observed to have different impact on the output torque of the motor. Outwards tooth bottom increases both the torque ripple and the saturation of the stator, therefore the optimum tooth bottom is selected to be the inwards tooth bottom, the same as the sample prototype. The final optimized prototype obtained from the previous optimization analysis, is produced and tested. The test is done for different current values and for each case the experimental efficiency and the torque is compared to the FEM efficiency and torque, respectively. Moreover, the final optimized prototype is compared to the sample prototype thermal and mechanically. The thermal and mechanical analysis of both models performed, show that the optimized prototype is not only electromagnetically better, but also thermally and mechanically than the sample prototype.

Low slot fill factor used in this optimized prototype decreases its efficiency as the conductor diameter is required to be small. If the production with higher slot fill factor would be possible, the produced prototype would be much more efficient than the actual case, since it would be possible to use wider conductor. Lower phase resistance would increase the efficiency as well as decrease the thermal stress on the windings of the motor.

REFERENCES

- [1] **Kostko, J. K.** (1923). Polyphase reaction synchronous motors. *Journal of the American Institute of Electrical Engineers*, 42(11), 1162-1168.
- [2] **Anderson, A. F., & Cruickshank, A. J. O.** (1966). Development of the reluctance motor. *Electronics and Power*, 12(2), 48.
- [3] **Tap, A.** (2017). Design of Permanent Magnet Assisted Synchronous Reluctance Motor. Institute of Technology and Science, Department of Electrical Engineering, Istanbul Technical University, Master Degree Thesis, Istanbul.
- [4] **Bauer, P.F.** (1956). *U.S. Patent No. 2,733,362*. Washington, DC: U.S. Patent and Trademark Office.
- [5] **Risch, N.** (1956). *U.S. Patent No. 2,769,108*. Washington, DC: U.S. Patent and Trademark Office.
- [6] **Url-1** < http://www.ieeeahn.org/wiki/index.php/Peter_Lawrenson > , access date 10.09.2016
- [7] **Lawrenson, P. J., & Agu, L. A.** (1963, July). A new unexcited synchronous machine. In *Proceedings of the Institution of Electrical Engineers* (Vol.110, No.7, pp.1275). IET Digital Library.
- [8] **Lawrenson, P. J., & Agu, L. A.** (1964, August). Theory and performance of polyphase reluctance machines. In *Proceedings of the Institution of Electrical Engineers* (Vol. 111, No. 8, pp. 1435-1445). IET Digital Library.
- [9] **Lawrenson, P. J., & Gupta, S. K.** (1967, May). Developments in the performance and theory of segmental-rotor reluctance motors. In *Proceedings of the Institution of Electrical Engineers* (Vol. 114, No. 5, pp. 645-653). IET Digital Library.
- [10] **Cruickshank, A. J. O., Anderson, A. F., & Menzies, R. W.** (1971, June). Theory and performance of reluctance motors with axially laminated anisotropic rotors. In *Proceedings of the Institution of Electrical Engineers* (Vol. 118, No. 7, pp. 887-894). IET Digital Library.
- [11] **Rao, S. C.** (1978). *U.S. Patent No. 4,110,646*. Washington, DC: U.S. Patent and Trademark Office.
- [12] **Chalmers, B. J., & Mulki, A. S.** (1972). Design and performance of reluctance motors with unlaminated rotors. *IEEE Transactions on Power Apparatus and Systems*, (4), 1562-1569.
- [13] **Fratta, A., & Vagati, A.** (1992). A reluctance motor drive for high dynamic performance application. *IEEE Transactions on Industry Applications*, 28(4), 873-879.
- [14] **Kiryama, H., Kawano, S., Honda, Y., Higaki, T., Morimoto, S., & Takeda, Y.** (1998, October). High performance synchronous reluctance motor with multi-flux barrier for the appliance industry. In *Industry Applications Conference, 1998. Thirty-Third IAS Annual Meeting. The 1998 IEEE* (Vol. 1, pp. 111-117). IEEE.

- [15] **Boglietti, A., & Pastorelli, M.** (2008, November). Induction and synchronous reluctance motors comparison. In *Industrial Electronics, 2008. IECON 2008. 34th Annual Conference of IEEE* (pp. 2041-2044). IEEE.
- [16] **FratTA, A., Vagati, A., & Villata, F.** (1992). Permanent magnet assisted synchronous reluctance drives: drive power limits.
- [17] **Vagati, A.** (1998). *U.S. Patent No. 5,818,140*. Washington, DC: U.S. Patent and Trademark Office.
- [18] **Moghaddam, R. R., & Gyllensten, F.** (2014). Novel high-performance SynRM design method: An easy approach for a complicated rotor topology. *IEEE Transactions on Industrial Electronics*, 61(9), 5058-5065.
- [19] **Moghaddam, R. R., Magnussen, F., & Sadarangani, C.** (2012, September). Novel rotor design optimization of Synchronous Reluctance Machine for low torque ripple. In *Electrical Machines (ICEM), 2012 XXth International Conference on* (pp. 720-724). IEEE.
- [20] **Moghaddam, R. R., Magnussen, F., & Sadarangani, C.** (2012). Novel rotor design optimization of synchronous reluctance machine for high torque density.
- [21] **Boldea, I.** (1996). *Reluctance synchronous machines and drives* (Vol. 38). Oxford University Press.
- [22] **Staton, D. A., Miller, T. J. E., & Wood, S. E.** (1993, July). Maximising the saliency ratio of the synchronous reluctance motor. In *IEE Proceedings B (Electric Power Applications)* (Vol. 140, No. 4, pp. 249-259). IET Digital Library.
- [23] **Toliyat, H. A., Xu, L., & Lipo, T. A.** (1992). A five-phase reluctance motor with high specific torque. *IEEE Transactions on Industry Applications*, 28(3), 659-667.
- [24] **Vagati, A., Pastorelli, M., Francheschini, G., & Petrache, S. C.** (1998). Design of low-torque-ripple synchronous reluctance motors. *IEEE Transactions on Industry Applications*, 34(4), 758-765.
- [25] **Morimoto, S., Sanada, M., & Takeda, Y.** (2001). Performance of PM-assisted synchronous reluctance motor for high-efficiency and wide constant-power operation. *IEEE Transactions on Industry Applications*, 37(5), 1234-1240.
- [26] **Sanada, M., Hiramoto, K., Morimoto, S., & Takeda, Y.** (2003, October). Torque ripple improvement for synchronous reluctance motor using asymmetric flux barrier arrangement. In *Industry Applications Conference, 2003. 38th IAS Annual Meeting. Conference Record of the* (Vol. 1, pp. 250-255). IEEE.
- [27] **Armando, E., Guglielmi, P., Pastorelli, M., Pellegrino, G., & Vagati, A.** (2008, October). Performance of IPM-PMASR motors with ferrite injection for home appliance washing machine. In *Industry Applications Society Annual Meeting, 2008. IAS'08. IEEE* (pp. 1-6). IEEE.
- [28] **Bianchi, N., Bolognani, S., Bon, D., & Dai Pre, M.** (2006, October). Rotor flux-barrier design for torque ripple reduction in synchronous reluctance motors. In *Industry Applications Conference, 2006. 41st IAS Annual Meeting. Conference Record of the 2006 IEEE* (Vol. 3, pp. 1193-1200). IEEE.

- [29] **Sanada, M., Inoue, Y., & Morimoto, S.** (2011, September). Rotor structure for reducing demagnetization of magnet in a PMSynRM with ferrite permanent magnet and its characteristics. In *Energy Conversion Congress and Exposition (ECCE), 2011 IEEE* (pp. 4189-4194). IEEE.
- [30] **Barcaro, M., & Bianchi, N.** (2011, May). Torque components in integral-and fractional-slot IPM machines. In *Electric Machines & Drives Conference (IEMDC), 2011 IEEE International* (pp. 1340-1345). IEEE.
- [31] **Pellegrino, G., Guglielmi, P., Vagati, A., & Villata, F.** (2010). Core losses and torque ripple in IPM machines: Dedicated modeling and design tradeoff. *IEEE Transactions on Industry Applications*, 46(6), 2381-2391.
- [32] **Bianchi, N., Fornasiero, E., & Soong, W.** (2014, September). Optimal selection of PM flux linkage in a PM assisted synchronous reluctance machine. In *Electrical Machines (ICEM), 2014 International Conference on* (pp. 1341-1347). IEEE.
- [33] **Wang, K., Zhu, Z. Q., Ombach, G., Koch, M., Zhang, S., & Xu, J.** (2013, March). Optimal slot/pole and flux-barrier layer number combinations for synchronous reluctance machines. In *Ecological Vehicles and Renewable Energies (EVER), 2013 8th International Conference and Exhibition on* (pp. 1-8). IEEE.
- [34] **Ortega Dulanto, A.** (2015). Design of a Synchronous Reluctance Motor Assisted with Permanent Magnets for Pump Applications.
- [35] **Moghaddam, R. R.** (2007). Synchronous reluctance machine (SynRM) design. *Stockholm: KTH Royal Institute of Technology*.
- [36] **Honsinger, V. B.** (1971). The inductances L_d and L_q of reluctance machines. *IEEE Transactions on Power Apparatus and Systems*, (1), 298-304.
- [37] **Jin, J. M.** (2015). *The finite element method in electromagnetics*. John Wiley & Sons.
- [38] **Url-2** < <https://cogent-power.com/cms-data/downloads/m700-50a.pdf> > , erişim tarihi 05.05.2017
- [39] **Url-3** < <https://cogent-power.com/cms-data/downloads/m350-50a.pdf> > , erişim tarihi 05.05.2017
- [40] **Mahmoudi, M.** (2012). Thermal modelling of the synchronous reluctance machine.
- [41] **Staton, D., Hawkins, D., & Popescu, M.** (2009, May). Thermal Behaviour of Electrical Motors—An Analytical Approach. In *INDUCTICA Technical Conference Program, CWIEME, Berlin* (pp. 5-7).
- [42] **Motor Design Ltd.** (2015). Motor-CAD Help.
- [43] **Url-4** < <http://www.marathonelectric.com/generators/docs/manuals/thermal-life.pdf> > , access date 01.09.2017
- [44] **Url-5** < http://www.eclipsemagnetics.com/media/wysiwyg/datasheets/magnet_materials_and_assemblies/ferrite_magnets-ceramic_magnets_atasheet_v1.pdf > , access date 01.09.2017



CURRICULUM VITAE



Name Surname : Liridon XHELADINI

Place and Date of Birth : Tetova, 08.06.1992

E-Mail : lirxheladini@gmail.com

EDUCATION :

- **B.Sc.** : 2016, Istanbul Technical University, Faculty of Electric and Electronic, Electrical Engineering Department.

PUBLICATIONS, PRESENTATIONS AND PATENTS ON THE THESIS:

- **Tap A., Xheladini L., İmeryüz M., Yılmaz M., Ergene L. T.**, "Effects of the stator design parameters on the torque performance of a PMSynRM," 2017 11th IEEE International Conference on Compatibility, Power Electronics and Power Engineering (CPE-POWERENG), Cadiz, Spain, 2017, pp. 346-351.
- **L. Xheladini, A. Tap, T. Aşan, M. Yılmaz and L. T. Ergene**, "Permanent Magnet Synchronous Motor and Universal Motor comparison for washing machine application," 2017 11th IEEE International Conference on Compatibility, Power Electronics and Power Engineering (CPE-POWERENG), Cadiz, Spain, 2017, pp. 381-386.
- **Tap A., Xheladini L., Aşan T., İmeryüz M., Yılmaz M., Ergene L. T.**, "Effects of the rotor design parameters on the torque production of a PMSynRM for washing machine applications," 2017 Intl Aegean Conference on Electrical Machines & Power Electronics (ACEMP), 2017 Intl Conference on Optimization of Electrical & Electronic Equipment (OPTIM), Brasov, Romania 2017.

- **L. Xheladini, A. Tap, T. Aşan, M. Yılmaz and L. T. Ergene**, “ Thermal and Mechanical Analysis of a Permanent-Magnet Assisted Synchronous Reluctance Motor for Washing Machines“, ELECO 2017 10th International Conference on Electrical and Electronics Engineering, November 30-December 2, 2017, Bursa.
- **Tap A., Xheladini L., İmeryüz M., Yılmaz M., Ergene L. T.**, "Sürekli Mıknatıs Destekli Senkron Relüktans Motorlarda Mıknatıs Yerleşiminin Performansa Etkisi“, 1. Ulusal Elektrik Enerji Dönüşümü Kongresi, 21-22 Eylül 2017, Elazığ.

